Evolution of the Spherical Cell Shape in Bacteria

A thesis presented in partial fulfilment of the

requirements for the degree of

Doctor of Philosophy

in

Genetics

at Massey University, Albany

New Zealand.

Paul Richard Jesena Yulo

2019

Abstract

Cell shape is an important feature of bacterial cells. It is involved in critical aspects of bacterial cell biology such as motility, growth, and the evasion of predators. Despite this, how cell shape has evolved in bacteria is unclear. For most rod-shaped bacteria, the maintenance of cell shape depends primarily on the bacterial actin-like protein, MreB. In this study, we show that the deletion of MreB from the rod-shaped model organism *Pseudomonas fluorescens* SBW25 results in the formation of aberrant spherical cells that have increased size and reduced fitness. This new MreB-null strain (Δ*mreB*) is susceptible to mechanical damage and grows poorly due to cell division defects. Furthermore, synthesized peptidoglycan (PG) chains were shorter and cell wall assembly was disorganised in this strain. A 1,000-generation evolution experiment comprised of multiple independent lineages produced spherical cells that have a reduced cell size and improved fitness. Mutations in the PG synthesis protein PBP1a were found across multiple lineages. Genetic reconstructions demonstrated that these mutations have a loss-of-function effect that reduced PG cross-linking and restored the ordered assembly of the cell wall, thereby reducing cell size and improving fitness in MreB-null cells. In one lineage, a five-gene deletion that included the gene coding for the outer membrane channel OprD was found to be beneficial. This deletion reduced cell size, improved fitness, and restored orderly cell wall construction. The mechanism responsible for this is unknown, but it may be related to modifications in septum localisation via the Min system. Finally, we show using phylogenetic analysis that PBP loss is a general trend in bacteria that evolved to become spherical, hinting at a plausible strategy for the evolution of the spherical cell shape from rod-shaped progenitors.

Acknowledgements

Table of Contents

List of Figures

List of Tables

Chapter 1

Introduction

Bacteria are commonly classified into three basic categories: rods, spirals, and spheres. Many of the best-known bacteria fall within these categories: *Escherichia coli* and *Bacillus subtilis* are simple rods; *Helicobacter pylori* is a common spiral; and *Staphylococcus aureus* is a typical coccus. Although this simple approach of grouping bacteria into basic shapes can be a convenient way to describe commonly studied species, it is far from an accurate account of the true diversity of bacterial cell shapes. To cite a few examples found in key text such as Bergey's Manual of Determinative Bacteriology (Holt *et al.*, 1994), bacteria can be oblongs or spheroids (*Pneumococcus*), star-shaped (*Stella*), or curved rods (*Caulobacter* and *Vibrio*). Furthermore, bacteria can modify their shapes by making specialised structures, such as extensions that act as appendages in *Caulobacter* (Mignolet, Panis and Viollier, 2018); or by switching between different forms in response to changing environments as seen in *Mycoplasma* (Feldner, Bredt and Kahane, 1983). If we also consider variations in cell size, then the range of bacterial types becomes even more staggering.

This thesis presents new insights into the genetic, molecular, and morphological consequences of evolving a rod-like organism into a spherical organism. In order to put this work into its historical and scientific context, I will review in this chapter the phylogeny of cell shape, then discuss the mechanisms responsible for the formation of cell shape (i.e. the structure and synthesis of the bacterial cell envelope). Following this, I will discuss the current understanding of the bacterial cytoskeleton, particularly MreB which is the main cytoskeletal determinant of the rod-like shape in bacteria. This overview will give a better understanding of the motivation for this study and provide a foundation for understanding the methods and results discussed in this thesis.

1.1. Evidence for the existence of rods first, then spheres

Bacteria are currently believed to have started out as rod-shaped cells. The primitive progenitors of bacteria were likely irregularly-shaped constructs resembling L-forms, but the first bacteria likely began development as rod-shaped cells upon the formation of the peptidoglycan (PG) cell wall (Errington, 2013). This argument is supported by the widespread distribution of rods in the bacterial domain, suggesting that this shape developed early in the course of bacterial evolution. Siefert & Fox (1998) showed that the deepest branches of a 16s rRNA phylogenetic tree of 180 species were made up of exclusively rod-shaped or filamentous species (Figure 1). Interestingly, as the tree branched out, many of the emerging clusters became mixed, having both rod-like and spherical species. Importantly, they noticed that when a branch has adopted a spherical shape, it no longer reverts to a rod-like shape, continuing to evolve with a spherical cell shape instead. This led Siefert & Fox (1998) to support the idea that the first bacteria were most likely rod-shaped, and that spherical cells evolved from these rods as an end-state morphology – an observation presented earlier by Stackebrandt & Woese (1979) and by Woese et al. (1982).
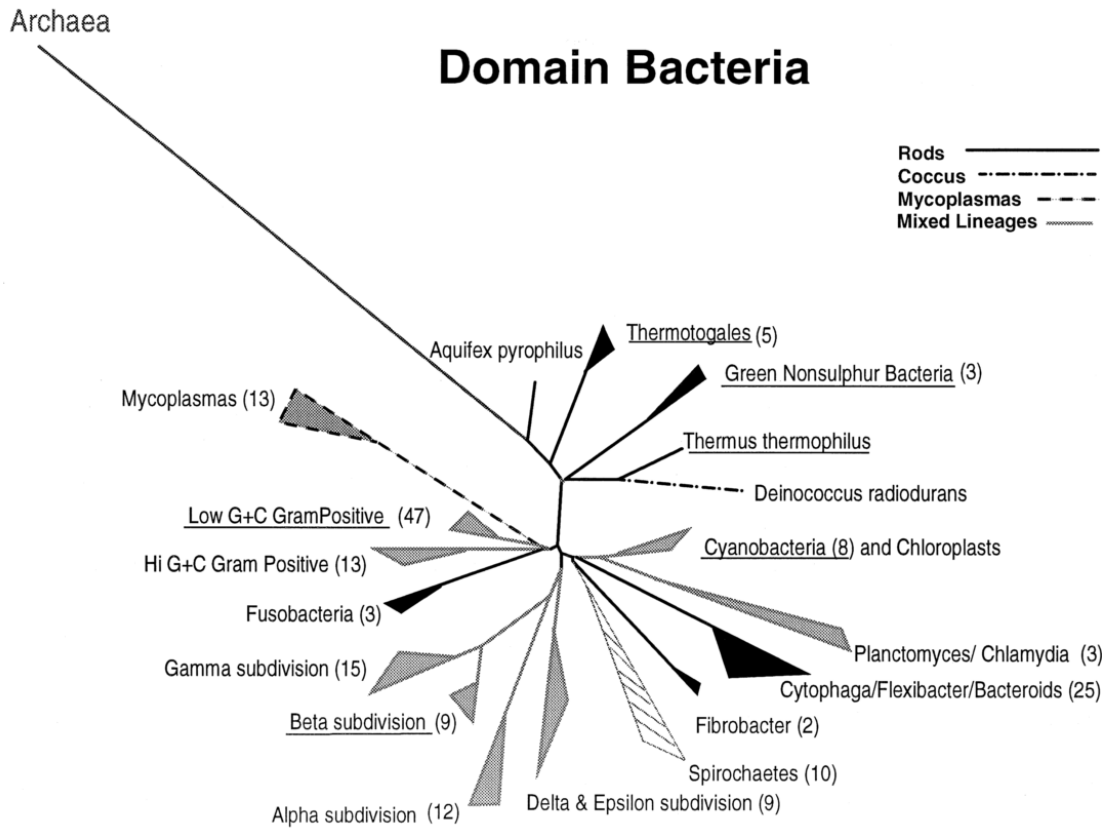
Figure 1 Phylogenetic tree of bacterial morphologies based on 16s rRNA sequences. The morphologies of each branch are represented as solid lines for lineages with purely rod-shaped cells, dotted lines for purely spherical cells, and dashed lines for lineages with both rod-like and spherical cells. Phylogenetic mapping based on 16S rRNA gene sequences show the deepest branches of the tree to be all rod-like, suggesting that the last common ancestor and the oldest lineages of bacteria had exclusively rod-like shapes, with round phenotypes occurring only later in evolutionary time. Adapted from Siefert & Fox (1998).

Tamames et al. (2001) also supported the idea that first bacteria were rod-shaped by analysing a cluster of genes involved in division and cell wall synthesis, also known as the *dcw* cluster. They found that gene order in the *dcw* cluster was better conserved in rods than in spheres, suggesting that rods were the first to acquire these genes, and that they likely formed first. These arguments support the notion that the first bacterial were indeed rod-shaped.

1.2. Cell shape has a selective value

The maintenance of characteristic cell shapes in bacteria implies that cell shape is not a mere coincidence, but an actively-regulated physical property that has selective value. Young (2007) argues that bacteria use cell shape to improve survival in the face of different selection pressures, the most basic of which being nutrient acquisition. Although variables like nutrient gradients and the ability to move towards food sources can influence a cell's ability to find nutrients, it is ultimately diffusion that delivers these nutrients from the external environment into the cell (Koch, 1996). This imposes a limit on how large a bacterial cell can become since it would need a large surface-to-volume ratio to support its needs. This is also the reason why many bacterial species have rod-shaped, filamentous, or vibroid cells as shapes that remain thin and instead increase in length provide a larger surface-to-volume ratio than spheres (Koch, 1996).
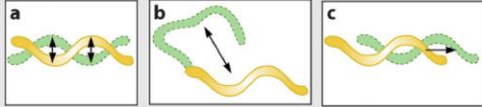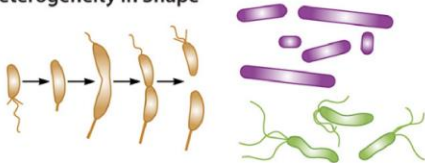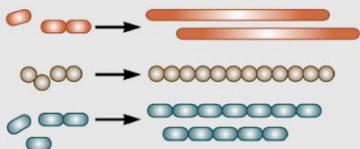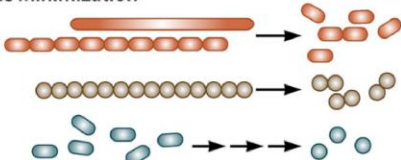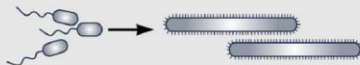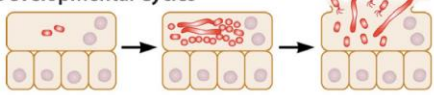
Another factor that can be strongly influenced by shape is motility. Mitchell (2002) demonstrated that energy costs for active movement can vary by as much as $1\text{x}10^5$ power (ergs) in cells that change in shape or size at sub-micron scales. The effect of shape on motility is further illustrated in *E. coli* cells that move more slowly when compared to a filamenting-mutant phenotype (Maki *et al.*, 2000) or swim in a different direction when shape is mechanically altered (Takeuchi *et al.*, 2005) (Figure 2). Different shapes have also been hypothesized to allow bacteria to swim better in various environments. An interesting example is *Helicobacter pylori*, a human pathogen with a characteristic corkscrew appearance. It has been shown that *H. pylori* uses its shape to travel through the thick mucus layer of the stomach epithelium to allow colonization, and that loss of this shape actually reduces their ability to colonise the stomach (Montecucco and Rappuoli, 2001).
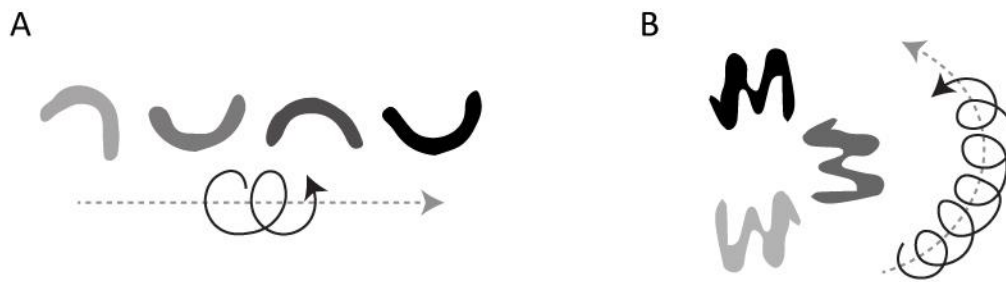
Figure 2 Artificially imposed cell shapes affect the motility of genetically identical *E. coli* cells. Time-lapse microscopy captured (A) crescent-shaped cells swimming in a straight line, and (B) tightly wound spiral-shaped cells swimming in a counter clockwise circle. Adapted from (Takeuchi *et al.*, 2005).

Cell shape can also influence survival by affecting other selective pressures such as predation, surface attachment, and passive dispersal (Young, 2006; Yang, Blair and Salama, 2016). In aqueous environments, bacterial predators such as heterotrophic nanoflagellates are estimated to graze between 25% to 100% of phytoplankton, including bacteria, in one day (Sherr and Sherr, 1994, 2002), imposing a substantial selective pressure on bacteria. It is estimated that approximately 50% of bacterial mortality in open oceans can be attributed to grazing by protists (Fuhrman and Noble, 1995). To survive, bacteria exhibit morphological plasticity that helps them evade predation (Pernthaler, 2005). Bacterial capture can be affected by irregularities in size and shape – filamentous bacteria can become too large for ingestion, exceptionally tiny cells may escape capture more easily, and the formation of strong surface attachments and biofilms may help reduce predation pressure (Jürgens and Matz, 2002; Pernthaler, 2005). In deep aquifers, most bacteria that are recovered are cocci or coccoid rods (Weiss *et al.*, 1995). Using artificial geological media and gravity filtration, Weiss *et al.* (1995) demonstrated that smaller, coccoid cells are able to move more rapidly through geological strata than rod-shaped cells, possibly showing a benefit to why rod-shaped cells would gain an advantage in becoming spherical. An insightful discussion of the different functional consequences of cell shape is elaborated further by Yang, Blair and Salama (2016), and is summarised in Table 1.

Table 1 Cell shape variation and functional consequences in bacteria (Yang, Blair and Salama, 2016).

Morphological Feature/Shape	Example Organism(s)	Functional Consequence
Curvature	*Caulobacter crescentus* *Vibrio cholerae* *Vibrio parahaemolyticus*	Cell curvature enhances surface colonization in aquatic environments with moderate flow.

Helical	*Helicobacter pylori*
	Campylobacter jejuni
	Spirochetes sp.
	  Spirochaeta aurantia
	  Leptospira interrogans
		Helical shape increases torque, which can enhance speed and facilitate escape from viscous solutions.

Waves	*Spirochetes* sp.
	  Borrelia burgdorferi
	  Treponema pallidum
		Flat-wave morphology allows alternative motility in gel-like media:
		a) wriggling
		b) lunging
		c) translocating

Heterogeneity in Shape	*Caulobacter crescentus* *Helicobacter pylori* *Mycobacterium tuberculosis*	Asymmetric growth and division can contribute towards directional motility, daughter cells with differing cell fates, and the formation of heterogeneous populations with varying susceptibility to antibiotics and other stresses. Increase/enhance successful adaptation to different host environments.
Filamentation	*Legionella pneumophila* *Streptococcus pneumoniae* Uropathogenic *Escherichia coli*	Evade phagocytosis-mediated killing (harder to engulf long filaments). Filaments can promote slow, ligand-mediated uptake and invasion. Increase/enhance attachment to host surfaces/cells. Promote/facilitate the development of antibiotic resistance (promote/enhance the emergence of beneficial mutations in response to stress).
Size Minimization	*Moraxella catarrhalis* *Neisseria meningitidis* *Salmonella typhimurium* *Streptococcus pneumoniae*	Cell size minimization helps to avoid complement-mediated killing by the host. Mucosa-associated bacterial lineages show size minimization from rods to cocci.
Swarm Cell Differentiation	*Pseudomonas aeruginosa* *Proteus mirabilis* *Vibrio parahaemolyticus*	Surface sensing via rotational inhibition of a polar flagellum elicits genetic reprogramming events that can lead to cell elongation and expression of factors which promote swarming motility.
Developmental Cycles	Uropathogenic *Escherichia coli* *Chlamydia* sp. *Rickettsia* sp.	Morphological changes associated with developmental cycles provide a mechanism for bacterial pathogens to grow intracellularly, subvert host immunity and facilitate subsequent rounds of invasion and infection. *Chlamydia* sp. and *Rickettsia* sp. developmental cycles are not pictured here.
Bacterial Appendage Number & Placement Flagella	*Borrelia burgdorferi* *Campylobacter jejuni* *Helicobacter pylori*	Flagella placement determines distinct modes of motility and morphological characteristics crucial for nutrient and niche acquisition.
Stalks or Prosthecae	*Asticcacaulis biprosthecium* *Asticcacaulis excentricus* *Caulobacter crescentus*	Stalks increase overall surface area and can allow for enhanced nutrient acquisition. Stalk elongation allows bacteria to physically separate from competitors.

The examples discussed above demonstrate that cell shape is a critical characteristic of bacterial morphology, one that is actively made and maintained throughout the cell cycle for adaptive purposes. In the following section, I will discuss the characteristics of the bacterial cell envelope which plays an important role in determining cell shape.

1.3.   The bacterial cell envelope

The bacterial envelope is made up of three main parts: the cell membrane, the PG layer, and the outer membrane which is present in many bacteria. I will first discuss the characteristics of the inner and outer membranes to provide context, then focus on the PG layer which provides the mechanical basis of cell shape.

1.3.1.   The cytoplasmic or inner membrane

The cytoplasmic or inner membrane (IM) is a lipid bilayer that acts as a boundary separating the internal space of the cell from its external environment (Figure 3). It holds important structures such as channels, transporters, receptors, and enzymes involved in the synthesis of other components of the membrane (Akiyama, 2009). Among these are lipoproteins and transmembrane α-helical proteins involved in cell signaling (Dufresne and Paradis-Bleau, 2015). It is also involved in metabolic processes that occur in the periplasm or the space between the inner and outer membranes of the cell (Silhavy, Kahne and Walker, 2010).

1.3.2. The outer membrane

Bacteria can be classified as either Gram-positive or Gram-negative, based on their ability to retain the Gram stain in their cell wall (Gram, 1884). Gram-negative bacteria possess a second membrane bilayer beyond the PG cell wall called the outer membrane (OM). The OM is a selectively-permeable layer, allowing select substances to enter the cell either through passive diffusion, or active transport using β-barrel proteins or porins (Dufresne and Paradis-Bleau, 2015). The OM is an asymmetrical layer – the inner layer is formed by glycerophospholipids whereas the outer layer consists of lipopolysaccharides (LPS). This unique structure gives Gram-negative bacteria the ability to resist damage from large polar molecules and lipophilic compounds (Henderson *et al.*, 2016). In addition, the OM also plays a role in growth and metabolism, protection from antibiotics, and even in triggering the innate immune response in humans, making it an important component of the bacterial cell envelope (Henderson *et al.*, 2016). Some proteins embedded in the OM are even thought to influence cell shape by linking the OM and the PG layer (De Mot and Vanderleyden, 1994; Koebnik and Krämer, 1995). Examples are Omp and Lpp, major outer membrane proteins which, in *E. coli*, produce spherical cells when their coding genes are deleted (Sonntag *et al.*, 1978; Typas *et al.*, 2010).

1.3.3. PG cell wall

Beyond the cytoplasmic membrane is the PG cell wall. Gram-positive cell walls are thick layers of PG that contain teichoic and lipoteichoic acid components; whereas Gram-negative cell walls are made up of a thin layer of PG inserted between an outer and inner membrane (Figure 3).
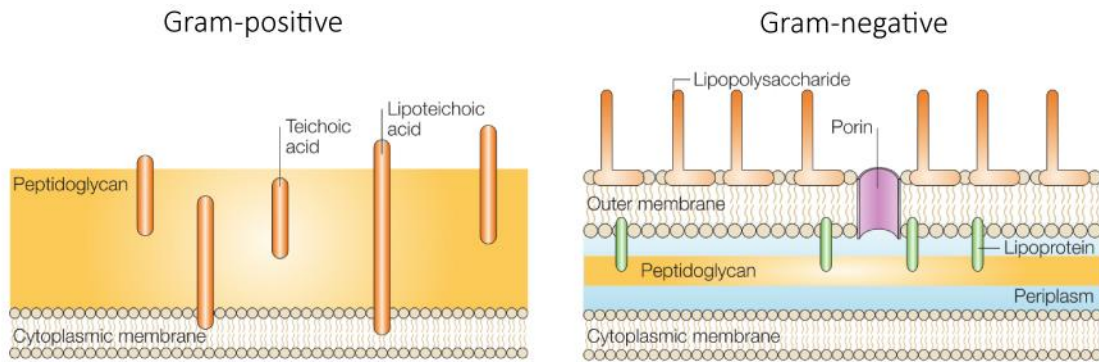
Figure 3 Gram-positive and Gram-negative cell walls. The Gram-positive cell wall is composed of multiple layers of PG formed outside the cytoplasmic membrane. Teichoic acids link the layers of PG together, and lipoteichoic acids link the PG to the cytoplasmic membrane. The Gram-negative cell wall is composed of an inner and outer membrane, and a thin layer of PG found in the periplasmic space formed between the two membranes. Embedded in the outer membrane are porins, lipopolysaccharides, and lipoproteins. Porins are channels that allow small hydrophilic molecules to pass across the outer membrane; whereas lipoproteins link the outer membrane to the PG layer. Adapted from Cabeen and Jacobs-Wagner (2007).

Bacterial cell shape is a characteristic attributed to the structure of PG, and to the enzymes that continually build and remodel it (Young, 2003). Most bacteria have a cell wall that provides shape and protection against osmotic pressure. This integral structure is composed of glycan chains linked together by peptide bridges, which together make up PG. The basic glycan chains are composed of two precursors: N-acetylglucosamine (NAG) and N-acetylmuramic acid (NAM). These are connected by a β-1,4 glycosidic bond which form long alternating strands of NAG and NAM (Figure 4A). Each NAG is connected to a short peptide chain that extends from it at a right angle. These peptide chains are cross-linked to other peptide chains from flanking glycan strands through the action of transpeptidases (Figure 4B) (Casey *et al.*, 2008). Together, these components form a strong mesh that provides structure and protects against osmotic lysis (Cabeen and Jacobs-Wagner, 2005).
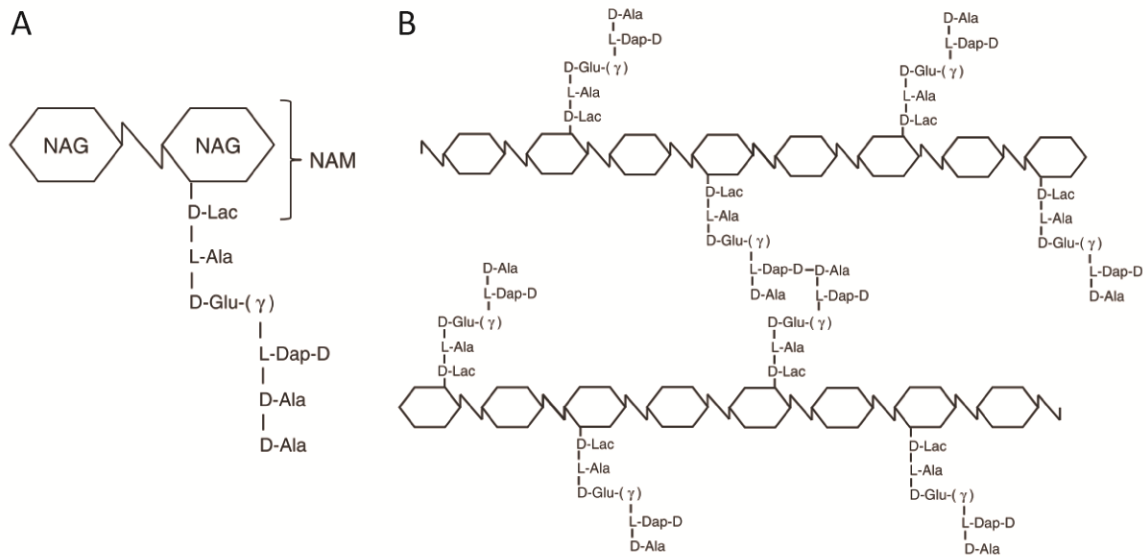
Figure 4 Chemical composition of PG. A) The basic PG subunits NAG and NAM. B) Representation of PG mesh showing glycan chains linked by pentapeptide cross-bridges. Adapted from Cava and Pedro (2014).

The cell wall was first believed to be purely rigid since PG removed from *E. coli* retains the native shape of normal living cells (Weidel, Frank and Martin, 1960; Weidel and Pelzer, 1964). However, it is now understood to be a flexible structure. Using low-angle laser light scattering, the cell wall of *E. coli* was observed to have the ability to expand up to 300% when affected by physical stress (Koch and Woeste, 1992). This observation is supported by Yao *et al.* (1999) who used atomic force microscopy to provide direct physical evidence of PG elasticity, and by Boulbitch, Quinn and Pink (2000) who derived equations that theoretically demonstrate the elasticity of PG.

In *E. coli* and *B. subtilis*, cell wall disruption can result in the formation of spheroplasts – round, osmotically sensitive cells (Weiss, 2013). Some bacteria also produce or can be induced to produce natural spheroplast variants which are also sensitive to osmotic effects (Errington *et al.*, 2016). This demonstrates that the cell wall confers a protective function against osmotic stress (Errington, 2017). Altogether, these observations describe a flexible yet strong cell wall – one that is able to adapt to osmotic stress and withstand internal pressures to maintain cell shape.

1.4.   PG synthesis

The synthesis and assembly of the PG cell wall is a critical aspect of bacterial biology. Having been under investigation for more than 50 years, we now have a good understanding of the major players involved in cell wall construction, mostly from studies using the model organisms *E. coli* and *B. subtilis*. However, recent advances have prompted a rethink of the behaviour of some of the major enzymes involved in this process, which I will discuss below.

PG construction begins with the synthesis of the precursor UDP-NAM-pentapeptide by the Mur proteins in the cytoplasm (Lovering, Safadi and Strynadka, 2012). This is ligated to a carrier lipid by the membrane-associated enzyme MraY, generating lipid I, which is then ligated to a NAG residue generating lipid II (Scheffers and Tol, 2015). Following this, lipid II is translocated or flipped from the cytoplasm to the outer face of the membrane for integration into the existing PG network (Lovering, Safadi and Strynadka, 2012). Upon translocation, lipid II is polymerised into glycan strands via a transglycosylation reaction, which are subsequently cross-linked to other glycan strands via a transpeptidation reaction (Sauvage *et al.*, 2008).

The final steps of assembly and modification are performed by enzymes called Penicillin Binding Proteins (PBPs). PBPs derive their name from their affinity to penicillins or beta-lactam antibiotics (Tomasz, 1979; Popham and Young, 2003). PBPs are classified into two categories: high molecular mass (HMM) PBPs, and the low molecular mass (LMM) PBPs. HMM PBPs have two major domains that are responsible for the polymerization and insertion of new PG strands into the pre-existing cell wall (Goffin and Ghuysen, 1998; Born, Breukink and Vollmer, 2006; Macheboeuf *et al.*, 2006; Lovering *et al.*, 2007). HMM PBPs can be further classified as either Class A or Class B PBPs, depending on the structure and function of their N-terminal domain. The N-terminal domain of Class A PBPs have transglycosylation or glycosyltransferase activity, elongating uncross-linked glycan chains. In Class B PBPs, the N-terminal domain plays a role in interacting with other proteins involved in the cell cycle (Holtje, 1998; Den Blaauwen *et al.*, 2008; Zapun, Vernet and Pinho, 2008). In both types of PBPs, the C-terminal penicillin-

binding domain performs transpeptidation, which cross-links adjacent glycan chains. Monofunctional enzymes (MGTs) that have glycosyltransferase domains similar to those in class A PBPs have also been identified, but their exact function is unknown (Reed *et al.*, 2011). LMM PBPs (also known as Class C PBPs) are monofunctional enzymes involved in cell separation, PG maturation, or PG recycling. For example, LMM PBPs in *E. coli* such as PBP5, PBP6, and PBP6b make stem peptides unavailable for cross-linking by cleaving the last D-alanine of stem pentapeptides (Typas *et al.*, 2012; Cava *et al.*, 2013). Other examples include PBPs such as PBP4 and PBP7 that perform endopeptidase activities by cleaving cross-links between PG strands (Vollmer and Höltje, 2004; Vollmer *et al.*, 2008).

Transglycosylation reactions were historically attributed to the function of only Class A PBPs (Sauvage *et al.*, 2008). However, this view was challenged by experiments in *B. subtilis* and *Enterococcus* spp. which showed that cells can grow (although poorly) in the absence of all Class A PBPs, suggesting the presence of another enzyme could be performing transglycosylation reactions (Mcpherson and Popham, 2003; Arbeloa *et al.*, 2004; Rice *et al.*, 2009). Recently, it was discovered that RodA has transglycosylation activity (Meeske *et al.*, 2016), and that growth defects of a *B. subtilis* strain lacking all aPBPs can be rescued by the overexpression of RodA (Meeske *et al.*, 2016; Emami *et al.*, 2017). Furthermore, RodA was also demonstrated to have TG activity in *E. coli* (Cho *et al.*, 2016).

Until recently, the most widely accepted model of cell wall construction posits that MreB guides the transglycosylation reactions of Class A PBPs, as well as the transpeptidation reactions of both Class A and B PBPs, directing the pattern of PG polymerisation and assembly (Typas *et al.*, 2012). MreB is a cytoskeletal element found in most rod-shaped bacteria, which performs a critical role in directional PG assembly during cell elongation (Errington, 2015). However, Cho *et al.* (2016) recently discovered that MreB and Class A PBPs operate in independent complexes and do not form distinct assemblies as previously believed. It was discovered that Class A PBPs had both a fast and diffusive motion, as well as a much slower movement speed (Lee *et al.*, 2016; Zhao *et al.*, 2017). This was interpreted by Zhao *et al.*, (2017) as short periods of fast diffusion spaced apart by temporary pauses. In addition, it was found that

MreB strongly interacts with Rod proteins in *E. coli*, which in turn interacts with PBP2, a Class B PBP (Morgenstein *et al.*, 2015). This complex (MreB-RodAZ-bPBP) is thus referred to as the "Rod complex" (Zhao *et al.*, 2017).

Based on these recent discoveries led Zhao *et al.* (2017) to propose a new scheme of PG synthesis called the "Break before Make" model (Figure 5). In this model, endopeptidases first cleave crosslinks in mature PG. From this break, the Rod complex generates a new PG template which is cross-linked to the existing cell wall through the action of Class B PBPs. Class A PBPs then generate additional strands that are crosslinked with the existing cell wall on one side, and with the PG strand generated by the Rod-complex on the other. The interaction between Class A PBPs and the Rod-complex is unknown and remains an open question in this model. This model reconciles previous models of PG synthesis with current discoveries and gives us a better understanding of the general pattern of cell wall construction in bacteria.
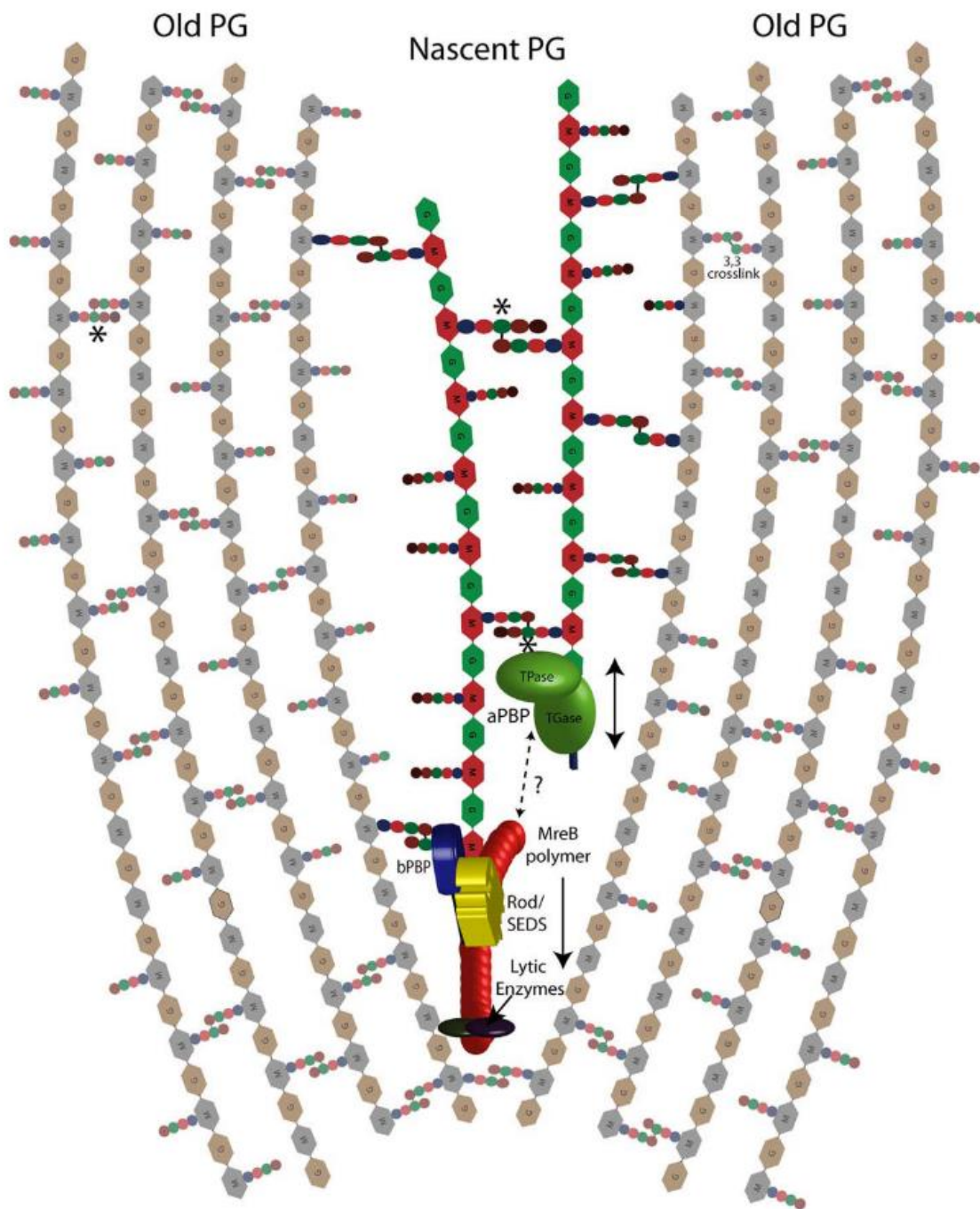
Figure 5 "Break before Make" model of PG synthesis. The process begins with Rod and MreB-associated lytic enzymes cleaving crosslinks in mature PG. From this, the Rod/SEDS complex generates a PG template that is cross-linked to the cell wall by bPBPs. Additional strands are generated by the TGase domain of aPBPs, which are then cross-linked with new PG on one side with mature PG on the other through the action of its TPase domain. The interaction of Class A PBPs with the Rod complex is undefined. Crosslinked pentapeptides are formed when a new PG strand containing a pentapeptide is crosslinked with another one (labelled with asterisks). PBP-independent 3,3 crosslinks are also represented, which are present only at low abundance under normal growth conditions. Adapted from Zhao *et al.* (2017).

1.5. Bacterial cytoskeleton

To spatially-organise and direct key cellular processes such as cell division, chromosome segregation, and intracellular transport, eukaryotic cells use cytoskeletal elements composed of three main structures: tubulin microtubules, intermediate filaments (IF), and actin microfilaments. Until the 1990s, the cytoskeleton was believed to have existed only in eukaryotes. Bacteria were simply thought to be unorganised bags with components randomly moving around inside (Ingerson-Mahar and Gitai, 2012). However, we now know that bacteria do indeed form highly organised internal structures that are coordinated by the action of bacterial cytoskeletal elements (Ingerson-Mahar and Gitai, 2012; Govindarajan and Amster-Choder, 2016). Bacterial homologues of the 3 eukaryotic cytoskeletal elements are now known to exist in bacteria (Matthew T Cabeen and Jacobs-Wagner, 2010) and understanding how these function independently is important for understanding how they might function when one is disrupted. I will describe their more or less independent functions below before moving on to the challenges involved in evolving cell shape.

1.5.1. Tubulin-like proteins

Tubulin is a dynamic, GTP-dependent microfilament that functions as a track for motor proteins in eukaryotes (Löwe and Amos, 2009). The most well-known homologue of tubulin in bacteria is FtsZ, a highly-conserved protein in free-living bacteria. FtsZ forms a contractile structure called the Z-ring that is composed of long filaments that use GTP hydrolysis to bend and pull the membrane inwards for septum formation (Li *et al.*, 2007; Erickson, Anderson and Osawa, 2010). Importantly, it also acts as a scaffold for other proteins that are necessary for cell division (Weihs *et al.*, 2018).

Other tubulin homologues in bacteria include TubZ in *Bacillus thuringiensis* (Larsen *et al.*, 2007), and RepX in *B. subtilis* which may have plasmid-partitioning functions (Matthew T. Cabeen and Jacobs-Wagner, 2010); and BtubA and BtubB in Prosthecobacter, whose functions are still unknown (Ingerson-Mahar and Gitai, 2012).

1.5.2. IF-like proteins

IF proteins form strong rods or fibres of dimeric α-helical coils that resist mechanical stresses in eukaryotic cells (Köster *et al.*, 2015). In bacteria, probably the best example of an IF-like protein is crescentin, or CresS. Similar to eukaryotic IFs, CresS has a coiled coil structure and self-assembles in a nucleotide-independent manner (Löwe and Amos, 2009). It is responsible for the bent-shape of *Caulobacter crescentus* (Figure 6). The deletion of CresS causes *C. crescentus* to lose its characteristic shape to become a straight rod (Ingerson-Mahar and Gitai, 2012).

Other examples of IF-like proteins have been found in bacteria, but their functions are not yet well understood. Examples of which are RsmP from *Corynebacterium glutamicum* and Ccrp from *Bdellovibrio bacteriovorus* (Ingerson-Mahar and Gitai, 2012). Similar to CresS, FilP from *Streptomyces coelicolor* also has a coiled coil structure that has been suggested to play a role in hyphal formation (Matthew T Cabeen and Jacobs-Wagner, 2010).
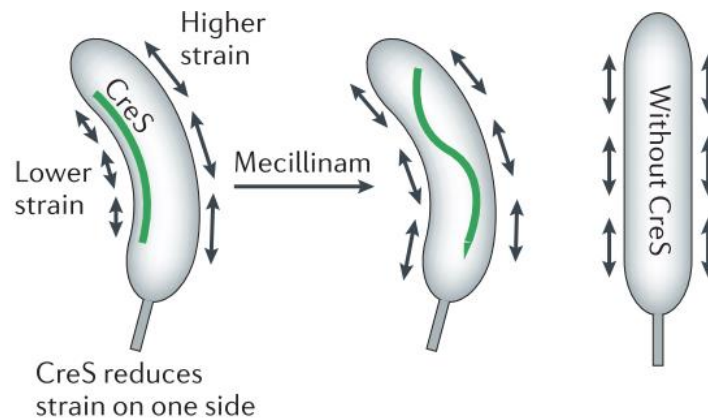
Figure 6 Crescentin (CreS) causes C. crescentus to grow with a bent shape by reducing strain on one side of the cell. Adapted from Typas et al. (2012).

1.5.3. Actin-like proteins

Actin-like proteins are present in all domains of life (Petek and Mullins, 2014). Actin-like proteins have a characteristic structure of four distinct domains stabilised by an ADP molecule. These proteins polymerise in the presence of ATP, and form either globular (G-actin) or filamentous (F-actin) structures (Ingerson-Mahar and Gitai, 2012).

In eukaryotes, actin is known to polymerise and undergo a treadmilling action wherein monomers are added to one end of the filament and removed from the opposite end (Naoz *et al.*, 2008). Similar characteristics are seen in bacterial actin homologues like MamK, ParM, and other plasmid-segregating homologues (Ozyamak, Kollman and Komeili, 2013). MamK forms filaments that organise magnetic vesicles, or magnetosomes, in *Magnetospirillum magneticum* (Pradel *et al.*, 2006; Bennet *et al.*, 2015). ParM is a plasmid-encoded actin-like protein involved in plasmid partitioning (Cabeen and Jacobs-Wagner, 2010).

In contrast, MreB, the major actin homologue responsible for determining cell shape in bacteria, has been demonstrated to have no intrinsic polarity and does not undergo treadmilling (Domínguez-Escobar *et al.*, 2011; van den Ent *et al.*, 2014; Schoenemann and Margolin, 2017), forming instead antiparallel double filaments. The structure and function of MreB will be further discussed in 1.6.

1.6. MreB – the major rod-shape determining protein

MreB is a highly conserved protein among most rod-shaped bacteria (Jones, Carballido-López and Errington, 2001) and has a very similar structure to eukaryotic actin (van den Ent, Amos and Löwe, 2001). MreB is a force-generating filament. Using a theoretical model, Lan et al. (2007) proposed that MreB modifies newly-synthesized PG strands by pre-stretching them prior to cell wall insertion. Evidence showing MreB has a direct influence on cell integrity was later provided by S. Wang et al. (2010) who showed using an optical trap experiment that in *E. coli*, approximately 50% of cell rigidity comes from MreB itself, showing that this actin-like protein contributes as much to mechanical integrity as the cell

wall. In contrast, to its role in providing bending stiffness, MreB does not provide longitudinal stiffness to cells (Tuson *et al.*, 2012).

1.6.1. MreB coordinates PG synthesis

The formation and maintenance of the rod shape is conferred by the Mre proteins, MreB, MreC, and MreD (Wachi *et al.*, 1989); RodZ (Alyahya *et al.*, 2009; Bendezú *et al.*, 2009); and the RodA-Pbp2 pair (Cho *et al.*, 2016). This complex, collectively called the Rod complex (or elongasome) is well-conserved in rod-shaped bacteria, and typically not found in cocci (Alyahya *et al.*, 2009; Carballido-Lopez, 2012). For this reason, the Rod complex is considered as the major determinant of the rod shape in bacteria (Jones, Carballido-López and Errington, 2001; Carballido-López, 2006)

Importantly, the spatial coordination of the Rod complex is conferred by MreB (Jones, Carballido-López and Errington, 2001; van den Ent, Amos and Löwe, 2001). The loss or depolymerization of MreB causes deformities in rod-shaped cells which ultimately grow as spheres (Jones, Carballido-López and Errington, 2001; Gitai, 2005; Bendezú *et al.*, 2009). MreB's sub-cellular localisation has been the subject of debate over the last two decades. Early works using fluorescent techniques indicated that MreB exists as helical filaments inside the cell (Defeu Soufo and Graumann, 2004; Figge, Divakaruni and Gober, 2004; Vats and Rothfield, 2007). This was supported by the observation that MreB-associated proteins involved in cell wall construction had a similar localisation pattern to MreB (Shih, Le and Rothfield, 2003; Leaver and Errington, 2005; Kawai, Daniel and Errington, 2009). This understanding was later challenged by a high-resolution electron cryotomography study stating that MreB filaments cannot be found inside bacteria (Swulius *et al.*, 2011). This was followed by a study showing that the helical patterns produced by a YFP-tagged MreB was an artefact of the fused YFP tag, and not a native characteristic of MreB (Swulius and Jensen, 2012).

Recent studies once again suggested the MreB does indeed form filaments around the cell (Salje *et al.*, 2011; Olshausen *et al.*, 2013; Reimold *et al.*, 2013; van den Ent *et al.*, 2014). These were used by

Errington (2015) to propose a revised model for MreB under the assumption that MreB does indeed form filaments that migrate with PG strand insertion, but with greater emphasis on the orientation of the filaments relative to cell shape. In this model, MreB filaments coordinate PG synthesis in a snake-like manner therefore driving the elongation of the smooth cylinder. In irregular rods, MreB filaments are observed as shorter structures, the result of the irregular cell shape interfering with filament formation. These filaments then go on to provide a corrective remodelling to the cell wall leading to the resumption of an orderly assembly of the cell wall (Figure 7).

a Regular, cylindrical shape
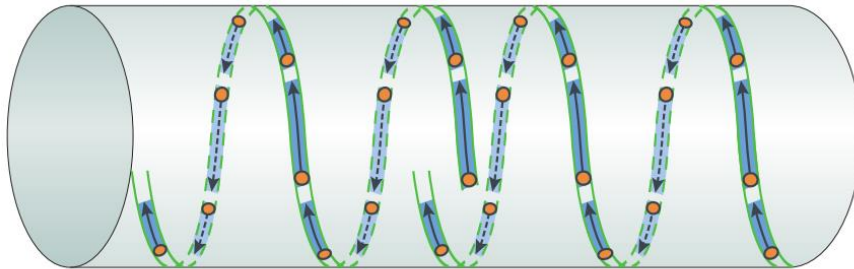
b Irregular shape
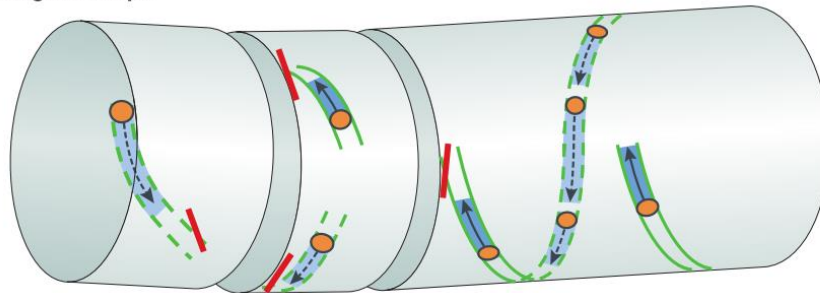
Figure 7 Revised model for the role of MreB in shape determination. (A) In a regularly-shaped cylinder, MreB filaments (solid and dashed green lines) elongate in response to the uniform cylindrical shape. PG-synthetic complexes are recruited (orange circles) to create new PG strands (blue shading) in directions that guided by the MreB filaments (as shown by the arrows). This activity is also the driving force behind the movement of MreB filaments. Two MreB filaments are shown, but multiple non-overlapping filaments can form in these cells. (B) In a cell with abnormal morphology, MreB can only form short filaments due to sites of incompatible geometry (indicated in red). Even then, short filaments are thought to correct aberrant geometry, thereby restoring a regular cylindrical cell shape. In both figures, solid and dashed lines represent the front and rear views, respectively, of the bacterial cell. Adapted from Errington (2015).

More recently, the laboratory of Ethan Garner presented an updated view of how MreB filaments orient to form and maintain the rod shape in bacteria (Hussain *et al.*, 2018). Using total internal reflection microscopy, Hussain *et al.* (2018) demonstrated that MreB filaments are able to sense the shape of bacteria, orienting along surfaces with the greatest negative curvature (Figure 8A). This allows MreB filaments to find the correct orientation and move around the circumference of rod-shaped cells. In contrast, MreB filaments move in all directions in spherical bacteria. They further found that MreB allows spherical bacteria to regenerate a rod shape by locating small surface bulges wherein MreB filaments can move in an oriented way, allowing the formation of the rod shape (Figure 8B). The group concludes that MreB thus creates the rod shape by directing cell wall synthesis by sensing and reinforcing differences in cell curvature.
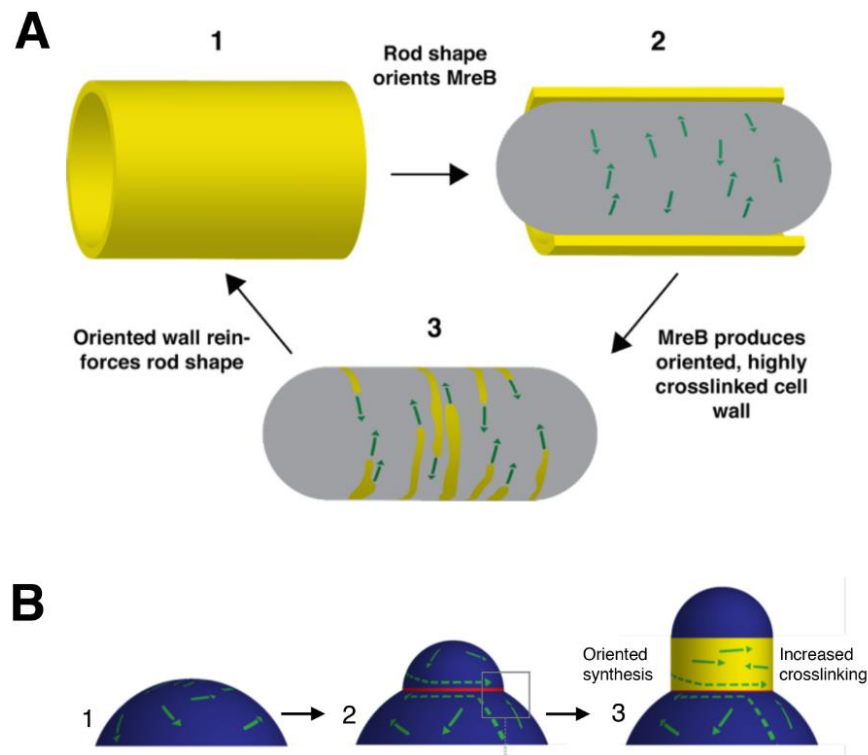
Figure 8 Model for MreB filament orientation. (1) In a rod-shaped cell, MreB filaments to orient along a single curved axis. (2) The direction of MreB motion follows this curved axis, (3) which directs the insertion of new cell wall material around cell, reinforcing the rod shape. B) (1) MreB motion is isotropic in spherical cells, following no specific axis. (2) the presence of an outward bulge creates a curved axis (red line) that initiates rod shape formation. (3) MreB filaments that reach the curved axis preferentially align to and rotate around the neck of the bulge, creating an area with aligned MreB motion which propagates rod-shape formation (yellow area). Adapted from (Hussain *et al.*, 2018)**.**

1.6.2. MreB can influence the cell division machinery

Aside from coordinating cell elongation, MreB is also known to interact with FtsZ for correct septum synthesis, thereby linking it to the cell division machinery. To understand this relationship, it is necessary to first discuss the cell division machinery.

Cell division in model organisms such as *E. coli* and *B. subtilis* begins with the polymerization of FtsZ, forming a contractile Z-ring at the centre of the cell via a treadmilling-action (Schoenemann and Margolin, 2017). There, it coordinates with other proteins to initiate and guide cell division (Harry, Monahan and Thompson, 2006; Adams and Errington, 2009; de Boer, 2010). Z-ring formation is a coordinated process. Studies have revealed that approximately 70% of FtsZ localizes into helical patterns at any given time (Stricker *et al.*, 2002; Anderson, Gueiros-Filho and Erickson, 2004), as a result of restricted diffusion (Niu and Yu, 2008). These patches are dynamic, migrating continuously and searching for new septation sites (Thanedar and Margolin, 2004). Aside from its role as a cell division coordinator, FtsZ also provides a contractile force that bends the inner membrane (Erickson, Anderson and Osawa, 2010). This bending is initially resisted by the rigid cell wall but is eventually overcome by the recruitment of proteins that remodel the cell wall (Erickson, Anderson and Osawa, 2010).

In line with this, Fenton & Gerdes (2013) demonstrated that MreB is recruited to the Z-ring and interacts with FtsZ in *E. coli* for the transfer of cell-wall biosynthetic enzymes from lateral growth activity to septal PG synthesis. Interestingly, they showed that the recruitment of a mutated form of MreB into the Z-ring results in elongated cells that are unable to divide, having Z-rings that have no PG synthesis activity. Furthermore, they observed that PBP2 and PBP1B foci that are normally present in the septum of dividing WT *E. coli* cells (in addition to their localisation to MreB) are not seen in cells that had the mutated form of MreB. In their model, Fenton & Gerdes (2013) propose that the recruitment of PBP2 and PBP1B from the elongasome to the cell division complex (divisome) through the action of MreB, plays an essential role in septal and/ or pre-septal PG synthesis. Thus, this shows that in rod-shaped bacteria, MreB is not only important to cell elongation, but to cell division as well.

1.6.3. Loss of MreB or MreB-like proteins lead to shape defects and cell death

Although MreB is regarded as the main rod-shape determining gene, it is not the only protein performing this function. In *B. subtilis*, two other proteins resembling MreB have been found – these are MreBH and Mbl. The deletion of each of these proteins produces slightly different effects, but in general, these lead to cells with shape defects that are only viable upon the addition of supplemental magnesium (Figure 9) (Carballido-López and Errington, 2003; Formstone and Errington, 2005; Kawai, Daniel and Errington, 2009). In *Spiroplasma* and *Haloplasma*, even more (five to seven) MreB homologues have been found. The exact function of these homologues are unknown, but their phylogeny led Ku, Lo and Kuo, (2014) to conclude that these multiple MreB homologues are the result of independent ancient duplications. In bacteria that have only one MreB homologue, such as *E. coli* (Turner *et al.*, 2013) and *C. crescentus* (Figge, Divakaruni and Gober, 2004), MreB is essential. The loss or deletion of MreB in these organisms causes a loss in shape, ultimately leading to cell death.
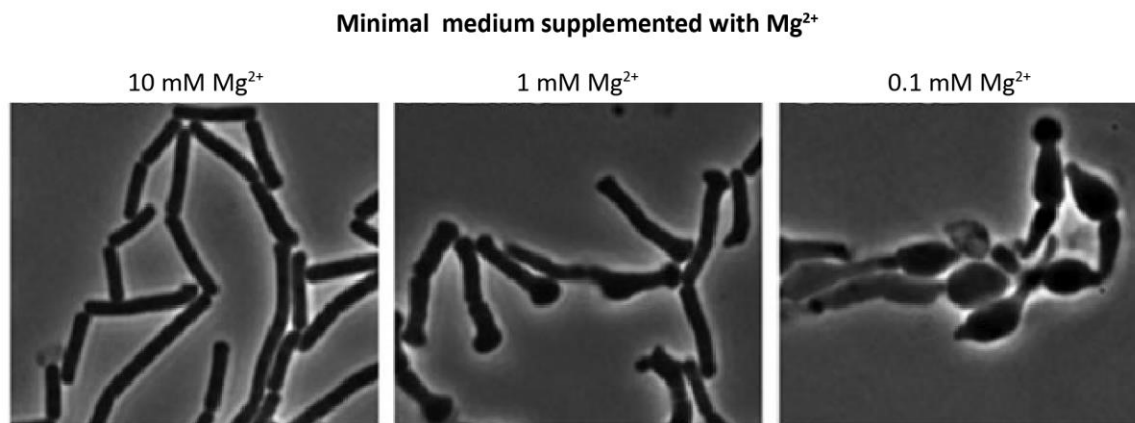
Figure 9 Morphological effects of *mreB* loss in *B. subtilis*. I–P. Cells were grown to exponential phase at 37°C in minimal medium supplemented with 10 mM Mg^{2+} then transferred onto minimal medium supplemented with decreasing levels of Mg^{2+}. Images were taken after 90 min of growth. Adapted from Kawai, Daniel and Errington (2009).

1.6.4. MreB loss may be an early first step to evolving spherical bacterial cells

As previously discussed, phylogenetic analysis has shown that spherical-shaped bacteria arose from rod-shaped precursors multiple times during the course of evolution (Siefert and Fox, 1998). Consistent with this, rod-shaped bacteria can be made to have a spherical morphology by the loss or perturbation of the *mreBCD* genes (Pichoff and Lutkenhaus, 2007). All three *mre* genes are important for maintaining the rod-shape in bacteria – loss of which leads to the formation of a spherical cell shape (Shi *et al.*, 2018). However, MreB is particularly interesting and important because aside from maintaining the rod-like shape, it is also absent in most spherical bacteria, unlike MreC and MreD which are present in extant spherical species such as *Streptococcus pneumoniae* and *Staphylococcus aureus* (Land and Winkler, 2011; Tavares *et al.*, 2015). Furthermore, loss of MreB results in cell death in model rod-shaped bacteria such as *E. coli* (Shi *et al.*, 2017), *C. crescentus* (Takacs *et al.*, 2010), and *Pseudomonas aeruginosa* (Robertson *et al.*, 2007), that are grown in standard culture media.

1.7. Rationale and objectives of the study

P. fluorescens SBW25 is a plant-associated pseudomonad that was isolated from the phyllosphere of a sugar beet grown in Oxfordshire in 1989 (Rainey and Bailey, 1996). Since then, it has been used as a model organism for numerous studies with varying interests, including responses to bacteriophage and antibiotic exposure (Escobar-Paramo, Gougat-Barbera and Hochberg, 2012; Scanlan and Buckling, 2012; Ramsayer, Kaltz and Hochberg, 2013), biofilm formation and multicellularity (Hammerschmidt *et al.*, 2014), and niche construction (Spiers and Rainey, 2005; Loudon *et al.*, 2016; Koza *et al.*, 2017).

In 2002, Spiers et al. discovered in a transposon mutagenesis experiment that the disruption of the *mreB* gene in *P. fluorescens* SBW25, results in the formation of spherical cells. Similar to other studies, this *mreB*-null strain (hereafter, Δ*mreB*) showed slow/ poor growth. However, this new Δ*mreB* strain remained viable in standard lysogeny broth (LB), unlike in the closely related pseudomonad, *P. aeruginosa*. This provided the opportunity to study how a previously rod-shaped bacterium would grow in response to the loss of *mreB*. Furthermore, this provides the framework for an experimental evolution experiment which can be used to study how Δ*mreB* would evolve in response to its new phenotype. Experimental evolution is a powerful tool that has been used to understand how organisms can adapt to new environments under specific conditions (Barrick and Lenski, 2013; Rainey *et al.*, 2017; Ho and Zhang, 2018), and *P. fluorescens* SBW25 has proven to be well-suited to this experimental design as it has already been used to study a variety of topics in the past (Rainey and Travisano, 1998; Beaumont *et al.*, 2009; Lind *et al.*, 2015). Following the discovery that *P. fluorescens* SBW25 is able to survive the loss of MreB, Dr. Monica Gerth separated the Δ*mreB* strain into 10 lines which were successfully propagated for ~1,000 generations in an evolution experiment. These 10 lines were sequenced by Dr. Heather Hendrickson at two timepoints (500 and 1,000 generations) in order to identify the major mutations that have swept through these populations. These works preceded the results presented in this thesis. Therefore, the main aim of my project is to characterise the evolutionary strategies that a formerly rod-shaped bacterium can use to adapt to a new spherical cell shape. The specific objectives are described below:

1. The first objective of my thesis is to characterise the effects of MreB loss in *P. fluorescens* SBW25. To do this, I will study the morphology (cell shape, size, integrity); growth characteristics (growth dynamics, relative fitness); and the PG cell well chemistry and architecture of both the *P. fluorescens* SBW25 wild-type (WT) and Δ*mreB* strains. This will allow me to determine how Δ*mreB* is affected by the radical change in cell shape caused by the loss of MreB. This also establishes a baseline for understanding the results of the evolution experiment.

2. My next objective is to study the effects of MreB-loss over time in the 10 lines from the evolution experiment. I will analyse the morphology, growth characteristics, PG chemistry and assembly of the evolved lines at different time points to determine how well these lines are able to adapt to their new spherical cell shape.

3. Finally, I will characterise the major mutations identified in the evolved lines. Prior sequencing work has identified mutations that may be allowing *P. fluorescens* SBW25 to compensate for the loss of MreB. By investigating the effects that these mutations cause in the WT and ancestral Δ*mreB* strains, I will be able to determine if these are indeed beneficial and elucidate the mechanisms that are driving this effect.

Chapter 2

Materials and Methods

2.1.   Media, bacterial strains, and growth conditions

P. fluorescens SBW25 cultures were grown at 28°C in 30 mL blue cap plastic vials containing 5 mL of Lysogeny Broth (LB: 10 g tryptone, 5 g yeast extract, 10 g NaCl in H_2O up to 1 L), shaken at 150 rpm. *Escherichia coli* and *S. aureus* cultures were likewise grown in shaken LB but incubated at 37°C. Agar plates were prepared by adding 1.5% w/v agar to the broth media prior to autoclaving, cooling, then plating. When required, antibiotics were dissolved in H_2O added to the medium at the following concentrations: ampicillin (Ap), 100 µg/mL; gentamicin (Gm), 25 µg/mL; kanamycin (Km), 50 µg/mL; spectinomycin (Sp), 100 µg/mL; and tetracycline (Tc), 10 µg/mL. Nitrofurantoin (NF) was dissolved in dimethyl sulfoxide (DMSO) to a final concentration of 100 µg/mL. All bacterial strains used in this work are stored at -80°C in glycerol saline solution (8.5 g NaCl, 300 mL H_2O, glycerol to 1 L); and are listed in Table 2. Glycerol-saline solutions were prepared for long-term storage of bacteria. Strains were inoculated in shaken LB containing appropriate antibiotic(s) and grown at the necessary temperatures overnight. The following day, 1 ml of the bacterial culture was added to 800 µl of glycerol-saline, mixed, then stored at -80°C.

Table 2 Bacterial strains and plasmids used in this work

Strain	Relevant characteristics	Reference
P. fluorescens		
SBW25	Wild-type strain isolated from sugar beet	Bailey *et al.*, 1995
ΔmreB	Ancestral MreB deletion mutant	This work
*lacO*_pLICTRY;	pLICTRY plasmid encoding LacI_CFP and TetR_YFP	Akarsh Mathrani and Heather Hendrickson (unpublished work)
EL1.50	Evolved Line 1 – 50 generations	This work
EL2.50	Evolved Line 2 – 50 generations	This work
EL3.50	Evolved Line 3 – 50 generations	This work
EL4.50	Evolved Line 4 – 50 generations	This work
EL5.50	Evolved Line 5 – 50 generations	This work
EL6.50	Evolved Line 6 – 50 generations	This work
EL7.50	Evolved Line 7 – 50 generations	This work

EL8.50	Evolved Line 8 – 50 generations	This work
EL9.50	Evolved Line 9 – 50 generations	This work
EL10.50	Evolved Line 10 – 50 generations	This work
EL1.250	Evolved Line 1 – 250 generations	This work
EL2.250	Evolved Line 2 – 250 generations	This work
EL3.250	Evolved Line 3 – 250 generations	This work
EL4.250	Evolved Line 4 – 250 generations	This work
EL5.250	Evolved Line 5 – 250 generations	This work
EL6.250	Evolved Line 6 – 250 generations	This work
EL7.250	Evolved Line 7 – 250 generations	This work
EL8.250	Evolved Line 8 – 250 generations	This work
EL9.250	Evolved Line 9 – 250 generations	This work
EL10.250	Evolved Line 10 – 250 generations	This work
EL1.500	Evolved Line 1 – 500 generations	This work
EL2.500	Evolved Line 2 – 500 generations	This work
EL3.500	Evolved Line 3 – 500 generations	This work
EL4.500	Evolved Line 4 – 500 generations	This work
EL5.500	Evolved Line 5 – 500 generations	This work
EL6.500	Evolved Line 6 – 500 generations	This work
EL7.500	Evolved Line 7 – 500 generations	This work
EL8.500	Evolved Line 8 – 500 generations	This work
EL9.500	Evolved Line 9 – 500 generations	This work
EL10.500	Evolved Line 10 – 500 generations	This work
EL1.1,000	Evolved Line 1 – 250 generations	This work
EL2.1,000	Evolved Line 2 – 250 generations	This work
EL3.1,000	Evolved Line 3 – 250 generations	This work
EL4.1,000	Evolved Line 4 – 250 generations	This work
EL5.1,000	Evolved Line 5 – 250 generations	This work
EL6.1,000	Evolved Line 6 – 250 generations	This work
EL7.1,000	Evolved Line 7 – 250 generations	This work
EL8.1,000	Evolved Line 8 – 250 generations	This work
EL9.1,000	Evolved Line 9 – 250 generations	This work
EL10.1,000	Evolved Line 10 – 250 generations	This work
WT-GFP	miniTn7(Gm)PrrnB P1 gfp-a	Created for this work based on Lambertsen, Sternberg and Molin (2004)
WTRL1	PFLU0406 D484N in WT SBW25	This work
WTRL4	PFLU0406 T362P in WT SBW25	This work
WTRL7	ΔPFLU4921-4925 in WT SBW25	This work
WTRL10	Tn7-PFLU4165 in WT SBW25	This work
Δ*mreB*.RL1	PFLU0406 D484N in Δ*mreB*	This work
Δ*mreB*.RL4	PFLU0406 T362P in Δ*mreB*	This work
Δ*mreB*.RL7	ΔPFLU4921-4925 in Δ*mreB*	This work
Δ*mreB*.RL10	Tn7-PFLU4165 in Δ*mreB*	This work
E. coli		
TOP10	F-*mcrA* Δ(*mrr-hsdRMS-mcr*BC) ɸ80*lacZ*ΔM15 Δ*lac*X74 *rec*A1 *ara*D139 Δ(*ara-leu*)7697 *gal*U *gal*K *rps*L (Str^R) *end*A1 *nup*G	Invitrogen

Plasmids		
pCR8/GW/TOPO	Cloning vector, Sp[r]	Invitrogen
pRK2013	Helper plasmid, Tra[+], Km[r]	Ditta *et al.*, 1980
pUIC3	Universal IVET construct, Apr[R] Tc[R]	Mahan, Slauch and Mekalanos, 1993
pUX-BF13	Helper plasmid for transposition of mini-Tn7 element, Ap[r]	Bao *et al.*, 1991

2.2.   Measurement of bacterial growth kinetics

P. fluorescens SBW25, the evolved lines, and reconstructed mutants were initially grown in 5 mL shaken LB at 28°C overnight. The following day, 10 µl of the overnight culture was mixed with 990 µl of fresh media to prepare a 1:100 dilution. A 200 µl aliquot of the cell suspension was then transferred into a well of a 96-well microplate. Three replicates were prepared for each strain. Growth kinetics of were monitored at 28°C using a Synergy 2 plate reader controlled by the Gen5 software (Bio-Tek). Absorbance at 600 nm was measured at 5 minutes intervals for a period of 48 or 72 hours. The plate was shaken for 10 seconds prior to each read.

2.3.   PCR methods and cloning techniques

Gene of interest were amplified by PCR following standard methods. A deoxyribonucleotide triphosphate stock solution was prepared from a dNTP set (Bioline) containing four 100 mM of dNTP solutions to generate a final concentration of 10 mM for each dNTP. Taq DNA polymerase (Invitrogen) was used for PCR amplification. The calculated melting temperature ™ of primers was used to determine the annealing temperature for each pair of primers. Reaction conditions and preparation of a typical 50 µl of PCR reaction is shown below (Table 3). PCR reactions were carried out using a gradient thermal Palm-Cycler™ (Corbett Life Science) (Table 4).

Table 3 Reagents in 50 μl of PCR reaction volume

	Volume (μl)	Final Concentration
10 Buffer	5.0	1x
MgCl$_2$ (50 mM)	1.5	1.5 mM
dNTP (10 mM)	1.0	0.2 mM
Forward Primer (10 μM)	1.0	0.2 mM
Reverse Primer (10 μM)	1.0	0.2 mM
Taq DNA Polymerase (5 U/μL)	0.2	1 U
Template DNA	5.0	1 to 5 ng
MilliQ H$_2$0	35.3	--
Total volume	50.0	--

Table 4 PCR reaction conditions

	Temperature (°C)	Time	Cycles
Initial Denaturation	94	3 min	1x
Denaturation	94	45 s	
Annealing	56	45 s	30x
Elongation	72	1 min/kb	
Final elongation	72	10 min	1x
Hold	4	--	--

2.3.1. Agarose gel electrophoresis

DNA fragments were separated on 1% agarose gels made with TBE buffer (Life Technologies) stained with 1X SYBR Safe™ DNA stain (Invitrogen). Before loading onto the gel, samples were mixed with 6x DNA loading dye (Fermentas) at a ratio of 1:5. Gels were run at 120 volts for 40-60 minutes. A 1 kb DNA ladder was used for estimating DNA fragment sizes. Separated DNA bands were visualised using a UV Transilluminator (UVP) and photographed using the DigiDoc-It Imaging System controlled by the Doc-It LS Analysis Software (UVP). Desired bands were removed from the gel and purified using a QIAquick Gel Extraction kit (Qiagen), following the manufacturer's recommendations.

2.3.2. Plasmid extraction, restriction enzyme digestion, and DNA ligation

Plasmid DNA was extracted from overnight cultures using the QIAprep Spin Miniprep Kit (Qiagen), following the manufacturer's instructions. DNA was eluted in 30 to 50 µl of MilliQ H_2O. Restriction enzyme digestion was performed using restriction enzymes from New England Biolabs in appropriate NEB buffers at 37°C for at least 2 hours. DNA vectors and inserts were mixed at a ratio of 1:3 together with 1 µl of T4 DNA ligase (Invitrogen) and 2µl of 5x ligation buffer. The mixture was brought up to a final volume of 10 µl with MilliQ water. Ligation reactions were incubated at 16°C overnight.

2.3.3. Construction of the ancestral Δ*mreB* strain

The construction of the ancestral Δ*mreB* strain was performed by Dr. Monica Gerth using gene splicing by overlap extension (SOE) PCR and a two-step allelic exchange (Horton *et al.*, 2013) in *P. fluorescens* SWB25. A knock-out construct was made by first amplifying ~1000 bp nucleotide regions flanking the *mreB* gene using the primer pairs shown below. Introduced BamHI sites are underlined.

- PF1 5'-GGATCCGAACTCGTCCATGTTGGTCTTG-3' and
- PR1 5'-GCTAATCAGCAAATGCGGGAAAGGGACCCTAGGCAAC-3';
- PF2 5'-AGGGTCCCTTTCCCGCATTTGCTGATTAGCCCATGTTTC-3' and
- PR2 5'-GGATCCGCTGGCCGGAATCGTGGATCAC – 3'

The flanking sequences were fused together via PCR using primers PF1 and PR2, and the resulting deletion fragment was TA-cloned into pCR8/GW/TOPO (Invitrogen) using the pCR8/GW/TOPO Cloning Kit (Invitrogen). The desired DNA insert was then removed from the pCR8/GW/TOPO vector via restriction digestion, checked by sequencing, then subcloned into the destination vector, pUIC3. Tri-parental conjugation was then used to introduce deletion constructs into *P. fluorescens* SBW25. This process is described in the following section.

2.3.4. Tri-parental conjugation

Recipient *P. fluorescens* SBW25 strains were grown overnight at 28°C. At the same time, *E. coli* DH5α λpir carrying the donor vector, pUIC3; and *E. coli* carrying pRK2013, a helper plasmid for mobilization of non-self-transmissible plasmids, were also grown overnight at 37°C. The following day, 0.5 mL of the recipient culture was heat shocked at 45°C for 20 minutes. Meanwhile, 0.5 mL of the donor and helper cell cultures were pelleted at 13,000 rpm for 1 minute, then mixed together in 0.5 mL of LB. After heat-shock, all cultures were spun down at 13,000 rpm for 1 minute then combined and resuspended in 100 μL LB. This resuspension was then transferred and spread onto an LB agar plate. The culture was incubated overnight at 28°C. After incubation, the bacterial lawn was washed from the plate and resuspended in 3 mL of sterile water. Following this, 100 μL aliquots were plated onto LB plates containing NF and Tc to select for transconjugants. These plates were incubated for two days at 28°C. Individual colonies were selected and further purified via cycloserine enrichment, as described in the next section.

2.3.5. Cycloserine enrichment

Cycloserine enrichment was used to isolate transconjugants from the tri-parental conjugation step. Transconjugant *P. fluorescens* colonies were inoculated in 400 mL LB (with shaking) and grown overnight at 28°C without antibiotics to allow the loss of the chromosomally-integrated pUIC3 construct via homologous recombination. The next day, 400 μL of the overnight culture were transferred into 20 mL of LB containing Tc (10 μg/mL), and incubated (with shaking) at 28°C. After 2 hours, D-cycloserine was added to a final concentration of 800 μg/mL. This was allowed to incubate for an additional 5 hours. Cycloserine was added to kill actively growing tetracycline-resistant *P. fluorescens* cells, which selected for cells that had undergone a second round of homologous recombination, resulting in the loss of either the original pUIC3 construct or the target gene. After this step, a 1 mL aliquot of the suspension was removed, and cells were harvested by centrifugation at 13,000 rpm for 1 minute. Cells were washed and diluted in sterile water. The resulting cell suspension was plated onto LB plates containing Xgal (60 μg/ml)

and incubated for two days at 28°C. White colonies were selected and gene mutations were verified by PCR.

2.3.6. Gene complementation

The reconstruction of the PFLU0406 mutations and the deletion of PFLU4921-4925 was performed by Dr. Xue-Xian Zhang and Dr. Yunhao Liu using splicing by overlap extension (SOE) PCR Primer design, as described above. The *csrA* amplification in *P. fluorescens* SBW25 was made using gene complementation. Gene complementation was performed by cloning the PCR-amplified coding region of *csrA* into the multiple cloning site of pUC18-mini-Tn7T-LAC which contains an IPTG-inducible P_{tac} promoter (Choi *et al.*, 2005). The resulting plasmid was introduced into *P. fluorescens* SBW25 by electroporation with the helper plasmid pUX-BF13 which carries the Tn7 transposon genes tnsABCDE (Bao *et al.*, 1991).

2.3.7. Construction of GFP-labeled *P. fluorescens* SBW25

The *P. fluorescens* WT strain was genetically tagged with a mini-Tn7 transposon expressing GFP and a gentamicin resistance marker (miniTn7(Gm)P_{rrnB} P1 gfp-a) (Lambertsen, Sternberg and Molin, 2004). The mini-Tn7 transposon system inserts as a single copy into the attTn7 site located just downstream of *glmS* which encodes an enzyme required for PG cell wall synthesis. The Tn7 transposon was transferred from *E. coli* pRK2013 by conjugation with help from the transposase plasmid, pUX-BF13 (Lambertsen, Sternberg and Molin, 2004).

2.4. Experimental evolution

Ten replicate populations of the ancestral Δ*mreB* strain were grown in 5 mL aliquots of LB broth at 28 °C with shaking at 180 rpm. Every 24 h, 5 µL was transferred to fresh media. Every 5 days samples of each population were collected and stored at -80°C in 15% (v/v) glycerol.

2.5.   Competitive fitness assay using flow cytometry

Competitive fitness was measured relative to the *P. fluorescens* SBW25 WT+GFP strain. Prior to the competition assay, competing strains were grown in 5 mL of shaken LB at 28°C overnight. The following day, 200 uL from each strain were mixed in 5 mL of fresh pre-warmed LB, then grown for 4h. This was done to ensure that the strains were in the same physiological state for the competition experiment. The initial ratio of WT+GFP and the competing strain was determined by counting 50,000 cells using flow cytometry (BD FACS Canto). GFP fluorescence was detected using the 488 nm laser and the 530/30 bandwidth filter. Suitable dilutions of the initial population were plated on LBA agar plates to determine viable counts. The mix of WT+GFP and the competing strain was diluted 1000-fold in LB and incubated for 24 hours in shaken LB at 28°C. The final ratio and viable counts of the competing strains were determined using the same protocol. The number of generations for the competition experiment was determined following the formula ln(final population/initial population)/ln(2). Selection coefficients were calculated using the regression model s = [ln(R(t)/R(0))]/[t], where R is the ratio of WT+GFP to the competing strain, and t is the number of generations. Control experiments with WT vs. WT+GFP were performed to compensate for the fitness cost of the miniTn7 insert with the GFP marker. The competition assay was performed at least three time for each strain.

2.6.   Mutation Detection

Genome sequencing of the strains used in this study was done by Dr. Heather Hendrickson. In order to detect mutations in the experimental lines, total DNA was extracted from the ancestral Δ*mreB* strain and from each of the 10 populations at 1,000 generations. Samples were submitted for 100 bp single-end Illumina DNA sequencing (AGRF). An average of 6,802,957 single reads were obtained per sample and these were aligned to the reference stain (NC_012660.1) to give approximately 100-fold coverage according to an alignment in Geneious (version 9.0.5 R9 http://www.geneious.com). Major mutations were then called if they were observed with a frequency of 0.75 or more in Geneious.

2.7.   Microscopy and Image analysis

Scanning electron microscopy was done by Niki Minards at the Manawatu Microscopy and Imaging Centre (MMIC), Massey University, Palmerston North. Cells were grown in LB and harvested in log phase. Cells were fixed in modified Karnovsky's fixative then placed between two membrane filters (0.4 μm, Isopore, Merck Millipore LTD) in an aluminium clamp. Following three washes of Phosphate-Buffered Saline (PBS) buffer (ThermoFisher Scientific), the cells were dehydrated in ethanol, placed in liquid CO_2, then dried in a critical-point drying chamber. The samples were mounted onto aluminium stubs and sputter coated with gold (BAL-TEC SCD 005 sputter coater) and viewed in a FEI Quanta 200 scanning electron microscope at an accelerating voltage of 20 kV.

Phase contrast and fluorescent images were taken using the BX61 upright microscope (Olympus) using the Cell^P and Cellsens programs (Olympus). Fluorescent images were captured for the *lacO*_pLICTRY strain which had a CFP-labelled origin of replication, and for strains labelled with 4',6-diamidino-2-phenylindole (DAPI; ThermoFisher Scientific) and BODIPY-FL 3-amino-d-alanine (BADA; Hsu *et al.*, (2017)). Images were first saved in TIFF format.

To measure cell shapes, phase contrast images were converted from grayscale to a binary format (Figure 10) using ImageJ 1.51n (Fiji), following the workflow below:

Images are converted to grayscale, if necessary:

- *Image> Type> 8 bit*

The image threshold is determined manually to ensure cells are selected properly and are separated from the background:

- *Image> Adjust> Threshold*

Pixel noise is reduced initially using automated commands:

- *Process> Binary> Open*

- *Process> Noise> Remove Outliers*

Large areas containing pixel noise or noise that has not been removed automatically can be further cleaned up by selecting the affected area then filling with the background colour:

- *Edit> Fill*

Cells are always set black against a white background. If the colours are reversed, the image is inverted:

- *Edit> Invert*

Ensuring the removal of all unnecessary pixels is necessary for proper analysis in CMEIAS, as described below. Images are then saved in TIFF format.
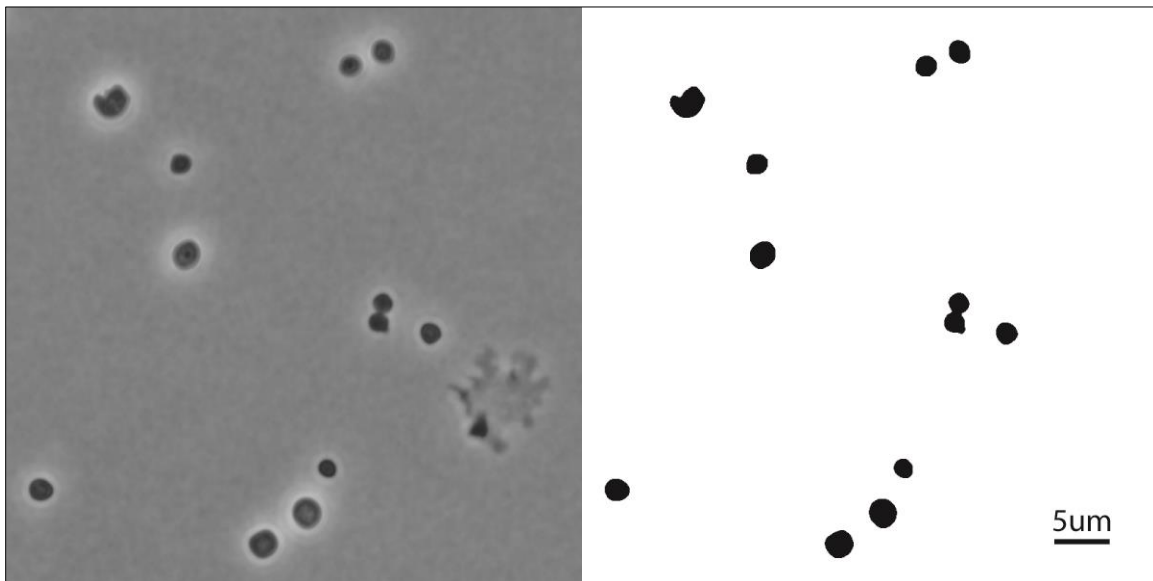
Figure 10 Result of binary conversion from a raw tiff file following the protocol described above. The creation of a binary image with no noise is critical for cell shape measurements using CMEIAS.

2.7.1. Cell Shape Quantification using CMEIAS

The Center for Microbial Ecology Image Analysis Software (CMEIAS) by Liu *et al.* (2001) was used to measure the cell shape of the strains used in this study. Prior to analysis, a calibration step was performed to set the correct scale for measurement. First, a phase contrast image with a correct scale bar was opened in CMEIAS. A line tool was used to measure the native scale bar, using the command: [Settings> Calibrate Spatial Measurements]. Once the measurement was made, the value of the scale bar in micrometres was entered. This sets the calibration for the current session. To save the calibration for later use, the measurement can be saved as a calibration file using: [Settings> Save Spatial Calibration]. After setting the spatial calibration, cell measurements were set to be recorded with an accuracy of 6 decimal places. This is performed in: [Settings> Preferences> Measurement Features].

To perform image analysis, converted TIFF images were first opened in CMEIAS. Cells were identified using the Find Objects button or using: [Analysis> Object Analysis> Find Objects]. This opens the "Find Objects Using the Brightness Threshold" window. Since the images have already been processed in ImageJ, "None" is selected. If the image was prepared in ImageJ correctly, cells will be identified and labelled automatically. It is important to note that stray pixels in the image will cause CMEIAS to crash. Finally, cell shape metrics were acquired using: [Analysis> Object Analysis> Object Analysis]. Results were then copied and saved in an Excel worksheet (Microsoft).

Measurements from at least 100 cells were collected for each strain. The information is collated in Excel (Microsoft). The filenames of the images used were noted and the Object Numbers were used as specific cell identifiers. The important metrics used for analysis were "Compactness" for measuring cell roundness, and "Length" and "Width" for computing the cell volume, as described below:

The basic equation for the volume of a cylinder was used to compute the volume of rod-shaped cells:

$$vol_{cylinder} = \pi \times radius^2 \times height \qquad\qquad (1)$$

which was then interpreted as:

$$vol_{cylinder} = \pi \times (width/2)^2 \times length \tag{2}$$

The volume of the cell poles was computed separately, so length was modified to remove the radius of the hemispherical cell poles:

$$vol_{cylinder} = \pi \times (width/2)^2 \times (length - width) \tag{3}$$

The volume of the cell poles was computed separately using the basic equation for the volume of a sphere:

$$vol_{sphere} = 4/3 \times \pi \times radius^3 \tag{4}$$

which was then interpreted as:

$$vol_{sphere} = 4/3 \times \pi \times (width/2)^3 \tag{5}$$

Finally, the volume of rod-shaped cells was computed using the combination of equations 3 and 5:

$$vol_{rod\ shaped\ cells} = (\pi \times (width/2)^2 \times (length - width)) + (4/3 \times \pi \times (width/2)^3) \tag{6}$$

The cell volume of spherical cells was computed using the basic equation for spheroid objects:

$$vol_{spheroid} = 4/3 \times \pi \times a^2 \times c \tag{7}$$

where a is the radius along the long axis; and c is the radius along the short axis.

This was then interpreted as:

$$vol_{spherical\ cells} = 4/3 \times \pi \times (length/2)^2 \times width \tag{8}$$

2.7.2. Cell shape (compactness vs volume) charts

Cell shape charts were prepared from the binary images that were previously processed in ImageJ. First, binary images were imported into Adobe Illustrator. Outlines of the cells were created by selecting the imported image, then running [Image Trace], followed by the [Embed] command. The selection was ungrouped, then the background and other unnecessary layers were deleted. This created individual objects in Adobe Illustrator, representing each cell. For clarity, illustrator objects will still be referred to as cells. Cells were arranged according to the object identifier assigned by CMEIAS. The long axis of the cells was then oriented along the horizontal axis.

37

Using the collated cell measurements in Excel, a dot plot was created with cell volume in the Y-axis and compactness in the X-axis. This dot plot was imported into Adobe Illustrator and used as the refence for positioning each cell in the cell shape chart. Cells were then moved to their corresponding locations in the dot plot. Strains were arranged in separate layers for easy modification. Special attention was given to ensure that the scale of the imported cell outlines was maintained in all the cell shape charts.

2.8.   PG isolation and UPLC analysis

To isolate the PG cell wall, cultures were initially grown from frozen stocks overnight in 5 mL shaken LB at 28°C. Overnight cultures were transferred 1:100 into 250 mL of LB then grown under the same conditions until it reached mid-exponential phase at an OD_{600} of 0.2 to 0.4. As the 250 mL cultures were growing, a boiling water bath was prepared on a hot plate. The water bath held 50 mL Falcon Tubes containing 6 mL of 6% sodium dodecyl sulfate (SDS). A small magnetic stirring bar was added to each Falcon Tube to continually mix the SDS solution in the water bath, then secured with tube caps.

As the SDS solutions are mixing, cells from the 250 mL cultures are harvested at 5,000 x g for 10 minutes at room temperature. Pellets are resuspended in 3 mL LB, then immediately pipetted into the 50 mL Falcon Tubes containing the boiling SDS solution. Slow and careful (drop by drop) addition of the concentrated cells into the SDS solution yields a clear solution (SDS lysate) with a final concentration of 4% SDS. Tubes are capped, then the SDS lysates are allowed to stir in the boiling water bath for 3 hours. As the water bath is boiling, water levels are regularly checked to ensure even heating and mixing of the SDS lysates, which prevents unnecessary damage to the PG structure. After 3 hours, the heat is turned off, but the lysates are kept on the hot plate to continue mixing overnight.

One Falcon Tube prepared in this manner is used for the isolation of PG from one replicate sample for each strain. Multiple replicates are prepared for each strain. Improper PG isolates (i.e. SDS lysates that do not become clear, indicating incomplete cell lysis) are discarded. The PG isolated were sent to the laboratory of Felipe Cava at Umea University for PG analysis using Ultra Performance Liquid

Chromatography (UPLC). UPLC analyses of muropeptides were performed at an absorbance of 202-208 nm in a 30-minute run (Alvarez *et al.*, 2016). Muropeptide identities were determined based on published peak identities (Desmarais *et al.*, 2015; Alvarez *et al.*, 2016; Espaillat *et al.*, 2016).

2.9.   Fluorescent D-amino acid staining

Short-pulse experiments were performed using the Fluorescent D-Amino Acid, BADA (Hsu *et al.*, 2017), following the protocol of Michael Van Nieuwenhze's lab (Kuru *et al.*, 2015). A stock solution of BADA was prepared by diluting BADA in Dimethyl sulfoxide (DMSO) to a concentration of 100 mM. From this, 1 µL was added to a 1.7 mL Eppendorf tube then prewarmed to 28°C. Next, 1mL of exponential culture with an OD_{600} of ~0.4 was typically pelleted at 10,000 x g in a microcentrifuge at room temperature for 1 minute. The Δ*mreB* strain which was sensitive to mechanical stress was spun at a lower setting (2,000 x g) for 1 minute to minimise cell death. The pellet was resuspended in 100 µl of prewarmed LB medium then added to the prewarmed, FDAA-containing Eppendorf tube to get a final FDAA concentration of 1 mM and a DMSO concentration of 1% (vol/vol) in LB medium.

Next, the tube was incubated with shaking at 28°C for 20% of the strain's generation time. Following this, 230 µl of ice-cold 100% ethanol was added to get a final ethanol concentration of 70% (vol/vol). Add an additional 1 ml of ice cold 70% ethanol was added to contribute to the removal of the excess dye. Cells were fixed on ice for 15 min then washed with 1 ml of 1 × PBS three times to remove excess FDAA. Finally, cells were resuspended in 20–100 µl of PBS which was then used for microscopy. Cells suspended in PBS that were not immediately analysed were resuspended in 20–100 µl of PBS + 10% (vol/vol) DMSO and stored at -20°C.

2.10.   Molecular modelling of PBP1A

The nucleotide sequence of PFLU0406 was obtained from NCBI BLAST and The Pseudomonas Genome Database and submitted to I-TASSER (Iterative Threading ASSEmbly Refinement) to create a

molecular model of the PBP1a protein in *P. fluorescens* SBW25. Briefly, I-TASSER identifies and retrieves structural templates of similar proteins from the Protein Database (PDB) library using an online service (Local Meta-Threading Server – LOMETS) for protein structure prediction. Matching protein fragments were extracted then reassembled into base models using replica-exchange Monte Carlo simulations. Structures were built by *ab initio* modelling for unaligned regions, or when no matching template is found. Simulation decoys were made, and probable models were identified by a clustering algorithm (SPICKER) before being remodelled. Final models were made by a protein structure construction algorithm (REMO). Biological functions were then determined by cross-referencing the predicted protein models to independent libraries looking at proteins of known enzyme classification (EC) number, gene ontology (GO) vocabulary, and ligand-binding sites. The protein model with the best prediction value (C-score) was then used for visualisation and further analysis. These steps are summarised below (Figure 11).
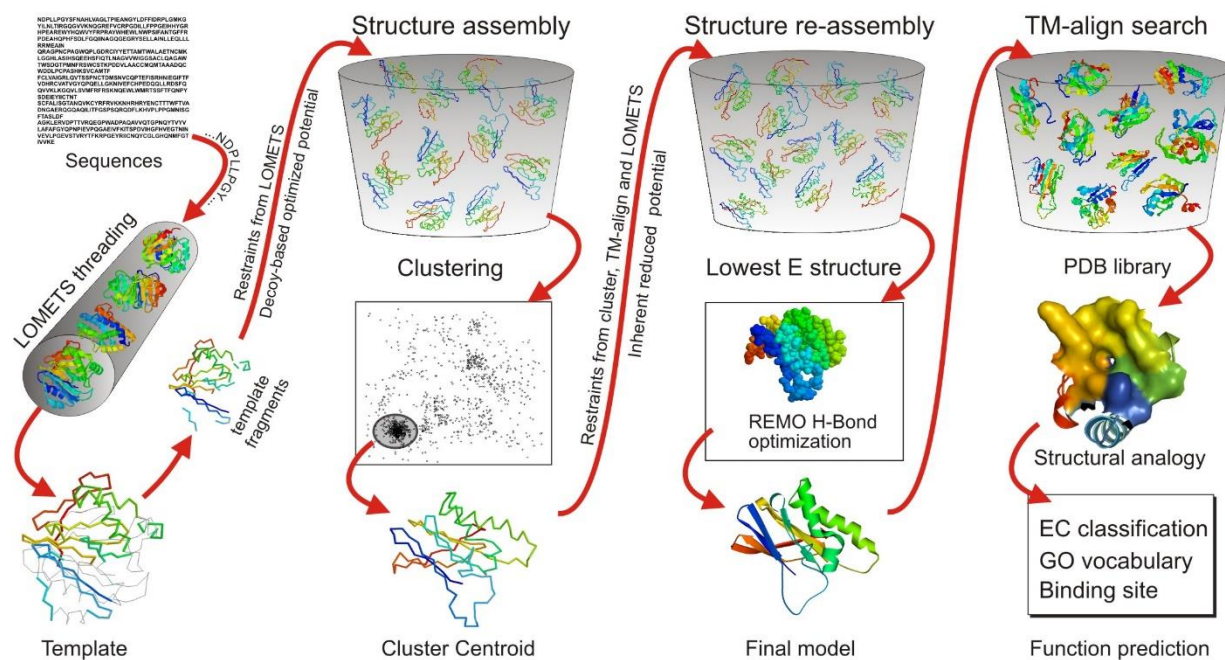
Figure 11 A schematic representation of the I-TASSER protocol for protein structure and function predictions. Adapted from Roy, Kucukural and Zhang (2010).

The protein model selected from the I-TASSER results was downloaded as a .pdb file and opened in the Visual Molecular Dynamics (VMD) program. Once the molecule has been loaded in VMD, the following steps were performed to create the visualisations of PBP1a presented in this paper.

1. Change background to white:

   Graphics> Colors> Categories: Display> Names: Background> Colors: 8 white

2. Change representation to New Cartoon:

   Graphics> Representations> Drawing Method: New Cartoon

3. Change colour to grey and make transparent:

   Selected Atoms: all> Coloring Method: ColorID: 2 gray> Material: Glass2

4. Overlay functional domains:

   Create Rep> Selected Atoms: residue # to #> Coloring Method: ColorID: *user select*> Material: Opaque

5. Highlight residues of interest:

   Create Rep> Selected Atoms: residue # to #> Drawing Method: VDW> Coloring Method: ColorID: *user select*> Material: Opaque

6. Confirm residue identity using the Sequence Viewer tool:

   Extension> Analysis> Sequence Viewer

For comparison, the published crystal structure of *Acinetobacter baumannii* PBP1a in complex with Aztreonam was also visualised (PBP1a from *A. baumannii* shares a 73% sequence identity (E value = 0.0) to the PBP1a of *P. fluorescens* SBW25). Sequences were aligned, and locations of the mutations in the evolved lines were mapped in the corresponding regions. The PDB file was downloaded from the RCSB Protein Data Bank (www.rcsb.org) using PDB ID 3UE0.

2.1. Molecular phylogenetic analysis

The evolutionary history of 31 species (30 paired rod and spherical bacteria rooted to one archaeal representative) was inferred using 16S rRNA sequences mined from the Ribosomal Database Project (https://rdp.cme.msu.edu) and constructed using the Maximum Likelihood method based on the Tamura-Nei model. The tree with the highest log likelihood (-14554.96) is shown. Initial tree(s) for the heuristic search were obtained automatically by applying Neighbor-Join and BioNJ algorithms to a matrix of pairwise distances estimated using the Maximum Composite Likelihood (MCL) approach, and then selecting the topology with superior log likelihood value. The tree is drawn to scale, with branch lengths measured in the number of substitutions per site. All positions containing gaps and missing data were eliminated. There were a total of 1108 positions in the final dataset. Evolutionary analyses were performed using MEGA X (Kumar *et al.*, 2018). To analyse the presence of MreB and PBP homologues in these 31 species, homologues were found using Protein BLAST (https://blast.ncbi.nlm.nih.gov/Blast.cgi) using the protein sequences of *E. coli* str. K-12 substr. MG1655.

Chapter 3

Characterisation of Δ*mreB* and WT

3.1.   Introduction

MreB is an important cell shape determining protein for most rod-shaped bacteria (White and Gober, 2012). Knockout studies have shown that the deletion of MreB causes rod-like bacteria to lose their shape and regress into spherical cells (Jones, Carballido-López and Errington, 2001; Cabeen and Jacobs-Wagner, 2005; Formstone and Errington, 2005; Kruse, Bork-Jensen and Gerdes, 2005). Using typical media under normal laboratory conditions, the deletion of MreB in these model organisms like *E. coli*, *B. subtilis*, and *C. crescentus* has always led to severe morphological defects which ultimately lead to cell death. In *B. subtilis*, MreB was shown to be important for the maintenance of cell width and cell viability as the deletion of *mreB* resulted in a lytic phenotype composed of severely swollen cells (Formstone and Errington, 2005). Only with the addition of high concentrations of magnesium were the effects of *mreB* deletion reversed and normal growth achieved (Formstone and Errington, 2005). Altogether, these processes point to the existence of mechanisms that guide and direct PG synthesis, and therefore shape, in bacterial cells.

In this chapter, I will present the phenotypic effects of MreB loss in *P. fluorescens* SBW25. My objective is to determine whether the characteristics seen in the Δ*mreB* strain are indeed due to the loss of MreB. To answer this, I will study the morphology, particularly cell shape, physical integrity, and PG cell wall construction of Δ*mreB*, and relate the findings to previously reported results. I will investigate the effect of supplemental Mg^{2+} which has been shown to rescue defects caused by the loss of MreB. I will determine if cell division defects are present, which have also been attributed to MreB-loss. And finally, by studying the characteristics of ectopically-producing MreB strains, I will be able to verify if the phenotype observed in Δ*mreB* is indeed a result of MreB-loss.

3.2. Results and Discussion

3.2.1. Δ*mreB* cells are spherical and highly variable in size

The hallmark characteristic of MreB loss in other rod-like bacteria such as *E. coli* and *B. subtilis* is the formation of spherical or bulging cells that ultimately die (Jones, Carballido-López and Errington, 2001; Kruse *et al.*, 2003). Similar changes in cell shape were seen in *P. fluorescens* SBW25 – phase contrast and scanning electron microscopy (SEM) reveal that Δ*mreB* cells are spherical to ovoid, and display a high variability in cell size compared to the rod-like WT strain (Figure 12).
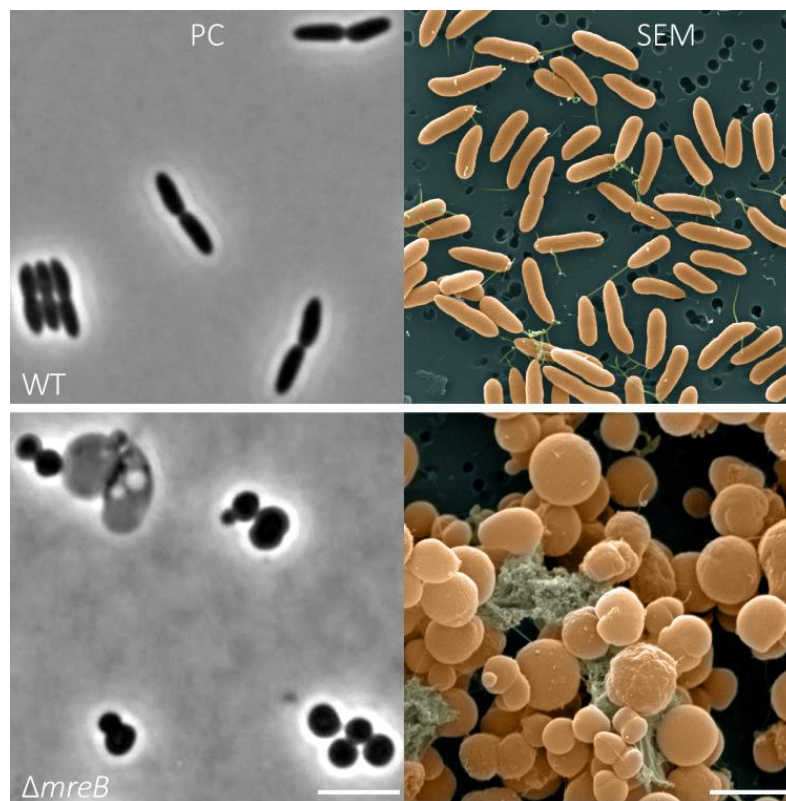
Figure 12 Phase contrast and scanning electron micrographs of WT and Δ*mreB*. WT cells are typical rod-shaped cells with tapered ends. Δ*mreB* cells are large and spherical to ovoid. SEM images are false-coloured. Scale bar = 5µm.

To measure the differences in cell shape between WT and Δ*mreB*, cell outlines were derived using Fiji – ImageJ (Schindelin *et al.*, 2012; Schneider, Rasband and Eliceiri, 2012) and quantified using the image analysis software CMEIAS (J Liu *et al.*, 2001; Dazzo *et al.*, 2013). Among the many measurements taken by CMEIAS, a metric called "compactness" was determined to be effective in categorising cells by shape, based on a principal component analysis (Figure 13) of all the measurements taken by CMEIAS. Compactness ranges from 0 to 1 – a convenient measure for comparing cells with different shapes. Cells with a value of 1.0 appear perfectly spherical whilst cells with a compactness value of 0.7 and below are typically rod-shaped. Other metrics (i.e. cell volume and surface area) were later computed from the length and width values recorded by CMEIAS.
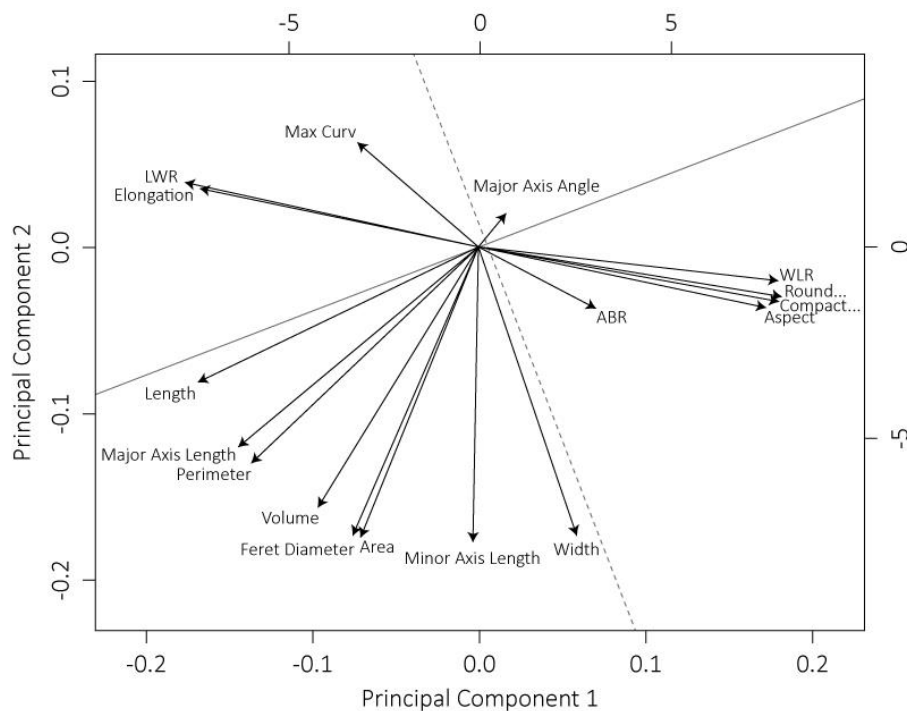
Figure 13 Principal component analysis (PCA) shows cell shape metrics from CMEIAS clustering together. Ratio of width to length (WLR), roundness, compactness, and aspect ratio can all be used to separate cells based on shape. (i.e. distinguishing rods from spheres). In this study, compactness was ultimately used as the primary way to classify cells based on shape as it uses an intuitive scale that ranges from 0 for elongated cells to 1 for spherical cells. Furthermore, it takes into account Feret diameter, a measurement commonly used to analyse cell size from photomicrographs (Hvichia *et al.*, 2016). This data was kindly provided by Dr. Olin Silander using PCA analysis in R (Team and R Development Core Team, 2016).

WT cells range in compactness from ~0.40 for dividing cells to ~0.70 for single short rods. These cells display a strong linear relationship between volume and compactness (R^2 = 0.64), where cells decrease in compactness as they become longer (Figure 14). This reflects the linear growth of dividing rod-shaped cells. WT cells range in volume from ~1.20 μm^3 to ~6.00 μm^3, averaging 3.27 μm^3 (SD ± 0.94 μm^3; n = 100).

In contrast, the Δ*mreB* cells range in compactness from ~0.7 to ~1.0, having cells that are almost perfectly spherical. Cells that have initiated septation have lower compactness values than those that have not, demonstrating that dividing cells still undergo elongation during cell division. Dividing Δ*mreB* cells show only a very weak correlation between compactness and cell volume (R^2 = 0.08) (Figure 14), suggesting that Δ*mreB* cells initiate cell division more erratically than WT. However, it is notable that all dividing cells have compactness measures of less than 0.9, with 89% which falling below a compactness of 0.85. This implies that Δ*mreB* cells need to have a compactness of ~0.85 for cell division to be initiated. The Δ*mreB* cells are also more variable in size, ranging from ~1.10 μm^3 to ~90 μm^3, averaging 20.65 μm^3 (SD ± 16.17 μm^3; n = 100) (Figure 14).
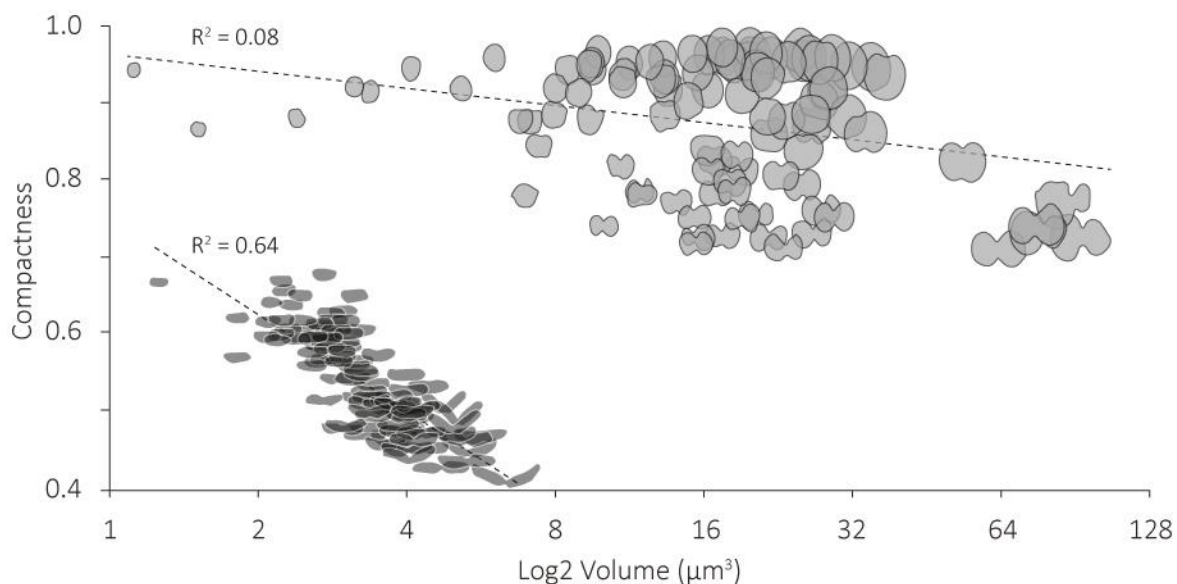
Figure 14 Cell volume vs compactness. In rod-shaped WT cells, a strong inverse relationship is seen between compactness cell volume. This relationship is not as strong in Δ*mreB*.

The surface area-to-volume (SA/V) ratios were also computed based on the length and width of the cells. It shows WT cells having a SA/V of 3.49 (SD ± 0.21; n = 100) (Figure 15). For comparison, this SA/V is similar to the measured SA/V of ~3.5 in *E. coli* (Harris and Theriot, 2016a). On the other hand, Δ*mreB* shows a significantly lower SA/V of 1.46 (SD ± 0.52; n = 100; p < 0.05, two-sample t-test) resulting from the greatly increased width of Δ*mreB* cells.
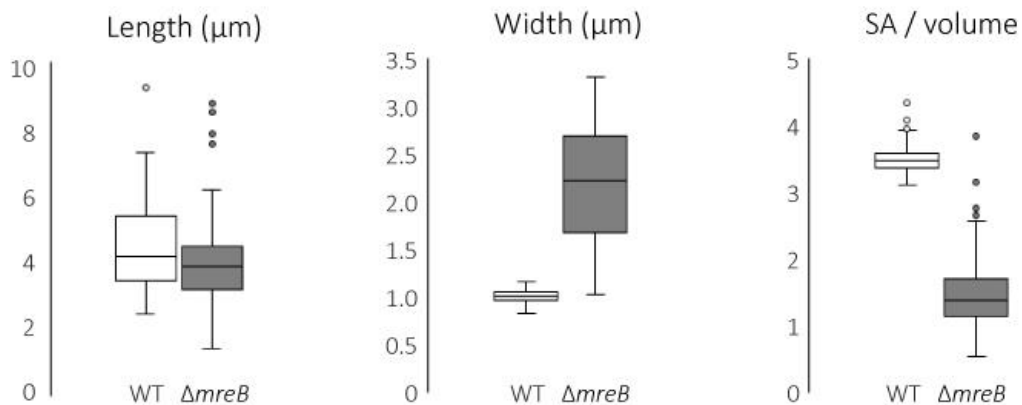
Figure 15 Morphological characteristics of WT and Δ*mreB*. A) Compared to WT, Δ*mreB* cells are wider and display a greater variability of length and width. Furthermore, SA/V measurements show a vast decline in Δ*mreB*, whereas WT cells display an SA/V that is typical of rod-shaped bacteria like *E. coli*. B) WT cells typically have a compactness <0.7 and display a strong correlation between cell size and compactness. Δ*mreB* cells are ovoid to spherical, and have large volumes reaching ~90 μm³.

Here, I show that MreB loss in *P. fluorescens* SBW25 likewise leads to the formation of misshapen cells. Particularly, Δ*mreB* exhibited a near-spherical morphology (Figure 14), demonstrating that our strain has had a complete loss of all MreB-related shape determining functions as discussed by Jones, Carballido-López and Errington, 2001. Similar spherical morphologies were observed in *E. coli* right before cells started to lyse (Kruse, Bork-Jensen and Gerdes, 2005). MreB makes rod-shaped cells by conferring a mechanical force to the cell (Jiang *et al.*, 2011), and by coordinating the function of cell wall synthesis enzymes responsible for lateral growth (Kawai, Daniel and Errington, 2009; White, Kitich and Gober, 2010). The loss of MreB, either by depletion or inhibition with drugs (i.e. A22), makes cells increase in

diameter and stop elongation (Gitai *et al.*, 2005; Takacs *et al.*, 2010). Therefore, the spherical cells in Δ*mreB* are a result of a loss of mechanical support from MreB, and of PG mislocalisation during growth.

3.2.2. Δ*mreB* grows poorly, has many dead cells, and has decreased fitness

WT cells grown in shaken LB has a generation time of 45 minutes, entering stationary phase upon reaching a maximum OD_{600} of ~1.6. The Δ*mreB* strain grows at a slower rate, having a generation time of 65 mins, entering exponential phase after 12 hours of incubation. Δ*mreB* enters stationary phase after it reaches a maximum OD_{600} of 0.8 to 1.0 (Figure 16).
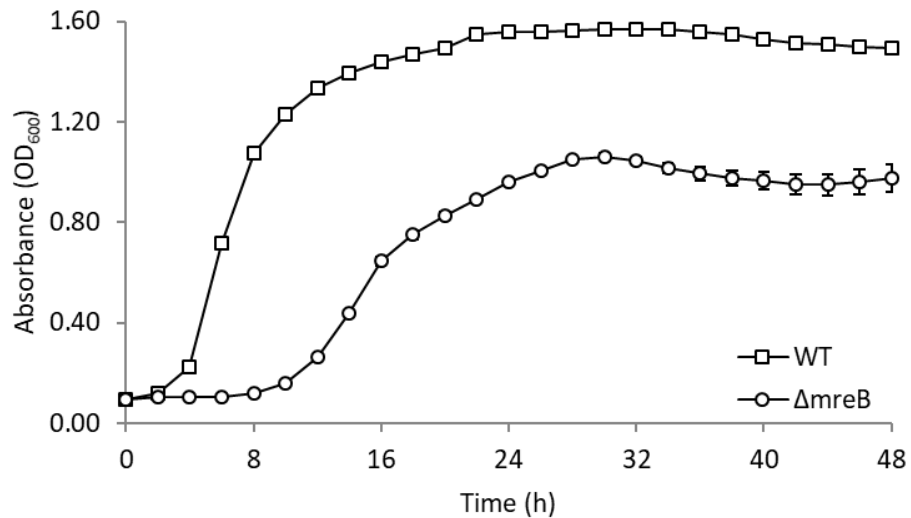
Figure 16 Growth characteristics of WT and Δ*mreB* in shaken LB at 28°C. Δ*mreB* has diminished growth characteristics compared to WT including a prolonged lag time, longer generation time, and lower maximum OD.

Live/Dead assays assessed using microscopy revealed many dead cells in the Δ*mreB* population (Figure 17). Following the standard LIVE/DEAD BacLight Bacterial Viability Kit protocol (pelleting the cells at 10,000 x g for 2 minutes), WT cultures only had 6.88% (SD ± 0.58%; n > 100; 3 biological replicates) dead cells in exponentially growing populations, whereas Δ*mreB* had significantly more dead cells at 41.25% (SD ± 9.09%; n > 100; 3 biological replicates; p < 0.05, two-sample t-test). Notably, the number of dead cells seen in Δ*mreB* decreased to 21.75% SD ± 1.11% (n > 100; 3 biological replicates) when cells were pelleted at a slower rate of 2,000 x g for 2 minutes, indicating that the Δ*mreB* cells are fragile and are more prone to mechanical damage than WT cells. The difference in dead cells for the WT population between slow and fast centrifugation was not significant (p = 0.48, two-sample t-test)
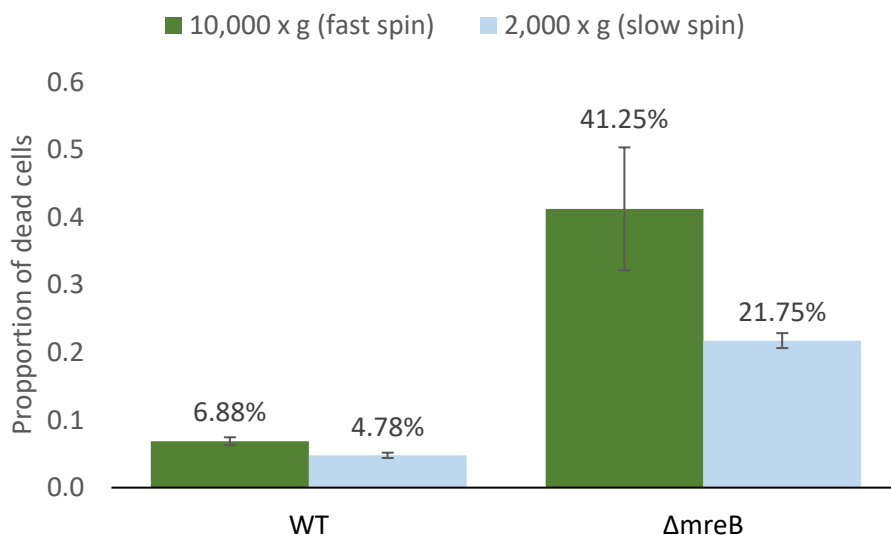
Figure 17 Live/Dead Viability Assay. Exponentially growing Δ*mreB* populations have significantly more dead cells than WT populations (p < 0.001). Δ*mreB* shows sensitivity to mechanical stress as more dead cells are seen when cells are pelleted at a 10,000 x g than at 2,000 x g.

Despite suffering growth defects, we have shown that the Δ*mreB* strain remains viable in standard growth conditions. To date, no other Δ*mreB* strain has remained viable in standard media under standard growth conditions. The closest candidate would be an Δ*mreB* strain of *B. subtilis*, but this only remained viable in special media (with additional Mg^{2+}) (Formstone and Errington, 2005). Therefore, this discovery

provides an opportunity for investigating the consequences of MreB-loss using *P. fluorescens* SBW25 as a model organism. Despite remaining viable, growth assays have shown Δ*mreB* to be growing more slowly compared to WT SBW25. To investigate further, I measured relative fitness to determine how well Δ*mreB* is doing compared to the ancestral WT population. Fitness is defined as the ability of an organism to survive and reproduce in a given environment (Orr, 2009). Specifically, we used relative fitness in order to compare the data with the fitness of WT. This is an important measure that is used later in the evolution experiment.

To measure relative fitness, Δ*mreB* was competed against WT in pairwise competition assays via flow cytometry and also via a traditional plate count method for comparison. In order to distinguish Δ*mreB* from WT, a chromosomally-labelled WT+GFP strain was constructed using a mini-Tn7 transposon system (Lambertsen, Sternberg and Molin, 2004), and used as the competitor. Competing the WT+GFP strain again the WT strain demonstrated that GFP production has no negative effect on the relative fitness of WT+GFP. The GFP strain had equal fitness to WT (selection coefficient = 1.00; SD ± 0.01; 3 biological replicates) whilst Δ*mreB* showed a significantly lower fitness of 0.78 (SD ± 0.02; 3 biological replicates; p < 0.05, two-sample t-test). A similar effect was seen using a standard plate count method, where Δ*mreB* had a significantly lower fitness of 0.73 (SD ± 0.05; 3 biological replicates; p < 0.05, two-sample t-test) compared to the GFP strain (1+ s = 0.94; SD ± 0.04; 3 biological replicates) (Figure 18).
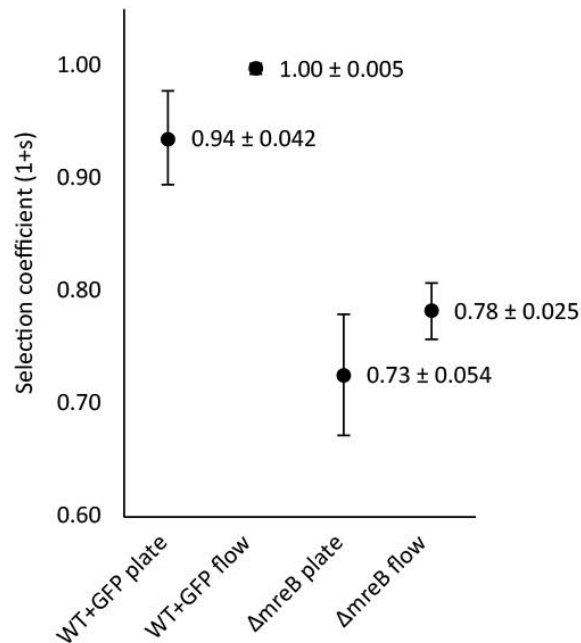
Figure 18 Competitive fitness assays show a marked decline in fitness in the Δ*mreB* strain. This pattern was seen using both a traditional plate count method and using flow cytometry (50,000 events).

It is worth noting that recreating the Δ*mreB* strain proved challenging as mutants were difficult to get in later trials. In two attempts, mutants were retrieved but the cells were smaller, and cultures became turbid after only an overnight incubation – by comparison, Δ*mreB* only becomes turbid after two nights. This suggests the presence of additional mutations that are compensating for the loss of MreB. I was able to create a new Δ*mreB* strain that had similar cell morphologies to the original strain (verified by microscopy and PCR), reinforcing the feasibility of MreB deletion in *P. fluorescens* SBW25. However, this strain had a smaller average cell volume (Figure 19). These results imply that the cells are under a high selection pressure, highlighting the deleterious nature of MreB loss.
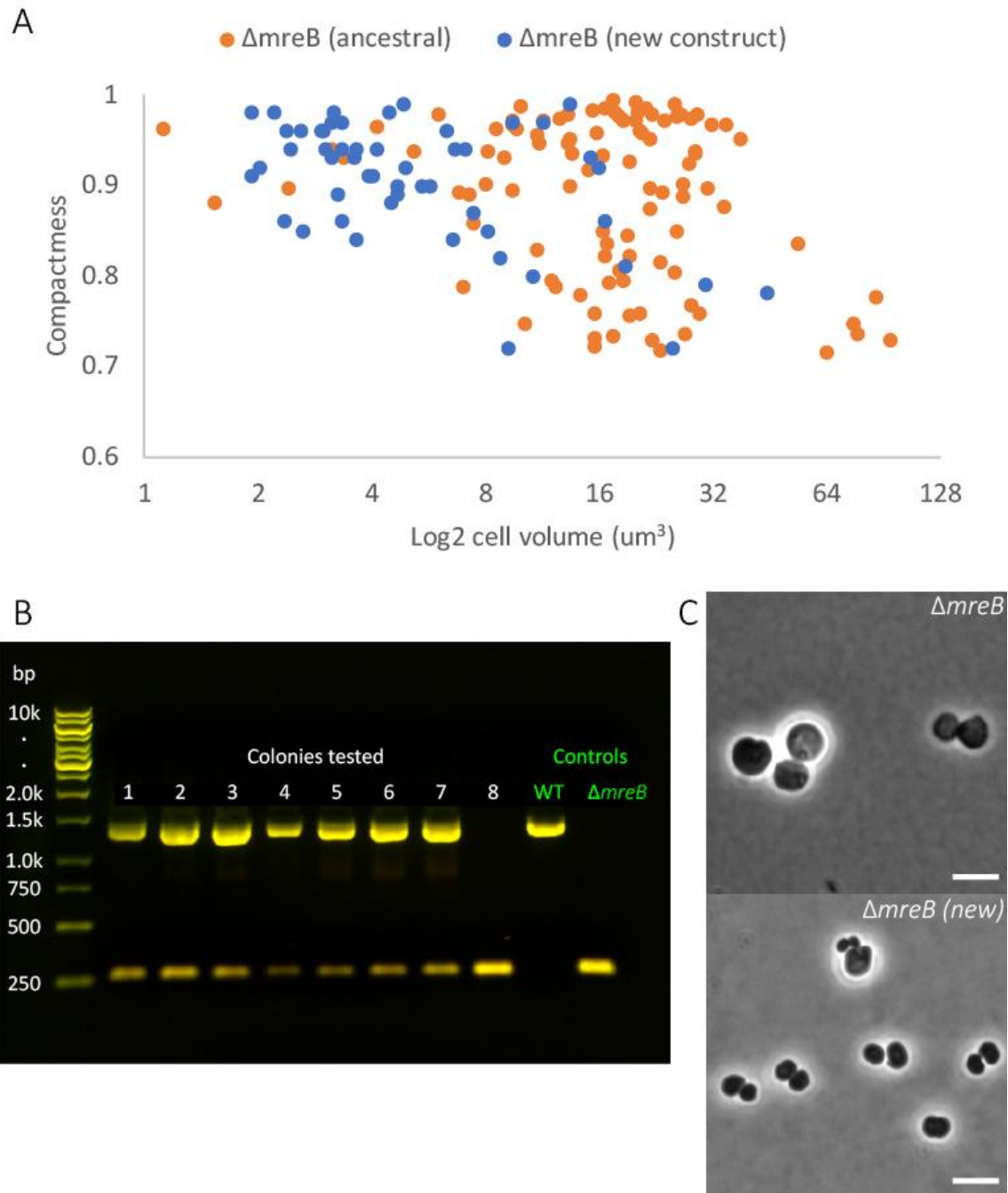
Figure 19 A new Δ*mreB* strain was created using SOE-PCR and tri-parental conjugation. A) The new Δ*mreB* strain had a smaller average volume compared to the ancestral Δ*mreB* strain but displayed similar compactness values. B) The deletion of MreB was verified by PCR – colony no. 8 (pure colony) with the ~260bp MreB-deletion fragment was selected as the example shown in (C); microscopic analysis shows similar, albeit smaller, morphologies to ancestral Δ*mreB.* Scale bar = 5µm.

3.2.3. Δ*mreB* has cell division defects

Using size as a proxy for growth, it has been shown that DNA content is tightly regulated and directly scales with cell growth in bacteria (Vargas-Garcia, Ghusinga and Singh, 2018). The relationship between DNA content and cell size was found to be a useful indicator for identifying cell division defects in *E. coli*. By labelling the origin and terminus regions of the *E. coli* chromosome, Kruse *et al.* (2003) found that chromosome copy numbers increased together with cell size in MreB-null *E. coli* mutants which were unable to divide due to a chromosome segregation defect.

I wanted to investigate if cell division is likewise compromised in Δ*mreB*. To study this, I used electron microscopy to look for signs of incomplete septa on the cell surface, as observed in other MreB-null mutants. I then used DAPI staining to observe chromosome segregation. Next, I used flow cytometry to see if the large cell sizes of Δ*mreB* cells correlate with increasing DNA content. Finally, I used a strain of *P. fluorescens* that had a fluorescently-labelled origin of replication to see if chromosome copy numbers increase together with cell size. Results are presented below.

3.2.3.1 Δ*mreB* cells form incomplete septa and show incomplete chromosome segregation

Features resembling incomplete septa can be seen in Δ*mreB*, particularly in large cells (Figure 20). This phenotype is consistent with cell morphologies seen in other MreB-null strains (Thanedar and Margolin, 2004; Kruse, Bork-Jensen and Gerdes, 2005; Shih, Kawagishi and Rothfield, 2005). In *E. coli*, Corbin et al. (2002) found similar structures which proved to be aberrant division planes forming partial Z-arcs around the MreB-depleted cells. Other groups showed that these partial septa form as a result of FtsZ-mislocalisation caused by the highly variable Min oscillation patterns (Corbin, Yu and Margolin, 2002; Huang and Wingreen, 2004; Thanedar and Margolin, 2004; Wu *et al.*, 2015). This indicates that although cell division can still proceed in cells that have lost MreB, the process could be hindered by incorrect placement of the division plane around the cell (Shih, Kawagishi and Rothfield, 2005).
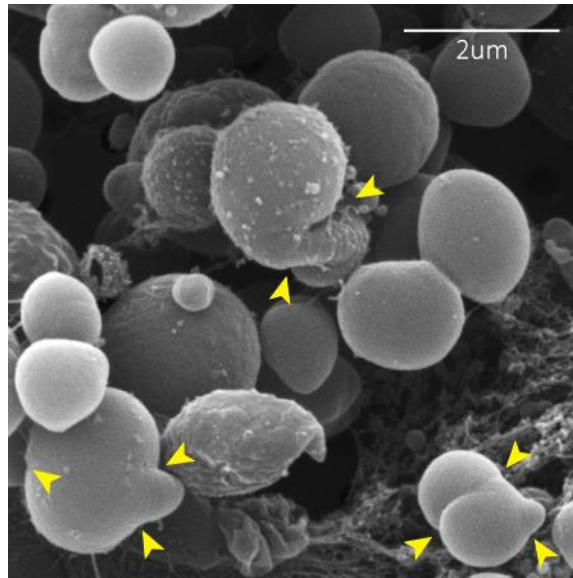
Figure 20 Morphological features resembling incomplete septa are seen in Δ*mreB,* indicated by yellow arrows.

Another factor that affects cell division is the correct partitioning of the nucleoid. In dividing WT cells, chromosomes stained with DAPI show clear separation from the septum. In contrast, some dividing Δ*mreB* cells show the presence of bulk DNA in the path of the constricting septum (Figure 21). These results suggest that chromosome segregation is defective in Δ*mreB.* Spherical cells that have trouble segregating replicated chromosomes may prevent septa from forming correctly due to the presence of DNA. Cambridge *et al.*, (2014) demonstrated using *E. coli* that the accumulation of multiple chromosomes at mid-cell blocks Z-ring formation and cell division. In addition, It has been suggested that MreB plays a role in the segregation of *ori*-proximal regions in *C. crescentus* (Gitai *et al.*, 2005). This is not the case for *E. coli* nor *B. subtilis* (Kruse and Gerdes, 2005; Karczmarek *et al.*, 2007). Whether this is true for Δ*mreB* or not has not been tested. In the future, further investigation using a chromosomally-labelled Δ*mreB* strain observed via time-lapse microscopy will help elucidate the relationship between chromosome segregation and MreB in *P. fluorescens* SBW25.
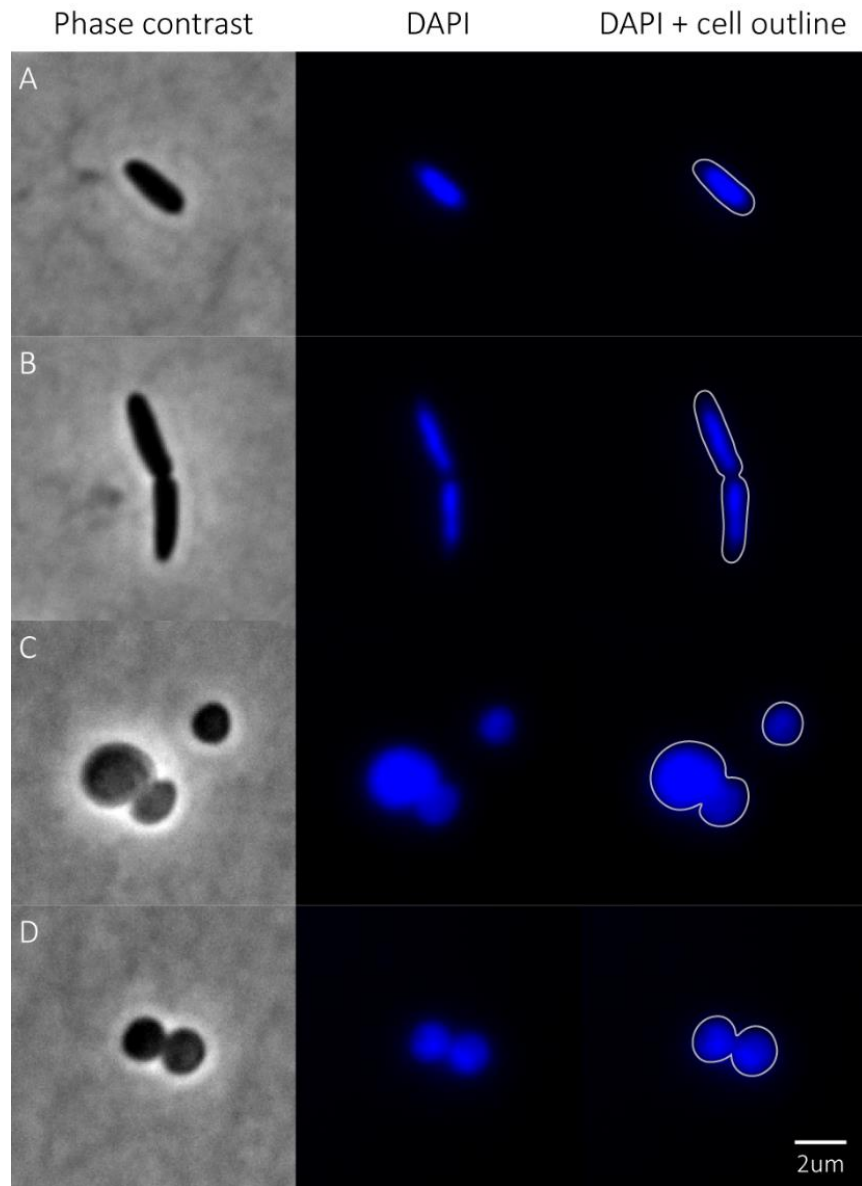
Figure 21 DAPI staining of WT and Δ*mreB.* A) Non-dividing WT cell showing a compact nucleoid in the centre of the cell. B) Dividing WT cell showing well-segregated nucleoids in forming daughter cells. C) Large dividing Δ*mreB* cell with the nucleoid blocking the constricting septum. A smaller non-dividing cell is also seen with the nucleoid in the centre of the cell. D) Dividing Δ*mreB* cell showing segregated nucleoids in the forming daughter cells.

3.2.3.2 Δ*mreB* has numerous copies of its chromosome

To test if DNA content scales with cell size in *P. fluorescens* SBW25, I first analysed WT and Δ*mreB* using flow cytometry. Flow cytometry was used to get large populations of cells, which would help form a robust comparison. This was done by staining exponentially growing WT and Δ*mreB* with the fluorescent stain, SYTO16, followed by flow cytometry analysis. SYTO16 is a membrane-permeable DNA-binding stain which makes it useful for quantifying DNA in both live and dead cells. Flow cytometry revealed that in both WT and Δ*mreB*, cell size (FSC-A) does indeed scale with DNA content (FITC-A). This is especially apparent in Δ*mreB*, where large cells are seen to have many times the amount of DNA seen in WT (Figure 22).
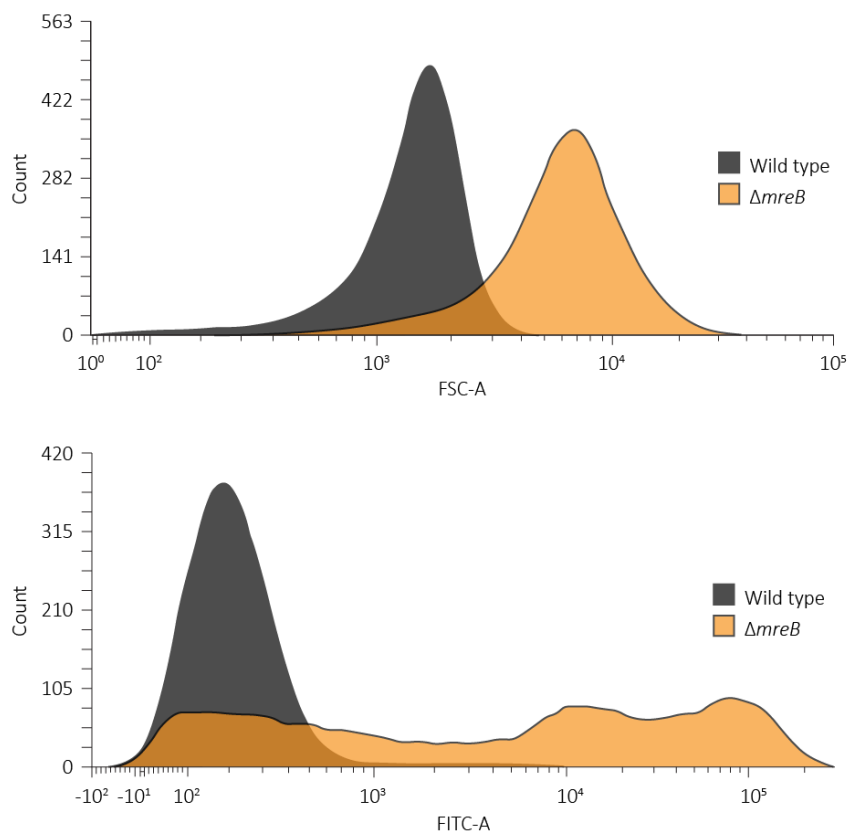
Figure 22 Flow cytometry reveals that cell sizes correlate with DNA content in both WT and Δ*mreB*. Cell size was measured using FSC-A, and DNA content was measured using the FITC-A channel which excites the nucleic acid stain SYTO16. FSC-A and FITC-A data is derived from the same population for 50,000 cells.

Uninterrupted growth has been attributed to cell division defects in Δ*mreB E. coli* mutants (Fenton and Gerdes, 2013). Kafri et al. (2013) previously used DNA content measurements to show that cell growth is linked to the cell cycle. Following this, I used chromosome copy number as an indicator of unabated cell cycle progression is *P. fluorescens* SBW25. To simulate the effects of MreB loss, I used the drug A22 (Iwai, Nagai and Wachi, 2002) on a strain of *P. fluorescens* SBW25 that had a fluorescently labelled origin (*lacO*_pLICTRY; Akarsh Mathrani, unpublished results). A22 directly binds and induces a low-affinity state to MreB (Bean *et al.*, 2009), and the fluorescently-labelled strain produces a brightly-labelled focus at the Tn7 site downstream of the *glmS* region near *ori*, allowing me to quantify chromosome copy numbers in *P. fluorescens* SBW25.

Prior to using the *lacO*_pLICTRY strain, a time-lapse experiment using WT cells was first done to confirm that A22 has the same effect on *P. fluorescens* SBW25 as it does in *E. coli*. Results show that A22 does indeed make the rod-shaped WT cells increasingly shorter and wider, ultimately producing ovoid cells. A22 does this by disrupting the polymerisation of MreB (Kawazura *et al.*, 2017). After growing in A22 for 1 hour, WT cells became wider, developing a bloated morphology. After 2 hours, cells continued to become wider, becoming lemon-shaped, a phenotype seen in *C. crescentus* cells depleted of MreB (Figge, Divakaruni and Gober, 2004). After 3 hours, many of the cells have started losing their pointed poles, becoming ovoid (Figure 23A). These cells were allowed to continue growing in the presence of A22 overnight. The following day, the cells were subcultured into fresh LB with A22, and imaged upon reaching log phase. Image analysis confirm that these cells are now almost perfectly spherical with a compactness of 0.92 (SD ± 0.08; n > 100). This is very similar to the compactness of Δ*mreB* which measures 0.89 (SD ± 0.09; n > 100) (Figure 23B).
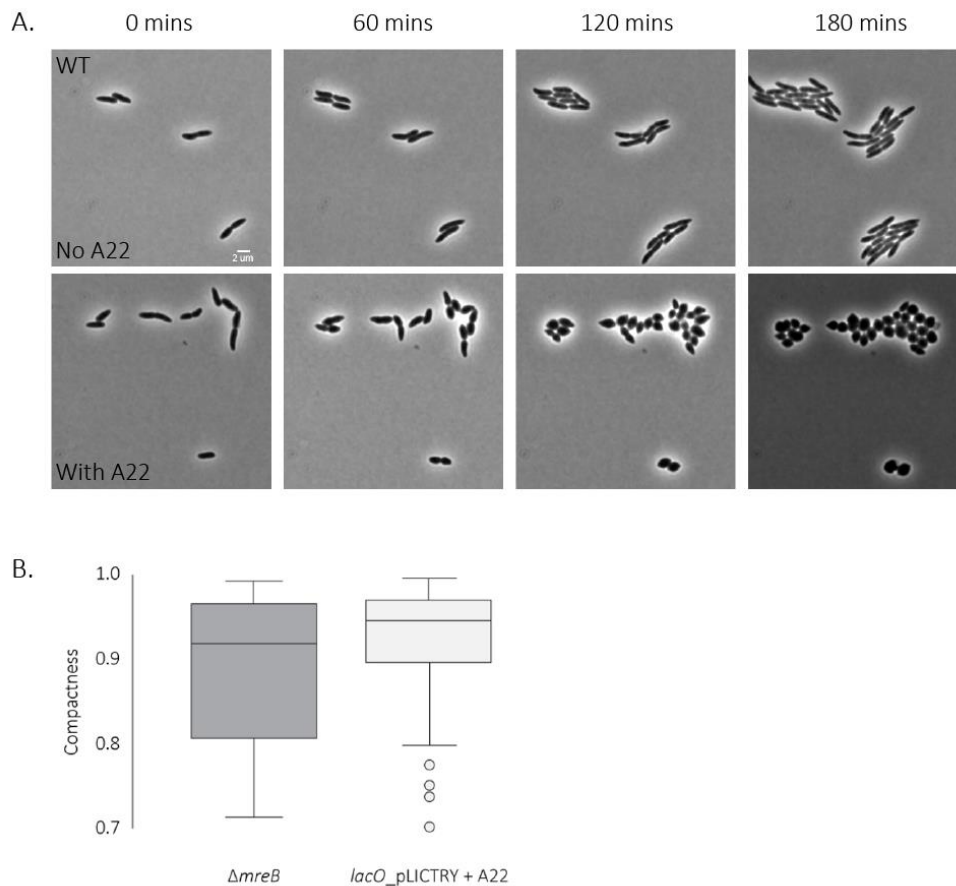
Figure 23 Rod-shaped *P. fluorescens* SBW25 cells becomes spherical when grown in the presence of A22. A. Rod-shaped cells lose control of width and grow into short and wide (ovoid) cells over time. B. Subcultured *lacO*_pLICTRY cells that continue to grow in A22 exhibit a near spherical morphology, with compactness values that are very similar to Δ*mreB*.

Seeing that A22 has the same effect on *P. fluorescens* SBW25 as in other model bacteria, I then grew the fluorescently labelled *lacO_pLICTRY* strain in LB with A22. The same protocol was observed, cells were grown in A22 overnight, then subcultured and grown with A22 to exponential phase the following day. Following this, cells were harvested and observed under the microscope. Typically, rod-shaped cells (*lacO_pLICTRY* cells not grown in A22) have between 2 to 4 ori-proximal foci (ave. = 2.4; SD ± 0.77; n > 50). In contrast, spherical cells that were grown in A22 showed significantly more foci than their rod-shaped counterparts (ave. = 4.26; SD ± 2.25; n = 50; p < 0.05, two-sample t-test) (Figure 24).
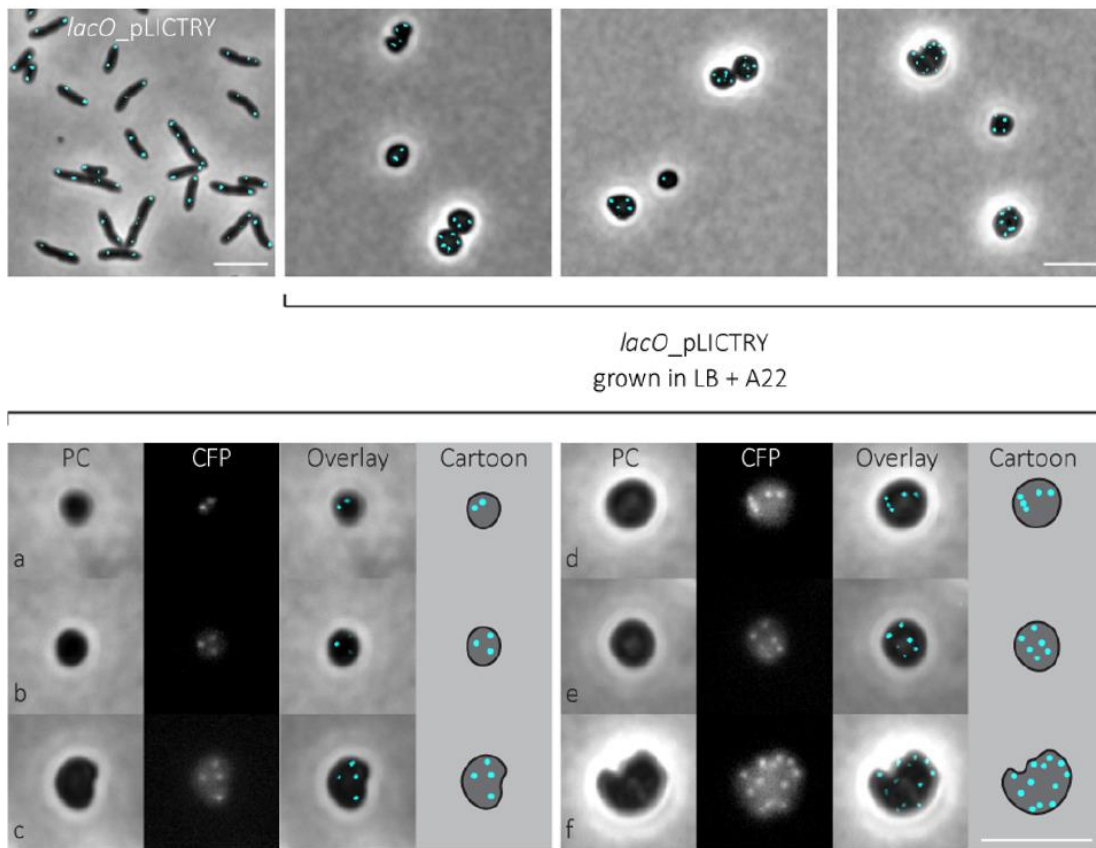
Figure 24 Rod-shaped lacO_pLICTRY cells with fluorescently labelled ori- typically show an average of 2 foci (top left). When grown in A22, these cells grow as spheroids with an average of 4 foci. The bottom panel shows that the number of foci in these cells increase with cell size.

Furthermore, I found that the number of fluorescent foci in spherical *lacO_pLICTRY* cells show a strong positive correlation with cell size ($R_2 = 0.74$) (Figure 25A), confirming what was previously observed using flow cytometry. Smaller cells with cell volumes < 4 μm^3 make up more than 60% of the population and have between 2 and 4 foci. Larger cells with cell volumes measuring 5-8 μm^3 make up around 30% of the population and have between 5 to 8 foci. The remainder of the population are comprised of massive cells with cells volumes > 8 μm^3 with or more foci (Figure 25B).
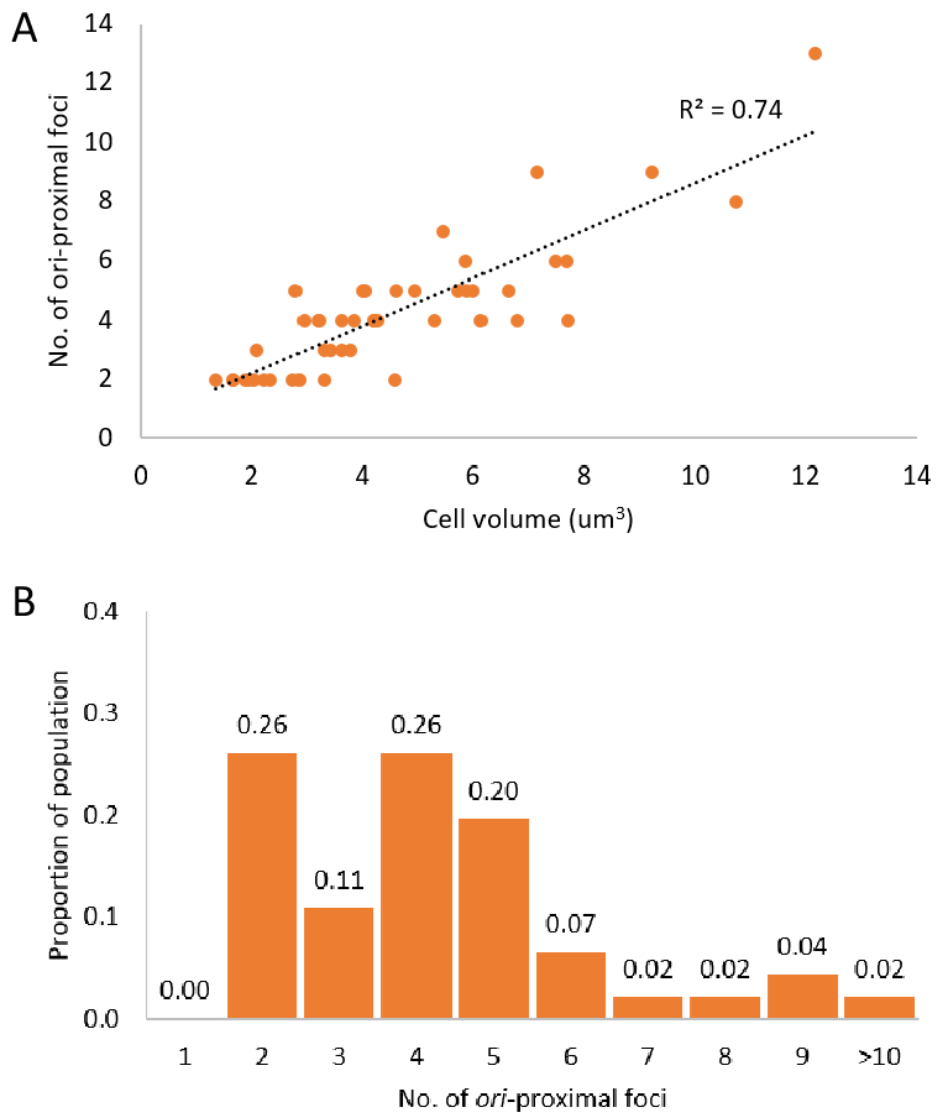
Figure 25 Cell size positively scales with chromosome copy numbers in spherical *P. fluorescens* SBW25 cells. A) The number of ori-proximal foci increase with cell size (n = 50). B) Most cells (63%) typically have between 2 to 4 foci. About 30% of the population are larger cells that have 5 foci or more.

The accumulation of more than 4 foci (the maximum number of foci seen in rod-shaped cells) coupled with a steady increase in cell volume indicate that cells have lost the ability to divide and instead keep growing into large cells. This is consistent with observations in MreB-null *E. coli* (Kruse *et al.*, 2003) where chromosome copy numbers increase with cell size, and with the general understanding that DNA content increases with cell size in bacteria (Shi *et al.*, 2017; Si *et al.*, 2017). These results show that a cell

division defect exists in Δ*mreB*, and support the idea that MreB loss impairs cell division in bacteria that have a native rod-like shape (Fenton and Gerdes, 2013).

3.2.4. Magnesium improves the growth of Δ*mreB*

It was previously reported that an Δ*mreB* mutant can be rescued with the addition of magnesium to its growth medium. In *B. subtilis*, an *mreB*-depleted strain that would normally swell and burst retained its rod-shaped morphology and maintained a WT growth rate when supplemented with 25 mM Mg^{2+} (Formstone and Errington, 2005). This effect was also seen, to a lesser extent, in MreC and MreD mutants (Leaver and Errington, 2005). So, I wanted to know if supplementing LB with Mg^{2+} can improve the growth of Δ*mreB*. By comparing the growth dynamics of Δ*mreB* cultures grown with or without supplemental Mg^{2+}, I found that adding Mg^{2+} to LB does indeed improve Δ*mreB* growth, up to a point (Figure 26).

In Δ*mreB*, additional magnesium did not revert the spherical cells to a rod-like. However, growth improvements were seen with supplemental Mg^{2+}. With an additional 10 mM Mg^{2+}, Δ*mreB* in LB had a shorter lag time and reached a higher maximum OD_{600} of 1.10. With 20 mM additional Mg^{2+}, Δ*mreB* reached a higher maximum OD_{600} of 1.05. Additional Mg^{2+} was no longer beneficial as 30 to 50 mM Mg^{2+} actually slowed the growth of Δ*mreB*. Additional Mg^{2+} had no effect on WT (Figure 26).
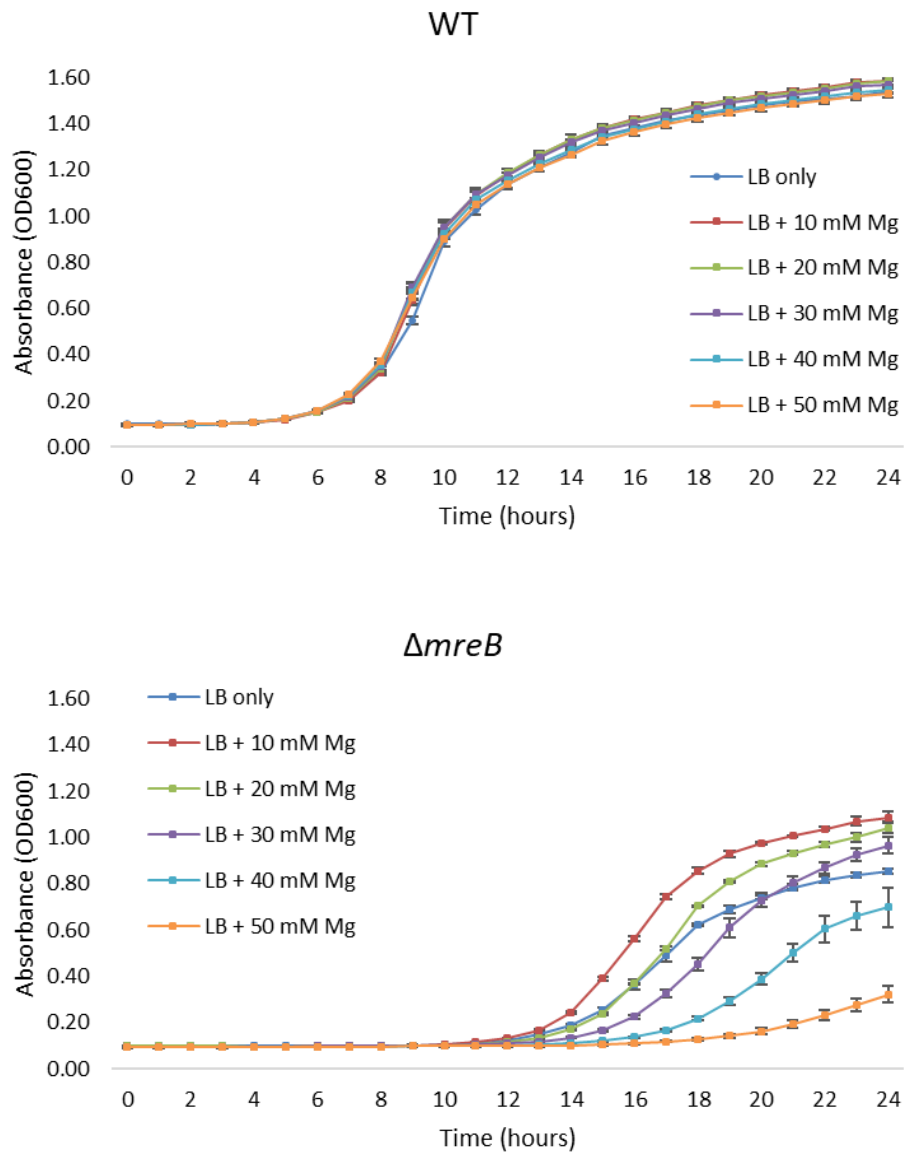
Figure 26 Effects of Mg^{2+} on growth. Additional Mg^{2+} has no beneficial effect on WT cells. In Δ*mreB*, additional Mg^{2+} improves growth at 10-20mM concentrations by shortening lag time and increasing maximum OD. Higher amounts of Mg^{2+} show the opposite effect, slowing growth and lowering maximum OD. Error bars represent SD of 3 biological replicates.

It is unclear how supplementary Mg^{2+} improves growth, but there are three possibilities from the literature that come to mind: Mg^{2+} improves cell wall integrity possibly by cross-linking with PG, Mg^{2+} promotes proper septation and, finally, Mg^{2+} helps in the coordination of PG synthesis. I will explain further in the sections below.

The first possibility is that Mg^{2+} is boosting cell wall integrity, thereby allowing more Δ*mreB* cells to survive and/or grow better. In Δ*mreB*, as much as 40% of cells die from a standard centrifugation step (10,000 x g for 2 minutes), compared to only 20% from a slower setting (2,000 x g for 2 minutes) (Figure 17). The increase in cell death in Δ*mreB* could be caused by the lysis of "weakened" cells. An early study by Rayman & MacLeod (1975) showed that in the marine Pseudomonad B-16, Mg^{2+} can prevent cell lysis by improving cellular integrity, possibly by cross-linking with PG. They found that the amount of Mg^{2+} needed to prevent lysis doubles when cellular integrity is compromised by the formation of mureinoplasts – a state where the outer membrane and periplasmic space are removed. Crosslinks between Mg^{2+} and PG have also been proposed for *P. aeruginosa* (Asbell and Eagon, 1966). In the halophilic bacterium *Haloarcula japonica*, magnesium is necessary for maintaining the structural integrity of its cell wall (Nakamura *et al.*, 1997). Removal of magnesium from the growth medium resulted in cells shedding parts of their cell wall, eventually turning into spheres. More recently, the study of Formstone & Errington (2005) demonstrated that the lysis of MreB-deficient cells was initiated by cell-to-cell contact – possibly a result of cells having a lower resistance to osmotic or mechanical stress. This defect was also mitigated by the addition of extra Mg^{2+}.

The second possibility is that Mg^{2+} is required for cell division to occur properly. Murray et al. (1998) argued that Mg^{2+} may be a requirement for septation as *B. subtilis* cells produce filaments if grown in low Mg^{2+}, and that extra Mg^{2+} is able to suppress defects in mutants lacking MreD which has been linked to cell division (Varley and Stewart, 1992). From their study, Murray et al. (1998) demonstrated that filamenting PBP1a mutants produced normal septation patterns when higher concentrations of Mg^{2+} are used. Furthermore, *Vibrio parahaemolyticus* cells that had cell division defects as a result of MreB overexpression were largely rescued by the addition of 25 mM Mg^{2+} (Shen W. Chiu, Chen and Wong, 2008). The link between magnesium and cell division may also apply to *P. fluorescens* SBW25. In this organism, the deletion of MreB is detrimental to growth, producing cells that grow poorly – possibly due to a cell division defect. The addition of 10 to 20 mM Mg^{2+} to Δ*mreB* improves growth, allowing cells to

enter exponential growth sooner and reach a higher maximum OD. It is possible that the loss of MreB raises the requirement for Mg^{2+} during cell division, which is then met by the supplemental Mg^{2+} added to LB. In line with this, WT cells are not affected by extra Mg^{2+}. My results show that 10 mM Mg^{2+} provides the best growth improvement – shortening lag time and allowing the highest amount of growth. This beneficial effect decreases as Mg^{2+} increases, especially beyond 20 mM Mg^{2+} (Figure 26). It is unknown why growth is impaired by higher amounts of Mg^{2+} (> 20mM Mg^{2+}).

A third possibility is that Mg^{2+} may have a positive effect on the coordination of PG synthesis in Δ*mreB*. In *V. parahaemolyticus*, swelling and growth defects caused by MreB mislocalisation are prevented by the addition of 25 mM Mg^{2+} (Shen W. Chiu, Chen and Wong, 2008). The same is true in *B. subtilis* (Formstone and Errington, 2005). Indeed, the unusually large Δ*mreB* cells do become significantly smaller when grown with 20 mM Mg^{2+} (4.91 μm^3, SD ± 3.50 μm^3 vs 20.65 μm^3, SD ± 16.17 for Δ*mreB*; n = 100 per strain; p < 0.001, two-sample t-test). No change was seen in WT cells. Rayman & MacLeod (1975) suggested that the cross-linking of Mg^{2+} to PG may only be needed if PG levels drop to a certain critical amount, possibly explaining why growth improvements were seen in Δ*mreB*, but not WT. Using the logic of the "relative rates" model by (Harris and Theriot, 2016a), the smaller Δ*mreB* cells seen after the addition of Mg^{2+} could indicate that the rate of cell surface (PG) synthesis has somehow caught up with the rate of volume synthesis in these cells. The topic of Mg^{2+} concentrations has received little attention in the most recent literature, but this effect on the survival and size of Δ*mreB* cells certainly brings the topic back to the fore. We did not pursue this interesting result further in this thesis, but it remains of interest to the Hendrickson laboratory.

3.2.5. Morphological defects are mitigated by ectopic MreB expression

In *B. subtilis*, as in *P. fluorescens* SBW25, *mreB* is co-expressed in the same operon as *mreC* (Formstone and Errington, 2005), making it important to check if the characteristics of Δ*mreB* are produced only as a result of MreB loss, and not anything else. To verify that the phenotypic traits seen in Δ*mreB* are specific to MreB loss, the *mreB* gene was inserted and ectopically expressed from the Tn*7* site near the *glmS* region of Δ*mreB* (hereafter, Δ*mreB* + MreB). The same was done in WT (hereafter, WT + MreB), which was used as a control. Ectopic MreB expression in Δ*mreB* + MreB completely restored its original WT morphology, whilst cell shape remained the same in the WT + MreB strain (Figure 27).

| Δ*mreB* + MreB | WT + MreB |
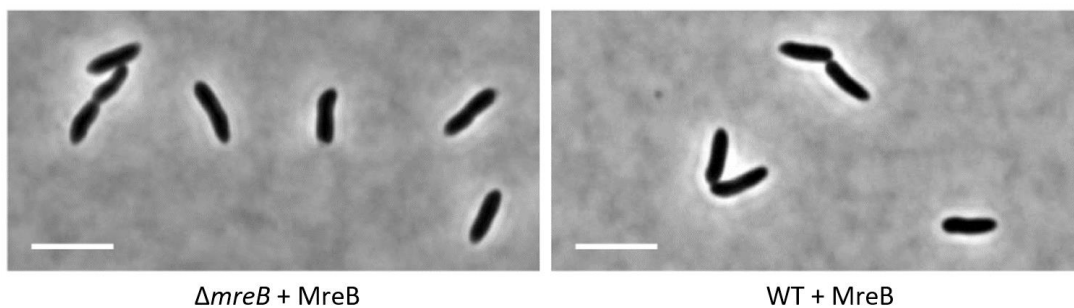
Figure 27 Δ*mreB* cells that are ectopically producing MreB grow as typical rods. WT cells ectopically producing extra MreB continue to grow as typical rods. Scale bar = 3μm.

In Δ*mreB* + MreB, compactness values were the same as WT, but cells were significantly shorter (3.86 μm; SD ± 1.07 μm vs 4.51 μm; SD ± 1.73 μm in WT; n = 100 per strain; p < 0.001, two-sample t-test) and thinner (0.81 μm; SD ± 0.00 μm vs 1.00 μm; SD ± 0.00 μm in WT; n = 100 per strain; p < 0.001, two-sample t-test). Interestingly, WT + MreB cells became significantly shorter (3.79 μm; SD ± 0.92 vs 4.51 μm for WT; n = 100 per strain; p < 0.001, two-sample t-test), thinner (0.83 μm; SD ± 0.00 vs 1.00 μm for WT; n = 100 per strain; p < 0.001, two-sample t-test), and appear significantly "straighter", having a lower average compactness compared to WT (0.50 μm; SD ± 0.00 vs 0.54 μm; SD ± 0.00 in WT; n = 100 per strain; p < 0.001, two-sample t-test) (Figure 28).
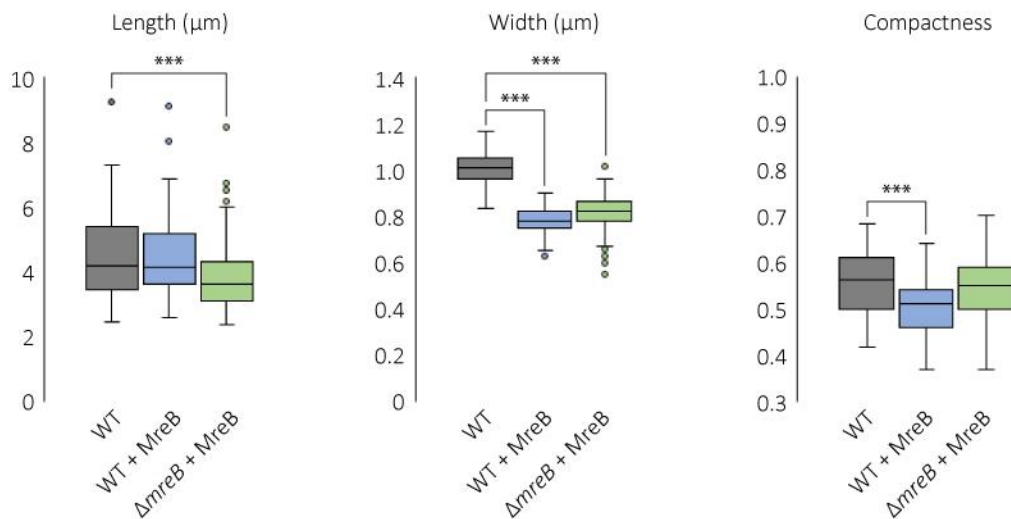
Figure 28 Effects of ectopic MreB production on the cell shape of WT and Δ*mreB*. In the WT background, the production of extra MreB has no effect on cell length, but produces significantly thinner/ narrower cells. Ectopic MreB production made WT cells straighter, significantly reducing compactness. In the Δ*mreB* background, ectopic MreB production enabled cells to grow as typical rods having the same compactness values as WT, but cells are significantly shorter and thinner compared to WT. Significance represented by asterisks.

Aside from altering cell shape, ectopic MreB expression also increased the fitness and the proportion of live cells in actively growing Δ*mreB* + MreB cells to WT levels. This indicates the restoration of normal MreB function (Figure 29). In the WT + MreB strain, fitness and live cell counts remained the same as in WT. This is similar to observations in *E. coli* and *V. parahaemolyticus*, where MreB overexpression had no effect on cell viability (Wachi and Matsuhashi, 1989; Shen W. Chiu, Chen and Wong, 2008). In contrast, MreB overexpression is lethal in *C. crescentus* (Gitai, Dye and Shapiro, 2004).
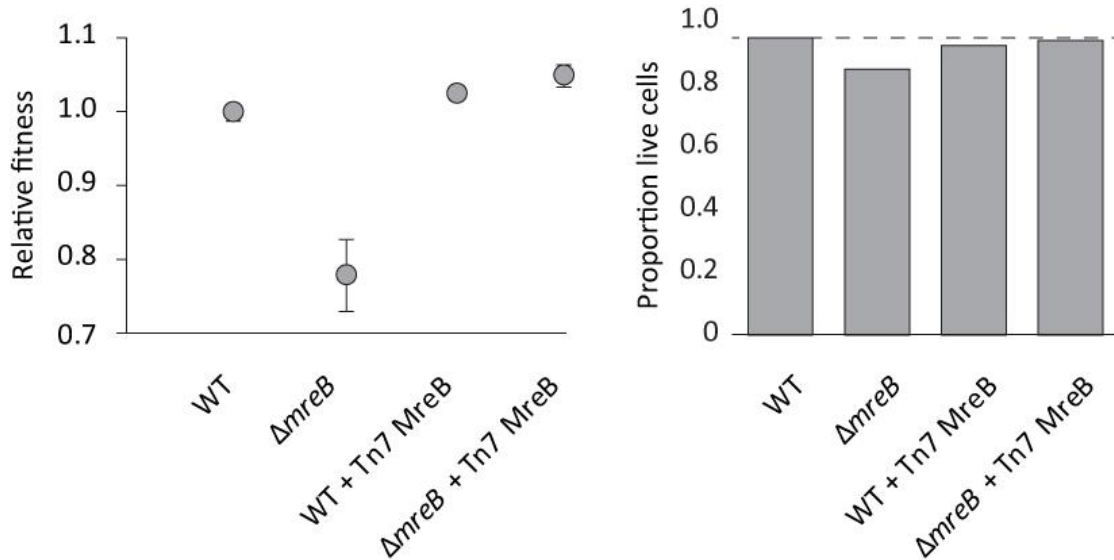
Figure 29 Competitive fitness and the count of live cells are restored to WT values in Δ*mreB* + Tn7 MreB. Fitness and live cell counts are unchanged in WT + MreB.

The growth dynamics of Δ*mreB* + MreB was not identical to WT. However, growth did improve – lag time was s 4 hours shorter compared to Δ*mreB*, and the strain reached had a higher maximum OD_{600} of 1.5 (Figure 30). In the WT background, ectopic MreB production caused delayed growth (lag time was 4 hours longer) but overall growth characteristics remained the same.
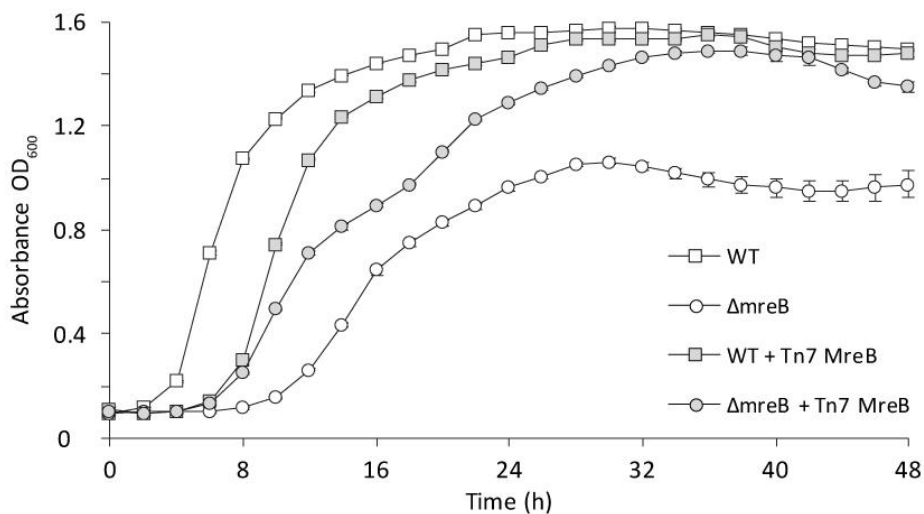
Figure 30 Growth characteristics of Δ*mreB* + MreB show a shorter lag time and higher maximum OD compared to Δ*mreB.* WT + MreB has a longer lag time compared to WT, but growth is the same as WT overall. Error bars represent SD for 3 biological replicates.

The reduction in width observed in the WT background in response to the ectopic expression of MreB is surprising as the overexpression of MreB in other bacteria such *V. parahaemolyticus*, *E. coli*, and *S. coelicolor* produced the opposite phenotype: branching, filamenting, or bulging cells (Wachi and Matsuhashi, 1989; Carballido-López and Errington, 2003; Shen W. Chiu, Chen and Wong, 2008). The phenotypes seen in other bacteria were proposed to be a result of MreB interfering with cell division, possibly due to a reduction in the activity of a cell division-associated gene, *ftsI* (PBP3) (Wachi and Matsuhashi, 1989). It has also been argued that excess MreB may form extra filaments that could disturb the longitudinal axis of cells during cell division, resulting in branched cells (Shen W. Chiu, Chen and Wong, 2008). Interestingly, the growth characteristics of WT + MreB were altered, showing a prolonged lag time of ~4 hours, which could indicate a defect in cell division as seen in *E. coli* cells that are overexpressing MreB (Wachi and Matsuhashi, 1989). This is consistent with the observation of a prolonged lag time in bacteria in a state of growth arrest, as seen in *S. aureus* (Vulin *et al.*, 2018). The exact effect of additional MreB in *P. fluorescens* SBW25 WT cells remains an open question and will benefit from further investigation. In contrast, we found that the ectopic expression of MreB in the Δ*mreB* background showed a remarkable rescue of cell shape, as well as improved growth, fitness, and viability. This confirms that the defective phenotype seen in Δ*mreB* can be directly attributed to the loss of MreB, and further affirms the known role of MreB as the coordinator of the rod cell shape in bacteria.

3.2.6. Analysing the cell wall of WT and Δ*mreB* strain

The phenotypic effects of *mreB* perturbation or loss in rod-shaped bacteria is remarkable. To review, loss of this single gene makes cells much larger on average and highly heterogeneous in dimension and size. This also leads to increased DNA copy numbers but whether this result is a symptom of MreB loss or of compensation for loss is not immediately clear. There is a tightly interwoven set of connections between cell shape, cell size, cell wall structure, and DNA content. In order to begin to understand the molecular basis of the changes we have seen, we decided to take advantage of techniques that would

allow us to inspect the cell wall in detail: Ultra Performance Liquid Chromatography (UPLC) and fluorescent D-amino acid staining of cell walls. These techniques allow us to dissect the biochemical components of the cell wall and to determine where cell wall construction is taking place.

After isolating the PG of the strains used in this study, samples were analysed at Umeå University, Sweden using established UPLC techniques (see methods). The data show that the most abundant muropeptides for *P. fluorescens* SBW25 are M4 monomers and cross-linked D44 dimers. Other minor peaks were also identified, such as monomers linked to lipoproteins (M3L) and dimers cross-linked by 4-3 bonds. Major anhydro peaks (D44N and T444N) were identified and used for the calculation of the average lengths of the glycan chains. The positions and identities of these PG components are shown below (Figure 31). These results are consistent with results from similar studies (Desmarais *et al.*, 2015; Espaillat *et al.*, 2016; Torrens *et al.*, 2017), further supporting the utility of UPLC analysis for understanding PG chemistry and cell wall characteristics in bacteria. The complete data sets for the UPLC analyses are presented in the Appendix.
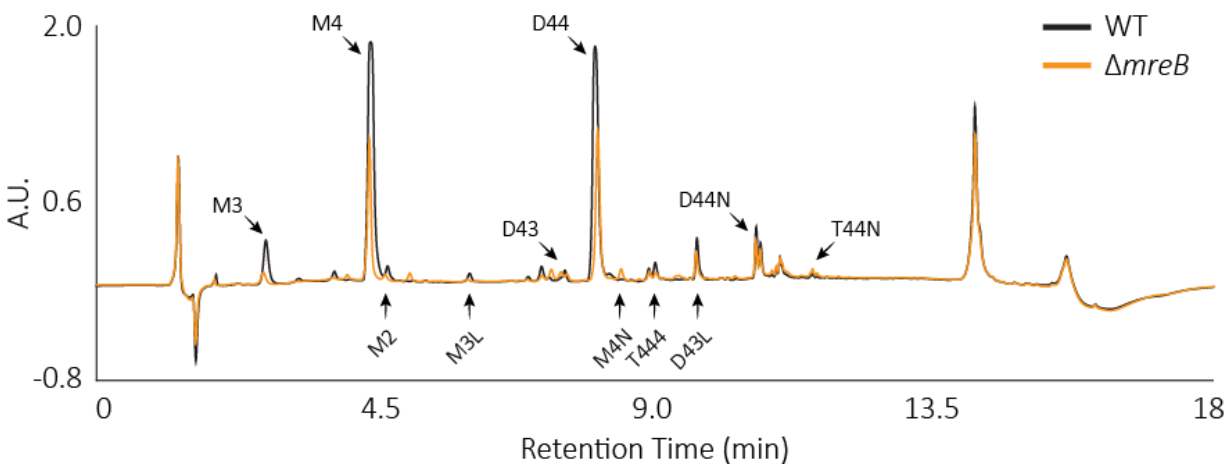
Figure 31 Major muropeptides identified in WT PG using ultra performance liquid chromatography (UPLC). The most abundant muropeptides are M4 monomers and D44 dimers.

The major components of WT PG are M4 monomers (39.61%; SD ± 0.83%; 3 replicates) and D44 dimers (34.82%; SD ± 1.37%; 3 replicates) (Figure 32). These two components show little variation across 3 biological replicates, indicating that the abundance of these components is tightly regulated in WT cells. Dividing D44 by M4 makes it easy to interpret the relative abundance of dimers compared to monomers in these cells. Values greater than 1 show a higher abundance of dimers, whereas values lower than 1 indicate a higher abundance of monomers. In WT, D44/M4 is 0.88 (SD ± 0.02; 3 replicates), showing a relatively higher abundance of monomers in these cells. The D44/M4 ratio is a useful tool for comparing the profiles of different strains. To calculate PG cross-linking, D44 dimers were counted with T444 trimers, giving the total amount of cross-linking in these cells. Cross-linking was determined to be 39.20 (SD ± 0.83%; 3 replicates) in WT. Finally, the average chain length of WT PG was measured using the D44N anhydro dimers and T444N anhydro trimers. Average PG chain length in WT was determined to be 26.16 (SD ± 2.53; 3 replicates) disaccharides.

In Δ*mreB*, the number of M4 monomers was significantly lower at 26.92% (SD ± 0.60%; 3 replicates; $p < 0.05$; two-sample t-test) (Figure 32). The amount of D44 remained the same as WT at 34.36% (SD ± 0.21%; 3 replicates). Together, these values show a significantly higher D44/M4 of 1.28% (SD ± 0.02; 3 replicates; $p < 0.05$; two-sample t-test). The average cross-linking percentage showed a significant increase, rising to 42.70% (SD ± 0.91%; $p < 0.05$; 3 replicates; two-sample t-test). The average chain length was significantly shorter, dropping to 12.38 disaccharides (SD ± 0.55 disaccharides; 3 replicates; $p < 0.05$; 3 replicates; two-sample t-test).
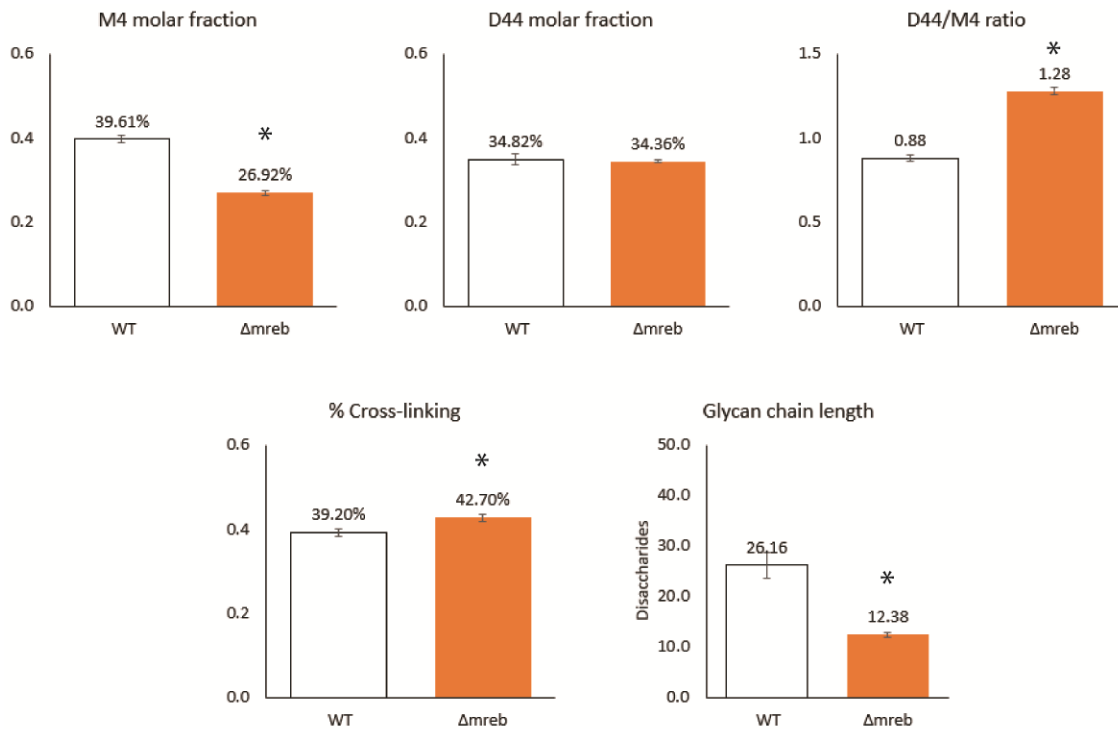
Figure 32 Major characteristics of WT and Δ*mreB* PG. Δ*mreB* PG has significantly fewer M4 monomers producing a higher D44/M4 ratio. Δ*mreB* PG has more cross-linking whilst having shorter glycan chains than WT PG. Asterisks indicate a significant difference in Δ*mreB* PG value compared to WT. Error bars represent SD for 3 biological replicates.

The prominent PG components in WT are M4 and D44. These are the same major muropeptides in *E. coli* and *P. aeruginosa*, which are similarly Gram-negative rod-shaped species (Desmarais *et al.*, 2015; Espaillat *et al.*, 2016; Torrens *et al.*, 2017). Analysis of Δ*mreB* PG reveals that the loss of MreB leads to a significant drop in M4, with no apparent effect on D44. Consequently, this led to a significant increase in D44/M4. The high D44/M4 in Δ*mreB* possibly translates to a stiffer PG, one that is able to expand less in response to turgor pressure (Desmarais *et al.*, 2013). The cross-linking percentage of the PG of Δ*mreB* also increased significantly, which would contribute more stiffness to the structure of the cell wall.

However, Δ*mreB* had significantly shorter glycan chains measuring 12.38 disaccharides (SD ± 0.55 disaccharides; 3 replicates; two-sample t-test). This is consistent with the observation that spherical *E. coli* cells with no MreB produce shorter glycan chains (Turner *et al.*, 2018). This, together with the a previous observation that spherical *B. subtilis* cells with a mutated *mreC* also showed much shorter glycan chains

(Hayhurst *et al.*, 2008) led Turner *et al.* (2018) to propose that the disruption of systems directing PG synthesis will generally result in the production of shorter glycan chains. The shorter chains would have the opposite effect of making the PG more flexible, making it difficult to infer how these changes would affect the overall flexibility of Δ*mreB*'s PG.

In addition to possible structural effects on cell wall flexibility, the loss of MreB may also be affecting the activity of PBPs. In *E. coli*, MreB inhibition by A22 result in a significant shortening of the average glycan chain length (Varma, de Pedro and Young, 2007; Uehara and Park, 2008). In *C. crescentus*, MreB inactivation also results in a shorter average glycan chain length, and the restoration of MreB activity results in an increase in the average glycan chain length (Takacs *et al.*, 2010). In *P. fluorescens* SBW25, the loss of MreB also resulted in shorter PG strands. These results support the argument of Takacs *et al.*, (2010) who states that MreB promotes, either directly or indirectly, the transglycosylase or PG elongation activity of PBPs. The authors suggest that this can be a result of changes in protein-protein interactions in the cell wall building machinery of the cell.

The short PG strands in Δ*mreB* may also be playing a role in its slowed growth. In *E. coli*, PG associated with the initiation of septation is made up of relatively long glycan strands measuring >20 disaccharides in length (Ishidate *et al.*, 1998). In line with this, Ursinus et al. (2004) found that in *E. coli*, PG strands need to be longer than 25 disaccharides to interact with the cell division proteins FtsN. The cell division machinery of SBW25 possesses this same protein, FtsN (PFLU0400; NCBI Reference Sequence: WP_012721808.1). Perhaps, similar to *E. coli*, the short glycan strands of Δ*mreB* may be negatively affecting the interaction of the cell division machinery with septal PG, leading to slowed growth.

3.2.7. PG characteristics are restored by ectopic MreB expression

To further elucidate the effects of ectopic MreB expression, the PG of Δ*mreB*+MreB was isolated and characterised by UPLC. Compared to Δ*mreB*, M4 increased to 33.25% (SD ± 9.83%; 3 replicates), and D44 decreased to 27.40% (SD ± 10.90%; 3 replicates) in Δ*mreB*+MreB (Figure 33). These values were not statistically different from those of Δ*mreB*, despite the increased variance. However, this significantly lowered the D44/M4 ratio to 0.80 (SD ± 0.10; p < 0.05; 3 replicates; two-sample t-test), bringing the ratio back to WT levels. The amount of cross-linking decreased substantially to 30.37% (SD ± 12.39%; 3 replicates). Glycan chain length increased to 24.10 disaccharides (SD ± 0.94 disaccharides; 3 replicates). The average cross-linking and glycan chain length values of Δ*mreB*+MreB have no significant difference from WT values (p = 0.28; two-sample t-test).
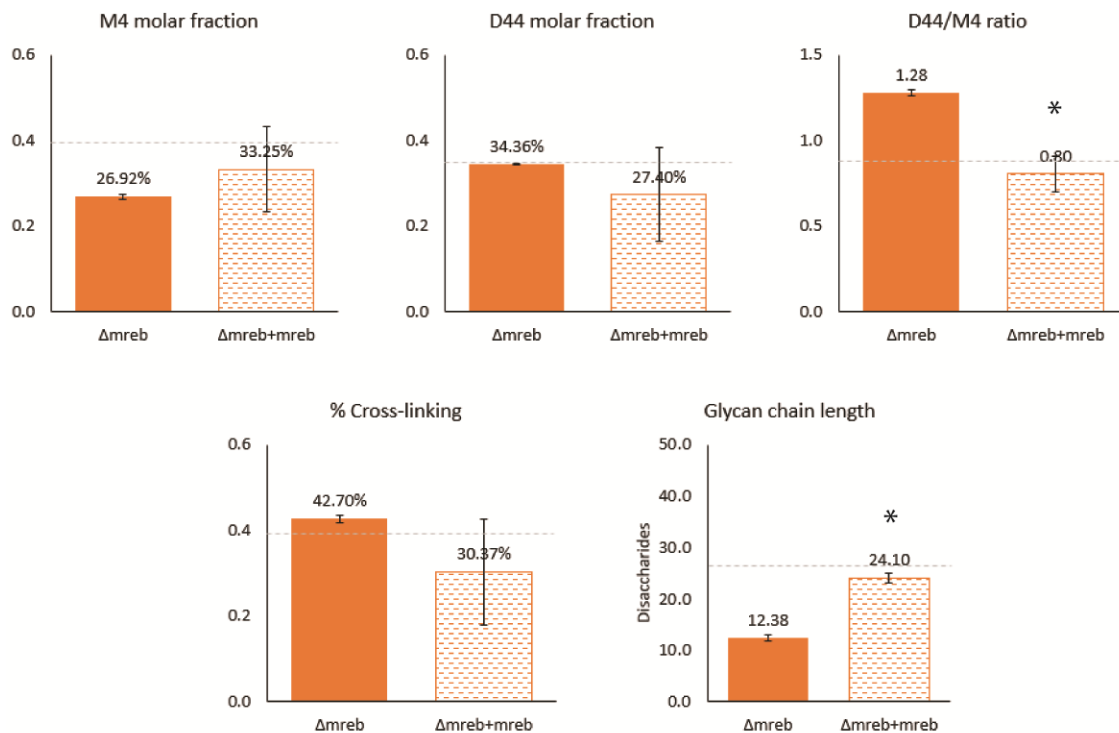
Figure 33 Ectopic MreB production in Δ*mreB* restored PG characteristics to WT levels. M4 and D44 increased, leading to a significant reduction in D44/M4. Cross-linking decreased, and glycan chains significantly increased in length. WT values for each PG component is represented by the grey dashed line. Asterisks indicate a significant difference in Δ*mreB* + MreB PG value compared to WT.

Ectopic MreB expression in WT resulted in significantly lower M4 levels, dropping to 33.31% (SD ± 1.16%; 3 replicates; $p < 0.05$, two-sample t-test). D44 decreased slightly to 30.41% (SD ± 2.04%; 3 replicates); D44/M4 levels increased slightly to 0.91 (SD ± 0.03; 3 replicates); and cross-linking decreased slightly to 33.42% (SD ± 3.22%; 3 replicates) (Figure 34). Statistical analysis revealed these changes to have no statistical difference from WT values. The most outstanding difference was the shortening of the glycan chain length which showed a significant reduction to 16.85 disaccharides (SD ± 0.28 disaccharides; 3 replicates; $p < 0.05$; two-sample t-test).
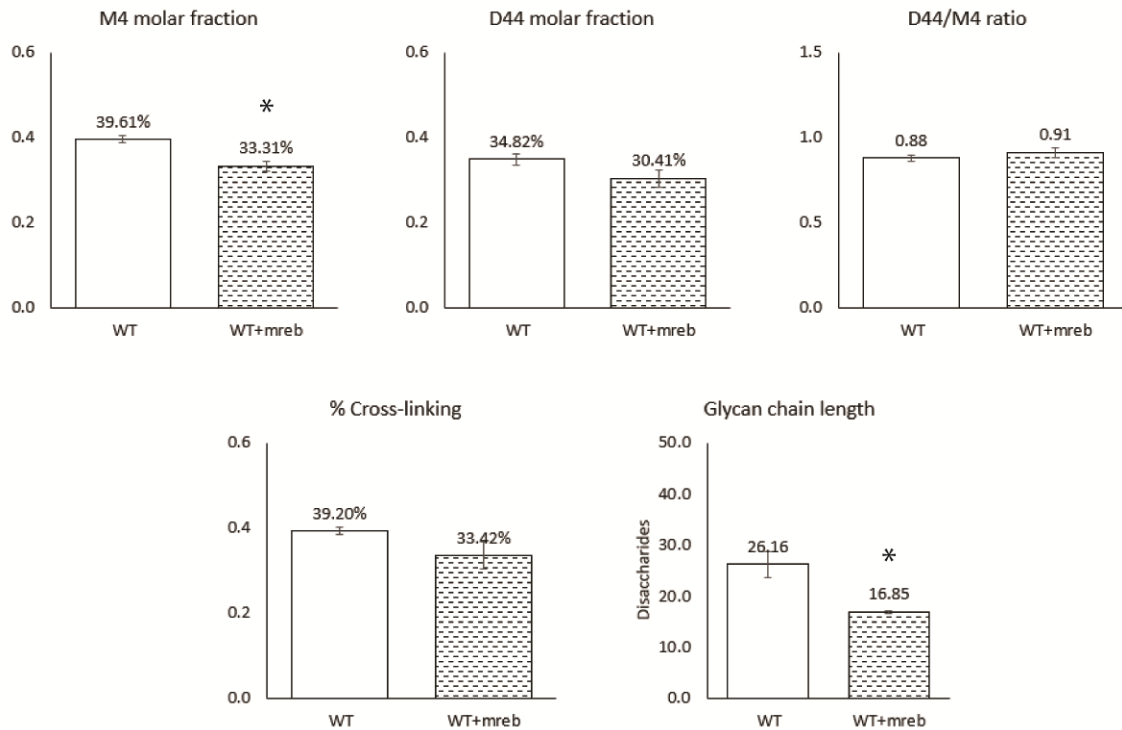
Figure 34 Ectopic MreB production in WT significantly reduced the amount of M4 monomers but had no effect on the D44/M4 ratio. Cross-linking reduced slightly, but was not significantly different to WT. Glycan chains were significantly shorter compared to WT. Asterisks indicate a significant difference in WT + MreB PG value compared to WT. Error bars represent SD for 3 biological replicates.

Notably, the ectopic expression of MreB in Δ*mreB* resulted in the relative percentages of all muropeptide components (M4, D44, D44/M4, cross-linking, and chain length) reverting to WT levels. There was greater variability, but statistically, PG values were the same as WT, indicating a full restoration of WT PG composition. Ectopic MreB expression in the WT background produced significantly fewer M4 monomers, but this had no impact on D44/M4 and cross-linking meaning PG elasticity was unaffected. The biggest change was the reduction of PG length to 16.85 (SD ± 0.28; 3 replicates) disaccharides. The mechanism behind this is unknown, and this seems to contradict the idea that MreB promotes PG elongation. However, it is worth noting that WT + MreB showed slightly defective growth characteristics compared to WT. In *E. coli*, growth arrest caused cells to have PG strands that are shorter by 25-30% (de Pedro and Cava, 2015). It is possible that the delayed growth of WT + MreB may be related to the reduction of its average PG length.

The variability in these results are likely due to non-native MreB levels, and therefore MreB dynamics, in these cells. In *E. coli*, MreB levels are maintained between 17,000 to 40,000 molecules per cell depending on growth rate (Kruse *et al.*, 2003), indicating that MreB production is well-regulated. It is not known how much MreB is produced by the Tn7_MreB fusion. Furthermore, it is clear that aberrant MreB levels can cause various defects (Wachi and Matsuhashi, 1989; Carballido-López and Errington, 2003; Shen W. Chiu, Chen and Wong, 2008) so maintaining correct MreB levels is crucial for proper cell wall assembly. Adding to this, MreB expression may also be misregulated as factors that control MreB production may not be working as intended in the Δ*mreB* background. For example, In *E. coli*, the regulatory stress-response protein, BolA, controls MreB levels by binding to the promoters of the *mreBCD* operon, thereby regulating MreB production (Freire, Moreira and Arraiano, 2009). By moving MreB production elsewhere, this control mechanism would no longer function normally. Interestingly, a protein BLAST search of the *E. coli* BolA protein (GenBank: AAB40191.1) in the *P. fluorescens* SBW25 showed that SBW25 also possesses a BolA homologue (PFLU431; % identity = 45.54; E-value = 8.0E-20). Although a direct link between BolA and MreB is yet to be found in *Pseudomonas*, BolA overexpression coupled with

carbon starvation is known to produce small and round cells in *Pseudomonas*, which is consistent with the idea of a regulatory relationship between BolA and cell shape (Koch and Nybroe, 2006).

In WT + Tn7 MreB, growth was similar to that of WT, but lag phase was prolonged by 4 hours (Figure 30). As MreB plays a direct role in coordinating PG synthesis (Jones, Carballido-López and Errington, 2001), it is possible that the slight delay in growth may be a result of excess MreB causing an imbalance in protein complexes responsible for cell wall synthesis. Similarly, ectopic overexpression of MreB in *S. coelicolor* also impaired growth by inhibiting cell division (Mazza *et al.*, 2006). In their discussion, Mazza *et al.* (2006) argue that this is possibly due to excess MreB recruiting PBPs away from their native locations, thereby preventing them from performing their normal cell wall-building functions.

The exact reason(s) why Δ*mreB* remains viable in this strain is unclear, but this has given us the opportunity to study how a previously rod-shaped bacterium can adapt to a new spherical shape using an experimental evolution approach in normal media. The results of which are presented in the next chapter.

Chapter 4

Adaptation of *P. fluorescens* SBW25 to a new spherical cell shape

4.1.   Introduction

P. fluorescens SBW25 has also been used as a platform for experimental evolution studies that look at several topics, including the diversity of evolutionary pathways (Lind *et al.*, 2015), adaptive radiation in different environments (Rainey and Travisano, 1998), and stochastic switching between phenotypic states (bet hedging) (Beaumont *et al.*, 2009). Experimental evolution is a useful method for studying genotypic and phenotypic changes that occur in populations that are maintained in controlled environments over many thousands of generations (Kawecki *et al.*, 2012). It gives us the ability to compete ancestors against descendants, or test whether evolutionary outcomes depend on the occurrence of a previous event from "fossil" records taken from different timepoints in the experiment. Experimental evolution is especially advantageous when using microorganisms because of their rapid generation times and viability in frozen cultures. Experimental evolution of microbial populations has been a powerful tool that has allowed us to discover, investigate, and directly evaluate complex evolutionary dynamics. For example, the >60,000 generation (and counting) Lenski Long-Term Evolution Experiment (LTEE), in which replicate *E. coli* populations have been passaged in a simple environment with only glucose for carbon and energy, has been instrumental in inspiring numerous studies that have investigated ecological and specialisation and genetic adaptation (Barrick and Lenski, 2013; Cooper, 2014).

Here, we used *P. fluorescens* SBW25 as a model organism in an adaptive evolution experiment to understand how a previously rod-shaped organism can adapt to a new spherical cell shape instigated by the loss of MreB. In this study, 10 parallel lines of Δ*mreB* were grown for 1,000 generations in shaken LB. This chapter presents results from the characterisation of these 10 evolved lines. My aim is to identify and study the beneficial mutations that rose to high frequencies in the evolved lines.

4.2. Results and Discussion

Having a viable Δ*mreB* mutant allowed us to study how a rod-shaped organism like *P. fluorescens* SBW25 can adapt to morphological defects caused by the loss of MreB, and by extension, to a new spherical cell shape. We used an experimental evolution approach to study this process. Specifically, we used shaken cultures in a serial transfer scheme to drive adaptive evolution of Δ*mreB* populations in 10 replicate lines. The evolution experiment was performed by Dr. Monica Gerth as part of her postdoctoral work with Professor Paul Rainey, but this was not characterised. My aim was to revive these preserved populations from different timepoints for characterisation similar to the work performed on the WT and Δ*mreB* strains reported in the previous chapter.

4.2.1. Evolved lines remain spherical but are much smaller

In order to understand what adaptive changes had taken place during 1,000 generations of evolution I first used phase contrast microscopy and observed that the evolved lineages all remained spherical in shape at the 1,000-generation timepoint (Figure 35).
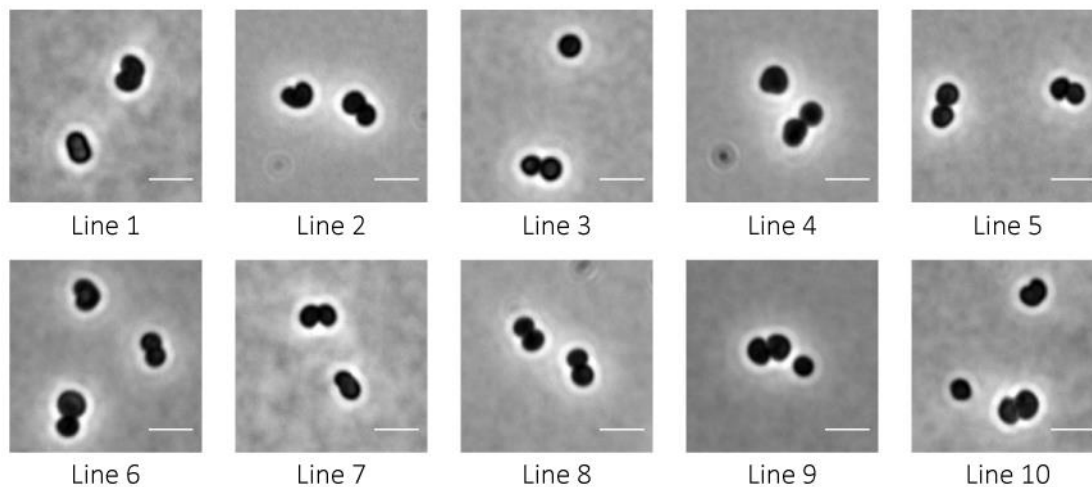
Figure 35 All the evolved lines at 1,000 generations grow as spheres. Scale bar = 3μm.

Average compactness values were similar to Δ*mreB* (0.87; SD ± 0.01 evolved lines vs 0.88; SD ±

0.09 Δ*mreB*; n = 100 per strain) (Figure 36). However, evolved lines 1, 3, 5, and 9 showed a significant

decrease in average compactness compared to Δ*mreB* (n = 100 per line; p < 0.05, two-sample t-test),

indicating that these cells are more ovoid than the ancestral strain. In addition, all the evolved lines had

become much smaller than Δ*mreB* (4.12 μm³; SD ± 0.72 μm³ evolved lines vs 20.65 μm³; SD ± 16.17 μm³

Δ*mreB*; n = 100 per strain) (Figure 36).
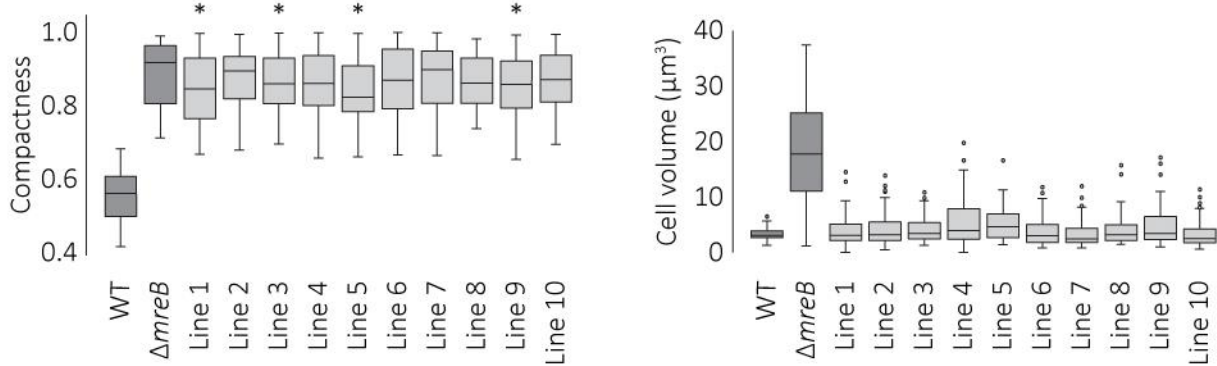
Figure 36 All the evolved lines are growing as spheres, but lines 1, 3, 5, and 9 have significantly lower compactness values compared to Δ*mreB*. The 10 evolved lines reduced in volume, decreasing to WT levels. Asterisks represent a significant difference compared to WT values.

4.2.2. Evolved lines are growing as well as WT

In addition to becoming smaller, all the evolved lines showed improved growth in shaken LB. The

evolved lines showed similar growth characteristics and reached the same maximum absorbance as WT.

The improved growth of the evolved lines is reflected in the enhanced fitness values obtained from

competition experiments against WT (Figure 37).
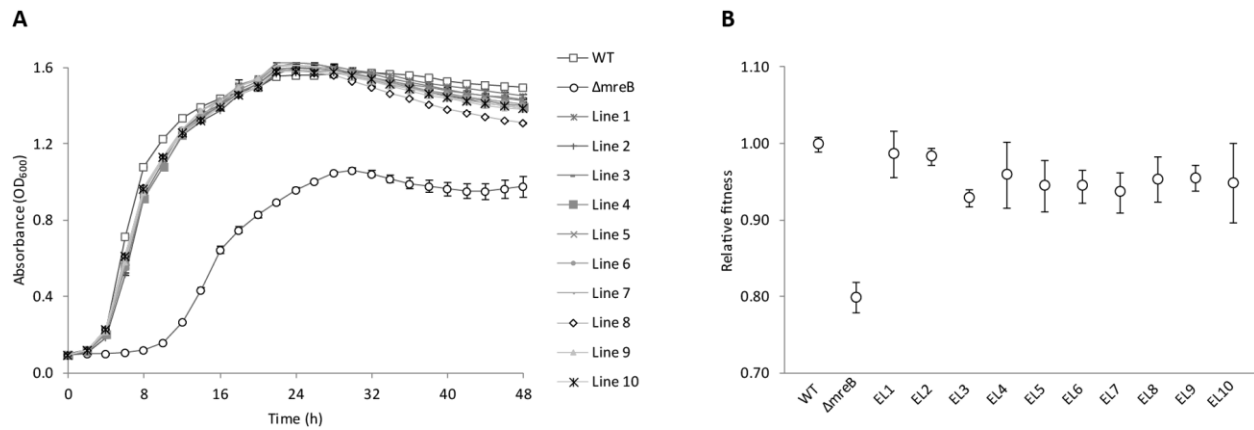
Figure 37 Growth dynamics and fitness of evolved lines. A) The growth characteristics of the 10 evolved lines are very similar to WT growth curves. B) Relative fitness also increased back to WT levels, reaching between 0.9 and 1.0 relative fitness.

4.2.3. Fitness improved early in the evolution experiment

To investigate how quickly fitness improved in the evolution experiment, relative fitness was measured between the a GFP-labelled WT strain and the revived populations at 4 time points: 50, 250, 500, and 1,000 generations. Each evolved line started with a fitness of 0.78 (SD ± 0.07; 3 replicates), which was the fitness of the ancestral Δ*mreB* strain. It was clear that fitness improved quickly in all the evolved lines. At 50 generations, the average fitness of all the evolved lines was 0.92 (SD ± 0.01; 3 replicates) (Figure 38). Fitness values across the 10 evolved lines improved further and persisted to the end of the experiment. At 250 generations, average fitness increased to 0.98 (SD ± 0.02; 3 replicates). At 500 generations, average fitness was 0.98 (SD ± 0.02). And finally, at 1,000 generations, average fitness was at 0.95 (SD ± 0.02; 3 replicates).
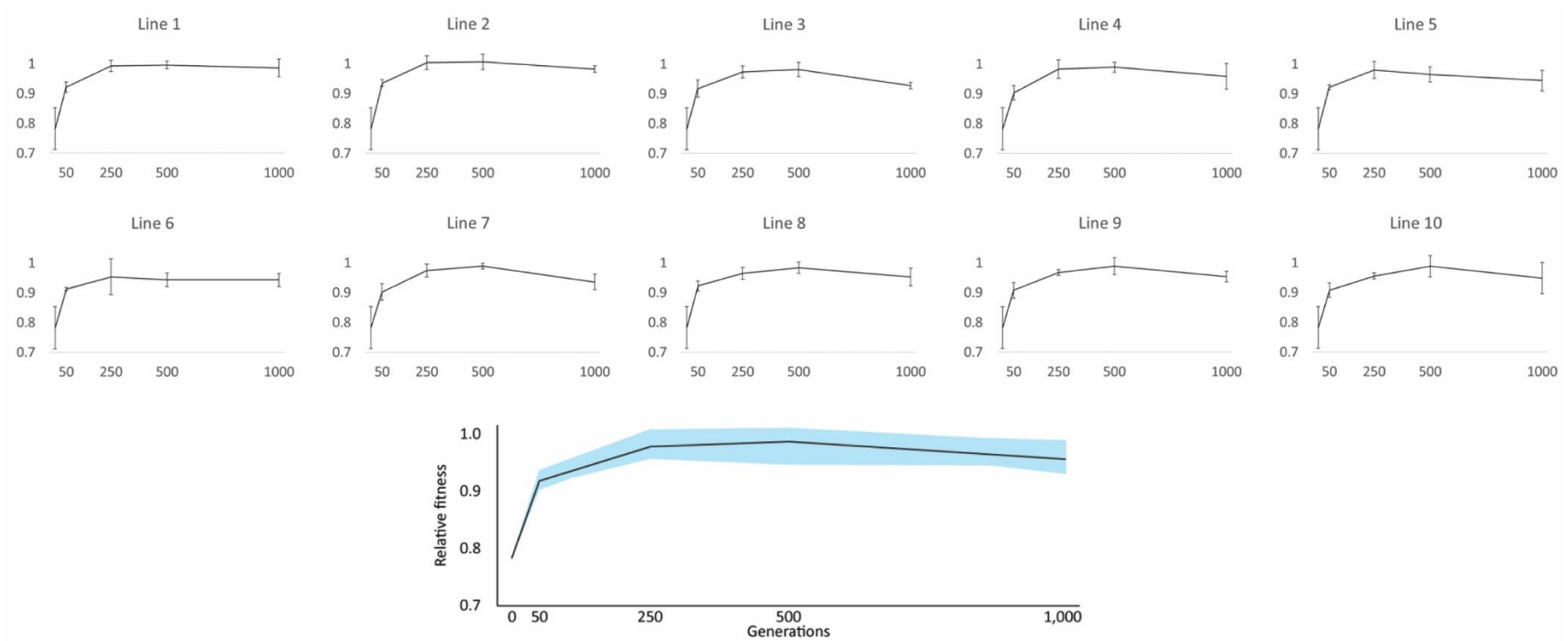
Figure 38 Fitness over time. Evolved lines 1 to 10 improved in fitness after growing in LB for 1,000 generations. Vertical axis represents relative fitness; horizontal axis represents number of generations. (K) Average fitness of all evolved lines (solid line). The shaded area represents the maximum and minimum fitness values from the evolved lines.

The fitness measures observed here reveal an interesting point – that MreB loss imposes a strong selection pressure on *P. fluorescens* SBW25. This is seen in the rapid increase in fitness across all lines, which jumps from ~0.8 (ancestral Δ*mreB* fitness) to almost 1.0 (WT fitness) in as little as 250 generations. These competition experiments show similar fitness trajectories for all the evolved lines: fitness levels reached an intermediate level of improvement (from ~0.8 to ~0.9, relative to WT) at 50 generations, then reached almost the same fitness as WT at 250 generations. Fitness levels then remained at similar levels all the way to 1,000 generations. At the end of the experiment, the 10 evolved lines had improved in fitness and growth dynamics that closely resemble WT growth dynamics. In addition, all the evolved lines had smaller cell volumes, whilst retaining a spherical cell shape but with a lower average compactness resembling ovococci. These demonstrate that the evolved lines have successfully adapted to a spherical cell shape within just 1,000 generations of growth in standard LB.

4.2.4. Identification and characterisation of the identified mutation

The rapid increase in fitness across the 10 evolved lines suggests that beneficial mutations occurred early in the evolution experiment. In order to identify these mutations, the populations of the evolved lines were sequenced at 500 and 1,000 generations by Dr. Heather Hendrickson using illumina sequencing by AGRF (Australia). The reads were mapped against the reference sequence (GCA_000009225.1) and mutations that appeared at a frequency of 0.75 or more in the population are outlined in Table 5.

Among the major mutations seen were unique missense mutations in PFLU0406 which codes for the major penicillin-binding protein, PBP1a. This was the most common mutation in lines 1, 3, 4, and 6. This mutation was also seen in line 10, however it did not reach fixation, and was seen in only ~37% of the population. Aside from these PBP1a mutations, a 5-gene deletion across PFLU4921-4925 was found in line 7, which includes the outer membrane protein, OprD, was also observed. Due to its links to cell wall synthesis and β-lactam resistance, OprD was chosen to be the focus of discussion henceforth. Finally, a

common amplification of a group of 14 genes was found in in 9/10 lines, spanning PFLU4164-4177. Different combinations of genes flanking this common region were also amplified across the 10 evolved lines. We opted to focus on the PFLU4165 (CsrA) amplification for this study. CsrA was selected among the genes in the amplified region because of its role in activating metabolic activities such as glycolysis and acetate metabolism (Sabnis, Yang and Romeo, 1995; Wei *et al.*, 2000), and because of its potential as a general modulator of bacterial gene expression (Romeo, 1998). To study the effects of these mutations, they were reconstructed in the WT and the ancestral Δ*mreB* backgrounds by Dr. Yunhao Liu and Dr Xue-Xian Zhang, which I later characterised.

Table 5 Mutations in Evolved Lines

Line	Generation	PFLU0406 (PBP1a) Nucleotide SNPs	Deletion	Amplifications (# of genes)
1	500	Position 1450, C → T (74.6%)		
	1,000	Position 1450, C → T (78.5%)		PFLU4143-4197 (54)
2	500			
	1000			PFLU4143-4190 (47)
3	500	Position 2163, T → G (98.7%)		
	1,000	Position 2163, T → G (86.6%)		PFLU4164 - 4190 (26)
4	500	Position 2158, C → T (59.6%)		
	1,000	Position 1084, T → G (98.1%)		
5	500			
	1,000			PFLU4161 - 4191 (30)
6	500	Position 2094, G → C (99.1%)		
	1,000	Position 2094, G → C (100.0%)		PFLU4143 - 4190 (47)
7	500		PFLU4921- PFLU4925 (~50%)	
	1,000		PFLU4921- PFLU4925 (100%)	PFLU4156 - 4190 (34)
8	500			
	1,000			PFLU4150 - 4177 (27)
9	500			
	1,000			PFLU4157 - 4198 (41)
10	500	Position 1085, T → G (33.9%)		
	1,000	Position 1740, C → T (36.9%)		PFLU4161 - 4190 (29)
				(Common)
				PFLU4164-4177 (13)

In the following section, I will present the results of my characterisation of the reconstructed strains. I will focus on the following major mutations:

1.   PBP1a mutations, particularly from lines 1 and 4;

2.   OprD-inclusive deletion from Line 7;

3.   CsrA amplification from Line 10.

4.2.4.1. *csrA* amplification

In this section, I will characterise the phenotypic effects of a selected amplification from that was common across most of the evolved lines. The selected gene was CsrA, a carbon storage regulator linked to cell metabolism and gene expression (Altier *et al.*, 2000; Baker *et al.*, 2002). The reconstructions were made by adding an IPTG-inducible copy of CsrA into a Tn7 site just downstream of the *glmS* region near *ori* in both the WT and Δ*mreB* backgrounds.

4.2.4.1.1.   Reconstruction in WT background

In the WT background, the CsrA amplification produced significantly thinner (0.89 μm; SD ± 0.07 μm vs 1.00 μm; SD ± 0.06 μm in WT; n = 100 per strain; p < 0.05; two-sample t-test) and shorter cells (2.16 $μm^3$; SD ± 0.54 $μm^3$ vs 3.27 $μm^3$; SD ± 0.94 $μm^3$ in WT; n = 100 per strain; p < 0.05; two-sample t-test) (Figure 39). Growth was negatively affected, prolonging lag time and interrupting exponential phase at OD_{600} 0.5. The exponential growth rate resumed after 2 hours, until it reached a maximum absorbance of OD_{600} 1.4 (Figure 40). Fitness was also slightly reduced to 0.93 (SD ± 0.02; 3 replicates).
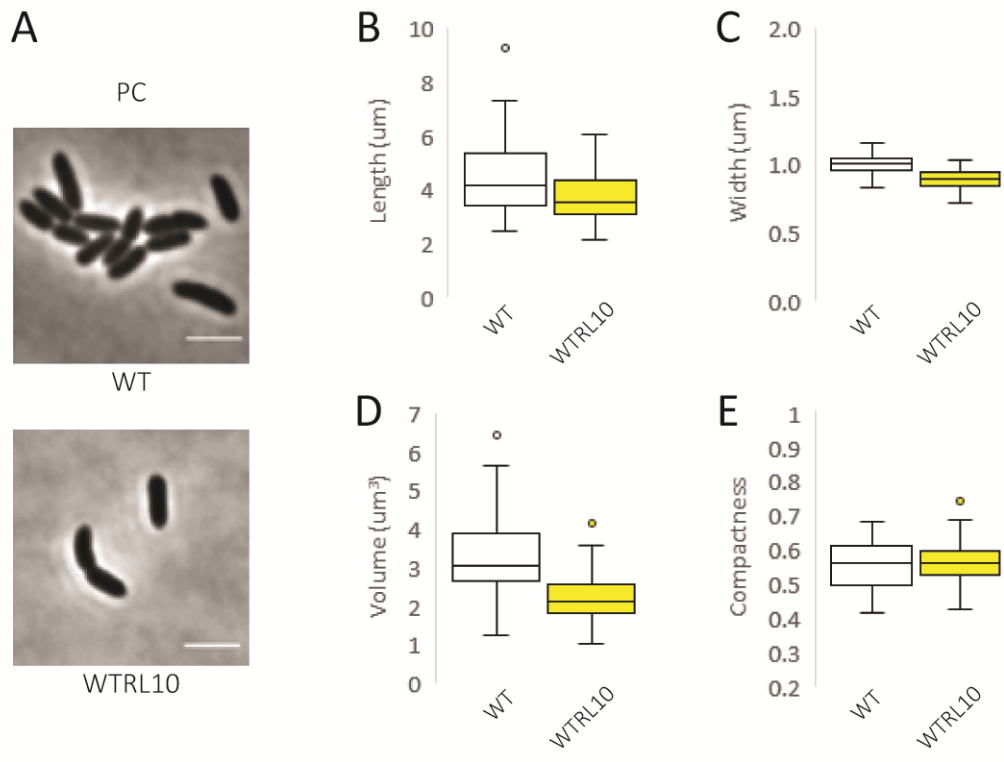
Figure 39 A) Reconstruction of the CsrA amplification in WT produced typical rods. WTRL10 produced (B) shorter and (C) narrower cells. As a result, cell volumes are lower (D) in WTRL10. Compactness values are similar to WT. Scale bar = 3μm.
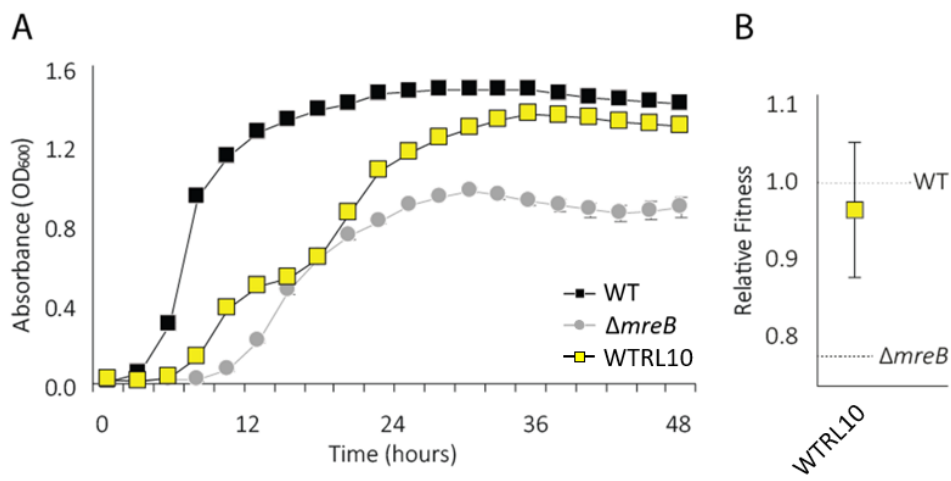
Figure 40 Growth and relative fitness of CsrA amplification in the WT background. A) The growth dynamics of WTRL10 are negatively impacted by the CsrA amplification – lag time is prolonged and logarithmic growth is interrupted. B) Relative fitness is also affected, increasing in variance compared to WT.

4.2.4.1.2. Reconstruction in Δ*mreB* background

In Δ*mreB*RL10, the amplification of CsrA exacerbated the morphological and growth defects already seen in Δ*mreB*. The CsrA reconstruction had large cells with an average volume of 19.04 µm³ (SD ± 16.61 µm³; n = 100) (Figure 41). Growth was similar to Δ*mreB* at first but slowed after reaching OD$_{600}$ 0.6, and fitness was reduced to 0.81 (SD ± 0.05; 3 replicates) (Figure 42).
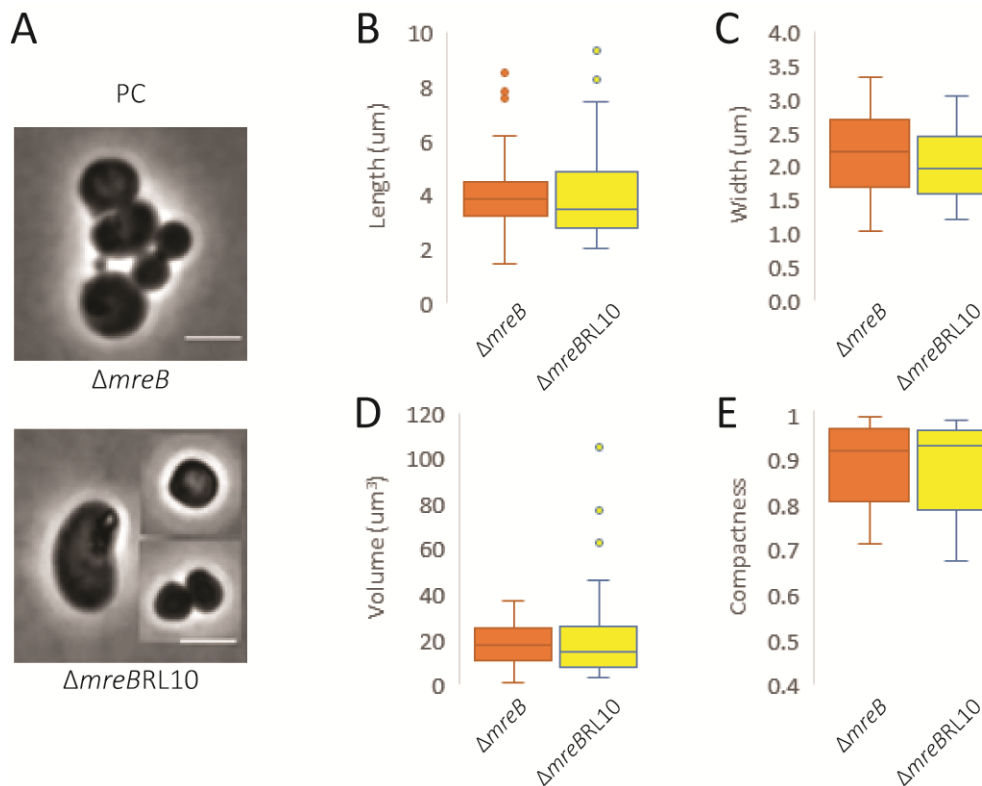
Figure 41 A) Reconstruction of the CsrA-amplification in Δ*mreB* produced spherical cells that resemble Δ*mreB* in shape and size, with some cells becoming significantly larger than Δ*mreB*. In general, Δ*mreB*RL10 cells were slightly (B) longer but had a similar (C) width to Δ*mreB*. (D) Overall cell volumes are similar to Δ*mreB*. Unusually large cells are shown as outliers. Compactness values are similar to Δ*mreB*. Scale bar = 3µm.
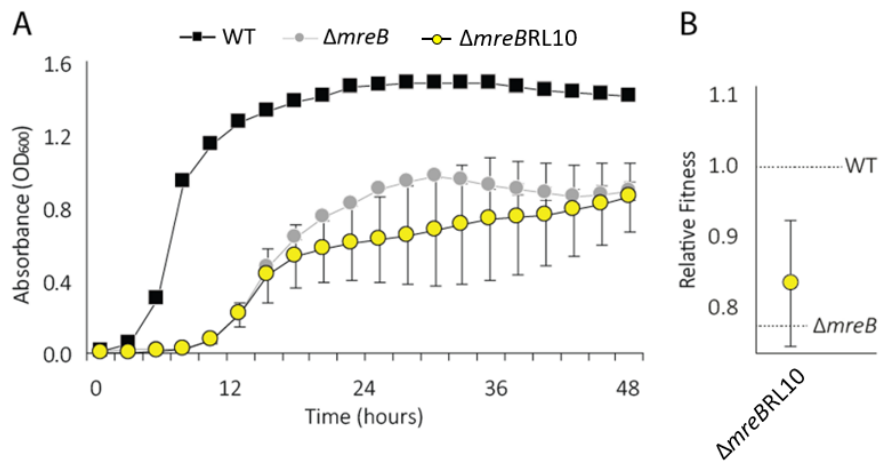
Figure 42 Growth and relative fitness of CsrA amplification in the Δ*mreB* background. A) Growth is slower and had greater variance. B) Relative fitness is very similar to Δ*mreB* but again has a much higher variance.

Overall, the amplification of CsrA did not improve the growth and viability of both Δ*mreB* and WT. In the Δ*mreB* background, cells became even larger and had more variability in fitness. This demonstrates that the CsrA mutation is not adaptive to MreB loss. For this reason, Δ*mreB*RL10 was not subjected to UPLC and FDAA analysis.

The amplification of CsrA proved to be deleterious to *P. fluorescens* SBW25. In both the WT and Δ*mreB* backgrounds, the reconstructions did not significantly improve fitness, and showed a severe growth defect. CsrA has been shown to negatively regulate gluconeogenesis (Romeo *et al.*, 1993) so the amplification of CsrA could lead to starvation as LB is a carbon-limited medium, providing only amino acids as gluconeogenic carbon sources (Jannière *et al.*, 2007; Sezonov, Joseleau-Petit and D'Ari, 2007). In addition, CsrA is a repressor of glycogen biosynthesis (Baker *et al.*, 2002), and in *Salmonella*, both the overexpression and disruption of *csrA* represses essential enzymes in carbohydrate metabolism (Altier *et al.*, 2000). This is consistent with the decreased size and slowed growth of the WT reconstruction strain. Consequently, bacteria that undergo carbon starvation experience additional oxidative stress (Shen Wen Chiu, Chen and Wong, 2008), which may be contributing to poor growth of the CsrA amplification reconstruction mutants. The size effects of CsrA overexpression is confounding as opposite effects were seen in WT (which became smaller), and in Δ*mreB* (which became larger). It seems that CsrA

overexpression has complex (perhaps opposite) effects in the WT and Δ*mreB* backgrounds. Interestingly, the overproduction of CsrA in *L. pneumophila* led to a reduction in cell size (Fettes *et al.*, 2001), whilst the interruption of CsrA in *E. coli* also led to a reduction in size (Romeo *et al.*, 1993).

In the future, other genes from the amplified region can be tested for adaptive effects in Δ*mreB*. I have identified two promising candidates: PFLU4171 and PFLU4172. These two genes make up the two-component CusRS system that helps bacteria survive heavy metal (Cu) stress (Outten *et al.*, 2001; Fung *et al.*, 2016). PFLU4171 codes for CusR, a cytoplasmic response regulatory protein; and PFLU4172 codes for CusS, a membrane-associated histidine sensor kinase. Interestingly, CusR has a good match (E-value = 7.0 E-09) to CckA, a histidine kinase linked to cell cycle progression and polar morphogenesis in *C. crescentus* (Jacobs *et al.*, 2003; Angelastro, Sliusarenko and Jacobs-Wagner, 2010). Similarly, CusS has a good match (2.0 E-05) to PdhS, a histidine kinase linked to cell shape alterations in Brucella (Van der Henst *et al.*, 2012). Coincidentally, these two genes are right in the middle of amplified region shared by the 9 evolved lines. It is possible that these proteins have a similar action to another kinase, StkP which coordinates peripheral and septal cell wall synthesis in *S. pneumoniae* (Pinho, Kjos and Veening, 2013). Altogether, these results demonstrate that the CsrA amplification is not adaptive to MreB-loss, and may have only been amplified due to genetic hitchhiking.

4.2.4.2. Mutations in PBP1a

PFLU0406 codes for the major penicillin binding protein, PBP1a. PBP1a is a high molecular weight PBP that extends the existing glycan chain of the cell wall (via transglycosylation or GT) and cross-links neighbouring peptide side chains to each other (via transpeptidation or TP) (Hong and Walker, 2016). Its major role is in building new cell wall material, specifically for lateral growth or cell elongation (Billings *et al.*, 2014). PBP1a is known to have a synergistic relationship with the Rod complex to form new PG in elongating cells (Cho *et al.*, 2016; Zhao *et al.*, 2017).

Three domains were identified in this PBP1a protein: the functional GT and TP domains, and a poorly-characterised OB domain. The mutations from lines 1, 3, and 6 were found in the TP domain in positions 484, 721, and 698, respectively. The line 4 mutation was found in the OB domain in position 362 (Figure 43).
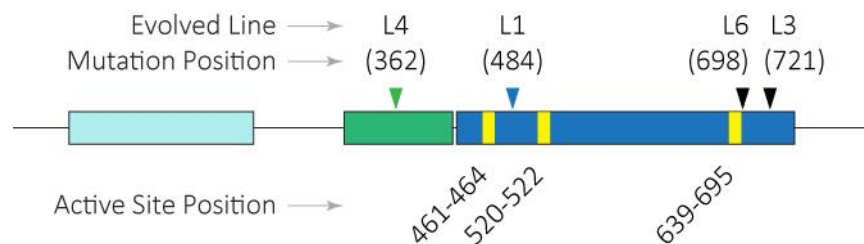
Figure 43 Map of PFLU0406 (PBP1a) showing the location of the mutations identified in evolved lines 1, 3, 4, and 6. The transglycosylase (TG) domain is in teal; the OB-domain where the L4 mutation was found is in green; and the transpeptidase (TP) domain where the L1, L3, and L6 mutations were found is in blue. The regions that come together to form the active site in the protein's 3D structure are shown in yellow.

Using the I-TASSER (Iterative Threading ASSEmbly Refinement) protein structure and function prediction server (Roy, Kucukural and Zhang, 2010; Yang *et al.*, 2015), I created several predicted models of the PBP1a of *P. fluorescens* SBW25. The model I selected had the best C-score of -1.41 which is a good confidence score. C-scores fall within a range of [-5 to 2], where a higher value signifies greater confidence. I then used this model to map the locations of the mutations from the evolved lines using the Visual Molecular Dynamics (VMD) software (Humphrey, Dalke and Schulten, 1996; Hsin *et al.*, 2008) (Figure 44). The PBP1a model shows that the line 1 and line 6 mutations are directly interacting with the TP active site, while the mutations in lines 3 and 4 are situated away from the active site. The locations of these mutations were verified using a similar model based on the published crystal structure of *Acinetobacter baumannii* PBP1a in complex with the β-lactam Aztreonam (Han *et al.*, 2011) (Figure 44).
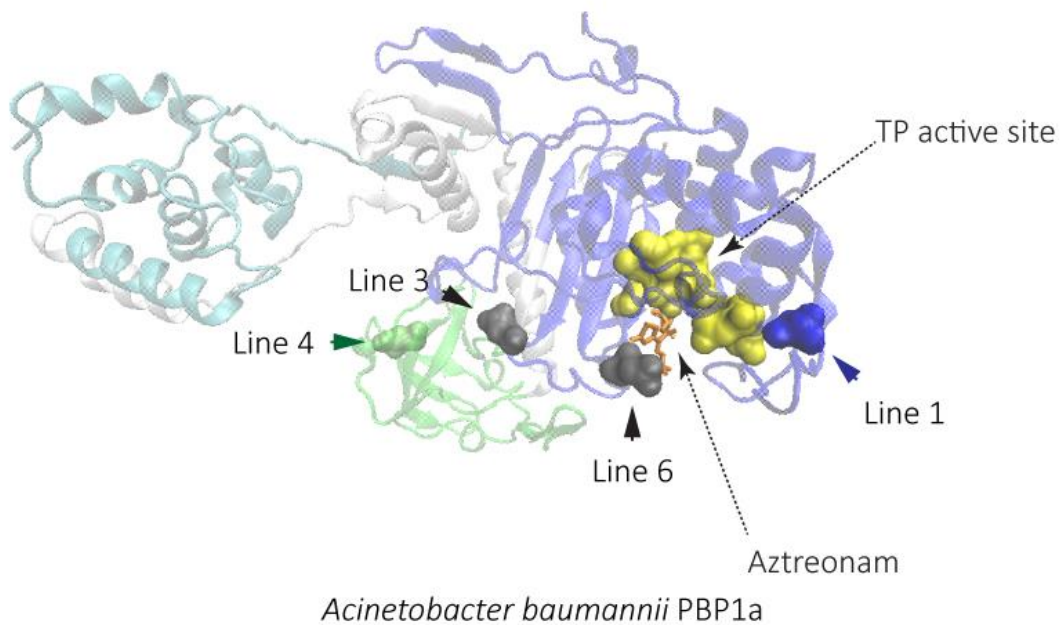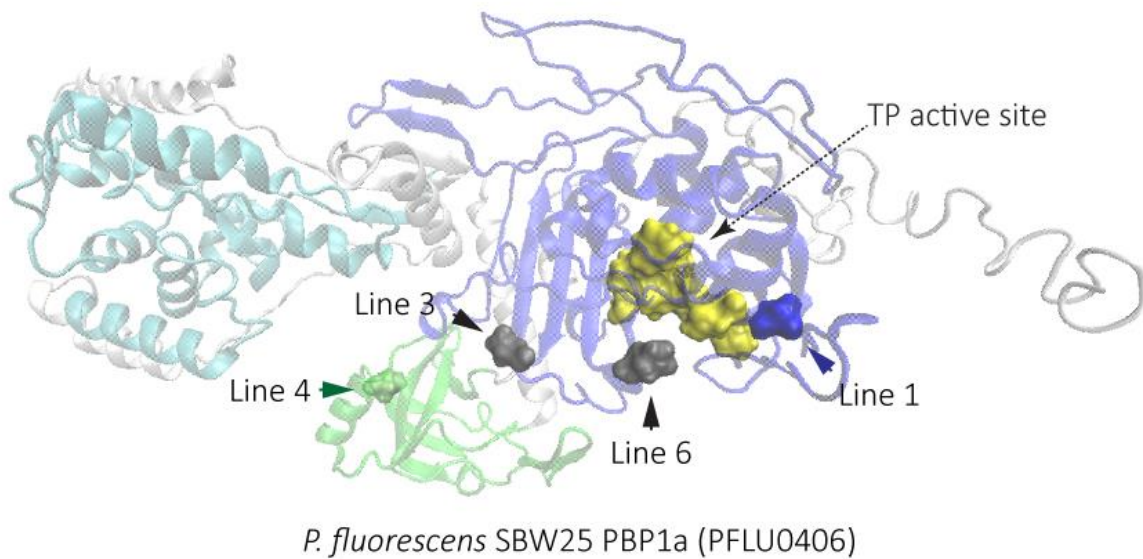
Figure 44 A 3D model of PBP1a from WT was constructed using I-TASSER and VMD. The protein is shown as ribbons and color-coded based on the conserved domains previously described. The positions of the mutations in evolved lines 1, 3, 4, and 6 are shown as spheres. The active site is presented as yellow spheres. A representative PBP1a model from *A. baumannii* was also constructed for comparison. Relevant structures are color-coded in the same manner. The locations of the mutations are shown in similar positions relative to the active site. The drug aztreonam is shown bound to the active site.

The mutations in PBP1a occurred independently across multiple evolved lines. Mutations in PBP1a were seen at high frequencies in evolved lines 1, 3, 4, and 6; sweeping from ~80% to 100% of the population (Table 5 Mutations in Evolved Lines). A mutation in PBP1a was also seen in line 10, albeit at a low frequency of ~30%. The mutations in lines 1, 3, and 6 were all in the TP domain, which is responsible for PG cross-linking. Mutations affecting the function of this region could potentially interfere with the tightly-regulated synthesis of PG for the cell.

In a survey of PBP1a homologues from other bacterial species, I found that the PBP1a mutations in lines 1, 3, and 6 are all in well-conserved regions of the protein (Figure 45). This highlights the importance of these sequences in maintaining protein activity, and indicates that the positions of the mutations in lines 1, 3, and 6 are in regions that are essential for protein function. The proximity of the line 1 and line 3 mutations to the TP active site suggest that they could be affecting the charge and stability of the TP active site. Since the active site of PBP1a is very narrow, ligands must be threaded into it to be recognized (Contreras-martel *et al.*, 2006). Any alterations affecting this would thus interfere with PBP1a activity (Contreras-martel *et al.*, 2006; Granger *et al.*, 2006; Job *et al.*, 2008). Mutations that affect accessibility to, or produce conformational changes around the active site have been shown to drive β-lactam resistance in *S. pneumoniae* (Contreras-martel *et al.*, 2006). The position of the line 6 mutation, especially, was identified by I-TASSER to be a ligand binding site. This is confirmed by the published crystal structure of *Acinetobacter baumannii* PBP1a (Figure 44) where the drug Aztreonam (ligand) can be seen forming a complex with the Line 6 mutation and the active site.

In contrast, the line 4 mutation is spatially-distant from the active site and is in a highly variable region of PBP1a (Figure 45). The line 4 mutation was found in the OB (oligonucleotide/oligosaccharide binding) domain. The exact function of the OB domain of PBP1a in *P. fluorescens* SBW25 is unknown, but it has been shown to have ligand binding properties that may be influencing protein activity in *A. baumannii* (Han *et al.*, 2011). Altogether, the data suggest that the perturbation of PBP1a is an adaptive response to MreB loss in *P. fluorescens* SBW25.
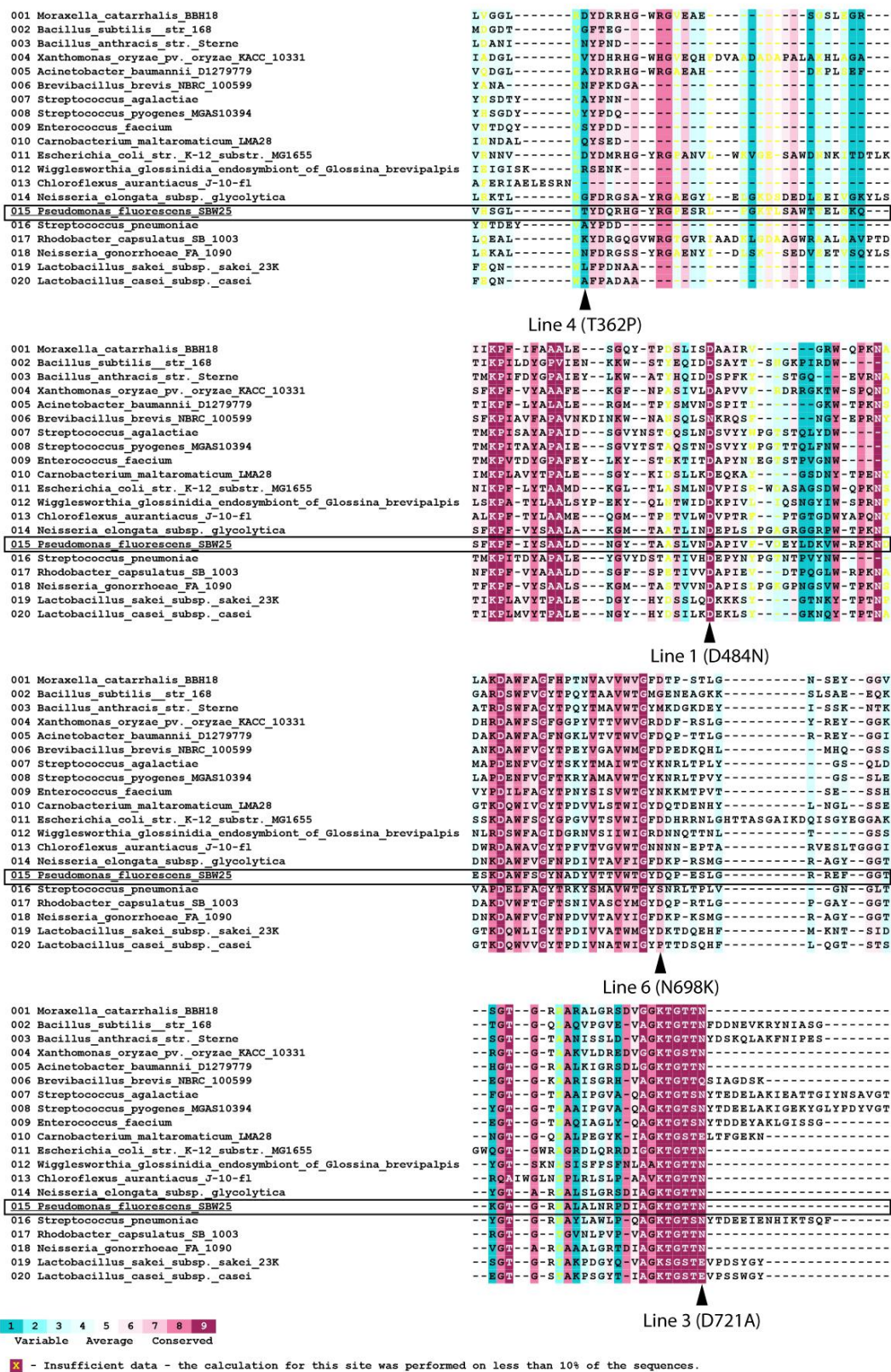
Figure 45 Protein sequence alignment of the PBP1a of 20 bacterial species using the ConSurf algorithm (Ashkenazy *et al.*, 2016). The data shows that mutations in the PBP1a of evolved lines 1, 3, and 6 are in well-conserved regions. In contrast, the line 4 mutation is in a highly variable region.

PBP1a mutation reconstruction in WT background

To investigate the effects of PBP1a mutations on cell shape and fitness, the mutations from line 1 (TP domain) and line 4 (OB domain) were selected to represent mutations of PBP1a. These were reconstructed in the WT background by introducing the mutations in their native positions using SOE PCR, thereby creating the strains: WTRL1 and WTRL4. Results from the characterisation of these reconstructions are discussed below.

PBP1a mutation reconstruction in WT made cells thinner and shorter

In the WT background, the PBP1a reconstructions maintained a rod-like shape (Figure 46A) but were significantly shorter (Figure 46B) (Line 1: 3.41 ± 0.76 µm, $p < 0.001$; Line 4: 3.69 ± 0.80 µm, $p < 0.001$; n = 100 per strain; two-sample t-test) compared to WT (4.51 µm; SD $\pm$ 1.32 µm; n = 100). These cells were also significantly narrower (Figure 46C) (Line 1: 0.89 ± 0.07 µm, $p < 0.001$; Line 4: 0.94 ± 0.05 µm; n = 100 per strain; $p < 0.001$; two-sample t-test) compared to WT (1.00 µm; SD $\pm$ 0.06 µm; n = 100) resulting in smaller total cell volumes (Figure 46D). The average cell volume of the line 1 reconstruction was of 1.93 µm^3 (SD$\pm$ 0.52 µm^3; n = 100), whilst line 4 was measured at 2.33 µm^3 (SD $\pm$ 0.49 µm^3; n = 100). There was no substantial effect on growth.
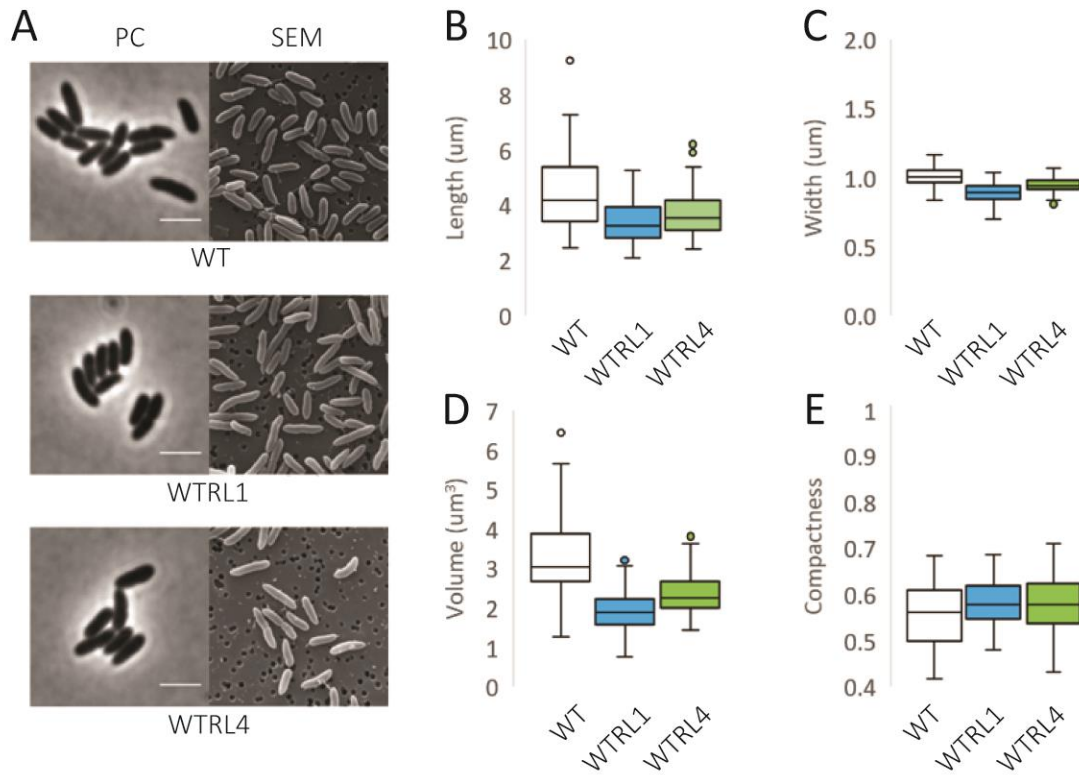
Figure 46 The reconstruction of the line 1 and line 4 mutations in the WT background. A) Microscopy shows that the reconstruction mutants have retained a rod-like shape. However, B) these mutants are shorter and C) thinner than WT. D) These contribute to lower average cell volumes. E) Compactness measurements support the visual observation that these reconstruction mutants have the same shape as WT. Scale bar = 3μm.

The growth dynamics of both reconstructions closely resemble that of WT. Fitness of the line 1 reconstruction showed slight variability (0.97 ± 0.03; 3 replicates) but was not statistically different from WT. Similarly, the line 4 reconstruction was as fit just as WT (1.00 ± 0.01; 3 replicates) (Figure 47).
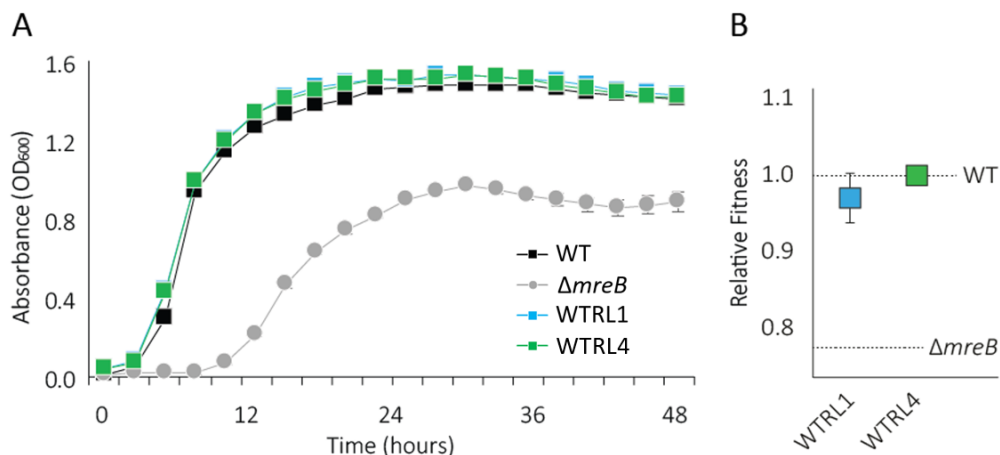
Figure 47 Growth and relative fitness effects of the PBP1A reconstructions in the WT background. A) The growth dynamics of WTRL1 and WTRL4 are very similar to that of WT. B) Relative fitness likewise similar to WT.

PBP1a mutations leave PG composition unaltered in a WT background

In order to learn about the molecular changes behind these shape changes we subjected the cell walls to UPLC analysis. The WT strains with the PBP1A mutations from Line 1 and Line 4 showed only a slight change in the M4 and D44 molar fractions of both mutations in the WT. WTRL4 showed a lower average D44/M4 ratio of 0.79 (SD ± 0.06; 3 replicates) and a lower average cross-linking percentage of 36.24% (SD ± 1.75%; 3 replicates), but these changes were not statistically significant compared to (Figure 48). Both WTRL1 and WTRL4 showed an increase in their average glycan chain length, but statistical analysis revealed these changes to be insignificant compared to WT ($p = 0.41$; and $p = 0.78$, respectively; two-sample t-test).
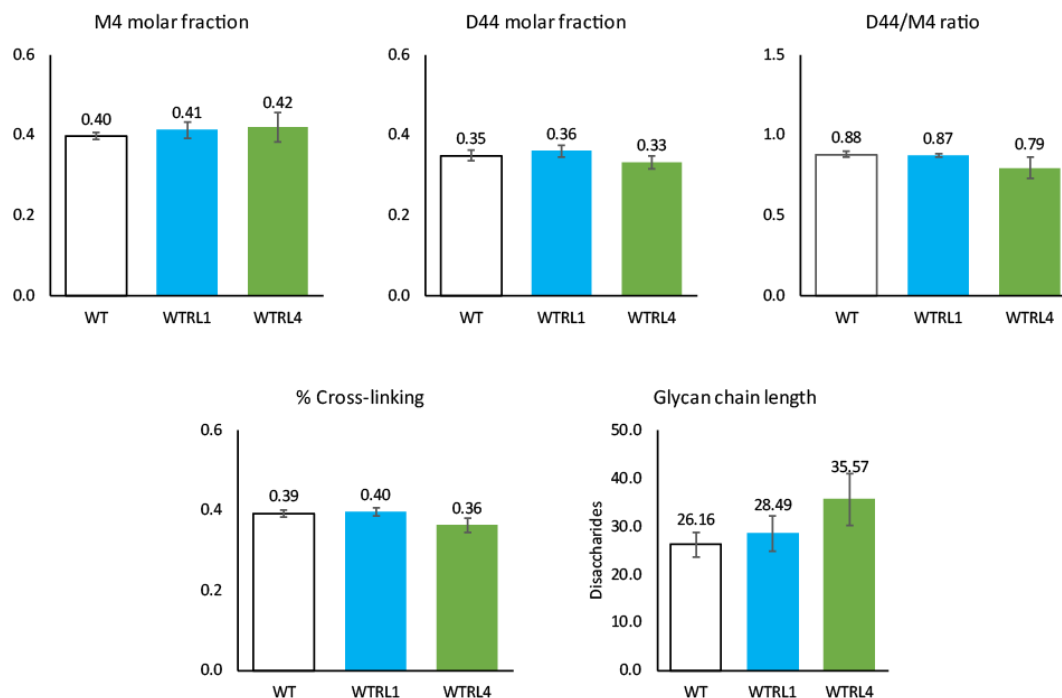
Figure 48 The PG characteristics of WTRL1 and WTRL4 are not significantly different from WT values.

The reconstruction the PBP1 mutations in the WT background produced thinner and shorter cells. This is consistent with results in *E. coli* showing the formation of smaller cells as a result of PBP1a loss (Banzhaf *et al.*, 2012). Despite this, the WT reconstruction mutants are able to grow as well, and were found to be as fit as WT. We also found that the PG characteristics of these mutants showed no statistical difference to those of WT cells. This is consistent with other studies showing that the loss of PBP1a is tolerable in organisms such as *E. coli* and *S. pneumoniae* that have multiple Class A PBP proteins (Denome *et al.*, 1999; Hoskins *et al.*, 1999). These findings reinforce the role of PBP1a in cell elongation and supports the idea that the PBP1a mutations found in the evolved lines are causing a loss-of-function effect.

Cells remain spherical but are significantly smaller and have higher fitness

The PBP1A mutations that were found at high frequency in the evolution experiment were also put into the Δ*mreB* background in order to see how they affected shape, size, and cell wall composition without any other mutations that might have been contributing to these features in the population. In the Δ*mreB* background, both reconstruction strains (Δ*mreB*RL1 and Δ*mreB*RL4) remained spherical in shape showing the same compactness as Δ*mreB* (Figure 49A). Cell lengths and widths for both strains were reduced, leading to significantly lower cell volumes decreasing to 3.86 µm^3 (SD ± 2.50 µm^3; n = 100; p < 0.05; two-sample t-test) for line 1, and 5.51 µm^3 (SD ± 3.58 µm^3; n = 100; p <0.05; two-sample t-test) for line 4 (Figure 49D).
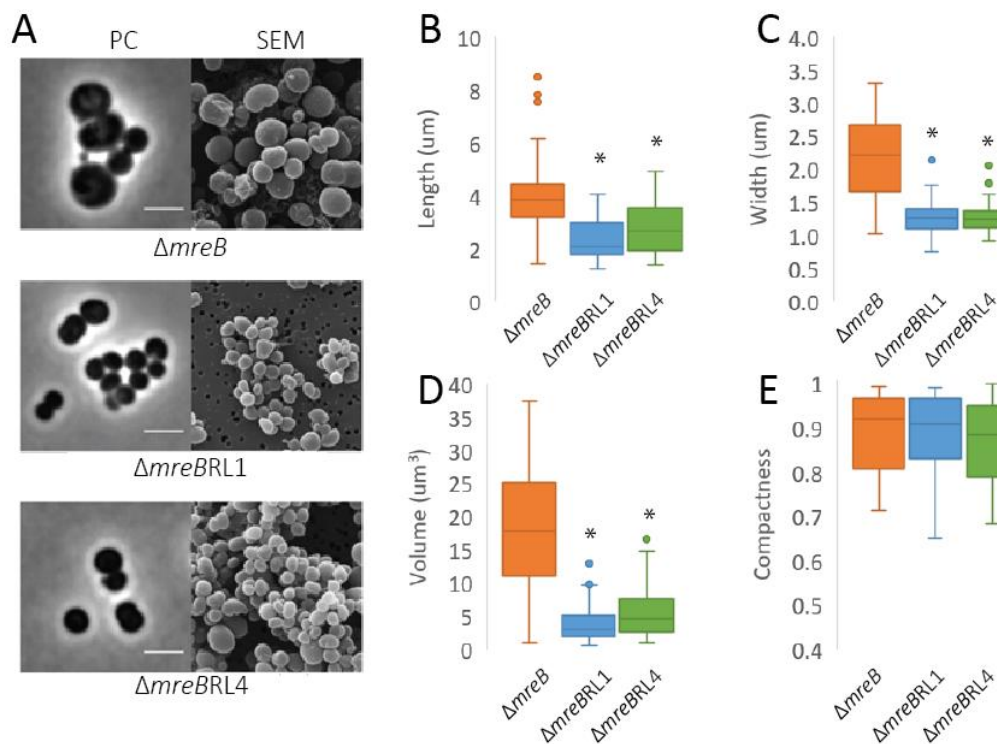
Figure 49 The reconstruction of the line 1 and line 4 mutations in Δ*mreB* produced significantly smaller cells. Microscopy shows that the reconstructions strains have retained a spherical morphology (A). However, cell length (B) and width (C) was significantly reduced, resulting in significantly smaller cell volumes for both reconstructions (D). Compactness values confirm that the reconstruction populations still retain a spherical cell shape. Scale bar = 3µm.

Both mutations improved the growth of the reconstruction strains, allowing them to grow almost as well as WT (Figure 50). Similarly, when these reconstructions were grown in a pair wise competition experiment against the GFP-labelled ancestor, both strains showed that the addition of the PBP1A mutations improved fitness to 0.98 (SD ± 0.06; 3 replicates) for the line 1 mutation, and 0.96 (SD ± 0.06; 3 replicates) for the line 4 mutation (Figure 50).
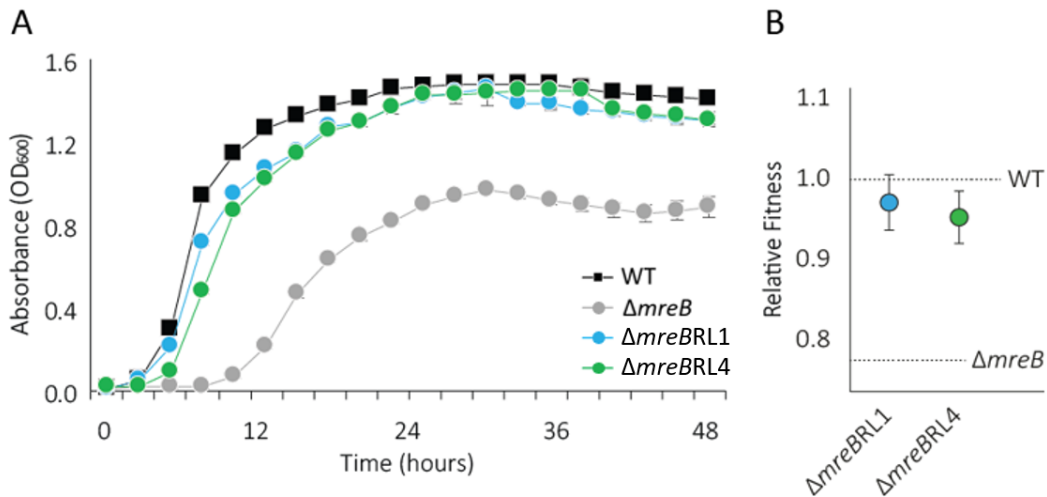
Figure 50 Growth and relative fitness effects of the PBP1A reconstructions in the Δ*mreB* background. A) Both line 1 (blue) and line 4 (green) reconstructions in Δ*mreB* improved growth dynamics to almost WT levels. B) Both reconstructions also had near-WT fitness values.

PG characteristics are restored to WT values

While the PBP1a line 1 and line 4 mutations in the WT background showed very little change in the chemical composition of the PG, this was not true when these mutations were inserted back into a clean Δ*mreB* background. The addition of the mutations resulted in an increase in their M4 molar fraction (from ~27% in Δ*mreB* to ~36% in both reconstructions), and a decrease in their D44 molar fraction (from ~34% in Δ*mreB* to ~26% in both reconstructions) (Figure 51). On their own, these changes were not significantly different from the M4 and D44 of Δ*mreB*. However, these changes resulted in a significant decrease in the D44/M4 ratio of Δ*mreB*RL1 (0.69; SD ± 0.09; $p < 0.05$, two-sample t-test) and Δ*mreB*RL4

(0.74; SD ± 0.03; p < 0.05, two-sample t-test). Cross-linking was also significantly reduced, dropping to ~30% in both strains (p < 0.05, two-sample t-test). Finally, the average chain lengths of both strains increased to 20.01 ± 0.50% disaccharides in Δ*mreB*RL1, and 17.5% (SD ± 3.04%) disaccharides in Δ*mreB*RL4. The glycan chain length of Δ*mreB*RL1 was statistically significant (p < 0.05, two-sample t-test), however, the increase in cross-linking of Δ*mreB*RL4 returned a p-value that is just above the significance threshold (p = 0.0503, two-sample t-test). In general, the PBP1A line 1 mutation produced a more consistent change in PG composition, reverting most values (D44, D44/M4, cross-linking, and chain length) back to WT levels.
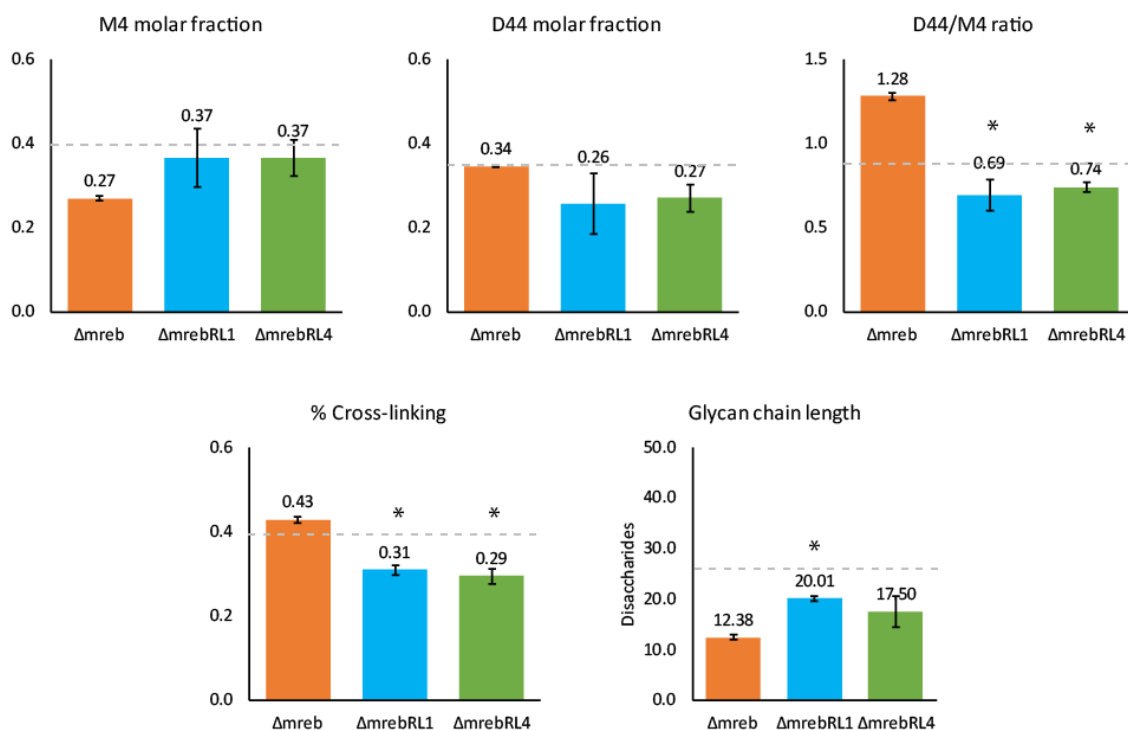
Figure 51 Reconstruction of the L1 and L4 mutations in the Δ*mreB* background significantly decreased the D44/M4 ratio. The amount of PG cross-linking was also significantly reduced. Glycan chain length increased in both reconstructions, but only Δ*mreB*RL1 showed a significant difference. The dashed line represents the value of WT readings for the same characteristics. Asterisks represent a significant difference compared to Δ*mreB*.

The mutation of PBP1a and increase in mutant alleles in independent lines suggest that modification of this protein is beneficial in cells that have lost MreB. To investigate, the PBP1a mutations from lines 1 and 4 were reconstructed in the Δ*mreB* and WT backgrounds. These mutations had little effect on WT growth, fitness and PG composition. However, these mutations in the Δ*mreB* background demonstrated large improvements in growth, fitness, and viability proving that these mutations are indeed beneficial in cells that have lost MreB. Interestingly, cell sizes decreased in WT, but especially in Δ*mreB*. These phenotypes are consistent with other studies that show a decrease in size in cells that have lost PBP1a (Murray, Popham and Setlow, 1998; Claessen *et al.*, 2008; Kawai, Daniel and Errington, 2009; Banzhaf *et al.*, 2012). Importantly, Kawai et al. (2009) found that in *B. subtilis*, Δ*mreB* cells bulge and lyse due to the action of PBP1a. They demonstrated that MreB-loss results in the accumulation of PBP1a that leads to bulging and lysis, and that the inactivation of PBP1a suppresses this defect. Kawai et al. (2009) made this discovery using a transposon-generated library, wherein MreB-null mutants were rescued by the disruption of PBP1a in 5/9 strains. It is interesting that we uncovered the same relationship using a natural evolution approach, where 5/10 lines had mutations in PBP1a.

4.2.4.2.3.   Analysis of PBP1a mutation effects using bioinformatics tools

To investigate if the phenotypes seen in the PBP1a reconstructions are in fact due to a loss of PBP1a function, I used several bioinformatics tools to infer the effects of these mutations on PBP1a. I started by running an analysis of the mutations on SIFT (Sorting Intolerant From Tolerant). SIFT is an algorithm used to predict if amino acid substitutions can be tolerated, or are deleterious to protein function (Ng and Henikoff, 2003). It provides predictions using SIFT confidence scores that range from 0 to 0.05 for deleterious substitutions (scores closer to 0 = high confidence), and 0.5 to 1.0 for tolerable substitutions (scores closer to 1 = high confidence). Results show that all 3 mutations (lines 1, 3, and 6) in the TP domain are predicted to be detrimental to PBP1a function, with high confidence scores of 0. On the other hand, the line 4 mutation in the OB domain seems to be a tolerable substitution, with a confidence score of 1. In addition, protein sequence analysis using MEGA and the Consurf algorithm (Ashkenazy *et al.*, 2016) (Figure 52) shows that the mutations in lines 1, 3, and 6 are all in exposed, highly-conserved regions. The residues affected by the line 1 and 6 mutations specifically have been identified as functional residues. Finally, a similar analysis using PolyPhen2 (Adzhubei *et al.*, 2010) (Figure 53) provided further support about the possibly damaging effects of the mutations mentioned above. A summary of these results is shown in Table 6.

It is unclear how the line 4 mutation in the OB domain is rescuing cells from the loss of MreB when bioinformatic tools are used to predict its effect across unrelated species. However, using the Protein Variation Effect Analyzer or PROVEAN tool (Choi and Chan, 2015), I found that the line 4 mutation is predicted to be deleterious when analysed in the context of other Pseudomonad species. PROVEAN used 139 automatically selected sequences to predict the line 4 mutation to have a deleterious effect with a score of -2.819 (scores equal to or below -2.5 are considered deleterious). Most of the sequences were from Pseudomonads containing OB domains, suggesting that the line 4 mutation is likely deleterious to PBP1a function in Pseudomonads. According to Han et al. (2011), the OB domain has ligand binding properties, so it is possible that the line 4 mutation may be affecting how PBP1a interacts with PG

subunits, perhaps making it difficult for ligand binding to occur, producing a similar loss of function effect.

Therefore, it is likely that the mutations in PBP1a are deleterious, and that the improved growth of evolved

lines 1, 3, 4, and 6 is due to the loss of function of PBP1a.
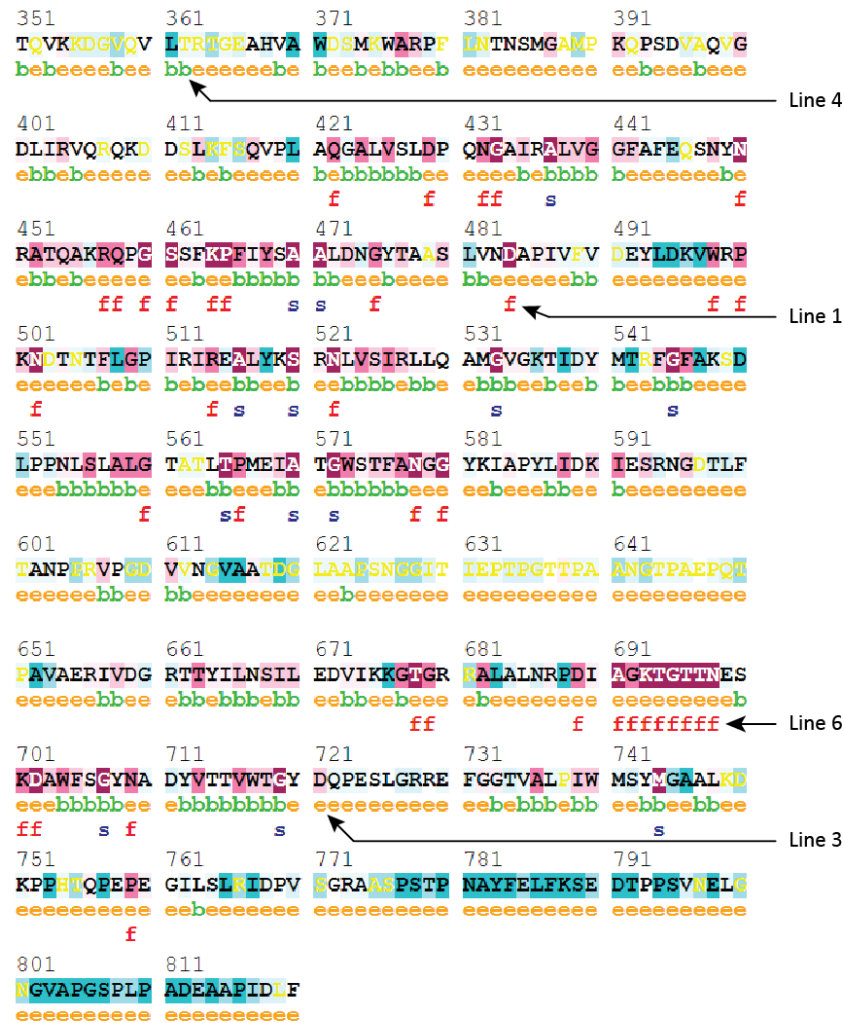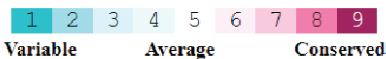
Figure 52 Protein sequence analysis using the Consurf algorithm (Ashkenazy *et al.*, 2016) shows that the mutations in lines 1, 3, and 6 are all in exposed, highly-conserved regions. In particular, the mutations in lines 1 and 6 are predicted to be in functional residues of PBP1a. In contrast, the line 4 mutation is predicted to be a buried residue of the protein.
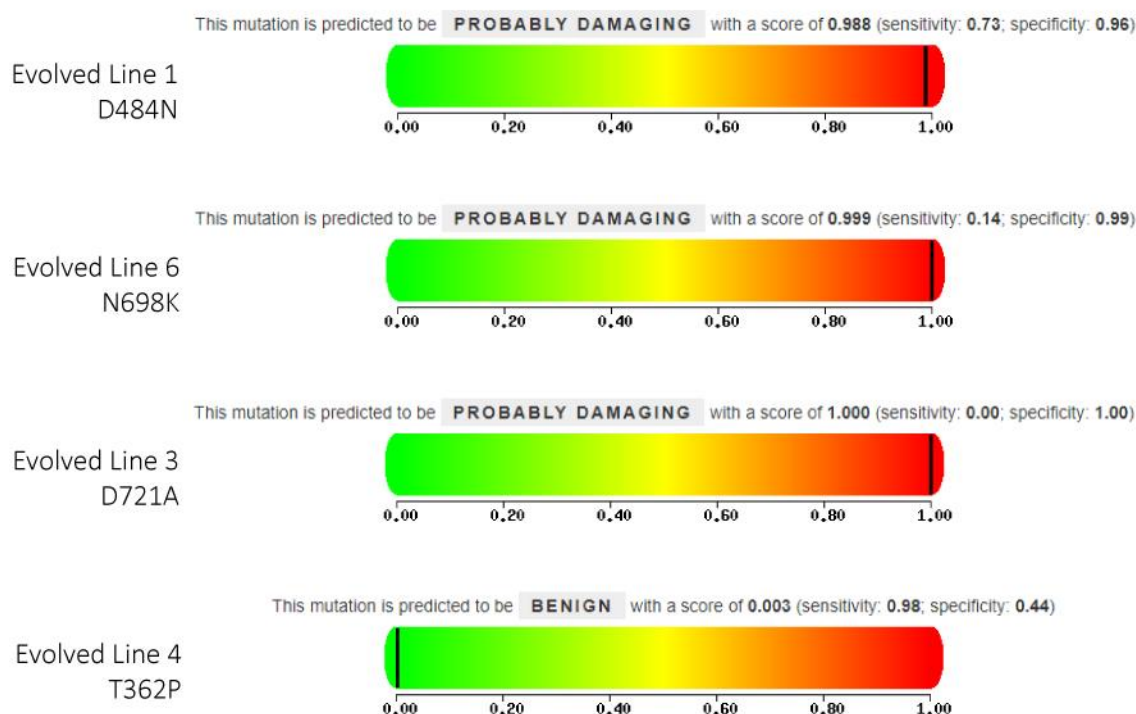
Figure 53 Analysis of the PBP1a mutations using Polyphen2 (Adzhubei *et al.*, 2010) confirms that the mutations in lines 1, 3, and 6 are damaging to protein function, whereas the mutation in line 4 may be benign. PolyPhen2 used 75 automatically selected sequences to predict SNP effects. Sequences were from different genera – 70 sequences with OB domains, and 5 without.

Table 6 Bioinformatic analysis of the identified mutations in PBP1a, and their effect on function.

Evo. Line	PBP1a Mutation	ConSurf Results Conservation[1]	Position	Functional	SIFT Score (1-S)[2]	PolyPhen Score[3]	Mutation Result
L1	D484N	9/9	Exposed	Yes	0 / 1	0.988 / 1	**Damaging**
L6	N698K	9/9	Exposed	Yes	0 / 1	0.999 / 1	**Damaging**
L3	D721A	7/9	Exposed	No	0 / 1	1.000 / 1	**Damaging**
L4	T362P	1/9	Buried	No	1 / 1	0.003 / 1	Benign

[1] ConSurf Conservation Score ranges from 1 (variable) to 9 (highly conserved).
[2] SIFT Score Ranges from 0 to 1. The amino acid substitution is predicted to be damaging is the score is <= 0.05, and tolerated if the score is > 0.05.
[3] PolyPhen Score ranges from 0 (benign) to 1 (damaging).

In summary, the line 1 and line 4 PBP1a mutations produced smaller cells in the both the WT and ΔmreB backgrounds. Importantly, both mutations rescued growth and fitness in the ΔmreB background. Aside from making the cells smaller, no major defects were observed in the WT background. Protein sequence analysis shows that the PBP1a mutations in evolved lines 1, 3, and 6 are in highly conserved regions, and bioinformatics analyses using I-TASSER, ConSurf, SIFT, and PolyPhen predict all three mutations to have deleterious effects. The line 4 mutation was found in a variable region called the OB domain, and was predicted by the same bioinformatics tools to be a benign mutation. However, this mutation was predicted to be deleterious when compared against more than 100 Pseudomonad sequences using the PROVEAN tool, suggesting a possible loss-of-function effect to PBP1a in Pseudomonads. One possible mechanism is the disruption of the OB domain which has been shown to have ligand binding properties that may ultimately affect the activity of PBP1a. Altogether, these results suggest that the mutations in PBP1a are decreasing growth (cell volume) possibly due to a perturbation or loss of PBP1a function.

4.2.4.3. OprD-inclusive deletion

The most common mutation in line 7 is a deletion of PFLU4921-4925. This five-gene-cluster is composed of three hypothetical proteins; a cold shock protein, CspC; and an outer membrane porin, OprD. OprD is an outer membrane protein that functions as an efflux pump that is also involved with the passive uptake of small peptides and basic amino acids (Hancock and Brinkman, 2002). In this study, OprD was selected as the focus of our analysis because of its link to the maintenance of cell wall integrity. In *P. aeruginosa*, the decrease of OprD expression is responsible for high-level resistance to the β-lactam antibiotics, imipenem and carbapenem (Pagès, James and Winterhalter, 2008). This suggests a link to PG modification which, as shown above, can be an effective strategy for adapting to a spherical cell shape. In order to investigate the phenotypic effects of this deletion, reconstructions were made in the ΔmreB and WT backgrounds. The effects of the mutation are described below.

Reconstructed cells are thinner, longer, show a filamenting phenotype, but have similar fitness to WT

In the WT background, the OprD-inclusive deletion produced significantly thinner cells (width = 0.74 μm; SD ± 0.06 μm; n = 100; p < 0.05; two-sample t-test) with smaller cell volumes (2.47 μm^3; SD± 1.18 μm^3; n = 100) (Figure 54). A proportion of the population exhibited a filamenting phenotype, occurring in 20% (SD ± 4%; n = 100) of the population. Despite this morphological defect, growth was not severely affected. Growth dynamics and relative fitness were very similar to that of WT (Figure 55).
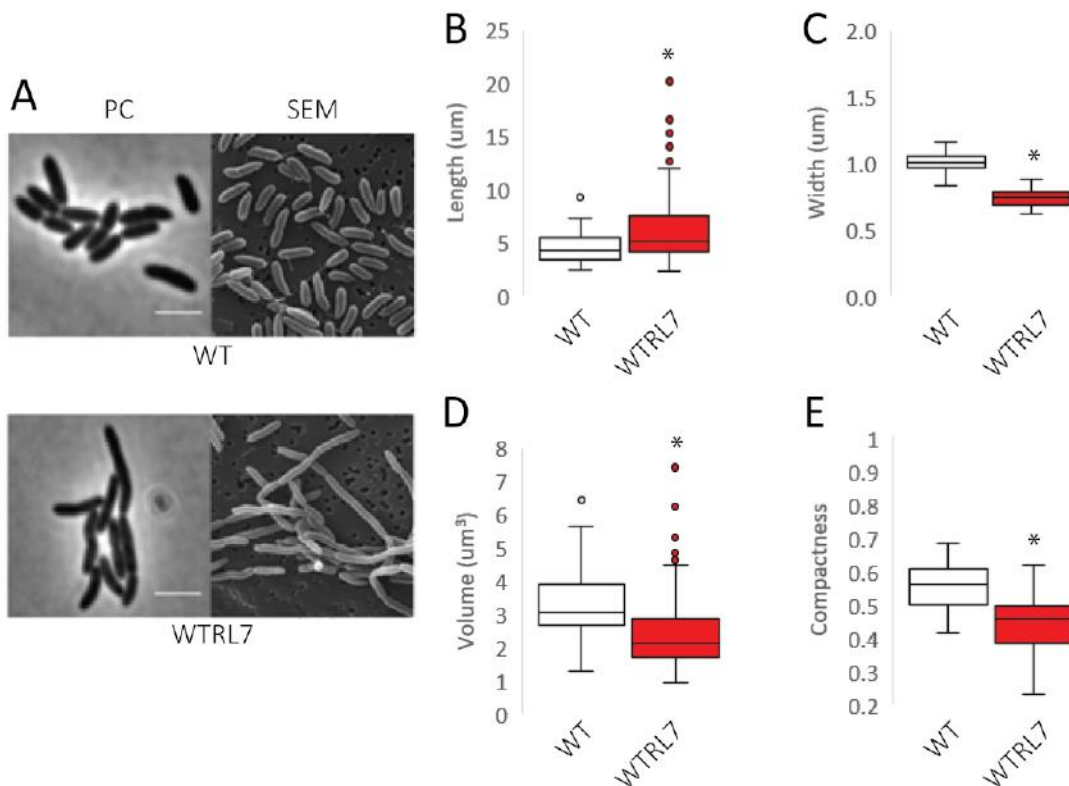
Figure 54 A) Reconstruction of the line 7 mutation in WT produced a filamenting phenotype in some cells. The OprD-inclusive deletion also produced (B) longer but (C) thinner cells. As a result, cell volumes are lower (D) in WTRL7. Compactness values are also lower (E) in this strain. Asterisks represent a significant difference of WTRL7 compared to WT. Scale bar = 3μm.
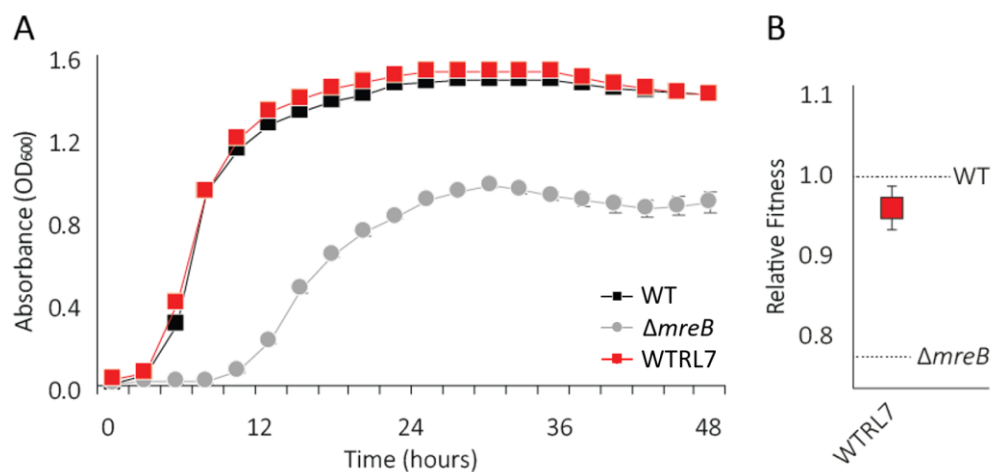
Figure 55 Growth and relative fitness effects of the OprD-inclusive deletion in the WT background. A) The OprD-inclusive deletion has no negative effect on the growth dynamics of WTRL7, shown by the red line. B) Similarly, relative fitness is very close to WT-levels. Error bars represent SD for 3 biological replicates.

PG has a lower D44/M4 ratio with a shorter average glycan chain length and less cross-linking

Compared to WT, the M4 and D44 molar percentages of WTRL7 are lower and have more variability (37.22%, SD ± 5.90% and 29.18%, SD ± 3.92%, respectively; 3 replicates) (Figure 56). These values are not significantly different from WT values. However, these produced a significantly lower D44/M4 ratio of 0.79 (SD ± 0.02; 3 replicates; $p < 0.05$, two-sample t-test). The average cross-linking percentage was also reduced to 31.80% (SD ± 2.09%; 3 replicates). Finally, the average glycan chain length of WTRL7 was significantly lower, shortening to 15.47 disaccharides (SD ± 1.21 disaccharides; 3 replicates; $p < 0.05$; two-sample t-test) in WTRL7.
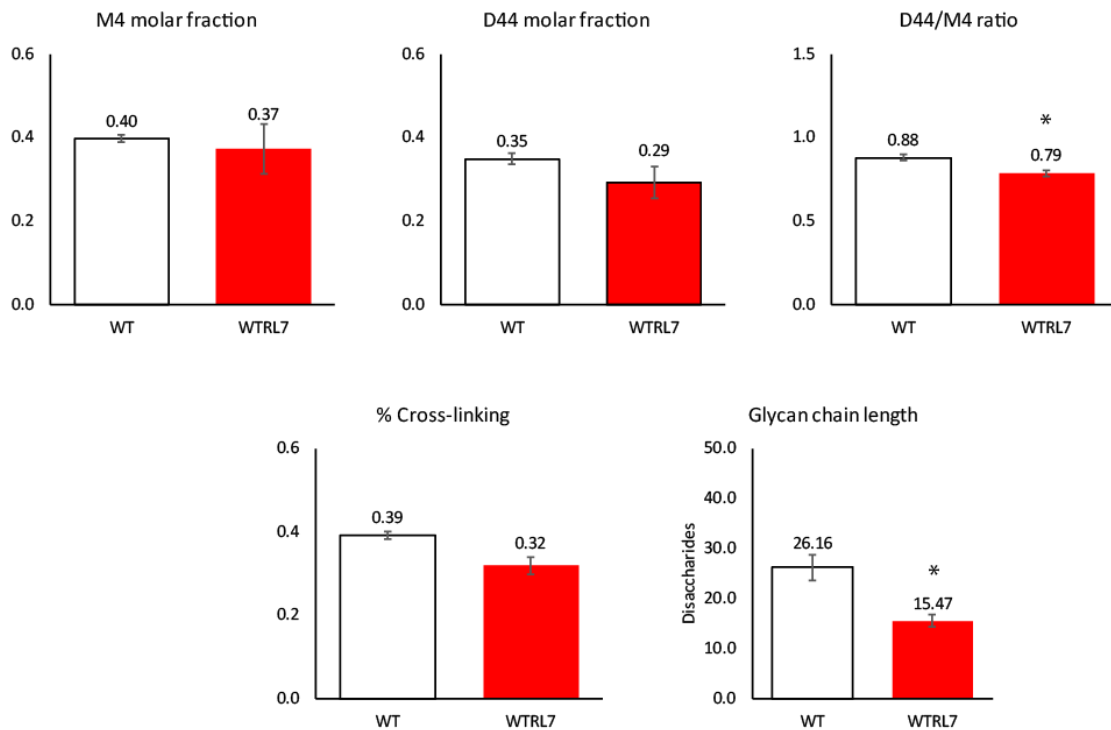
Figure 56 Variations in the M4 and D44 of WTRL7 produced a significantly lower D44/M4 compared to WT. Cross-linking decreased slightly, but the difference was not significant. Glycan chain length was significantly shorter in WTRL7. Asterisks represent a significant difference of WTRL7 compared to WT. Error bars represent SD for 3 biological replicates.

The reconstruction of the OprD-inclusive deletion in the WT background produced significantly thinner but longer cells with lower average cell volumes. The PG composition of the reconstruction strain showed a significantly lower D44/M4 ratio and shorter glycan chains, with a slightly reduced percentage of cross-linking. It is unknown how the OprD-inclusive deletion is causing these phenotypes in the WT background. Turner *et al.* (2018) proposed that reduced glycan chain lengths are produced as a result of a disruption in systems directing PG synthesis. This hints at a possible modification of PG assembly resulting from the deletion of this group of 5-genes.

4.2.4.3.2. Reconstruction of the five gene deletion in the Δ*mreB* background

Cells are smaller, have higher fitness, and remain spherical but exhibit a filamenting phenotype

In Δ*mreB*RL7, cells remained spherical to ovoid in shape (Figure 57A), but cells became significantly smaller than Δ*mreB*, having an average volume of 5.32 µm³ (SD ± 3.18 µm³; n = 100) (Figure 57D). In addition, 25.61% (SD ± 6.42%; n = 100) of this reconstruction in the Δ*mreB* background produced cells with notable septation defects, producing clumps of spherical cells. Thus, the smaller cells and clumping or snaking phenotypes suggest that the OprD-inclusive deletion may be affecting cell division, perhaps affecting the placement and rate of synthesis of new division planes. The reconstruction of the OprD-inclusive deletion also improved the growth dynamics and relative fitness (0.96; SD ± 0.02; 3 replicates) in the Δ*mreB* background (Figure 58).
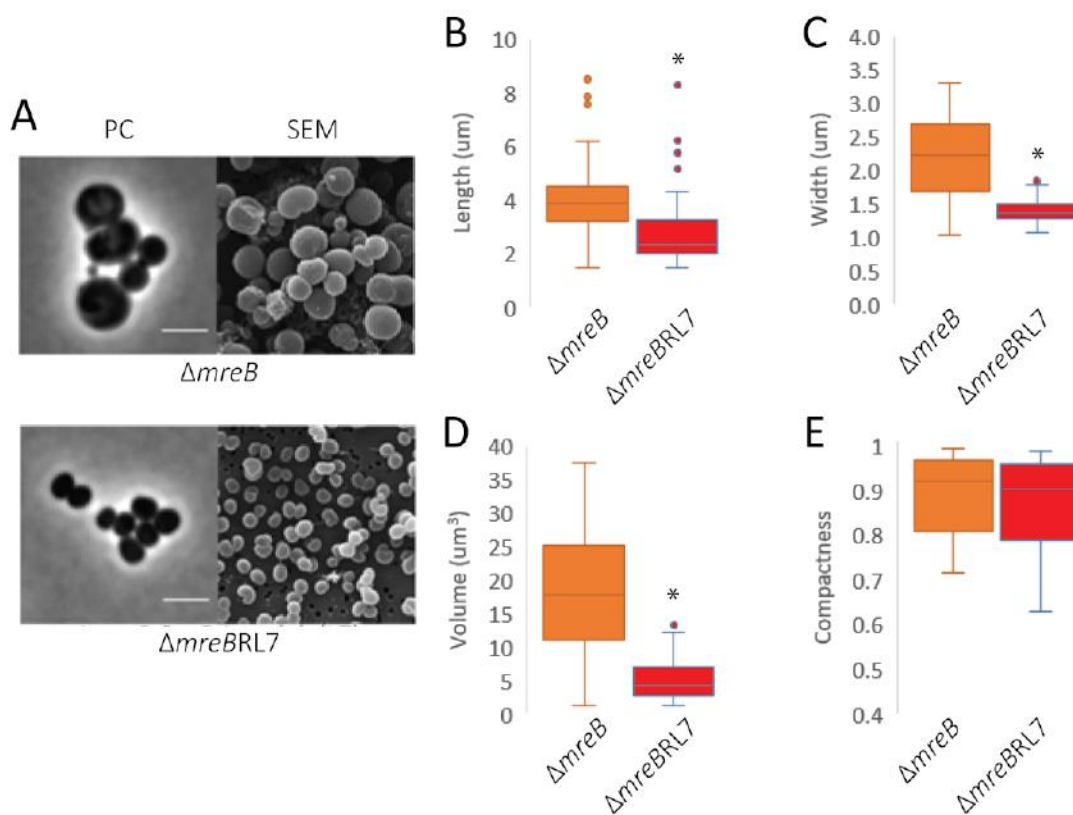
Figure 57 A) Reconstruction of the line 7 mutation in Δ*mreB* produced smaller spherical cells with a filamenting phenotype seen in some cells. The OprD-inclusive deletion produced (B) shorter and (C) narrower cells. As a result, cell volumes are lower (D) in Δ*mreB*RL7. Compactness values are similar to Δ*mreB* (E). Asterisks represent a significant difference of *mreBRL7* compared to WT. Scale bar = 3µm.
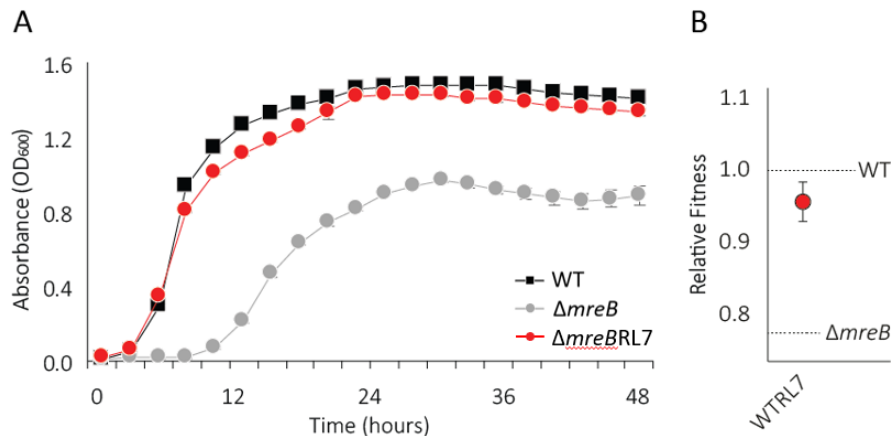
Figure 58 Growth and relative fitness effects of the OprD-inclusive deletion in the Δ*mreB* background. A) The growth characteristic of Δ*mreB*RL7, shown by the red line, closely resembles that of WT. B) The fitness of Δ*mreB*RL7 also increased to near-WT fitness values. Error bars represent SD for 3 biological replicates.

The OprD-inclusive deletion is an adaptive mutation in the Δ*mreB* background. Reconstruction of this 5-gene deletion in Δ*mreB* significantly improves growth, and fitness. This also had the effect of decreasing the D44/M4 of Δ*mreB*RL7's PG, meaning the balance between PG flexibility and rigidity is restored to WT levels. Cells are also much smaller whilst continuing to grow as spheres. Interestingly, the reconstructions in both the WT and Δ*mreB* backgrounds also produced defective cells with clumping or snaking phenotypes, suggesting that septa may be forming but not reaching completion in these cells. The exact mechanism responsible for this is unknown. However, an interesting clue can be found in the paper by Skurnik et al. (2013). Their report shows that transcription levels of *minD* are at least 10 times higher in an *oprD*-deficient strain of *P. aeruginosa*. This hints at a possible scenario wherein the deletion of *oprD* may be altering mechanisms governing septum formation (FtsZ inhibition by the Min system). Cell division is a finely tuned process, and cells with imbalanced levels of Min and FtsZ proteins are known to produce filamenting phenotypes (Justice, García-Lara and Rothfield, 2000; MacCready and Vecchiarelli, 2018; Wehrens *et al.*, 2018), similar to what we see in our reconstructions. If septum formation is indeed affected by OprD-loss in *P. fluorescens*, then this could also be influencing the ability of Δ*mreB* to divide, perhaps allowing it to overcome issues with the formation of incomplete septa described in Chapter 3.

PG cross-linking reverted to WT levels with a slight increase in glycan chain length

In Δ*mreB*RL7, M4 increased to 31.47% (SD ± 2.30%; 3 replicates), while D44 decreased to 30.09% (SD ± 3.37%; 3 replicates) (Figure 59). These changes were not statistically significant. However, these resulted in a significant reduction in D44/M4 which decreased to 0.95 (SD ± 0.05; 3 replicates; $p < 0.05$, two-sample t-test). Average glycan cross-linking was likewise reduced to 35.07% (SD ± 4.86%; 3 replicates). Finally, the average cross-linking percentage in Δ*mreB*RL7 showed a slight increase to 16.25 disaccharides (SD ± 2.07 disaccharides; 3 replicates). All values reverted to WT levels, except glycan chain length which did increase but was still significantly shorter than WT glycan chain length ($p < 0.05$, two-sample t-test).
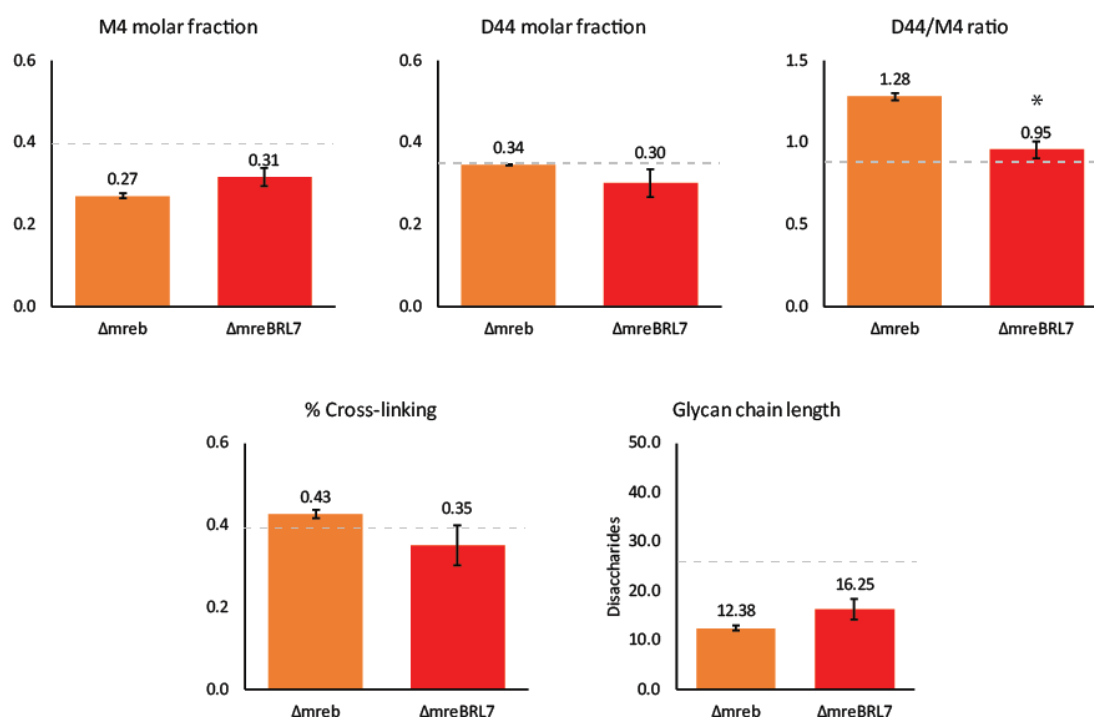
Figure 59 Variations in the M4 and D44 of Δ*mreB*RL7 produced a significantly lower D44/M4 compared to Δ*mreB*. Cross-linking decreased slightly, reverting to WT levels. Glycan chain length was slightly longer in Δ*mreB*RL7. The dashed line represents the value of WT readings for the same characteristics. Asterisks represent a significant difference of *mreBRL*7 compared to WT. Error bars represent SD for 3 biological replicates.

At this point, the link between the OprD-deletion, the Min system, and septum formation is inconclusive. PG analysis shows that the D44/M4 ratio has reverted to WT levels, but the other components of the cell wall (M4, D44, cross-linking percentage, and glycan chain length) only changed slightly. This suggests that the improvement in growth conferred by this deletion cannot be fully attributed to changes in systems affecting PG synthesis. It is therefore possible that other mechanisms, such as the altered Min dynamics discussed above, are at play. To better understand this topic, it will be beneficial to analyse cell division in these cells in the future. This can be done by studying MinD expression levels, observing Z-ring formation, or observing chromosome segregation using fluorescent tags in run-out experiments, for example. Further investigation is also needed to confirm that the phenotypes observed are truly due to the deletion of OprD, and not one of the other 4 genes in the 5-gene cluster.

4.2.5. PG synthesis patterns are restored by reconstructed mutations

Using fluorescent D-amino acids (FDAAs), I studied how the mutations discussed above are affecting PG assembly in Δ*mreB*. FDAAs are metabolic probes that are useful for studying PG insertion patters *in situ* (Banzhaf *et al.*, 2012; Hsu *et al.*, 2017). This technique uses the action of transpeptidases (TPs), penicillin-binding proteins (PBPs), and/ or L,D-transpeptidases to insert small fluorescent molecules conjugated to a D-amino acid backbone into sites of active PG synthesis in bacteria (Cava *et al.*, 2011; Lupoli *et al.*, 2011). The use of FDAAs gives us the ability to perform spatiotemporal tracking of PG synthesis and modification (Hsu *et al.*, 2017) and has been an effective tool for investigating PG synthesis in real time across a number of bacterial species (Liechti *et al.*, 2016; Bisson-Filho *et al.*, 2017; Hsu *et al.*, 2017; Zhu *et al.*, 2017).

I used the green-fluorescent probe BADA (BODIPY-FL 3-amino-D-alanine) to observe the patterns of new PG insertion using a short-pulse labeling technique. Briefly, cells were exposed to BADA for 5 to 10% of their generation time before being fixed, washed, and imaged. The resulting images of cells where active sites of PG growth are marked by BADA, allowing us to differentiate old from new PG. Despite

getting clear and bright fluorescent signals from many cells, it is worth noting that not all of the cells stained well. I believe this can be improved with further optimisation of staining parameters in the future (FDAA concentration, staining time, incubation setup).

In WT, we observe a pattern of PG assembly that is typical of a rod-shaped bacterium. PG insertion can be seen throughout the length of the cell, with little activity seen in the polar caps (Figure 60). Fluorescent bands are observed running perpendicular to the cell length following a helical pattern, which is reminiscent of the movement pattern of MreB in rod-shaped bacteria (Daniel and Errington, 2003; Scheffers and Pinho, 2005). In dividing cells, a single bright band or spot can be seen in the center of the cell, with less activity along the lateral walls, indicating a focused insertion of new PG material in the forming septum, and a shift from lateral to septal growth (Scheffers and Pinho, 2005). In longer cells, bright bands could be seen at 25% and 75% of the cell length, corresponding with the location of future septal PG Figure 61.
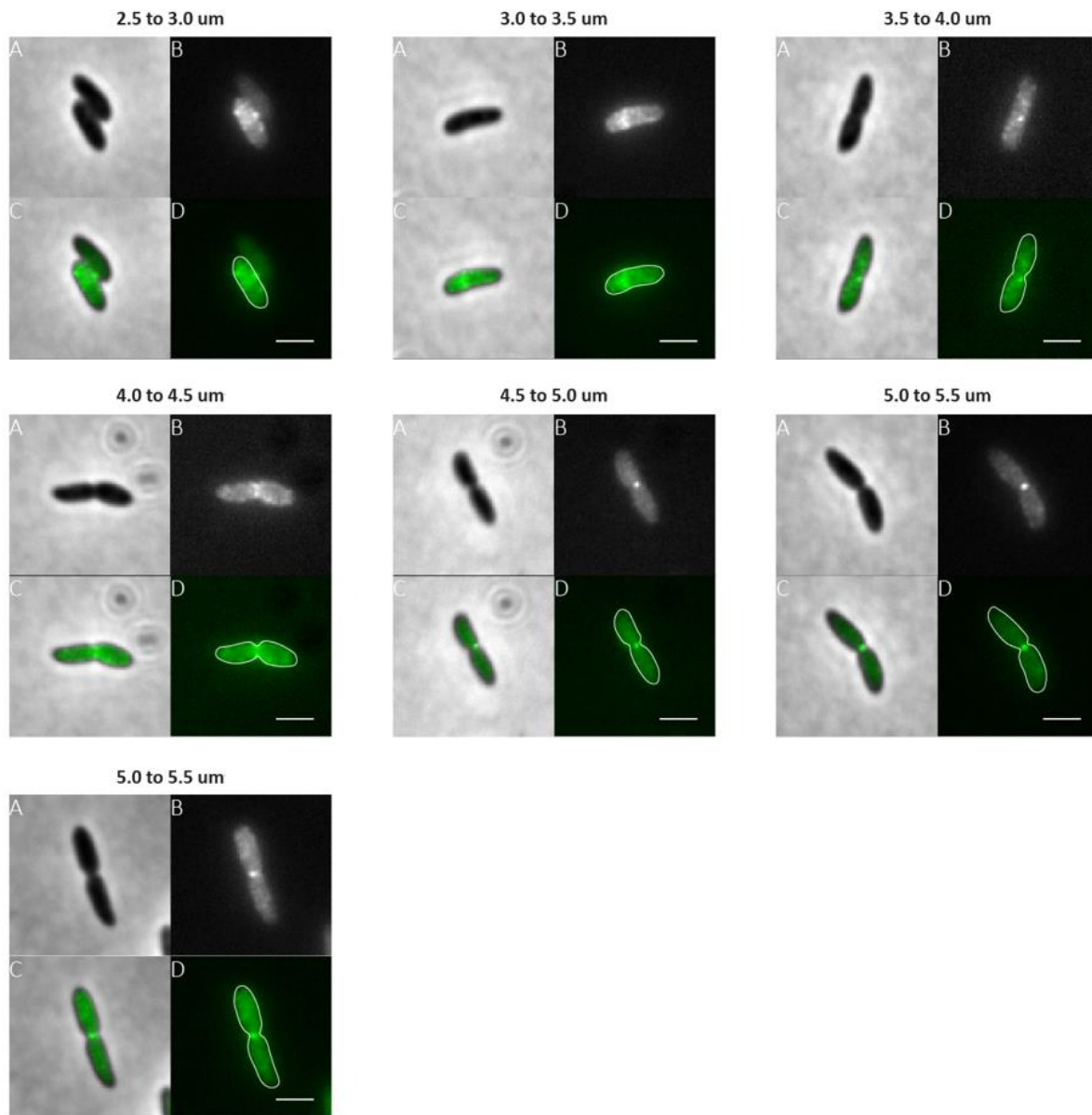
Figure 60 The incorporation of FDAAs in WT shows PG assembly along the lateral walls during elongation. Perpendicular bands can be seen running along the long axis of the cell, akin to the pattern of the MreB-associated PG assembly seen in other bacteria. The cell poles are notably dark showing no PG synthesis activity. Dividing cells show a bright spot at the septum, highlighting strong PG synthesis activity at the septum during cell division. A = phase contrast, B = fluorescent image (GFP), C = combine phase contrast + GFP, D = GFP + cell outline. Scale bar = 2μm.
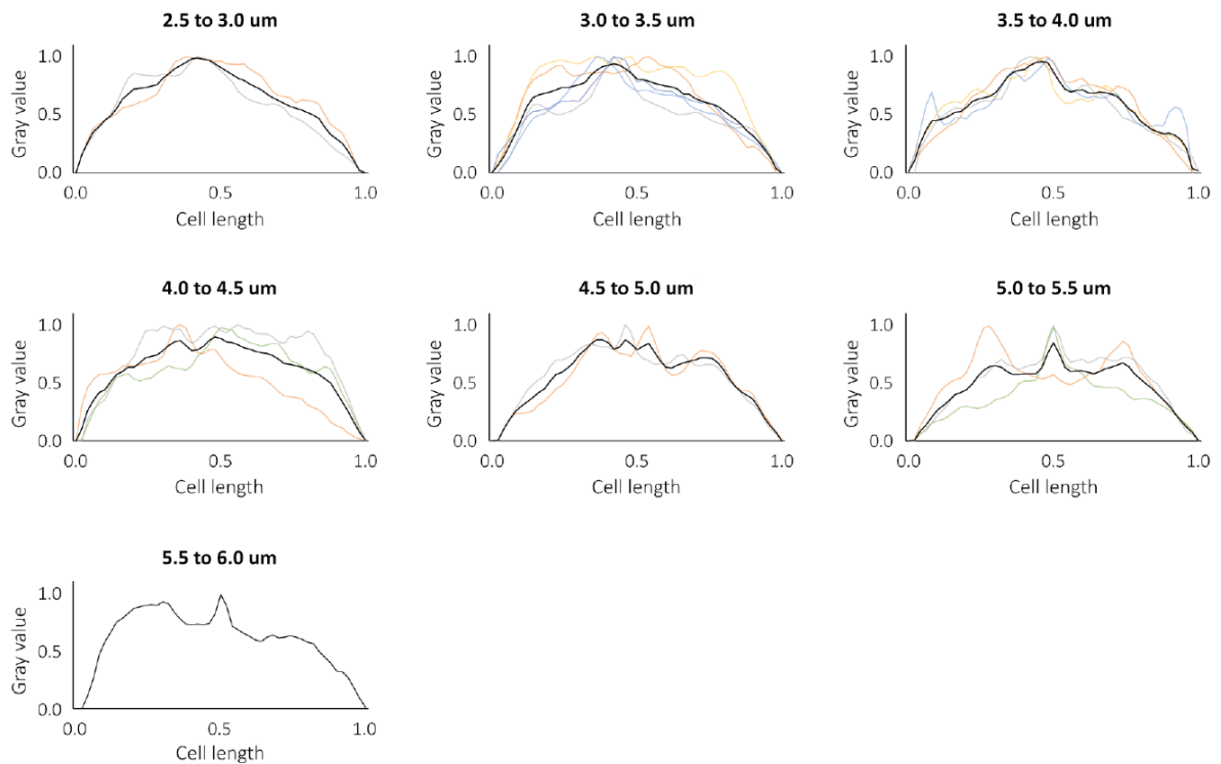
Figure 61 Line scans along the length of the cell show no PG synthesis activity at the poles with dispersed activity along the length of the cell. Peaks along the cell length represent directed PG synthesis that runs perpendicular to the cell's long axis. Dividing cells show strong activity at midcell where the septum is forming, and at the quarter positions which are the potential future division sites of dividing cells. Coloured lines indicate data for 1 cell, and black line indicates the average of all cells in each cell length category.

In Δ*mreB*, PG activity is distributed throughout the cell in a non-specific manner. Numerous bright spots are seen, often forming clusters that are spread out across the cell (Figure 62). Bright bands can be seen in dividing cells, forming either a complete ring around the cell, or partial bands that resemble incomplete septa or Z-rings (Thanedar and Margolin, 2004). Even in cells that do form a complete septal ring, bright spots can still be seen, indicating the continued insertion of new PG in areas other than the septum during cell division. Line scans show none of the peaks seen in WT (Figure 63) showing the absence of directional growth.

115
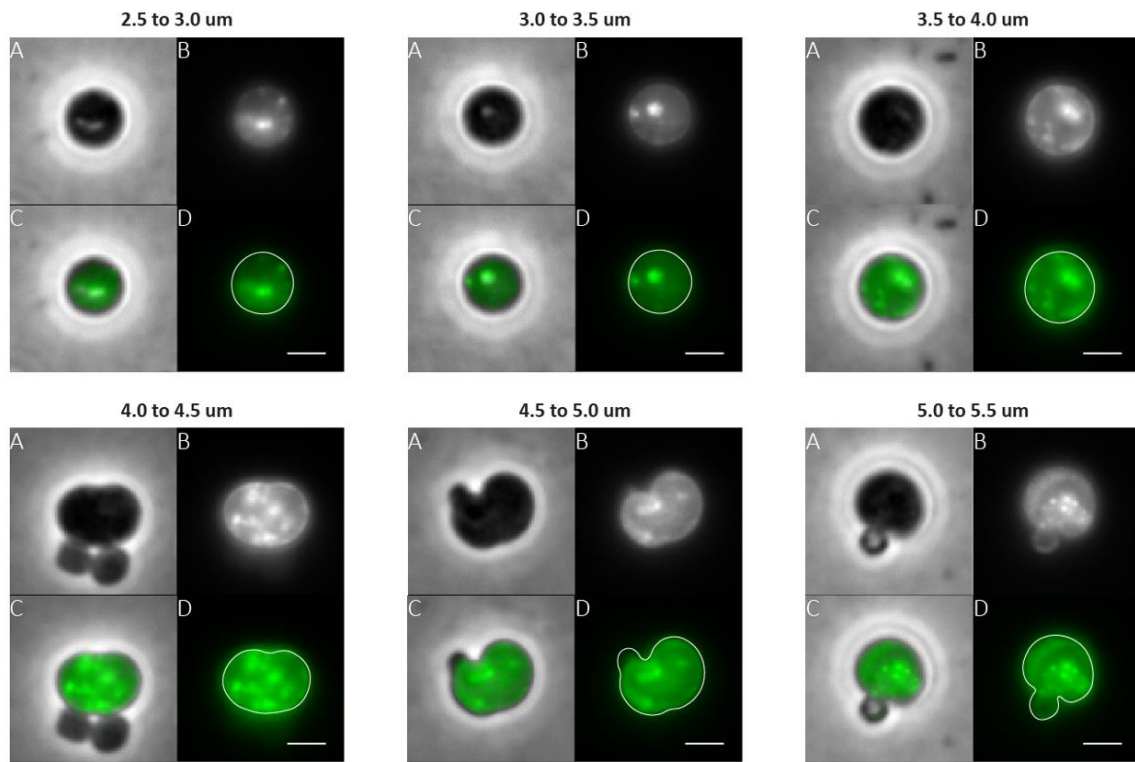
Figure 62 Δ*mreB* cells show a disorganized pattern of PG assembly. PG assembly is uneven, showing scattered bright spots as well as dark areas throughout the cell. This is especially apparent in larger cells measuring > 4μm^3. A = phase contrast, B = fluorescent image (GFP), C = combine phase contrast + GFP, D = GFP + cell outline. Scale bar = 2μm.
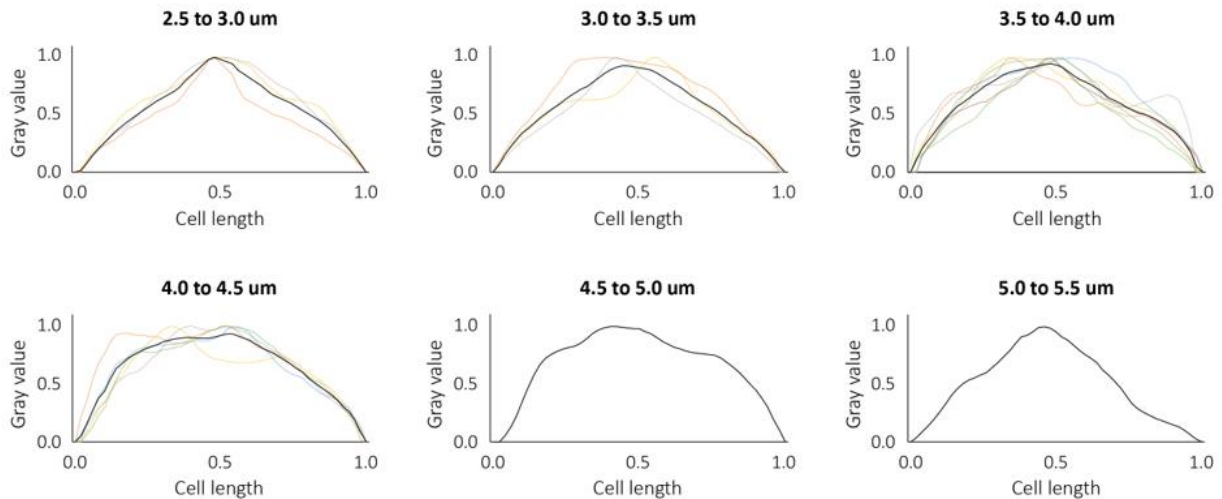
Figure 63 Line graphs of Δ*mreB* show a smooth distribution of PG synthesis activity throughout the cell. The jagged peaks seen along the length of WT are no longer present, indicating the absence of directional PG assembly. Coloured lines indicate data for 1 cell, and black line indicates the average of all cells in each cell length category.

To understand how the mutations from the evolution experiment (discussed previously) may be affecting PG insertion, I performed the same short-pulse labeling experiment on the L1, L4, and L7 reconstructions in the WT and Δ*mreB* backgrounds. In the WTRL1 (Figure 64 & Figure 65) and WTRL4 (Figure 66 & Figure 67) reconstructions, there was no effect change seen in the PG insertion patterns. Cell growth is still dispersed along the cell, and helical bands can still be seen running perpendicular to the length of the cell.
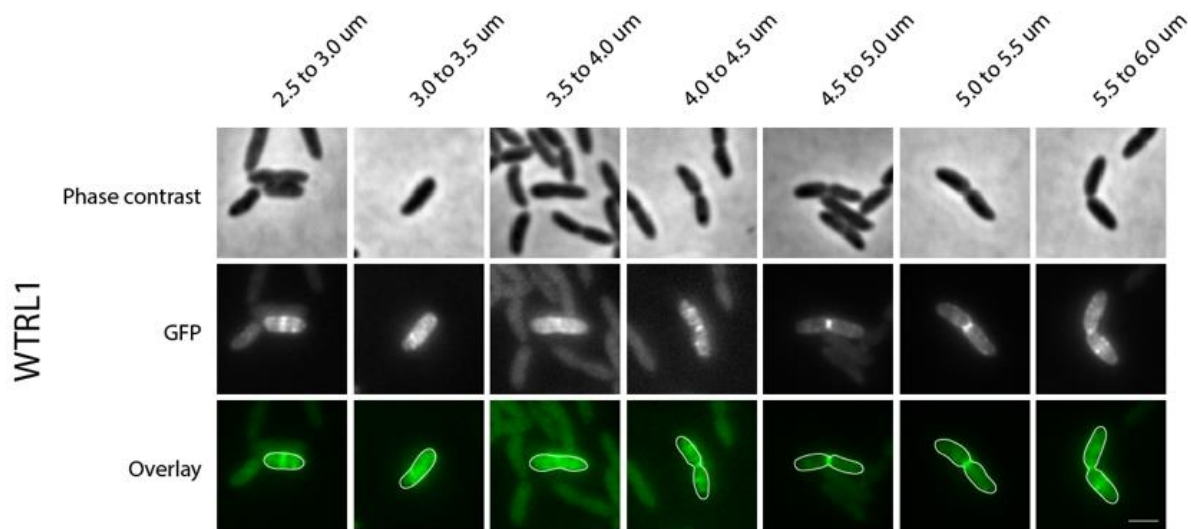
Figure 64 PG synthesis in WTRL1 resembles that of WT. Activity is seen throughout the cell length, with perpendicular bands visible. Dividing cells show strong activity at the septum with decreased activity along the cell length. Scale bar = 2μm.
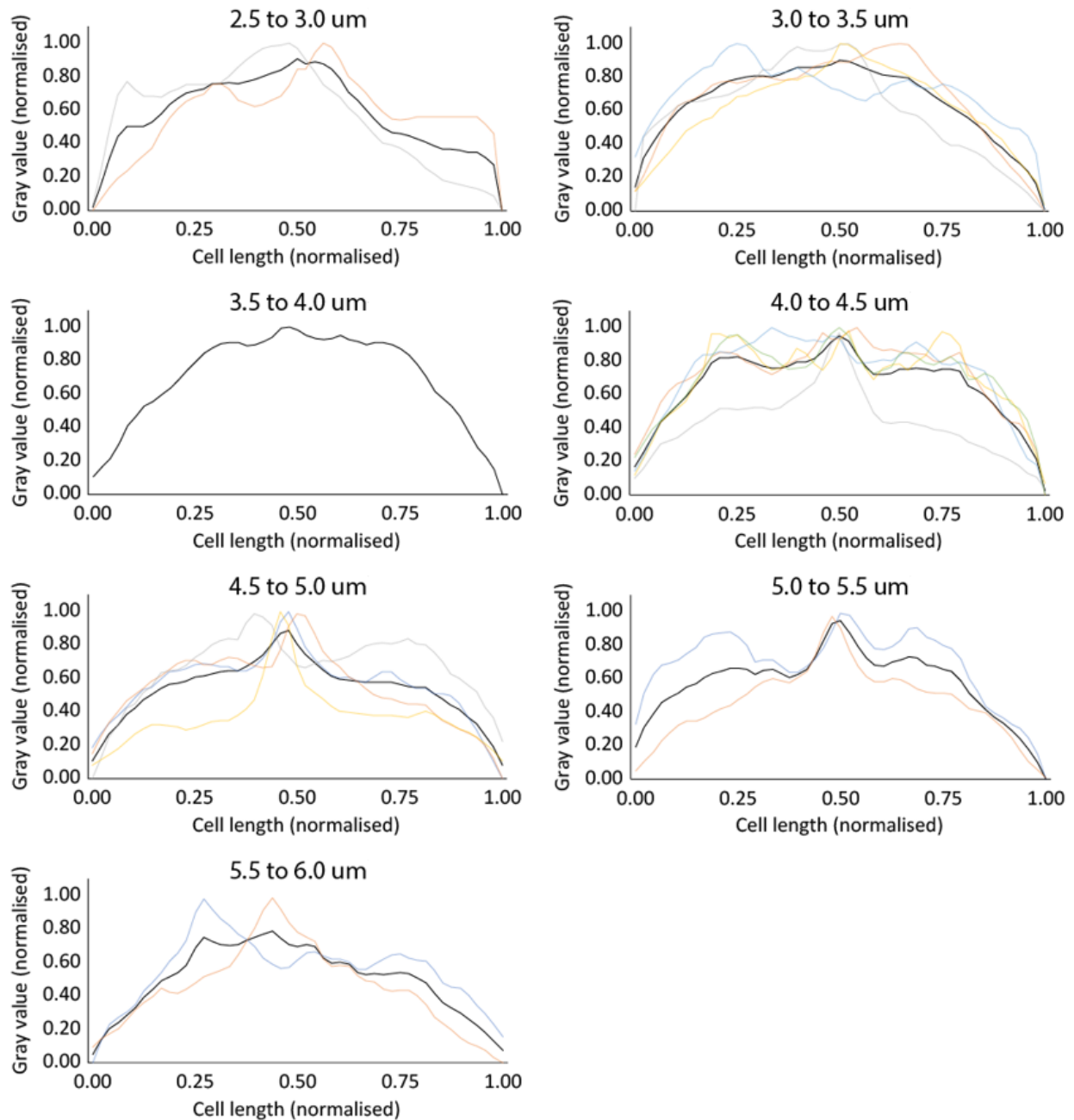
Figure 65 Line scans of WTRL1 cells resemble that of WT. PG synthesis activity is not seen at the poles, and dispersed activity is seen along the length of the cell. Sharp peaks along the cell length represent directed PG synthesis running perpendicular to the cell's long axis. Dividing cells with cell lengths longer than 4.0 µm show strong activity at midcell where the septum is forming, and at the quarter positions which are the potential future division sites of dividing cells. Coloured lines indicate data for individual cells, and black line indicates the average of all cells in each cell length category.
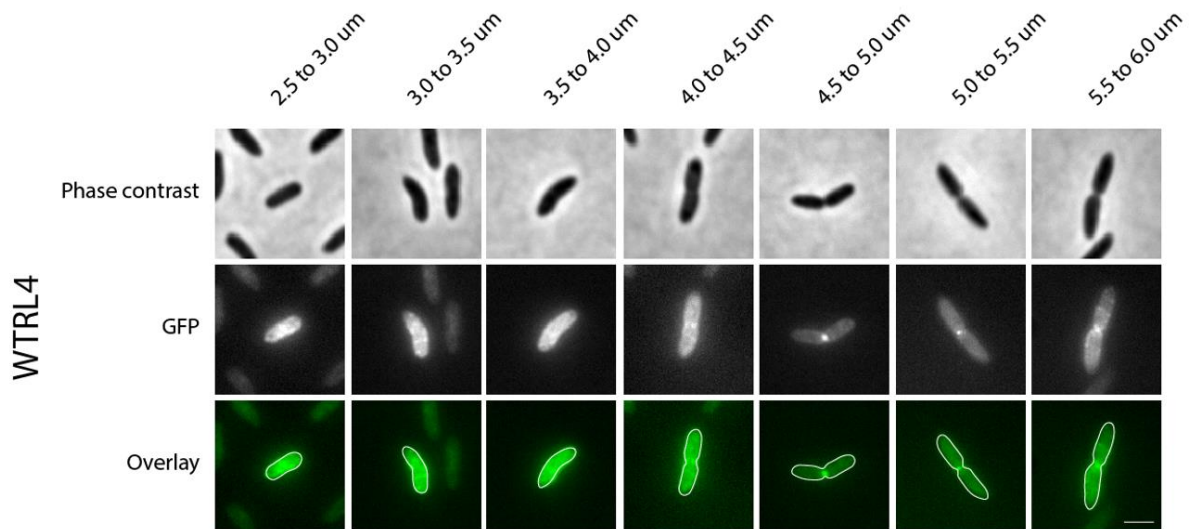
Figure 66 PG synthesis in WTRL4 resembles that of WT. Activity is seen throughout the cell length, with perpendicular bands visible. Dividing cells show strong activity at the septum with decreased activity along the cell length. Scale bar = 2 µm.
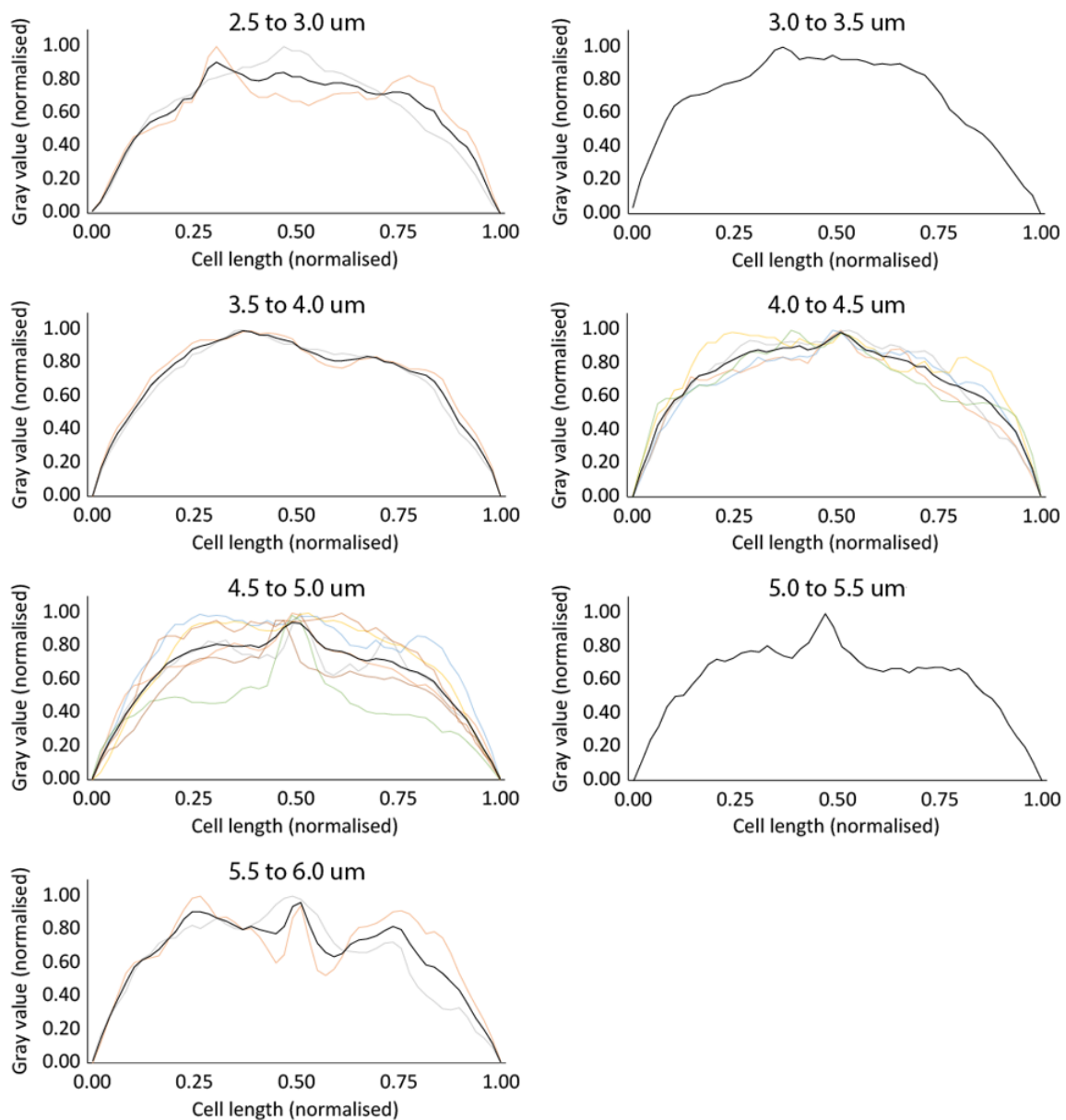
Figure 67 Line scans of WTRL4 cells resemble that of WT. PG synthesis activity is not seen at the poles, and dispersed activity is seen along the length of the cell. Sharp peaks along the cell length represent directed PG synthesis running perpendicular to the cell's long axis. Dividing cells show strong activity at midcell where the septum is forming, and at the quarter positions which are the potential future division sites of dividing cells. Coloured lines indicate data for 1 cell, and black line indicates the average of all cells in each cell length category.

However, in the Δ*mreB* background, growth now seems to be focused only at or near the site of septal PG formation. Bright bands are only seen running across the dividing daughter cells, with no spots or stray bands occurring anywhere else in the cell. This is similar to the growth characteristics of spherical bacteria such as *S. aureus* and S. pneumoniae, where PG insertion occurs mostly at the septum (Stamsås *et al.*, 2018). This indicates that in the absence of MreB, both the line 1 (Figure 68 & Figure 69) and line 4 (Figure 70 & Figure 71) mutations are preventing unrestricted lateral growth, perhaps by interfering with or preventing PBP1a activity, thereby allowing new PG material to be inserted only at the division site by other PBPs.
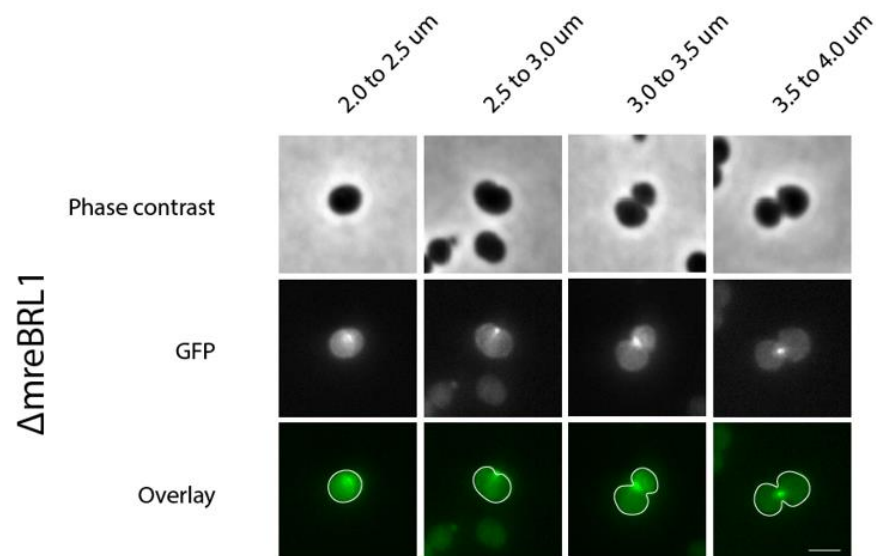
Figure 68 PG synthesis in Δ*mreB*RL1 shows decreased peripheral growth. The bright spots seen in Δ*mreB* are no longer present, and PG assembly is strongest at and around the septum. Scale bar = 2μm.
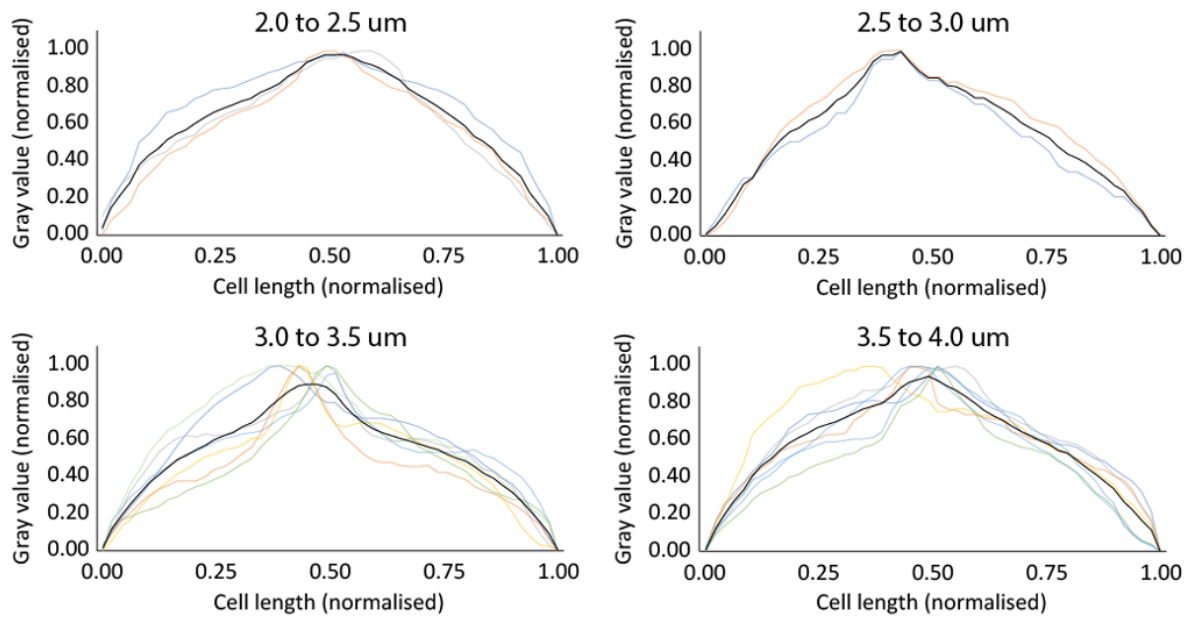
Figure 69 Line scans of Δ*mreB*RL1 show reduced peripheral activity and a strong activity at or near the center of the cell. Coloured lines indicate data for 1 cell, and black line indicates the average of all cells in each cell length category.
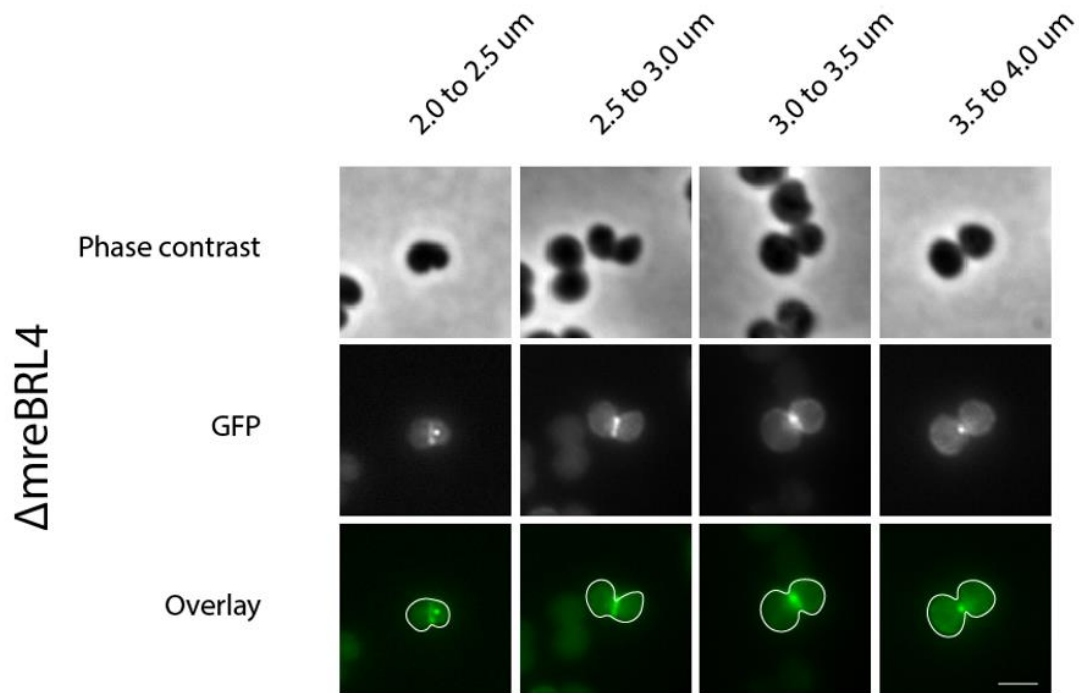
Figure 70 PG synthesis in Δ*mreB*RL4 shows decreased peripheral growth. The bright spots seen in Δ*mreB* are no longer present, and PG assembly is strongest at and around the septum. Scale bar = 2µm.
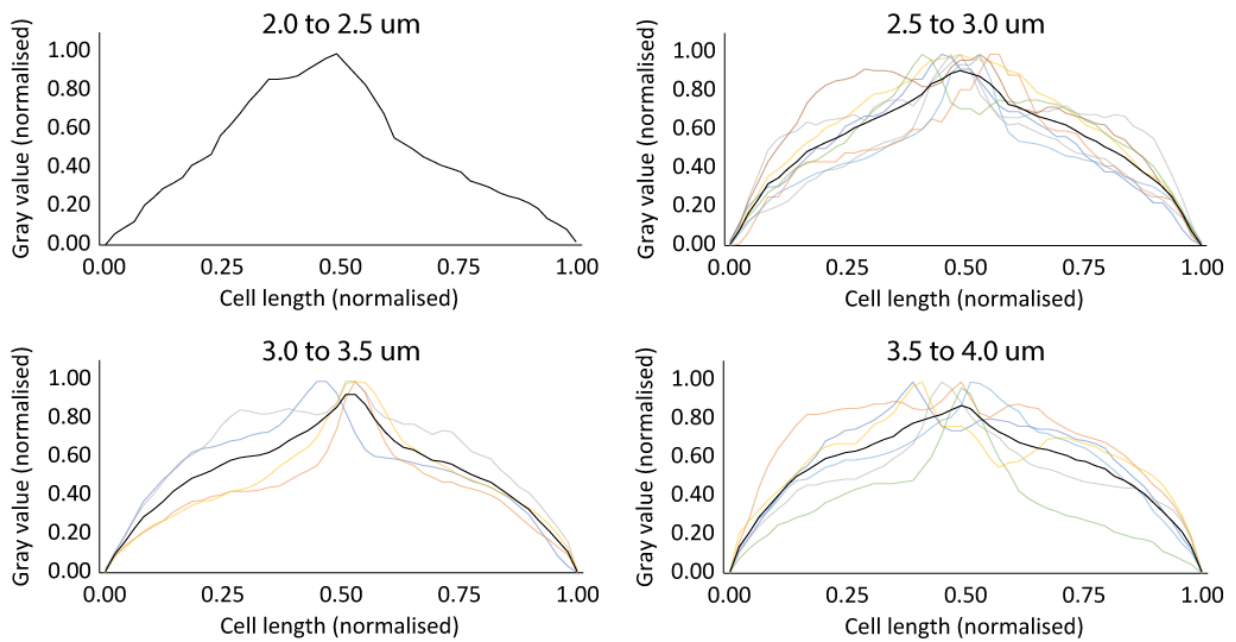
Figure 71 Line scans of Δ*mreB*RL1 show reduced peripheral activity and a strong activity at or near the centre of the cell. Coloured lines indicate data for 1 cell, and black line indicates the average of all cells in each cell length category.

Similar results were seen in the OprD-inclusive deletion from Line 7. In the WT background, the PG activity of single cells is similar to that of WT – bright bands can be seen running across cells, perpendicular to the cell length, in a helical pattern. In dividing cells, a bright band can be seen running around the cell following septum formation (Figure 72). As previously described, a proportion of this population produces a snaking or filamenting phenotype with multiple incomplete septa in cells that are greater than 5.0μm in length. In these elongated cells, PG activity seems to shift from septum formation back to lateral growth before the septum is fully closed. As this happens, PG activity in some parts of the cell continue to occur as other parts seem to stop growing (Figure 73).
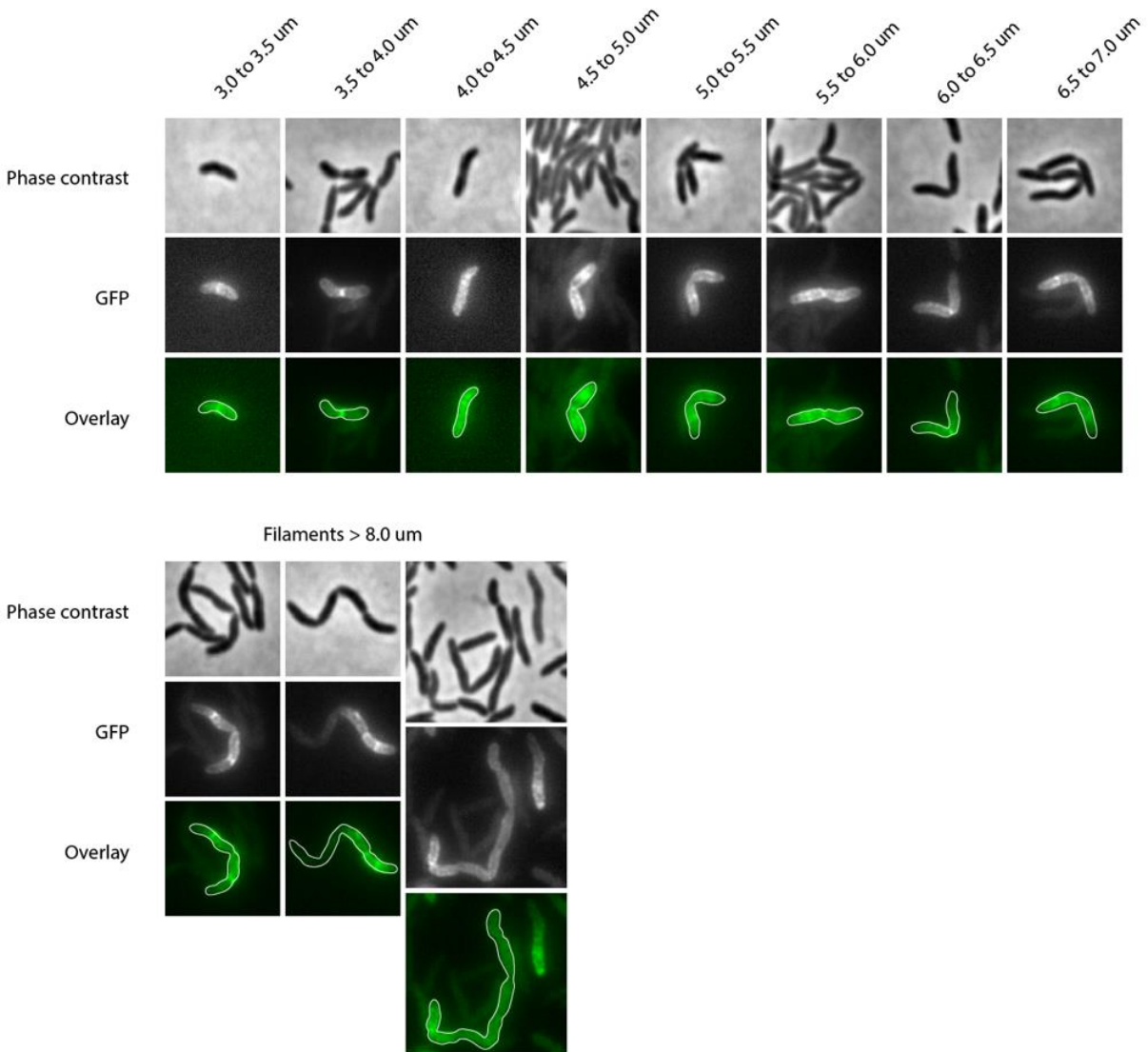
Figure 72 PG synthesis in WTRL7 exhibits typical characteristics of rod-shaped growth. Bright bands are seen running perpendicular to the cell length, and dividing cells show activity at the septum and at the future sites of septum formation. This population exhibits filamenting phenotypes that show uneven patterns of PG synthesis. In these long cells, bright bands can be seen at or near septa and along the length of the cell, while other parts appear to have decreased PG activity. Scale bar = 2μm.
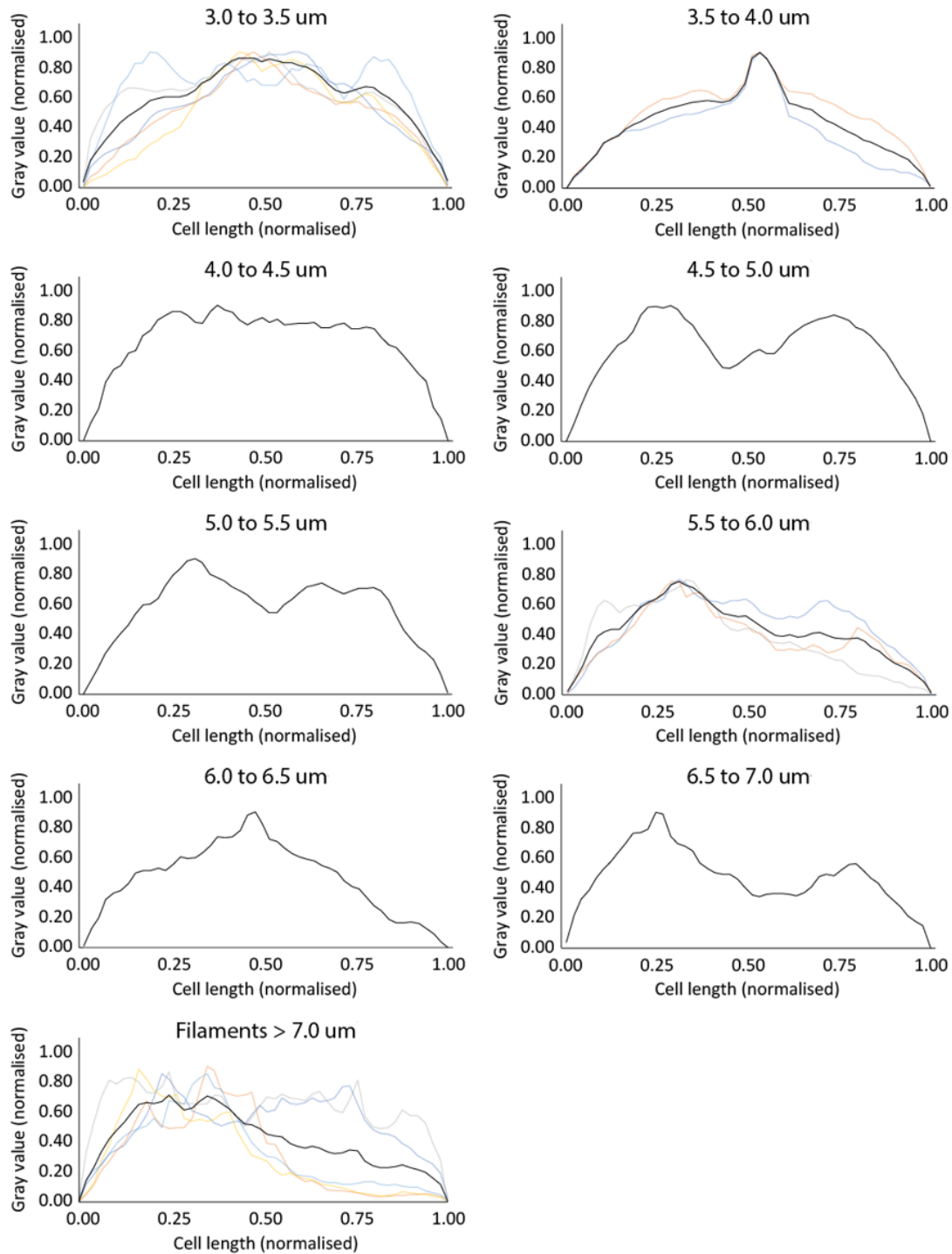
Figure 73 Line scans of WTRL7 reveal numerous peaks of activity along the length of the cell. This indicates that the directional orientation of PG synthesis has become erratic. This is especially apparent in filamenting cells. In some filamenting cells, PG assembly can be seen tapering off on one half of the cell while remaining active in the other.

In *ΔmreB*RL7, cell growth is mostly restricted to the septum with no stray spots of activity happening anywhere else in the cell. Most cells follow this pattern of growth and successfully complete cell division to form distinct spherical daughter cells (Figure 74). However, a filamenting phenotype can also be seen in a proportion of these spherical cells. As in the WT background, some cells seem to shift from cell division back to lateral growth, producing incomplete septa which eventually cause the formation of filamenting cells. In these cases, some lateral growth can be seen near the septum, with activity being visible in only some parts of the cell (Figure 75).
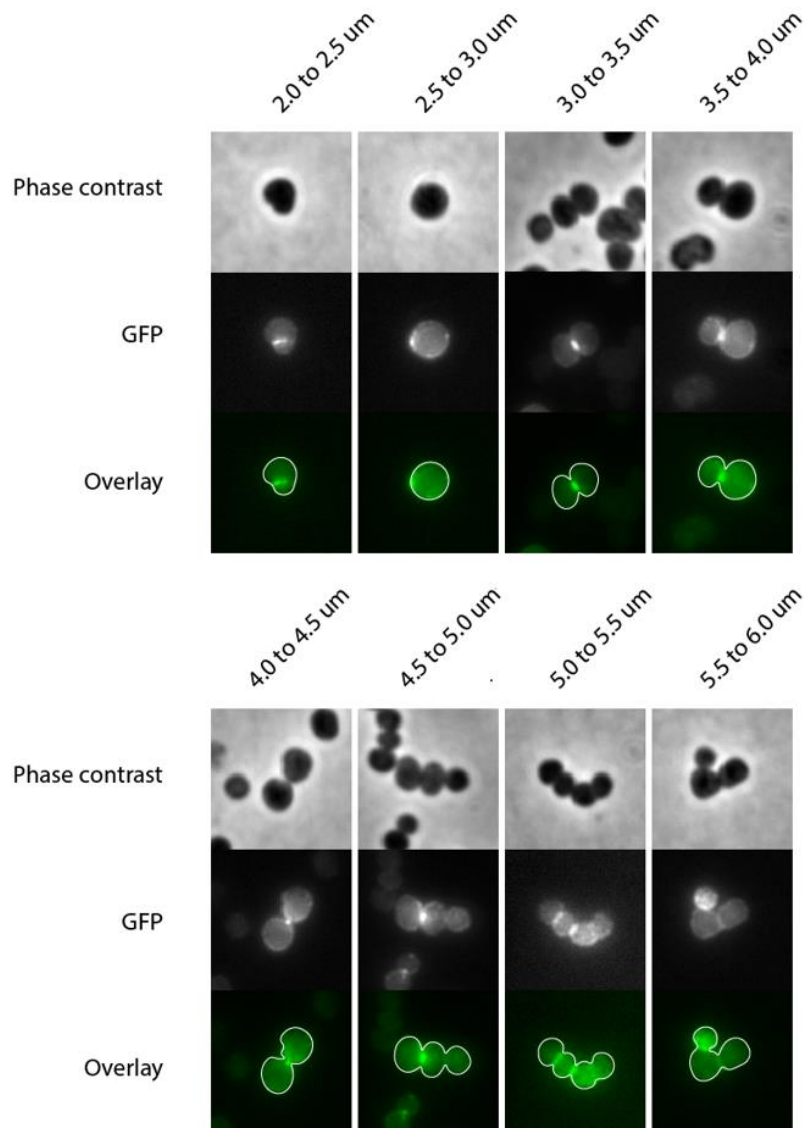
Figure 74 PG synthesis in Δ*mreB*RL7 shows decreased peripheral growth. The bright spots seen in Δ*mreB* are no longer present, and PG assembly is strongest at and around the septum. Similar to WTRL7, the Δ*mreB*RL7 population also exhibits a filamenting phenotype. In these cells, activity is also unevenly distributed throughout the cell. Scale bar = 2μm.
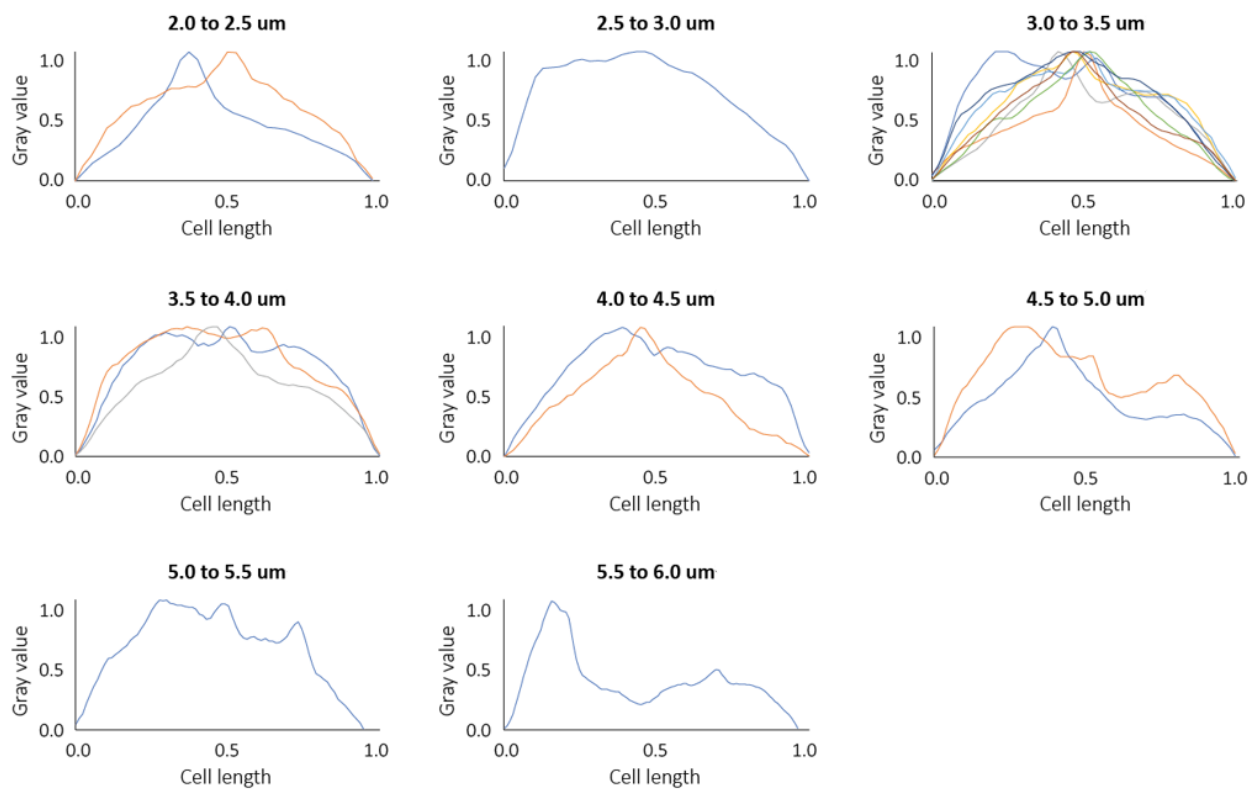
Figure 75 Line scans of Δ*mreB*RL7 show uneven PG synthesis patterns. In filamenting cells, heightened activity can be seen at the septum or at quarter positions which represent the future sites of septal formation. To perform the line scans, lines are drawn following the longitudinal axis of the filamenting cells.

These data suggest than in WTRL7, the snaking phenotype may be a result of the disruption of cell division. This supports the idea that the deletion of OprD increases MinD expression levels, thereby affecting the placement of septa during cell division. Perhaps this mechanism is causing septal formation to be aborted before the cell division is completed in these cells.

In this section, I have demonstrated that the fluorescent D-amino acid BADA can be successfully used to study the patterns of cell wall assembly in *P. fluorescens* SBW25. Rod-shaped *P. fluorescens* SBW25 cells are characterised by a diffused pattern of active cell wall construction along the length of the cell, with bright bands running perpendicular to the cell's longitudinal axis. This likely represents strong PBP activity directed by MreB which coordinates enzymes responsible for cell elongation, adding orientational order and strength to the PG structure of WT cells (Turner *et al.*, 2018). In addition, the cell poles of WT cells show no fluorescent activity, indicating the absence of active cell wall assembly in these regions.

Without MreB, cells continue to synthesize PG, allowing size enlargement, but in a less ordered manner. Turner et al. (2018) showed that spherical *E. coli* cells that have lost MreB produce a less ordered PG structure, leading to the production of shorter glycan chains due to a lower processivity of glycosidic bonds. The same characteristics are seen in Δ*mreB* – cells enlarge as they continue to grow and build new cell wall material, and PG processivity is lower producing shorter glycan chains. The PG structure is also less organized as the banded pattern seen in WT is replaced by a clumpy distribution of PG-assembly activity (Figure 62). Interestingly, FDAA staining revealed that the L1 and L4 (PBP1a), and L7 (OprD-inclusive deletion) mutations resulted in the inactivation of the aberrant PG activity seen in Δ*mreB*. This allowed cells to focus PG assembly only at or near the septum, allowing cell division to occur normally, resulting in the formation of smaller cells. The growth patterns seen in these reconstruction mutants resemble those of other ovococci such as *S. pneumoniae* suggesting that PG-assembly modification may be a key strategy that bacteria use for adapting to a spherical cell shape.

4.2.6. Recapitulating spherical cell shape evolution

So far, I have demonstrated that mutations in PBP1a, and an OprD-inclusive deletion can rescue growth and fitness defects associated with MreB loss. This led us to ask if the mutations we observed might be recapitulating events in the evolution of extant spherical cells. To investigate, I constructed a phylogenetic tree of 30 paired spherical and rod-like species from amongst completely sequenced bacterial genomes (Figure 76). PBP homologues were identified using BLAST based on the known PBPs of *E. coli*. I then compared the abundance of Penicillin Binding Proteins (PBPs) and OprD homologs in these organisms.

No interpretation can be made for the OprD homologues as they were too rare for analysis. OprD homologs are common in Pseudomonads but are rare in other species (Li *et al.*, 2012). In contrast, a strong relationship was seen in the number of PBPs in organisms that have remained rod-like, and in organisms that lost MreB (naturally spherical cells). In rods, 39 Class A, and 81 Class B PBPs were seen, amounting to 120 PBPs across 15 species. In spherical bacteria, only 21 Class A, and 33 Class B PBPs were seen, totalling 54 PBPs across 15 species. This shows that rods have significantly more PBPs, having 8.00 on average (SD ± 5.28) than spheres, which only have 3.6 on average (SD ± 2.23) PBPs ($p < 0.05$; two-sample t-test), suggesting that PBP loss may be a general strategy for adaptation to a spherical cell shape upon the loss of MreB. This is consistent with the observations of Meeske *et al.* (2016) who found that SEDS proteins and Class B PBPs are more broadly conserved than Class A PBPs, and may be the core PG synthases responsible for cell wall elongation and division machineries.
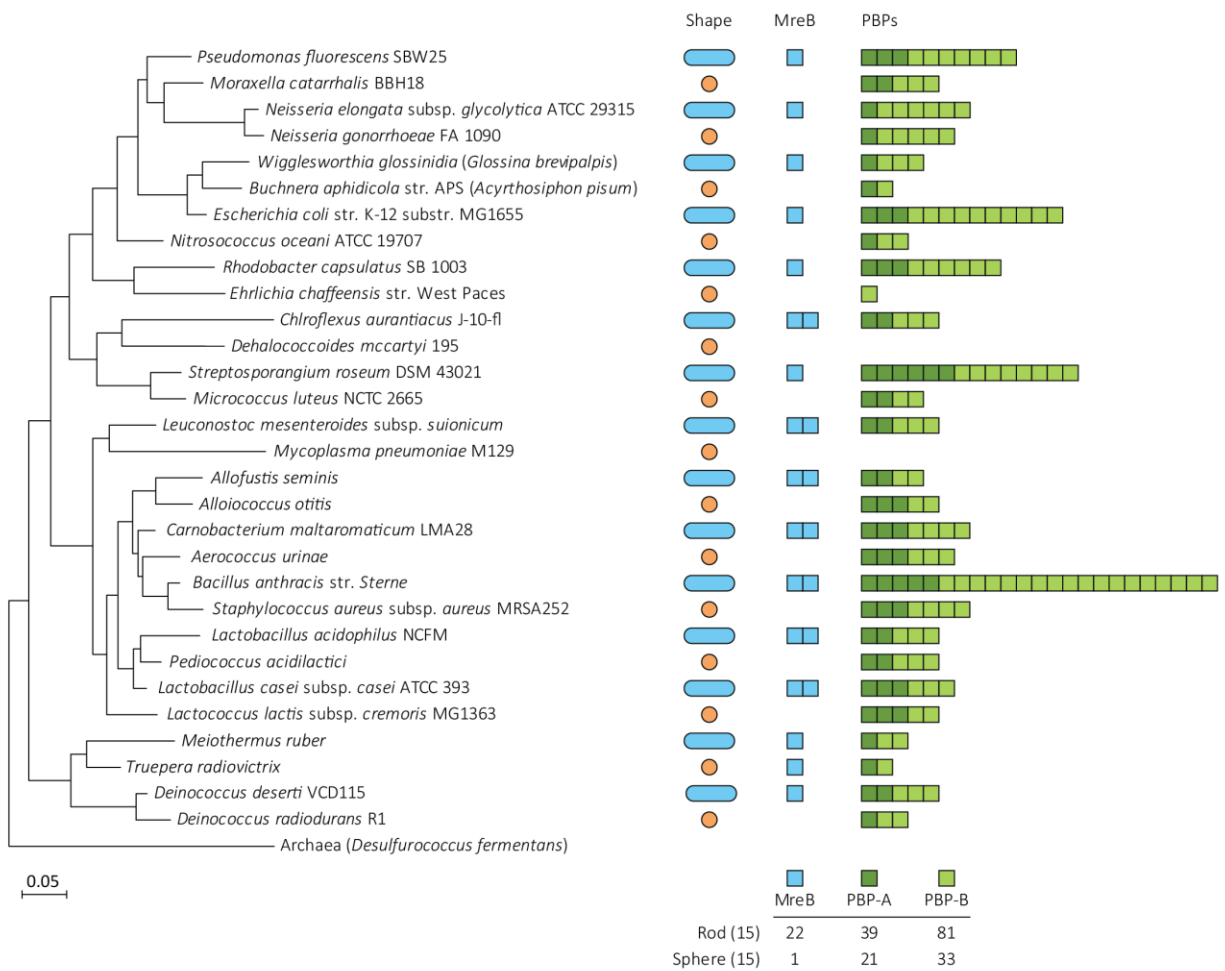
Figure 76 Penicillin-Binding Proteins (PBPs) observed in extant spherically-shaped cells. A selection of 26 paired rod-shaped and spherical cells were analysed for their PBP and OprD homologs. Naturally evolved spherical cells were seen to have fewer PBPs than rod-shaped species. OprD homologs were rare.

In conclusion, we used an experimental evolution approach to study natural strategies that the typically rod-shaped organism *P. fluorescens* SBW25 might take to adapt to a new spherical cell shape caused by the loss of MreB. By sequencing the evolved lines, we identified mutations that were responsible for improving their growth and fitness. We demonstrated that mutations in PBP1a, and the deletion of a five-gene-cluster that included the outer membrane protein OprD, can rescue growth and fitness in Δ*mreB*. Finally, we demonstrate that naturally-spherical bacteria have fewer PBPs than their rod-shaped relatives, suggesting that PBP loss is a natural adaptation strategy for a becoming spherical.

Chapter 5

Model for the adaptation of *P. fluorescens* SBW25

to a spherical cell shape

5.1.   Introduction

The formation and maintenance of bacterial cell shape is a well-coordinated process involving the bacterial cytoskeleton and numerous enzymatic complexes and processes. Recent advances in the imaging (e.g. atomic force microscopy by Turner *et al.*, 2018; and single molecule imaging by Lee *et al.*, 2016) and chemical analysis (e.g. UPLC by Alvarez *et al.*, 2016) of PG have allowed us to refine our understanding of cell wall construction and regulation, and therefore cell shape, in bacteria.

Previously, Holtje (1998) proposed an influential conceptual framework for PG synthesis called the "3-for-1" model, or a "Make before Break" model as referred to by Zhao *et al.*, (2017). The model assumes that bacteria synthesize three parallel, crosslinked PG strands before breaking any existing bond in the PG network to maintain cell wall integrity. Recently, Zhao *et al.* (2017) proposed an updated model called the "Break before Make" model of PG synthesis. In this model, mature PG is first broken by endopeptidases before new cell wall material is made and cross-linked to the mature PG mesh by the MreB-associated Rod-complex. New strands are then made and cross-linked independently, but synergistically, by Class A PBPs.

Using the framework of the "Break before Make" model, I present a new model that explains the data gathered from the experimental evolution of spherical cells from *P. fluorescens* SBW25. The model begins with rod-shaped (wild type) *P. fluorescens* SBW25 cells undergoing cell elongation through the action of the MreB-associated Rod-complex and PBP1a. In Figure 77A, the Rod-complex is shown associating with MreB, and working independently but cooperatively with PBP1a. After MreB is deleted Figure 77B, the directional insertion of new PG is lost. The resulting Δ*mreB* cells are unable to maintain their rod-like shape as the Rod-complex diffuses throughout the cell. At this point, new PG is still produced, allowing Δ*mreB* to grow continuously which causes a defect in cell division. PBP1a also diffuses throughout the cell but is attracted to the nicks or gaps in the PG that are made by Rod-associated endopeptidases. This leads to localised, inefficient cross-linking seen as hotspots of activity in the FDAA-labeling experiments (Figure 62). As MreB is no longer present to provide directional movement, newly synthesized PG glycan chains become shorter (Figure 32) and, as demonstrated by Turner *et al.* (2018) using spherical *E. coli*, less organized This is consistent with the observations of Turner *et al.*, (2018) who showed using atomic force microscopy that spherical *E. coli* treated with A22 produce PG with shorter average chains that are assembled in a disordered manner. The authors argue that this could lead to the formation of larger pores in the peptidoglycan mesh which would cause problems for cellular integrity, possibly explaining why Δ*mreB* is sensitive to mechanical damage (Figure 17).

5.2. Results and Discussion

PBP1a mutations

I propose that the mutations in PBP1a are deleterious to protein function. In Figure 77C, I show an Δ*mreB* cell that has lost PBP1a activity as a result of mutations that interfere with the enzyme's active site. Here, the Rod-complex is dispersed throughout the cell, presumably still synthesizing and assembling new PG, albeit very slowly. In *E. coli*, although the activity of the Rod-complex and PBP1a are spatially independent, their transglycosylase activities are functionally coupled such that inactivation of one or the other leads to an 80% reduction in the incorporation of new PG (Cho *et al.*, 2016). This is consistent with the loss of the activity hotspots in the FDAA experiments (Figure 68 & Figure 70). Without PBP1a, peripheral PG assembly decreases considerably, allowing the cell division machinery to create and complete Z-ring formation, thereby restoring cell division (Figure 77D). At this point, the cell division machinery takes over, concentrating growth at or near the septum. This is similar to the growth characteristic of ovococcus bacteria like *Streptococcus pneumoniae* which carries out both peripheral and septal PG synthesis (Mura *et al.*, 2017).

OprD-inclusive deletion

I propose that the OprD-inclusive deletion is likely altering the dynamics of Min proteins which are involved in determining cell division site in bacteria. The Min system is best understood from cell division studies using the model bacteria *E. coli* and *B. subtilis* (Eswara and Ramamurthi, 2017). In these organisms, the continuous chase and release of MinD (and the associated MinC) from the inner membrane through the action of MinE results in the continuous movement of Min proteins from one cell pole to the other. This oscillation forms a time-averaged minimum concentration of MinC (which inhibits Z-ring formation) at midcell, thereby allowing the assembly of the cell division machinery at the cell's midpoint (Lutkenhaus, 2007). Skurnik *et al.* (2013) previously showed that the transcription levels of *minD* are at

least 10 times higher in a healthy *oprD*-deficient strain of *P. aeruginosa*. Higher levels of MinD relative to MinE has the effect of lengthening the Min oscillation period, while lower MinD levels has the opposite effect of shortening the Min oscillation period (Raskin and de Boer, 1999; Hu, Gogol and Lutkenhaus, 2002). This suggests a scenario wherein the loss of OprD increases MinD expression, thereby slowing the Min oscillation period and allowing septum formation to proceed. This is further supported by the Pereira *et al.* (2016) who demonstrated that FtsZ filaments are able to generate elongated cells from cocci.

In Figure 77E, both the Rod-complex and PBP1a proteins are still present and are still actively synthesizing new PG. This does not seem to pose a problem for smaller cells as reconstruction mutants do not have the numerous PG synthesis hotspots seen in large Δ*mreB* cells (Figure 74). Although PG synthesis and growth continue, altered Min dynamics now allow septum formation to proceed, thus restoring cell division (Figure 77F). Consistent with this, cells that exhibit a long or filamenting phenotype in the OprD-inclusive deletion reconstructions show active PG construction across multiple septa (Figure 72 & Figure 74), indicating the concurrent assembly of multiple cell division sites (Figure 77G). This is reminiscent of the asymmetric cell division pattern of filamenting *Vibrio parahaemolyticus* swarmer cells which position the cell division machinery off-center, based on multi-nodal patterns of the Min system (Liao and Rust, 2018; Muraleedharan *et al.*, 2018). This is also similar to the Min-driven positioning of aberrant Z-rings in filamenting *Myxococcus xanthus* cells (Treuner-Lange *et al.*, 2013).
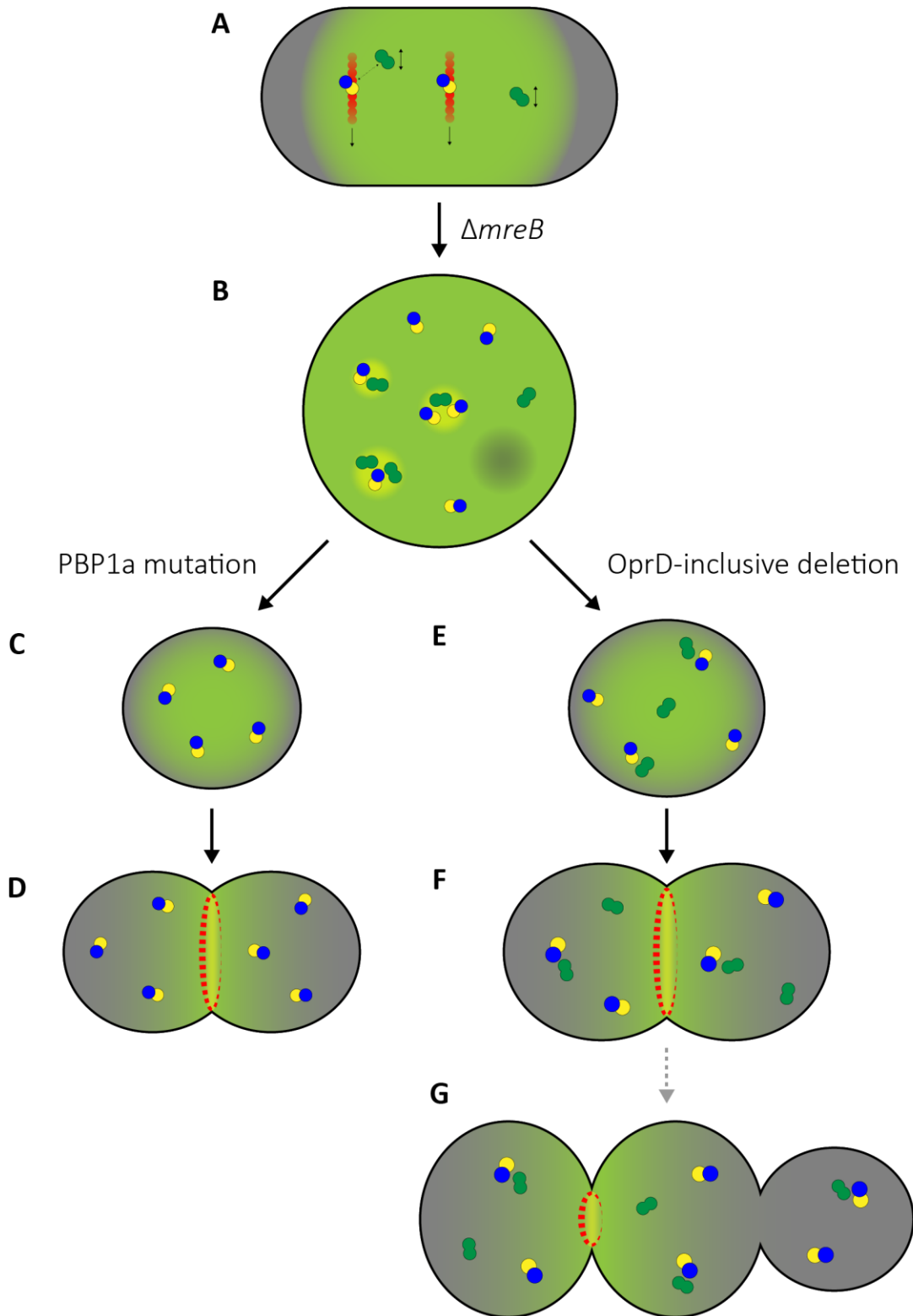
Figure 77 Model for the adaptation of *P. fluorescens* SBW25 to a spherical cell shape. Description on following page.

A) Rod-shaped WT cells are formed by the directed insertion of new PG to the existing sacculus by the action of the MreB-associated rod complex. In this model, the red filament represents MreB, which forms a complex with Rod proteins (yellow sphere) and a Class B PBP (blue sphere). Areas of the cell with active PG growth is shown in green, whereas areas with little or no PG synthesis are shown in grey. The rod complex can form a transient synergistic interaction with PBP1a (green spheres) or can act independently. Similarly, PBP1a can act independent of the Rod complex, filling gaps in the PG mesh with new material. B) Upon the deletion of MreB, the directional motion of the Rod complex is lost. Cells grow as spheres and enlarge. Both the rod complex and the PBP1a diffuse throughout the cell. Both proteins continue to perform transglycosylation and transpeptidation reactions which keeps growing the cell. PBP1a is recruited into areas where the rod complex continues to break and build the PG mesh, forming hotspots of activity. Some areas experience a temporary halt in PG growth, appearing as dark spots. C) The mutation in the transpeptidase domain of PBP1a is assumed to inactivate PBP1a, thereby reducing the amount of peripheral growth and preventing the formation of activity hotspots. D) This slows the growth of the cell, allowing the formation of Z-rings which allow cell division to occur. E) Alternatively, the OprD-inclusive deletion is proposed to modify the dynamics of the Min system, slowing the oscillation of Min proteins, allowing septum formation to occur (F). G) Demonstrates a filamenting phenotype that could form as a result of inaccurate Min oscillation, as seen in the OprD-inclusive deletion reconstructions in both the WT and Δ*mreB* backgrounds.

This chapter presents an updated perspective on how a rod-shaped organism like *P. fluorescens* SBW25 can adapt to a new spherical cell shape. By combining the "Break before Make" model of PG cell wall synthesis by Zhao *et al.* (2017) with data obtained in this thesis, I have developed a model that explains how the uncoordinated synthesis and construction of the PG cell wall could be causing cell division defects as well as the uncontrolled growth of the Δ*mreB* strain. This model explains how the inactivation of PBP1a stops uncoordinated growth, thereby allowing the cell division machinery to take over and direct cell growth, which is a growth strategy employed by many extant spherical bacteria. This model also presents a possible scenario where modifications to the min system could be beneficial, as it enhances the Δ*mreB* strain's ability to form complete septa at appropriate locations within its cells, thereby promoting cell division and improving overall growth. Finally, this model improves our current understanding of cell shape formation by adding a novel evolutionary context to what was previously a purely mechanistic and molecular framework of bacterial growth.

Chapter 6

Concluding remarks

6.1.   Background

Cell shape is an important bacterial characteristic. It can have a direct impact on a cell's ability to acquire nutrients (Koch, 1996; Young, 2007), swim (Maki *et al.*, 2000; Montecucco and Rappuoli, 2001; Mitchell, 2002), and evade predation (Yang, Blair and Salama, 2016). It is currently believed that all bacteria evolved from a rod-shaped ancestor which gave rise to the multitude of cell shapes seen today (Siefert and Fox, 1998; Errington, 2013). Phylogenetic analysis shows that the deepest branches of the bacterial evolutionary tree are exclusively composed of rod-shaped or filamentous species, from which the spherical cell shape evolved (Siefert and Fox, 1998).

Cell shape is determined by the organisation of the PG cell wall (Zhao *et al.*, 2017). Most bacteria possess a strong but flexible PG cell wall that provides protection and structure (Errington, 2017). Construction of the PG cell wall involves numerous components such as Mur proteins that synthesise PG precursors, transporters that translocate precursors from the cytoplasm to the existing cell wall, and PBPs which modify and assemble the PG cell wall (Lovering, Safadi and Strynadka, 2012; Cho *et al.*, 2016). PG construction is also influenced by bacterial cytoskeletal elements which are responsible for the spatio-temporal organisation of the cell wall (Govindarajan and Amster-Choder, 2016). MreB is recognised as the major cytoskeletal element responsible for maintaining the rod shape in bacteria (Jones, Carballido-López and Errington, 2001). MreB is present in most rod-shaped species, where it coordinates the spatial activity of proteins that make and maintain cell shape (Cho *et al.*, 2016). The loss of MreB is not viable under normal growth conditions in model bacteria such as *B. subtilis* (Kawai, Daniel and Errington, 2009), *E. coli* (Turner *et al.*, 2013), *C. crescentus* (Figge, Divakaruni and Gober, 2004), and *P. aeruginosa* (Robertson *et al.*, 2007). MreB-loss leads to cell shape defects and ultimately, cell death.

The evolutionary strategies that bacteria used to evolve from being rod-shaped to spherical is not known. However, it is apparent that this transition involves the loss of MreB as an early first step. In 2002, Spiers *et al.* discovered that the disruption of *mreB* in *P. fluorescens* SBW25 produced spherical cells that remain viable in standard LB under normal growth conditions. A subsequent deletion of *mreB* in *P. fluorescens* SBW25 was done by Dr. Monica Gerth to produce a viable Δ*mreB* strain. This provided the framework for an evolution experiment where Δ*mreB* was separated into 10 distinct lines and evolved for ~1,000 generations. I continued the investigation by using this body of work to elucidate possible strategies that a formerly rod-shape organism can use to adapt to a new spherical cell shape.

6.2. Findings

The Δ*mreB* strain produced characteristic defects associated with MreB loss. The cells of Δ*mreB* *were* misshapen, had poor growth, and were very susceptible to mechanical stress. Single Δ*mreB* cells were nearly perfectly spherical and were up to 10x larger in size than WT cells. Growth and fitness assays showed that Δ*mreB* has a much longer lag time and generation time, and lower relative fitness compared to WT. I found that when Δ*mreB* cells are harvested following a standard centrifugation step, up to 50% of cells would die (Figure 17), indicating that Δ*mreB* cells are fragile and are more susceptible to mechanical damage. The Δ*mreB* strain also exhibited defects in cell division. Microscopic analysis revealed the presence of incomplete septa (Figure 20) and increased chromosome copy numbers (Figure 22 & Figure 25) in single, non-dividing cells. This defect in cell division is likely contributing to the slow growth of the Δ*mreB* strain.

The composition of the PG cell wall is altered in Δ*mreB*. Analysis of purified PG material via UPLC shows that the cell wall of Δ*mreB* has much fewer monomers and more cross-linking compared to WT (Figure 32). This suggests that the PG of Δ*mreB* has adopted a more inflexible structure which may be responsible for its increased susceptibility to physical stress. In addition, the glycan chains of Δ*mreB* are much shorter than the glycan chains of WT (Figure 32), which may be a result of the decreased TG activity

of PBPs caused by MreB-loss. Looking at PG assembly patterns, I found that cell wall activity is greatly disordered in Δ*mreB* (Figure 62 & Figure 63), indicating a loss of spatio-temporal coordination of PBP activity.

The growth of Δ*mreB* is enhanced by supplemental Mg^2. When Δ*mreB* is grown with supplemental Mg^{2+}, growth is improved albeit not completely restored (Figure 26). The exact mechanism(s) behind this is not known, but previous studies suggest that supplemental Mg^{2+} is boosting cell wall integrity (Asbell and Eagon, 1966; Rayman and MacLeod, 1975; Nakamura *et al.*, 1997) and aiding cell division (Varley and Stewart, 1992; Murray, Popham and Setlow, 1998; Chiu, Chen and Wong, 2008) and PG synthesis (Rayman and MacLeod, 1975; Formstone and Errington, 2005; Shen W. Chiu, Chen and Wong, 2008; Harris and Theriot, 2016b), thereby improving growth and survival. This supports my observation that the loss of MreB negatively impacts the physical structure (integrity) of cells, as well as the spatio-temporal coordination of PG synthesis in *P. fluorescens* SBW25. Furthermore, the ectopic production of MreB in the Δ*mreB* strain restored both the native rod-shape of this organism, as well as improved the growth and fitness of Δ*mreB* back to WT levels. Since DNA analysis of Δ*mreB* did not reveal the presence of any mutation that could be compensating for the loss of MreB, these results therefore show that the defects discussed above are a direct result of the loss the major rod-shape determining protein, MreB.

Following the characterisation of the Δ*mreB* strain, I then studied the ~1,000 generation evolution experiment. I found that as early as 50 generations into the experiment, all of the evolved lines had much higher fitness than Δ*mreB* (Figure 38). This shows that Δ*mreB* is under a strong selection pressure, further highlighting the importance of cell shape in bacteria. At the 1,000-generation timepoint, all of the evolved lines have remained spherical (Figure 35 & Figure 36) and had fitness levels that were comparable to that of WT SBW25 (Figure 37 & Figure 38). This indicates that mutations compensating for the loss of MreB have occurred in all populations, giving us the unique opportunity to identify strategies that rod-shaped bacteria can use to survive the loss of MreB, and evolve into a new spherical organism. I selected three of

the major mutations identified in the evolved lines for further study. Specifically, I studied the amplification of *csrA*, a gene linked to carbon metabolism and gene expression; mutations in PFLU0406, a gene coding for the PBP1a enzyme; and the deletion of a group of 5-genes that includes a gene coding for the outer-membrane protein, OprD.

The amplification of *csrA* did not compensate for the loss of MreB. When reconstructed in the WT background, cells were smaller (Figure 39), growth was slower and fitness slightly lower (Figure 40), showing increased variability. In the Δ*mreB* background, *csrA* amplification produced cells that were larger and more variable in size (Figure 41). Both growth and relative fitness were comparable to and even more variable than the growth and fitness of Δ*mreB* (Figure 42). Previous studies in other bacteria showed that *csrA* amplification negatively regulates gluconeogenesis (Romeo *et al.*, 1993), which may be subjecting the reconstruction mutants to starvation as LB is a carbon-limited medium (Jannière *et al.*, 2007; Sezonov, Joseleau-Petit and D'Ari, 2007). Altered *csrA* expression levels has also been shown to affect glycogen biosynthesis (Baker *et al.*, 2002) by repressing enzymes that are needed for carbohydrate metabolism (Altier *et al.*, 2000). These could possible lead to slowed growth and a decrease in size in the WT background. Similarly, growth becomes slower when *csrA* is amplified in the Δ*mreB* background. However, it is unclear why cell size increases the Δ*mreB* background when *csrA* is amplified. Since *csrA* amplification did not show any compensatory effects in the context of MreB-loss, I did not pursue investigating this mutation further.

Unique missense mutations in PFLU0406, the gene coding for the PBP1a enzyme, were seen in several lines in the evolution experiment. This identifies the modification of PBP1a as a possible strategy for adapting to a spherical cell shape. Mutations were found in 2 of the 3 domains of the protein sequence, namely, the TP domain responsible for PG cross-linking, and the poorly-characterised OB domain (Figure 43 & Figure 44). I investigated the effects of 2 of these mutations in PBP1a, one representing the mutation in the OB domain, and the other representing the mutations in the TP domain. I found that reconstructing

these mutations in both the WT and Δ*mreB* backgrounds leads to a reduction in cell size (Figure 46 &Figure 49). Growth in the WT background is unchanged (Figure 47), whereas growth in the Δ*mreB* background becomes greatly improved (Figure 50). PG analysis shows that these mutations do not alter the cell wall chemistry in the WT background (Figure 51). In contrast, PG composition in the Δ*mreB* background is reverted to WT levels (Figure 56). Using bioinformatics tools, I found that the mutations in the TP domain are likely damaging to the active site of this domain. The effects of the mutation in the OB domain is less clear, but it is possibly affecting the substrate-binding efficiency of PBP1a, particularly in Pseudomonads. Finally, analysis of PG construction patterns in the reconstruction mutants reveal no change in the WT background (Figure 48), but a major improvement in the Δ*mreB* background – activity is no longer random, instead occurring only at or near the middle of the cell or the septum (Figure 68 & Figure 70). Overall, these findings indicate that the deactivation of PBP1a is a vital step towards evolving a spherical cell shape. This is further supported by a phylogenetic analysis showing that spherical bacteria have much lower numbers of PBPs than rod-shaped bacteria (Figure 76).

The third major mutation I analysed was the deletion of a group of 5-genes spanning PFLU4921-4925. These 5 genes were composed of genes coding for 3 hypothetical proteins, a cold-shock protein, and the PFLU4925 gene which codes for the outer-membrane protein, OprD. I focused my analysis on PFLU4925 due to its link to the maintenance of cell wall integrity in *P. aeruginosa* (Pagès, James and Winterhalter, 2008), which was also observed in *P. fluorescens* SBW25. The deletion of PFLU4925 in Δ*mreB* resulted in improved growth and fitness (Figure 58), made cells less susceptible to physical damage, and have smaller cell sizes (Figure 57). This deletion had no impact on growth, fitness, and cell integrity in the WT background (Figure 55), but it made the cells smaller (Figure 54). Most cells with this deletion exhibit a typical division pattern wherein a single cell divides into two cells, but there are also cells in both the WT and Δ*mreB* background that exhibit a snaking or filamentous phenotype that have multiple septa (Figure 54). Analysis of PG composition showed a reduction in the D44/M4 ratio in both the WT and Δ*mreB* backgrounds (Figure 56Figure 59), a reduction of glycan chain length in the WT background, and a slight

143

increase in glycan chain length in the Δ*mreB* background (Figure 59). This demonstrates that the 5-gene deletion causes a modification of PG synthesis activity in *P. fluorescens* SBW25. Remarkably, the PG assembly pattern seen in the Δ*mreB* background is altered by this 5-gene deletion. Instead of appearing as random spots of activity, PG assembly is focused mostly at the division plane (Figure 74). In filamenting cells, PG synthesis activity seems to shift from cell division back to lateral growth thereby leading to the formation of long cells with incomplete septa (Figure 72 & Figure 74). This phenotype suggests that cell division is being disrupted in these cells. A previous study by Skurnik *et al.* (2013) found that the loss of *oprD* in the closely-related *P. aeruginosa* causes and overexpression of *minD*. The MinD protein is a key component of the min system, an important process related to cell division, which determines septum placement in rod-shaped cells. Alterations in the min system cause changes to the spatial regulation of developing septa (Justice, García-Lara and Rothfield, 2000; MacCready and Vecchiarelli, 2018; Wehrens *et al.*, 2018), which could be causing the uneven PG activity seen in the septa of filamenting SBW25 cells. Although the exact mechanism is unknown, it is evident that this 5-gene deletion is a beneficial mutation that allows *P. fluorescens* SBW25 to adapt to the loss of MreB.

Combining the results above with data from the most recent model for cell shape determination (Zhao *et al.,* 2017), I presented a new model that explains how the beneficial mutations identified in this study have allowed the Δ*mreB* strain to improve growth and fitness despite suffering the effects of MreB-loss. This model combines data from various techniques to show that the loss of MreB (and its associated consequences) can be mitigated using one of two strategies. First, the inactivation of PBP1a, a major protein involved in cell elongation, stops peripheral growth, making the cell division machinery the main system responsible for new PG synthesis and assembly, and therefore, growth. This resembles the pattern of cell growth and division of many extant spherical bacteria. Alternatively, the *oprD*-inclusive deletion is proposed to modify the activity of the min system to enhance the ability of the Δ*mreB* strain to properly locate the division plane and form a septum, thereby allowing cell division to occur. This model effectively

synthesises new information from this thesis with the current understanding of how cell shape is made and maintained in bacteria.

6.3.   Final comments

This thesis presents new insights on how spherical bacteria may have evolved from a rod-shaped ancestor. Using the rod-shaped model organism *P. fluorescens* SBW25, I have shown that the loss of MreB leads to the disordered assembly of the PG cell wall (Figure 62), which causes morphological deformities (Figure 20), poor growth and fitness (Figure 16 & Figure 18), as well as cell division defects (Figure 20 & Figure 21). Despite suffering numerous deficiencies, this is the first time that an Δ*mreB* strain has remained viable under normal growth conditions, allowing me to identify natural evolutionary strategies that bacteria can use to adapt to a new spherical cell shape. How the Δ*mreB* strain has remained viable is unknown. There were no obvious compensatory mutations found in the ancestral Δ*mreB* strain, so it would be interesting to learn how this organism is able to survive this deletion when many other bacteria could not.

Using experimental evolution, I was able to show that a robust spherical mutant can be evolved within a relatively short period spanning ~1,000 bacterial generations (Figure 38). I have also identified two strategies that bacteria use to adapt to a new spherical cell shape. The first strategy involves the possible inactivation of PBP1a, the major enzyme responsible for cell elongation in *P. fluorescens* SBW25. Together with the observation that extant spherical bacteria generally have fewer PBPs than their closely related rod-shaped counterparts (Figure 76), the multiple occurrences of mutations in PBP1a observed in the evolution experiment (Table 5) strongly identify PBP-loss as a natural evolutionary strategy for adapting to a spherical cell shape. Although most of the PBP1a mutations seen in this study are predicted to cause a loss of function, this has not yet been shown experimentally. In the future, the deletion or direct inactivation of PBP1a in *the* Δ*mreB* strain would be beneficial as this would provide direct evidence supporting PBP-loss as an adaptive strategy for evolving a spherical cell shape. The second adaptive

evolutionary strategy identified in the evolution experiment is the possible modification of the min system brought about by the deletion of *oprD*. At this stage, this is link is likely, as supported by literature (Justice, García-Lara and Rothfield, 2000; Skurnik *et al.*, 2013; MacCready and Vecchiarelli, 2018; Wehrens *et al.*, 2018), but inconclusive. This can be investigated further by specifically deleting *oprD* in the Δ*mreB* strain. This would demonstrate if *oprD*-loss is indeed an adaptive mutation. Furthermore, the potential effect of *oprD*-loss on min system dynamics can be investigated by studying the expression levels of the min proteins, and by tracing min oscillation patterns and Z-ring formation via fluorescent labelling and single-cell microscopy. These experiments would provide invaluable evidence that would better explain of how the mutations seen in the evolution experiment are helping the Δ*mreB* strain recover growth and fitness and adapt to its new spherical cell shape.

Clearly, cell shape is an important aspect of bacterial biology. It affects all major processes from growth and nutrient acquisition to chromosome segregation and cell division. Despite this, we have very limited knowledge of how spherical bacteria came to be. The model I have presented as the final part of my discussion effectively combines our current understanding of how cell shape is made and maintained in bacteria, with the new discoveries made in this study. I have shown that by modifying spatio-temporal mechanisms responsible for PG cell wall synthesis and cell division, bacteria are able to overcome gross defects associated with MreB-loss and evolve to become healthy spherical organisms. Therefore, this thesis adds important new information that advances our understanding of how spherical bacteria may have evolved from a rod-shaped ancestor.

Bibliography

Adams, D. W. and Errington, J. (2009) 'Bacterial cell division: assembly, maintenance and disassembly of the Z ring.', *Nature reviews. Microbiology*, 7(9), pp. 642–53. doi: 10.1038/nrmicro2198.

Adzhubei, I. A. *et al.* (2010) 'A method and server for predicting damaging missense mutations', *Nature Methods*, pp. 248–249. doi: 10.1038/nmeth0410-248.

Akiyama, Y. (2009) 'Quality control of cytoplasmic membrane proteins in escherichia coli', *Journal of Biochemistry*, 146(4), pp. 449–454. doi: 10.1093/jb/mvp071.

Altier, C. *et al.* (2000) 'Characterization of two novel regulatory genes affecting Salmonella invasion gene expression.', *Molecular microbiology*, 35(3), pp. 635–646. doi: 10.1046/j.1365-2958.2000.01734.x.

Alvarez, L. *et al.* (2016) 'Ultra-Sensitive, High-Resolution Liquid Chromatography Methods for the High-Throughput Quantitative Analysis of Bacterial Cell Wall Chemistry and Structure', in *Bacterial Cell Wall Homeostasis - Methods and Protocols*. doi: 10.1007/978-1-4939-3676-2.

Alyahya, S. A. *et al.* (2009) 'RodZ, a component of the bacterial core morphogenic apparatus', *Proceedings of the National Academy of Sciences*. doi: 10.1073/pnas.0810794106.

Anderson, D. E., Gueiros-Filho, F. J. and Erickson, H. P. (2004) 'Assembly dynamics of FtsZ rings in Bacillus subtilis and Escherichia coli and effects of FtsZ-regulating proteins', *Journal of Bacteriology*, 186(17), pp. 5775–5781. doi: 10.1128/JB.186.17.5775-5781.2004.

Angelastro, P. S., Sliusarenko, O. and Jacobs-Wagner, C. (2010) 'Polar localization of the CckA histidine kinase and cell cycle periodicity of the essential master regulator CtrA in Caulobacter crescentus', *Journal of Bacteriology*, 192(2), pp. 539–552. doi: 10.1128/JB.00985-09.

Arbeloa, A. *et al.* (2004) 'Role of Class A Penicillin-Binding Proteins in PBP5-Mediated β-Lactam Resistance in Enterococcus faecalis', *Journal of Bacteriology*. doi: 10.1128/JB.186.5.1221-1228.2004.

Asbell, M. a and Eagon, R. G. (1966) 'Role of Multivalent Cations in the Organization, Structure, and Assembly of the Cell Wall of Pseudomonas aeruginosa.', *Journal of bacteriology*, 92(2), pp. 380–7.

Ashkenazy, H. *et al.* (2016) 'ConSurf 2016: an improved methodology to estimate and visualize evolutionary conservation in macromolecules', *Nucleic acids research*, 44(W1), pp. W344–W350. doi: 10.1093/nar/gkw408.

Bailey, M. J. *et al.* (1995) 'Site directed chromosomal marking of a fluorescent pseudomonad isolated from the phytosphere of sugar beet; stability and potential for marker gene transfer.', *Molecular Ecology*, 4(6), pp. 755–764. doi: 10.1111/j.1365-294X.1995.tb00276.x.

Baker, C. S. *et al.* (2002) 'CsrA regulates glycogen biosynthesis by preventing translation of glgC in Escherichia coli', *Molecular Microbiology*, 44(6), pp. 1599–1610. doi: 10.1046/j.1365-2958.2002.02982.x.

Banzhaf, M. *et al.* (2012) 'Cooperativity of peptidoglycan synthases active in bacterial cell elongation', *Molecular Microbiology*, 85(1), pp. 179–194. doi: 10.1111/j.1365-2958.2012.08103.x.

Bao, Y. *et al.* (1991) 'An improved Tn7-based system for the single-copy insertion of cloned genes into chromosomes of gram-negative bacteria.', *Gene*, 109(1), pp. 167–168. doi: 10.1016/0378-1119(91)90604-A.

Barrick, J. E. and Lenski, R. E. (2013) 'Genome dynamics during experimental evolution.', *Nature reviews. Genetics*, 14(12), pp. 827–39. doi: 10.1038/nrg3564.

Bean, G. J. *et al.* (2009) 'A22 disrupts the bacterial actin cytoskeleton by directly binding and inducing a low-affinity state in MreB', *Biochemistry*, 48(22), pp. 4852–4857. doi: 10.1021/bi900014d.

Beaumont, H. J. E. *et al.* (2009) 'Experimental evolution of bet hedging.', *Nature*, 462(7269), pp. 90–3. doi: 10.1038/nature08504.

Bendezú, F. O. *et al.* (2009) 'RodZ (YfgA) is required for proper assembly of the MreB actin cytoskeleton and cell shape in E. coli', *EMBO Journal*. doi: 10.1038/emboj.2008.264.

Bennet, M. *et al.* (2015) 'Biologically controlled synthesis and assembly of magnetite nanoparticles.', *Faraday discussions*, 181, pp. 71–83. doi: 10.1039/c4fd00240g.

Billings, G. *et al.* (2014) 'De novo morphogenesis in L-forms via geometric control of cell growth', *Molecular Microbiology*, 93(5), pp. 883–896. doi: 10.1111/mmi.12703.De.

Bisson-Filho, A. W. *et al.* (2017) 'Treadmilling by FtsZ filaments drives peptidoglycan synthesis and bacterial cell division', *Science*. doi: 10.1126/science.aak9973.

Den Blaauwen, T. *et al.* (2008) 'Morphogenesis of rod-shaped sacculi', *FEMS Microbiology Reviews*, pp. 321–344. doi: 10.1111/j.1574-6976.2007.00090.x.

de Boer, P. a J. (2010) 'Advances in understanding E. coli cell fission.', *Current opinion in microbiology*. Elsevier Ltd, 13(6), pp. 730–7. doi: 10.1016/j.mib.2010.09.015.

Born, P., Breukink, E. and Vollmer, W. (2006) 'In vitro synthesis of cross-linked murein and its attachment to sacculi by PBP1A from Escherichia coli', *Journal of Biological Chemistry*. doi: 10.1074/jbc.M604083200.

Boulbitch, a, Quinn, B. and Pink, D. (2000) 'Elasticity of the rod-shaped gram-negative eubacteria.', *Physical review letters*, 85(24), pp. 5246–9.

Cabeen, M. T. and Jacobs-Wagner, C. (2005) 'Bacterial cell shape.', *Nature reviews. Microbiology*, 3(8), pp. 601–10. doi: 10.1038/nrmicro1205.

Cabeen, M. T. and Jacobs-Wagner, C. (2010) 'The bacterial cytoskeleton', *Annual Review of Genetics*, (44), pp. 365–392. doi: 10.1016/j.ceb.2007.12.006.

Cabeen, M. T. and Jacobs-Wagner, C. (2010) 'The Bacterial Cytoskeleton (2010)', *Annual Review of Genetics*, 44, pp. 365–392. doi: 10.1146/annurev-genet-102108-134845.

Cambridge, J. *et al.* (2014) 'A replication-inhibited unsegregated nucleoid at mid-cell blocks Z-ring formation and cell division independently of SOS and the SlmA nucleoid occlusion protein in Escherichia coli.', *Journal of bacteriology*, 196(1), pp. 36–49. doi: 10.1128/JB.01230-12.

Carballido-Lopez, R. (2012) 'The actin-like MreB proteins in Bacillus subtilis a new turn', *Frontiers in Bioscience*. doi: 10.2741/s354.

Carballido-López, R. (2006) 'The bacterial actin-like cytoskeleton.', *Microbiology and molecular biology reviews : MMBR*, 70(4), pp. 888–909. doi: 10.1128/MMBR.00014-06.

Carballido-López, R. and Errington, J. (2003) 'The bacterial cytoskeleton: in vivo dynamics of the actin-like protein Mbl of Bacillus subtilis.', *Developmental cell*, 4(1), pp. 19–28.

Casey, K. *et al.* (2008) 'Cell shape and cell-wall organization in Gram-negative bacteria', *Proc Natl Acad Sci U S A*, 105(49), pp. 19282–7. doi: 10.1073/pnas.0805309105.

Cava, F. *et al.* (2011) 'Distinct pathways for modification of the bacterial cell wall by non-canonical D-amino acids', *EMBO Journal*. doi: 10.1038/emboj.2011.246.

Cava, F. *et al.* (2013) 'Modes of cell wall growth differentiation in rod-shaped bacteria', *Current Opinion in Microbiology*. Elsevier Ltd, 16(6), pp. 731–737. doi: 10.1016/j.mib.2013.09.004.

Cava, F. and Pedro, M. A. De (2014) 'Peptidoglycan plasticity in bacteria : emerging variability of the murein sacculus and their associated biological functions', *Current Opinion in Microbiology*. Elsevier Ltd, 18, pp. 46–53. doi: 10.1016/j.mib.2014.01.004.

Chiu, S. W., Chen, S. Y. and Wong, H. C. (2008) 'Dynamic localization of MreB in Vibrio parahaemolyticus and in the ectopic host bacterium Escherichia coli', *Applied and Environmental Microbiology*, 74(21), pp. 6739–6745. doi: 10.1128/AEM.01021-08.

Chiu, S. W., Chen, S. Y. and Wong, H. C. (2008) 'Localization and expression of MreB in Vibrio parahaemolyticus under different stresses', *Applied and Environmental Microbiology*, 74(22), pp. 7016–7022. doi: 10.1128/AEM.01020-08.

Cho, H. *et al.* (2016) 'Bacterial cell wall biogenesis is mediated by SEDS and PBP polymerase families functioning semi-Autonomously', *Nature Microbiology*, 1(10), pp. 1–8. doi: 10.1038/nmicrobiol.2016.172.

Choi, K. *et al.* (2005) 'A Tn 7 -based broad-range bacterial cloning and expression system', 2(6), pp. 443–448. doi: 10.1038/NMETH765.

Choi, Y. and Chan, A. P. (2015) 'PROVEAN web server: A tool to predict the functional effect of amino acid substitutions and indels', *Bioinformatics*. doi: 10.1093/bioinformatics/btv195.

Claessen, D. *et al.* (2008) 'Control of the cell elongation-division cycle by shuttling of PBP1 protein in Bacillus subtilis', *Molecular Microbiology*, 68(4), pp. 1029–1046. doi: 10.1111/j.1365-2958.2008.06210.x.

Contreras-martel, C. *et al.* (2006) 'Crystal Structure of Penicillin-binding Protein 1a (PBP1a) Reveals a Mutational Hotspot Implicated in b -Lactam Resistance in Streptococcus pneumoniae', pp. 684–696. doi: 10.1016/j.jmb.2005.10.030.

Cooper, V. S. (2014) 'The origins of specialization: insights from bacteria held 25 years in captivity.', *PLoS biology*, 12(2), p. e1001790. doi: 10.1371/journal.pbio.1001790.

Corbin, B. D., Yu, X. C. and Margolin, W. (2002) 'Exploring intracellular space: Function of the Min system in round-shaped Escherichia coli', *EMBO Journal*, 21(8), pp. 1998–2008. doi: 10.1093/emboj/21.8.1998.

Daniel, R. a and Errington, J. (2003) 'Control of cell morphogenesis in bacteria: two distinct ways to make a rod-shaped cell.', *Cell*, 113(6), pp. 767–76. doi: 10.1016/s0092-8674(03)00421-5.

Dazzo, F. B. *et al.* (2013) 'In situ ecophysiology of microbial biofilm communities analyzed by CMEIAS computer-assisted microscopy at single-cell resolution', *Diversity*. doi: 10.3390/d5030426.

Defeu Soufo, H. J. and Graumann, P. L. (2004) 'Dynamic movement of actin-like proteins within bacterial cells', *EMBO Reports*, 5(8), pp. 789–794. doi: 10.1038/sj.embor.7400209.

Denome, S. A. *et al.* (1999) 'Escherichia coli mutants lacking all possible combinations of eight penicillin binding proteins: Viability, characteristics, and implications for peptidoglycan synthesis', *Journal of Bacteriology*, 181(13), pp. 3981–3993.

Desmarais, S. M. *et al.* (2013) 'Peptidoglycan at its peaks: How chromatographic analyses can reveal bacterial cell wall structure and assembly', *Molecular Microbiology*, pp. 1–13. doi: 10.1111/mmi.12266.

Desmarais, S. M. *et al.* (2015) 'High-throughput, highly sensitive analyses of bacterial morphogenesis using ultra performance liquid cahromatography', *Journal of Biological Chemistry*, 290(52), pp. 31090–31100. doi: 10.1074/jbc.M115.661660.

Ditta, G. *et al.* (1980) 'Broad host range DNA cloning system for gram-negative bacteria: construction of a gene bank of Rhizobium meliloti.', *Proceedings of the National Academy of Sciences*. doi: 10.1073/pnas.77.12.7347.

Domínguez-Escobar, J. *et al.* (2011) 'Processive movement of MreB-associated cell wall biosynthetic complexes in bacteria.', *Science*, 333(6039), pp. 225–8. doi: 10.1126/science.1203466.

Dufresne, K. and Paradis-Bleau, C. (2015) 'Biology and assembly of the bacterial envelope', in *Advances in Experimental Medicine and Biology*, pp. 41–76. doi: 10.1007/978-3-319-23603-2_3.

Emami, K. *et al.* (2017) 'RodA as the missing glycosyltransferase in Bacillus subtilis and antibiotic discovery for the peptidoglycan polymerase pathway', *Nature Microbiology*. doi: 10.1038/nmicrobiol.2016.253.

van den Ent, F. *et al.* (2014) 'Bacterial actin MreB forms antiparallel double filaments', *eLife*, 2014(3), pp. 1–22. doi: 10.7554/eLife.02634.

van den Ent, F., Amos, L. a and Löwe, J. (2001) 'Prokaryotic origin of the actin cytoskeleton.', *Nature*, 413(6851), pp. 39–44. doi: 10.1038/35092500.

Erickson, H. P., Anderson, D. E. and Osawa, M. (2010) 'FtsZ in Bacterial Cytokinesis: Cytoskeleton and Force Generator All in One', *Microbiology and Molecular Biology Reviews*, 74(4), pp. 504–528. doi: 10.1128/MMBR.00021-10.

Errington, J. (2013) 'L-form bacteria, cell walls and the origins of life', *Open Biology*, 3(1), pp. 120143–120143. doi: 10.1098/rsob.120143.

Errington, J. (2015) 'Bacterial morphogenesis and the enigmatic MreB helix', *Nature Reviews Microbiology*, 13(4), pp. 241–248. doi: 10.1038/nrmicro3398.

Errington, J. *et al.* (2016) 'L-form bacteria, chronic diseases and the origins of life', *Philosophical Transactions of the Royal Society B: Biological Sciences*, 371(1707), p. 20150494. doi: 10.1098/rstb.2015.0494.

Errington, J. (2017) 'Cell wall-deficient, L-form bacteria in the 21st century: a personal perspective', *Biochemical Society Transactions*, 45(2), pp. 287–295. doi: 10.1042/BST20160435.

Escobar-Paramo, P., Gougat-Barbera, C. and Hochberg, M. E. (2012) 'Evolutionary dynamics of separate and combined exposure of Pseudomonas fluorescens SBW25 to antibiotics and bacteriophage', *Evolutionary Applications*, 5(6), pp. 583–592. doi: 10.1111/j.1752-4571.2012.00248.x.

Espaillat, A. *et al.* (2016) 'Chemometric Analysis of Bacterial Peptidoglycan Reveals Atypical Modifications That Empower the Cell Wall against Predatory Enzymes and Fly Innate Immunity', *Journal of the American Chemical Society*, 138(29), pp. 9193–9204. doi: 10.1021/jacs.6b04430.

Eswara, P. J. and Ramamurthi, K. S. (2017) 'Bacterial Cell Division: Nonmodels Poised to Take the Spotlight', *Annual Review of Microbiology*. doi: 10.1146/annurev-micro-102215-095657.

Feldner, J., Bredt, W. and Kahane, I. (1983) 'Influence of cell shape and surface charge on attachment of Mucoplasma pneumoniae to glass surfaces', *Journal of Bacteriology*.

Fenton, A. K. and Gerdes, K. (2013) 'Direct interaction of FtsZ and MreB is required for septum synthesis and cell division in Escherichia coli', *The EMBO Journal*, 32(13), pp. 1953–1965. doi: 10.1038/emboj.2013.129.

Fettes, P. S. *et al.* (2001) 'Overexpresssion of a Legionella pneumophila homologue of the E. coli regulator csrA affects cell size, flagellation, and pigmentation.', *International journal of medical microbiology : IJMM*, 291(5), pp. 353–60. doi: 10.1078/1438-4221-00141.

Figge, R. M., Divakaruni, A. V and Gober, J. W. (2004) 'MreB , the cell shape-determining bacterial actin homologue , co-ordinates cell wall morphogenesis in Caulobacter crescentus', 51, pp. 1321–1332. doi: 10.1046/j.1365-2958.2003.03936.x.

Formstone, A. and Errington, J. (2005) 'A magnesium-dependent mreB null mutant: implications for the role of mreB in Bacillus subtilis.', *Molecular microbiology*, 55(6), pp. 1646–57. doi: 10.1111/j.1365-2958.2005.04506.x.

Freire, P., Moreira, R. N. and Arraiano, C. M. (2009) 'BolA inhibits cell elongation and regulates MreB expression levels.', *Journal of molecular biology*. Elsevier B.V., 385(5), pp. 1345–51. doi: 10.1016/j.jmb.2008.12.026.

Fuhrman, J. A. and Noble, R. T. (1995) 'Viruses and protists cause similar bacterial mortality in coastal seawater', *Limnology and Oceanography*. doi: 10.4319/lo.1995.40.7.1236.

Fung, D. K. C. *et al.* (2016) 'Signaling by the heavy-metal sensor CusS involves rearranged helical interactions in specific transmembrane regions', *Molecular Microbiology*, 100(5), pp. 774–787. doi: 10.1111/mmi.13348.

Gitai, Z. *et al.* (2005) 'MreB actin-mediated segregation of a specific region of a bacterial chromosome.', *Cell*, 120(3), pp. 329–41. doi: 10.1016/j.cell.2005.01.007.

Gitai, Z. (2005) 'The new bacterial cell biology: moving parts and subcellular architecture.', *Cell*, 120(5), pp. 577–86. doi: 10.1016/j.cell.2005.02.026.

Gitai, Z., Dye, N. and Shapiro, L. (2004) 'An actin-like gene can determine cell polarity in bacteria.', *Proceedings of the National Academy of Sciences of the United States of America*, 101(23), pp. 8643–8. doi: 10.1073/pnas.0402638101.

Goffin, C. and Ghuysen, J. M. (1998) 'Multimodular penicillin-binding proteins: an enigmatic family of orthologs and paralogs', *Microbiol Mol Biol Rev*.

Govindarajan, S. and Amster-Choder, O. (2016) 'Where are things inside a bacterial cell?', *Current Opinion in Microbiology*, pp. 83–90. doi: 10.1016/j.mib.2016.07.003.

Gram, H. C. (1884) 'Gram staining', *Fortschritte der Medicin*, 2, pp. 185–189. doi: 10.1002/0471142735.ima03os23.

Granger, D. *et al.* (2006) 'Molecular characteristics of pbp1a and pbp2b in clinical Streptococcus pneumoniae isolates in Quebec, Canada', *Journal of Antimicrobial Chemotherapy*, 57(1), pp. 61–70. doi: 10.1093/jac/dki401.

Hammerschmidt, K. *et al.* (2014) 'Life cycles, fitness decoupling and the evolution of multicellularity', *Nature*, 515(7525), pp. 75–79. doi: 10.1038/nature13884.

Han, S. *et al.* (2011) 'Distinctive Attributes of β-Lactam Target Proteins in Acinetobacter baumannii Relevant to Development of New Antibiotics', pp. 20536–20545.

Hancock, R. E. W. and Brinkman, F. S. L. (2002) 'Function of *Pseudomonas* Porins in Uptake and Efflux', *Annual Review of Microbiology*. doi: 10.1146/annurev.micro.56.012302.160310.

Harris, L. K. and Theriot, J. A. (2016a) 'Relative rates of surface and volume synthesis set bacterial cell size', *Cell*, 165(6), pp. 1479–1492. doi: 10.1016/j.cell.2016.05.045.

Harris, L. K. and Theriot, J. A. (2016b) 'Relative rates of surface and volume synthesis set bacterial cell size', *Cell*. Elsevier Inc., 165(6), pp. 1479–1492. doi: 10.1016/j.cell.2016.05.045.

Harry, E., Monahan, L. and Thompson, L. (2006) 'Bacterial cell division: the mechanism and its precison.', *International review of cytology*, 253(06), pp. 27–94. doi: 10.1016/S0074-7696(06)53002-5.

Hayhurst, E. J. *et al.* (2008) 'Cell wall peptidoglycan architecture in Bacillus subtilis', *Proceedings of the National Academy of Sciences*, 105(38), pp. 14603–14608. doi: 10.1073/pnas.0804138105.

Henderson, J. C. *et al.* (2016) 'The Power of Asymmetry: Architecture and Assembly of the Gram-Negative Outer Membrane Lipid Bilayer', *Annual Review of Microbiology*, 70(1), pp. 255–278. doi: 10.1146/annurev-micro-102215-095308.

Van der Henst, C. *et al.* (2012) 'The histidine kinase PdhS controls cell cycle progression of the pathogenic alphaproteobacterium Brucella abortus', *Journal of Bacteriology*, 194(19), pp. 5305–5314. doi: 10.1128/JB.00699-12.

Ho, W. C. and Zhang, J. (2018) 'Evolutionary adaptations to new environments generally reverse plastic phenotypic changes', *Nature Communications*. doi: 10.1038/s41467-017-02724-5.

Holt, J. G. *et al.* (eds) (1994) *Bergey's Manual of Determinative Bacteriology, 9th Edition*. Baltimore, Md: Williams & Wilkins.

Holtje, J. V (1998) 'Growth of the stress-bearing and shape-maintaining murein sacculus of Escherichia coli.', *Microbiology and molecular biology reviews : MMBR*, 62(1), pp. 181–203.

Hong, H.-J. and Walker, J. M. (eds) (2016) *Bacterial Cell Wall Homeostasis - Methods and Protocols*. New York, NY: Springer Science+Business Media. doi: 10.1007/978-1-4939-3676-2.

Horton, R. M. *et al.* (2013) 'Gene splicing by overlap extension: Tailor-made genes using the polymerase chain reaction', *BioTechniques*. doi: 10.2144/000114017.

Hoskins, J. A. *et al.* (1999) 'Gene disruption studies of penicillin-binding proteins 1a, 1b, and 2a in Streptococcus pneumoniae', *Journal of Bacteriology*.

Hsin, J. *et al.* (2008) 'Using VMD: An introductory tutorial', *Current Protocols in Bioinformatics*. doi: 10.1002/0471250953.bi0507s24.

Hsu, Y.-P. *et al.* (2017) 'Full color palette of fluorescent d-amino acids for in situ labeling of bacterial cell walls', *Chem. Sci.* Royal Society of Chemistry, 8, pp. 6313–6321. doi: 10.1039/C7SC01800B.

Hu, Z., Gogol, E. P. and Lutkenhaus, J. (2002) 'Dynamic assembly of MinD on phospholipid vesicles regulated by ATP and MinE', *Proceedings of the National Academy of Sciences*. doi: 10.1073/pnas.102059099.

Huang, K. C. and Wingreen, N. S. (2004) 'Min-protein oscillations in round bacteria.', *Physical biology*, 1(3–4), pp. 229–35. doi: 10.1088/1478-3967/1/4/005.

Humphrey, W., Dalke, A. and Schulten, K. (1996) 'VMD: Visual molecular dynamics', *Journal of Molecular Graphics*. doi: 10.1016/0263-7855(96)00018-5.

Hussain, S. *et al.* (2018) 'MreB filaments align along greatest principal membrane curvature to orient cell wall synthesis', *eLife*, 7, pp. 1–45. doi: 10.7554/eLife.32471.

Hvichia, G. E. *et al.* (2016) 'A novel microfluidic platform for size and deformability based separation and the subsequent molecular characterization of viable circulating tumor cells', *International Journal of Cancer*. doi: 10.1002/ijc.30007.

Ingerson-Mahar, M. and Gitai, Z. (2012) 'A growing family: the expanding universe of the bacterial cytoskeleton', *Federation of European Microbiological Societies*, 36(1), pp. 256–266. doi: 10.1111/j.1574-

6976.2011.00316.x.A.

Ishidate, K. *et al.* (1998) 'Analysis of the length distribution of murein glycan strands in ftsZ and ftsI mutants of E. coli', *FEMS Microbiology Letters*. doi: 10.1016/S0378-1097(98)00421-2.

Iwai, N., Nagai, K. and Wachi, M. (2002) 'Novel S -Benzylisothiourea Compound That Induces Spherical Cells in Escherichia coli Probably by Acting on a Rod-shape-determining Protein(s) Other Than Penicillin-binding Protein 2', *Bioscience, Biotechnology, and Biochemistry*, 66(12), pp. 2658–2662. doi: 10.1271/bbb.66.2658.

Jacobs, C. *et al.* (2003) 'Functions of the CckA histidine kinase in Caulobacter cell cycle control', *Molecular Microbiology*, 47(5), pp. 1279–1290. doi: 10.1046/j.1365-2958.2003.03379.x.

Jannière, L. *et al.* (2007) 'Genetic evidence for a link between glycolysis and DNA replication', *PLoS ONE*, 2(5). doi: 10.1371/journal.pone.0000447.

Jiang, H. *et al.* (2011) 'Mechanical control of bacterial cell shape.', *Biophysical journal*. Biophysical Society, 101(2), pp. 327–35. doi: 10.1016/j.bpj.2011.06.005.

Job, V. *et al.* (2008) 'Common alterations in PBP1a from resistant Streptococcus pneumoniae decrease its reactivity toward β-lactams: Structural insights', *Journal of Biological Chemistry*, 283(8), pp. 4886–4894. doi: 10.1074/jbc.M706181200.

Jones, L. J., Carballido-López, R. and Errington, J. (2001) 'Control of cell shape in bacteria: helical, actin-like filaments in Bacillus subtilis.', *Cell*, 104(6), pp. 913–22.

Jürgens, K. and Matz, C. (2002) 'Predation as a shaping force for the phenotypic and genotypic composition of planktonic bacteria', *Antonie van Leeuwenhoek, International Journal of General and Molecular Microbiology*. doi: 10.1023/A:1020505204959.

Justice, S. S., García-Lara, J. and Rothfield, L. I. (2000) 'Cell division inhibitors SulA and MinC/MinD block septum formation at different steps in the assembly of the Escherichia coli division machinery', *Molecular Microbiology*, 37(2), pp. 410–423. doi: 10.1046/j.1365-2958.2000.02007.x.

Kafri, R. *et al.* (2013) 'Dynamics extracted from fixed cells reveal feedback linking cell growth to cell cycle', *Nature*, 494(7438), pp. 480–483. doi: 10.1038/nature11897.

Karczmarek, A. *et al.* (2007) 'DNA and origin region segregation are not affected by the transition from rod to sphere after inhibition of Escherichia coli MreB by A22', *Molecular Microbiology*, 65(1), pp. 51–63. doi: 10.1111/j.1365-2958.2007.05777.x.

Kawai, Y., Daniel, R. and Errington, J. (2009) 'Regulation of cell wall morphogenesis in Bacillus subtilis by recruitment of PBP1 to the MreB helix.', *Molecular microbiology*, 71(5), pp. 1131–44. doi: 10.1111/j.1365-2958.2009.06601.x.

Kawazura, T. *et al.* (2017) 'Exclusion of assembled MreB by anionic phospholipids at cell poles confers cell polarity for bidirectional growth', *Molecular Microbiology*, 104(3), pp. 472–486. doi: 10.1111/mmi.13639.

Kawecki, T. J. *et al.* (2012) 'Experimental evolution.', *Trends in ecology & evolution*. Elsevier Ltd, 27(10), pp. 547–60. doi: 10.1016/j.tree.2012.06.001.

Koch, a L. (1996) 'What size should a bacterium be? A question of scale.', *Annual review of microbiology*, 50, pp. 317–48. doi: 10.1146/annurev.micro.50.1.317.

Koch, a L. and Woeste, S. (1992) 'Elasticity of the sacculus of Escherichia coli.', *Journal of bacteriology*, 174(14), pp. 4811–9.

Koch, B. and Nybroe, O. (2006) 'Initial characterization of a bolA homologue from Pseudomonas fluorescens indicates different roles for BolA-like proteins in P. fluorescens and Escherichia coli', *FEMS Microbiology Letters*. doi: 10.1111/j.1574-6968.2006.00359.x.

Koebnik, R. and Krämer, L. (1995) 'Membrane assembly of circularly permuted variants of the E. coli outer membrane protein OmpA', *Journal of Molecular Biology*. doi: 10.1006/jmbi.1995.0403.

Köster, S. *et al.* (2015) 'Intermediate filament mechanics in vitro and in the cell: From coiled coils to filaments, fibers and networks', *Current Opinion in Cell Biology*, pp. 82–91. doi: 10.1016/j.ceb.2015.01.001.

Koza, A. *et al.* (2017) 'Adaptive radiation of Pseudomonas fluorescens SBW25 in experimental microcosms provides an understanding of the evolutionary ecology and molecular biology of A-L interface biofilm formation', *FEMS Microbiology Letters*. doi: 10.1093/femsle/fnx109.

Kruse, T. *et al.* (2003) 'Dysfunctional MreB inhibits chromosome segregation in Escherichia coli.', *The EMBO journal*, 22(19), pp. 5283–92. doi: 10.1093/emboj/cdg504.

Kruse, T., Bork-Jensen, J. and Gerdes, K. (2005) 'The morphogenetic MreBCD proteins of Escherichia coli form an essential membrane-bound complex.', *Molecular microbiology*, 55(1), pp. 78–89. doi: 10.1111/j.1365-2958.2004.04367.x.

Kruse, T. and Gerdes, K. (2005) 'Bacterial DNA segregation by the actin-like MreB protein.', *Trends in cell biology*, 15(7), pp. 343–5. doi: 10.1016/j.tcb.2005.05.002.

Ku, C., Lo, W. S. and Kuo, C. H. (2014) 'Molecular evolution of the actin-like MreB protein gene family in wall-less bacteria', *Biochemical and Biophysical Research Communications*. doi: 10.1016/j.bbrc.2014.03.039.

Kumar, S. *et al.* (2018) 'MEGA X: Molecular evolutionary genetics analysis across computing platforms', *Molecular Biology and Evolution*, 35(6), pp. 1547–1549. doi: 10.1093/molbev/msy096.

Kuru, E. *et al.* (2015) 'Synthesis of fluorescent D-amino acids and their use for probing peptidoglycan synthesis and bacterial growth in situ', *Nature Protocols*, 10(1), pp. 33–52. doi: 10.1038/nprot.2014.197.

Lambertsen, L., Sternberg, C. and Molin, S. (2004) 'Mini-Tn7 transposons for site-specific tagging of bacteria with fluorescent proteins', *Environmental Microbiology*, 6, pp. 726–732. doi: 10.1111/j.1462-2920.2004.00605.x.

Lan, G., Wolgemuth, C. W. and Sun, S. X. (2007) 'Z-ring force and cell shape during division in rod-like bacteria', *Proceedings of the National Academy of Sciences*, 104(41), pp. 16110–16115. doi: 10.1073/pnas.0702925104.

Land, A. D. and Winkler, M. E. (2011) 'The requirement for pneumococcal MreC and MreD is relieved by inactivation of the gene encoding PBP1a', *Journal of Bacteriology*. doi: 10.1128/JB.05245-11.

Larsen, R. A. *et al.* (2007) 'Treadmilling of a prokaryotic tubulin-like protein, TubZ, required for plasmid stability in Bacillus thuringiensis', *Genes and Development*, 21(11), pp. 1340–1352. doi: 10.1101/gad.1546107.

Leaver, M. and Errington, J. (2005) 'Roles for MreC and MreD proteins in helical growth of the cylindrical cell wall in Bacillus subtilis', *Molecular Microbiology*, 57(5), pp. 1196–1209. doi: 10.1111/j.1365-2958.2005.04736.x.

Lee, T. K. *et al.* (2016) 'Single-molecule imaging reveals modulation of cell wall synthesis dynamics in live bacterial cells', *Nature Communications*, 7, pp. 1–9. doi: 10.1038/ncomms13170.

Li, H. *et al.* (2012) 'Structure and function of OprD protein in Pseudomonas aeruginosa: from antibiotic resistance to novel therapies.', *International journal of medical microbiology : IJMM*, 302(2), pp. 63–8. doi: 10.1016/j.ijmm.2011.10.001.

Li, Z. *et al.* (2007) 'The structure of FtsZ filaments in vivo suggests a force-generating role in cell division', *EMBO Journal*, 26(22), pp. 4694–4708. doi: 10.1038/sj.emboj.7601895.

Liao, Y. and Rust, M. J. (2018) 'The Min Oscillator Defines Sites of Asymmetric Cell Division in Cyanobacteria during Stress Recovery', *Cell Systems*. Elsevier Inc., 7(5), pp. 1–11. doi: 10.1016/j.cels.2018.10.006.

Liechti, G. *et al.* (2016) 'Pathogenic Chlamydia Lack a Classical Sacculus but Synthesize a Narrow, Mid-cell Peptidoglycan Ring, Regulated by MreB, for Cell Division', *PLoS Pathogens*. doi: 10.1371/journal.ppat.1005590.

Lind, P. a *et al.* (2015) 'Experimental evolution reveals hidden diversity in evolutionary pathways', pp. 1–17. doi: 10.7554/eLife.07074.

Liu, J. *et al.* (2001) 'CMEIAS: A Computer-Aided System for the Image Analysis of Bacterial Morphotypes in Microbial Communities', *Microbial Ecology*, 41(3), pp. 173–194. doi: 10.1007/s002480000004.

Liu, J. *et al.* (2001) 'CMEIAS: A Computer-Aided System for the Image Analysis of Bacterial Morphotypes in Microbial Communities', *Microb Ecol*, 41, pp. 173–194. doi: 10.1007/s002480000004.

Loudon, C. M. *et al.* (2016) 'Experimental evidence that evolution by niche construction affects dissipative ecosystem dynamics', *Evolutionary Ecology*, 30(2), pp. 221–234. doi: 10.1007/s10682-015-9802-7.

Lovering, A. L. *et al.* (2007) 'Structural insight into the transglycosylation step of bacterial cell-wall biosynthesis', *Science*. doi: 10.1126/science.1136611.

Lovering, A. L., Safadi, S. S. and Strynadka, N. C. J. (2012) 'Structural Perspective of Peptidoglycan Biosynthesis and Assembly', *Annual Review of Biochemistry*, 81(1), pp. 451–478. doi: 10.1146/annurev-biochem-061809-112742.

Löwe, J. and Amos, L. A. (2009) 'Evolution of cytomotive filaments: The cytoskeleton from prokaryotes to eukaryotes', *International Journal of Biochemistry and Cell Biology*, pp. 323–329. doi: 10.1016/j.biocel.2008.08.010.

Lupoli, T. J. *et al.* (2011) 'Transpeptidase-mediated incorporation of d-amino acids into bacterial peptidoglycan', *Journal of the American Chemical Society*. doi: 10.1021/ja2040656.

Lutkenhaus, J. (2007) 'Assembly dynamics of the bacterial MinCDE system and spatial regulation of the Z ring.', *Annual review of biochemistry*, 76, pp. 539–62. doi: 10.1146/annurev.biochem.75.103004.142652.

MacCready, J. S. and Vecchiarelli, A. G. (2018) 'In long bacterial cells, the Min system can act off-center', *Molecular Microbiology*. doi: 10.1111/mmi.13995.

Macheboeuf, P. *et al.* (2006) 'Penicillin binding proteins: Key players in bacterial cell cycle and drug resistance processes', *FEMS Microbiology Reviews*. doi: 10.1111/j.1574-6976.2006.00024.x.

Mahan, M. J., Slauch, J. M. and Mekalanos, J. J. (1993) 'Selection of bacterial virulence genes that are specifically induced in host tissues', *Science*. doi: 10.1126/science.8430319.

Maki, N. *et al.* (2000) 'Motility and chemotaxis of filamentous cells of Escherichia coli', *Journal of Bacteriology*, 182(15), pp. 4337–4342. doi: 10.1128/JB.182.15.4337-4342.2000.

Mazza, P. *et al.* (2006) 'MreB of Streptomyces coelicolor is not essential for vegetative growth but is

required for the integrity of aerial hyphae and spores.', *Molecular microbiology*, 60(4), pp. 838–52. doi: 10.1111/j.1365-2958.2006.05134.x.

Mcpherson, D. C. and Popham, D. L. (2003) 'Peptidoglycan Synthesis in the Absence of Class A Penicillin-Binding Proteins in Bacillus subtilis', 185(4), pp. 1423–1431. doi: 10.1128/JB.185.4.1423.

Meeske, A. J. *et al.* (2016) 'SEDS proteins are a widespread family of bacterial cell wall polymerases', *Nature*, 537(7622), pp. 634–638. doi: 10.1038/nature19331.

Mignolet, J., Panis, G. and Viollier, P. H. (2018) 'More than a Tad: spatiotemporal control of Caulobacter pili', *Current Opinion in Microbiology*. doi: 10.1016/j.mib.2017.10.017.

Mitchell, J. G. (2002) 'The energetics and scaling of search strategies in bacteria.', *The American naturalist*, 160(6), pp. 727–740. doi: 10.1086/343874.

Montecucco, C. and Rappuoli, R. (2001) 'Living dangerously: How helicobacter pylori survives in the human stomach', *Nature Reviews Molecular Cell Biology*, pp. 457–466. doi: 10.1038/35073084.

Morgenstein, R. M. *et al.* (2015) 'RodZ links MreB to cell wall synthesis to mediate MreB rotation and robust morphogenesis', *Proceedings of the National Academy of Sciences*. doi: 10.1073/pnas.1509610112.

De Mot, R. and Vanderleyden, J. (1994) 'The C-terminal sequence conservation between OmpA-related outer membrane proteins and MotB suggests a common function in both Gram-positive and Gram-negative bacteria, possibly in the interaction of these domains with peptidoglycan', *Molecular Microbiology*. doi: 10.1111/j.1365-2958.1994.tb01021.x.

Mura, A. *et al.* (2017) 'Roles of the essential protein FtsA in cell growth and division in Streptococcus pneumoniae', *Journal of Bacteriology*. doi: 10.1128/JB.00608-16.

Muraleedharan, S. *et al.* (2018) 'A cell length-dependent transition in MinD-dynamics promotes a switch in division-site placement and preservation of proliferating elongated Vibrio parahaemolyticus swarmer cells', *Molecular Microbiology*. doi: 10.1111/mmi.13996.

Murray, T., Popham, D. L. and Setlow, P. (1998) 'Bacillus subtilis cells lacking penicillin-binding protein 1 require increased levels of divalent cations for growth', *Journal of Bacteriology*, 180(17), pp. 4555–4563.

Nakamura, S. *et al.* (1997) 'The cell surface glycoprotein of Haloarcula japonica TR-1', *Bioscience*, 1(1), pp. 29–35. doi: 10.1271/bbb.56.996.

Naoz, M. *et al.* (2008) 'Protein localization by actin treadmilling and molecular motors regulates stereocilia shape and treadmilling rate', *Biophysical Journal*, 95(12), pp. 5706–5718. doi: 10.1529/biophysj.108.143453.

Ng, P. C. and Henikoff, S. (2003) 'SIFT: Predicting amino acid changes that affect protein function', *Nucleic Acids Research*, 31(13), pp. 3812–3814. doi: 10.1093/nar/gkg509.

Niu, L. and Yu, J. (2008) 'Investigating Intracellular Dynamics of FtsZ Cytoskeleton with Photoactivation Single-Molecule Tracking', *Biophysical Journal*, 95(4), pp. 2009–2016. doi: 10.1529/biophysj.108.128751.

Olshausen, P. V. *et al.* (2013) 'Superresolution imaging of dynamic MreB filaments in B. subtilis - A multiple-motor-driven transport?', *Biophysical Journal*, 105(5), pp. 1171–1181. doi: 10.1016/j.bpj.2013.07.038.

Orr, H. A. (2009) 'Fitness and its role in evolutionary genetics', *Nature Reviews Genetics*. doi: 10.1038/nrg2603.

Outten, F. W. *et al.* (2001) 'The Independent cue and cus Systems Confer Copper Tolerance during Aerobic and Anaerobic Growth in Escherichia coli', *Journal of Biological Chemistry*, 276(33), pp. 30670–30677. doi: 10.1074/jbc.M104122200.

Ozyamak, E., Kollman, J. M. and Komeili, A. (2013) 'Bacterial actins and their diversity', *Biochemistry*, 52(40), pp. 6928–6939. doi: 10.1021/bi4010792.

Pagès, J.-M., James, C. E. and Winterhalter, M. (2008) 'The porin and the permeating antibiotic: a selective diffusion barrier in Gram-negative bacteria.', *Nature reviews. Microbiology*, 6(12), pp. 893–903. doi: 10.1038/nrmicro1994.

de Pedro, M. a. and Cava, F. (2015) 'Structural constraints and dynamics of bacterial cell wall architecture', *Frontiers in Microbiology*, 6(May), pp. 1–10. doi: 10.3389/fmicb.2015.00449.

Pereira, A. R. *et al.* (2016) 'FtsZ-dependent elongation of a coccoid bacterium', *mBio*, 7(5). doi: 10.1128/mBio.00908-16.

Pernthaler, J. (2005) 'Predation on prokaryotes in the water column and its ecological implications', *Nature Reviews Microbiology*. doi: 10.1038/nrmicro1180.

Petek, N. A. and Mullins, R. D. (2014) 'Bacterial actin-like proteins: Purification and characterization of self-assembly properties', *Methods in Enzymology*, 540, pp. 19–34. doi: 10.1016/B978-0-12-397924-7.00002-9.

Pichoff, S. and Lutkenhaus, J. (2007) 'Overview of cell shape: cytoskeletons shape bacterial cells.', *Current opinion in microbiology*, 10(6), pp. 601–5. doi: 10.1016/j.mib.2007.09.005.

Pinho, M. G., Kjos, M. and Veening, J.-W. (2013) 'How to get around mechanisms controlling growth and division of coccoid bacteria.', *Nature reviews. Microbiology*, 11(9), pp. 601–14. doi: 10.1038/nrmicro3088.

Popham, D. L. and Young, K. D. (2003) 'Role of penicillin-binding proteins in bacterial cell morphogenesis', *Current Opinion in Microbiology*, 6(6), pp. 594–599. doi: 10.1016/j.mib.2003.10.002.

Pradel, N. *et al.* (2006) 'Biogenesis of actin-like bacterial cytoskeletal filaments destined for positioning prokaryotic magnetic organelles', *Proceedings of the National Academy of Sciences*, 103(46), pp. 17485–17489. doi: 10.1073/pnas.0603760103.

Rainey, P. B. *et al.* (2017) 'Darwin was right: where now for experimental evolution?', *Current Opinion in Genetics & Development*. Elsevier Ltd, 47, pp. 102–109. doi: 10.1016/j.gde.2017.09.003.

Rainey, P. B. and Bailey, M. J. (1996) 'Physical and genetic map of the Pseudomonas fluorescens SBW25 chromosome.', *Molecular microbiology*, 19(3), pp. 521–33.

Rainey, P. B. and Travisano, M. (1998) 'Adaptive radiation in a heterogeneous environment', *Nature*, 394(6688), pp. 69–72. doi: 10.1038/27900.

Ramsayer, J., Kaltz, O. and Hochberg, M. E. (2013) 'Evolutionary rescue in populations of Pseudomonas fluorescens across an antibiotic gradient', *Evolutionary Applications*, 6(4), pp. 608–616. doi: 10.1111/eva.12046.

Raskin, D. M. and de Boer, P. A. J. (1999) 'Rapid pole-to-pole oscillation of a protein required for directing division to the middle of Escherichia coli', *Proceedings of the National Academy of Sciences*. doi: 10.1073/pnas.96.9.4971.

Rayman, M. K. and MacLeod, R. A. (1975) 'Interaction of Mg2+ with peptidoglycan and its relation to the prevention of lysis of a marine pseudomonad', *Journal of Bacteriology*, 122(2), pp. 650–659.

Reed, P. *et al.* (2011) 'Monofunctional transglycosylases are not essential for Staphylococcus aureus cell wall synthesis', *Journal of Bacteriology*, 193(10), pp. 2549–2556. doi: 10.1128/JB.01474-10.

Reimold, C. *et al.* (2013) 'Motion of variable-length MreB filaments at the bacterial cell membrane influences cell morphology.', *Molecular biology of the cell*, 24(15), pp. 2340–9. doi: 10.1091/mbc.E12-10-0728.

Rice, L. B. *et al.* (2009) 'Role of class A penicillin-binding proteins in the expression of β-lactam resistance in Enterococcus faecium', *Journal of Bacteriology*. doi: 10.1128/JB.01834-08.

Robertson, G. T. *et al.* (2007) 'A novel indole compound that inhibits Pseudomonas aeruginosa growth by targeting MreB is a substrate for MexAB-OprM', *Journal of Bacteriology*, 189(19), pp. 6870–6881. doi: 10.1128/JB.00805-07.

Romeo, T. *et al.* (1993) 'Identification and molecular characterization of csrA, a pleiotropic gene from Escherichia coli that affects glycogen biosynthesis, gluconeogenesis, cell size, and surface properties', *Journal of Bacteriology*, 175(15), pp. 4744–4755. doi: 10.1128/JB.175.15.4744-4755.1993.

Romeo, T. (1998) 'Global regulation by the small RNA-binding protein CsrA and the non- coding RNA molecule CsrB', *Molecular Microbiology*, pp. 1321–1330. doi: 10.1046/j.1365-2958.1998.01021.x.

Roy, A., Kucukural, A. and Zhang, Y. (2010) 'I-TASSER: A unified platform for automated protein structure and function prediction', *Nature Protocols*. doi: 10.1038/nprot.2010.5.

Sabnis, N. a, Yang, H. and Romeo, T. (1995) 'Pleiotropic regulation of central carbohydrate metabolism in Escherichia coli via the gene csrA.', *The Journal of biological chemistry*, 270(49), pp. 29096–104. doi: 10.1074/JBC.270.49.29096.

Salje, J. *et al.* (2011) 'Direct Membrane Binding by Bacterial Actin MreB', *Molecular Cell*, 43(3), pp. 478–487. doi: 10.1016/j.molcel.2011.07.008.

Sauvage, E. *et al.* (2008) 'The penicillin-binding proteins : structure and role in peptidoglycan biosynthesis', 32, pp. 234–258. doi: 10.1111/j.1574-6976.2008.00105.x.

Scanlan, P. D. and Buckling, A. (2012) 'Co-evolution with lytic phage selects for the mucoid phenotype of Pseudomonas fluorescens SBW25', *ISME Journal*, 6(6), pp. 1148–1158. doi: 10.1038/ismej.2011.174.

Scheffers, D. J. and Tol, M. B. (2015) 'LipidII: Just Another Brick in the Wall?', *PLoS Pathog*. doi: 10.1371/journal.ppat.1005213.

Scheffers, D. and Pinho, M. G. (2005) 'Bacterial Cell Wall Synthesis : New Insights from Localization Studies Bacterial Cell Wall Synthesis : New Insights from Localization Studies', 69(4). doi: 10.1128/MMBR.69.4.585.

Schindelin, J. *et al.* (2012) 'Fiji: An open-source platform for biological-image analysis', *Nature Methods*. doi: 10.1038/nmeth.2019.

Schneider, C. A., Rasband, W. S. and Eliceiri, K. W. (2012) 'NIH Image to ImageJ: 25 years of image analysis', *Nature Methods*. doi: 10.1038/nmeth.2089.

Schoenemann, K. M. and Margolin, W. (2017) 'Bacterial Division: FtsZ Treadmills to Build a Beautiful Wall', *Current Biology*, pp. R301–R303. doi: 10.1016/j.cub.2017.03.019.

Sezonov, G., Joseleau-Petit, D. and D'Ari, R. (2007) 'Escherichia coli physiology in Luria-Bertani broth', *Journal of Bacteriology*, 189(23), pp. 8746–8749. doi: 10.1128/JB.01368-07.

Sherr, E. B. and Sherr, B. F. (1994) 'Bacterivory and herbivory: Key roles of phagotrophic protists in pelagic

food webs', *Microbial Ecology*. doi: 10.1007/BF00166812.

Sherr, E. B. and Sherr, B. F. (2002) 'Significance of predation by protists in aquatic microbial food webs', *Antonie van Leeuwenhoek, International Journal of General and Molecular Microbiology*. doi: 10.1023/A:1020591307260.

Shi, H. *et al.* (2017) 'Deep Phenotypic Mapping of Bacterial Cytoskeletal Mutants Reveals Physiological Robustness to Cell Size', *Current Biology*. Elsevier Ltd., pp. 1–11. doi: 10.1016/j.cub.2017.09.065.

Shi, H. *et al.* (2018) 'How to Build a Bacterial Cell: MreB as the Foreman of E. coli Construction', *Cell*. Elsevier Inc., 172(6), pp. 1294–1305. doi: 10.1016/j.cell.2018.02.050.

Shih, Y. L., Kawagishi, I. and Rothfield, L. (2005) 'The MreB and Min cytoskeletal-like systems play independent roles in prokaryotic polar differentiation', *Molecular Microbiology*, 58(4), pp. 917–928. doi: 10.1111/j.1365-2958.2005.04841.x.

Shih, Y. L., Le, T. and Rothfield, L. (2003) 'Division site selection in Escherichia coli involves dynamic redistribution of Min proteins within coiled structures that extend between the two cell poles', *Proc Natl Acad Sci U S A*, 100(13), pp. 7865–7870. doi: 10.1073/pnas.1232225100.

Si, F. *et al.* (2017) 'Invariance of Initiation Mass and Predictability of Cell Size in Escherichia coli', *Current Biology*. doi: 10.1016/j.cub.2017.03.022.

Siefert, J. L. and Fox, G. E. (1998) 'Phylogenetic mapping of bacterial morphology.', *Microbiology*, 144, pp. 2803–2808.

Silhavy, T. J., Kahne, D. and Walker, S. (2010) 'The bacterial cell envelope.', *Cold Spring Harbor perspectives in biology*, 2(5), p. a000414. doi: 10.1101/cshperspect.a000414.

Skurnik, D. *et al.* (2013) 'Enhanced in vivo fitness of carbapenem-resistant oprD mutants of Pseudomonas aeruginosa revealed through high-throughput sequencing', *Proceedings of the National Academy of Sciences*, 110(51), pp. 20747–20752. doi: 10.1073/pnas.1221552110.

Sonntag, I. *et al.* (1978) 'Cell Envelope and Shape of Escherichia coli : Multiple Mutants Missing the Outer Membrane Lipoprotein and Other Major Outer Membrane Proteins Lpp-', 136(1), pp. 280–285.

Spiers, A. J. *et al.* (2002) 'Adaptive divergence in experimental populations of Pseudomonas fluorescens. I. Genetic and phenotypic bases of wrinkly spreader fitness.', *Genetics*, 161(1), pp. 33–46.

Spiers, A. J. and Rainey, P. B. (2005) 'The Pseudomonas fluorescens SBW25 wrinkly spreader biofilm requires attachment factor, cellulose fibre and LPS interactions to maintain strength and integrity', *Microbiology*, 151(9), pp. 2829–2839. doi: 10.1099/mic.0.27984-0.

Stackebrandt, E. and Woese, C. R. (1979) 'A Phylogenetic Dissection of the Family Micrococcaceae', *Current Microbiology*, 2, pp. 317–322.

Stamsås, G. A. *et al.* (2018) 'CozEa and CozEb play overlapping and essential roles in controlling cell division in Staphylococcus aureus', *Molecular Microbiology*. doi: 10.1111/mmi.13999.

Stricker, J. *et al.* (2002) 'Rapid assembly dynamics of the Escherichia coli FtsZ-ring demonstrated by fluorescence recovery after photobleaching', *Proceedings of the National Academy of Sciences*, 99(5), pp. 3171–3175. doi: 10.1073/pnas.052595099.

Swulius, M. T. *et al.* (2011) 'Long helical filaments are not seen encircling cells in electron cryotomograms of rod-shaped bacteria.', *Biochemical and biophysical research communications*. Elsevier Inc., 407(4), pp. 650–5. doi: 10.1016/j.bbrc.2011.03.062.

Swulius, M. T. and Jensen, G. J. (2012) 'The helical mreb cytoskeleton in Escherichia coli MC1000/pLE7 is an artifact of the N-terminal yellow fluorescent protein tag', *Journal of Bacteriology*, 194(23), pp. 6382–6386. doi: 10.1128/JB.00505-12.

Takacs, C. N. *et al.* (2010) 'MreB drives de novo rod morphogenesis in Caulobacter crescentus via remodeling of the cell wall', *Journal of Bacteriology*, 192(6), pp. 1671–1684. doi: 10.1128/JB.01311-09.

Takeuchi, S. *et al.* (2005) 'Controlling the shape of filamentous cells of Escherichia coli', *Nano Letters*, 5(9), pp. 1819–1823. doi: 10.1021/nl0507360.

Tamames, J. *et al.* (2001) 'Bringing gene order into bacterial shape.', *Trends in genetics : TIG*, 17(3), pp. 124–6.

Tavares, A. C. *et al.* (2015) 'MreC and MreD proteins are not required for growth of staphylococcus aureus', *PLoS ONE*, 10(10), pp. 1–17. doi: 10.1371/journal.pone.0140523.

Team, R. D. C. and R Development Core Team, R. (2016) 'R: A Language and Environment for Statistical Computing', *R Foundation for Statistical Computing*. doi: 10.1007/978-3-540-74686-7.

Thanedar, S. and Margolin, W. (2004) 'FtsZ Exhibits Rapid Movement and Oscillation Waves in Helix-like Patterns in Escherichia coli', 14, pp. 1167–1173. doi: 10.1016/j.

Tomasz, A. (1979) 'The Mechanism of the Irreversible Antimicrobial Effects of Penicillins: How the Beta-Lactam Antibiotics Kill and Lyse Bacteria', *Annual Review of Microbiology*. doi: 10.1146/annurev.mi.33.100179.000553.

Torrens, G. *et al.* (2017) 'Targeting the permeability barrier and peptidoglycan recycling pathways to disarm Pseudomonas aeruginosa against the innate immune system', *PLoS ONE*. doi: 10.1371/journal.pone.0181932.

Treuner-Lange, A. *et al.* (2013) 'PomZ, a ParA-like protein, regulates Z-ring formation and cell division in Myxococcus xanthus', *Molecular Microbiology*. doi: 10.1111/mmi.12094.

Turner, R. D. *et al.* (2013) 'Cell wall elongation mode in Gram-negative bacteria is determined by peptidoglycan architecture.', *Nature communications*, 4, p. 1496. doi: 10.1038/ncomms2503.

Turner, R. D. *et al.* (2018) 'Molecular imaging of glycan chains couples cell-wall polysaccharide architecture to bacterial cell morphology', *Nature Communications*. Springer US, 9(1). doi: 10.1038/s41467-018-03551-y.

Tuson, H. H. *et al.* (2012) 'Measuring the stiffness of bacterial cells from growth rates in hydrogels of tunable elasticity', *Molecular Microbiology*, 84(5), pp. 874–891. doi: 10.1111/j.1365-2958.2012.08063.x.

Typas, A. *et al.* (2010) 'Regulation of peptidoglycan synthesis by outer-membrane proteins.', *Cell*, 143(7), pp. 1097–109. doi: 10.1016/j.cell.2010.11.038.

Typas, A. *et al.* (2012) 'From the regulation of peptidoglycan synthesis to bacterial growth and morphology.', *Nature reviews. Microbiology*, 10(2), pp. 123–36. doi: 10.1038/nrmicro2677.

Uehara, T. and Park, J. T. (2008) 'Growth of Escherichia coli: significance of peptidoglycan degradation during elongation and septation.', *Journal of bacteriology*, 190(11), pp. 3914–22. doi: 10.1128/JB.00207-08.

Ursinus, A. *et al.* (2004) 'Murein (peptidoglycan) binding property of the essential cell division protein FtsN from Escherichia coli', *Journal of Bacteriology*. doi: 10.1128/JB.186.20.6728-6737.2004.

Vargas-Garcia, C. A., Ghusinga, K. R. and Singh, A. (2018) 'Cell size control and gene expression

homeostasis in single-cells', *Current Opinion in Systems Biology*. Elsevier Ltd, 8(January), pp. 109–116. doi: 10.1016/j.coisb.2018.01.002.

Varley, A. W. and Stewart, G. C. (1992) 'The divIVB region of the Bacillus subtilis chromosome encodes homologs of Escherichia coli septum placement (MinCD) and cell shape (MreBCD) determinants', *Journal of Bacteriology*, 174(21), pp. 6729–6742.

Varma, A., de Pedro, M. a and Young, K. D. (2007) 'FtsZ directs a second mode of peptidoglycan synthesis in Escherichia coli.', *Journal of bacteriology*, 189(15), pp. 5692–704. doi: 10.1128/JB.00455-07.

Vats, P. and Rothfield, L. (2007) 'Duplication and segregation of the actin (MreB) cytoskeleton during the prokaryotic cell cycle.', *Proceedings of the National Academy of Sciences of the United States of America*, 104(45), pp. 17795–17800. doi: 10.1073/pnas.0708739104.

Vollmer, W. *et al.* (2008) 'Bacterial peptidoglycan (murein) hydrolases', *FEMS Microbiology Reviews*, pp. 259–286. doi: 10.1111/j.1574-6976.2007.00099.x.

Vollmer, W. and Höltje, J. V. (2004) 'The architecture of the murein (peptidoglycan) in gram-negative bacteria: Vertical scaffold or horizontal layer(s)?', *Journal of Bacteriology*, pp. 5978–5987. doi: 10.1128/JB.186.18.5978-5987.2004.

Vulin, C. *et al.* (2018) 'Prolonged bacterial lag time results in small colony variants that represent a sub-population of persisters', *Nature Communications*. doi: 10.1038/s41467-018-06527-0.

Wachi, M. *et al.* (1989) 'New mre genes mreC and mreD, responsible for formation of the rod shape of Escherichia coli cells', *Journal of Bacteriology*, 171(12), pp. 6511–6516.

Wachi, M. and Matsuhashi, M. (1989) 'Negative Control of Cell Division by mreB, a Gene That Functions in Determining the Rod Shape of Escherichia coli Cells', 171(6).

Wang, S. *et al.* (2010) 'Actin-like cytoskeleton filaments contribute to cell mechanics in bacteria.', *Proceedings of the National Academy of Sciences of the United States of America*, 107(20), pp. 9182–5. doi: 10.1073/pnas.0911517107.

Wehrens, M. *et al.* (2018) 'Size Laws and Division Ring Dynamics in Filamentous Escherichia coli cells', *Current Biology*. Elsevier Ltd., 28(6), p. 972–979.e5. doi: 10.1016/j.cub.2018.02.006.

Wei, B. *et al.* (2000) 'Global regulatory mutations in csrA and rpoS cause severe central carbon stress in Escherichia coli in the presence of acetate', *Journal of Bacteriology*, 182(6), pp. 1632–1640. doi: 10.1128/JB.182.6.1632-1640.2000.

Weidel, W., Frank, H. and Martin, H. M. (1960) 'The Rigid Layer of the Cell Wall of Escherichia coli Strain B', *J. gen. Microbiol.*, 22(1), pp. 158–166.

Weidel, W. and Pelzer, H. (1964) 'Bagshaped Macromolecules—A New Outlook on Bacterial Cell Walls', in *Advances in Enzymology and Related Areas of Molecular Biology*.

Weihs, F. *et al.* (2018) 'Heterogeneous localisation of membrane proteins in Staphylococcus aureus', *Scientific Reports*, 8(1), p. 3657. doi: 10.1038/s41598-018-21750-x.

Weiss, D. S. (2013) 'Escherichia coli shapeshifters.', *Journal of bacteriology*, 195(11), pp. 2449–51. doi: 10.1128/JB.00306-13.

Weiss, T. H. *et al.* (1995) 'Effect of Bacterial Cell Shape on Transport of Bacteria in Porous Media', *Environmental Science and Technology*. doi: 10.1021/es00007a007.

White, C. L. and Gober, J. W. (2012) 'MreB: pilot or passenger of cell wall synthesis?', *Trends in*

microbiology. Elsevier Ltd, 20(2), pp. 74–9. doi: 10.1016/j.tim.2011.11.004.

White, C. L., Kitich, A. and Gober, J. W. (2010) 'Positioning cell wall synthetic complexes by the bacterial morphogenetic proteins MreB and MreD.', *Molecular microbiology*, 76(3), pp. 616–33. doi: 10.1111/j.1365-2958.2010.07108.x.

Woese, C. R. *et al.* (1982) 'Phylogenetic relationships among various helical bacteria', *Current Microbiology*, 7(2), pp. 119–124. doi: 10.1007/BF01568426.

Wu, F. *et al.* (2015) 'Symmetry and scale orient Min protein patterns in shaped bacterial sculptures', *Nature Nanotechnology*, (June). doi: 10.1038/nnano.2015.126.

Yang, D. C., Blair, K. M. and Salama, N. R. (2016) 'Staying in Shape: the Impact of Cell Shape on Bacterial Survival in Diverse Environments', *Microbiology and Molecular Biology Reviews*, 80(1), pp. 187–203. doi: 10.1128/MMBR.00031-15.

Yang, J. *et al.* (2015) 'The I-TASSER Suite: protein structure and function prediction', *Nature Methods*, 12(1), pp. 7–8. doi: 10.1038/nmeth.3213.

Yao, X. *et al.* (1999) 'Thickness and Elasticity of Gram-Negative Murein Sacculi Measured by Atomic Force Microscopy Thickness and Elasticity of Gram-Negative Murein Sacculi Measured by Atomic Force Microscopy', 181(22).

Young, K. D. (2003) 'Bacterial shape', *Molecular Microbiology*, pp. 571–580. doi: 10.1046/j.1365-2958.2003.03607.x.

Young, K. D. (2006) 'The selective value of bacterial shape.', *Microbiology and Molecular Biology Reviews*, 70(3), pp. 660–703. doi: 10.1128/MMBR.00001-06.

Young, K. D. (2007) 'Bacterial morphology: why have different shapes?', *Current opinion in microbiology*, 10(6), pp. 596–600. doi: 10.1016/j.mib.2007.09.009.

Zapun, A., Vernet, T. and Pinho, M. G. (2008) 'The different shapes of cocci', *FEMS Microbiology Reviews*, 32(2), pp. 345–360. doi: 10.1111/j.1574-6976.2007.00098.x.

Zhao, H. *et al.* (2017) 'Don't let sleeping dogmas lie: new views of peptidoglycan synthesis and its regulation', *Molecular Microbiology*, 106(6), pp. 847–860. doi: 10.1111/mmi.13853.

Zhu, J. *et al.* (2017) 'A Periplasmic Polymer Curves Vibrio cholerae and Promotes Pathogenesis', *Cell*. doi: 10.1016/j.cell.2016.12.019.

Appendix

Raw UPLC Data and Analysis

UPLC analysis of peptidoglycan isolates

1. P. fluorescens SBW25 Wild Type
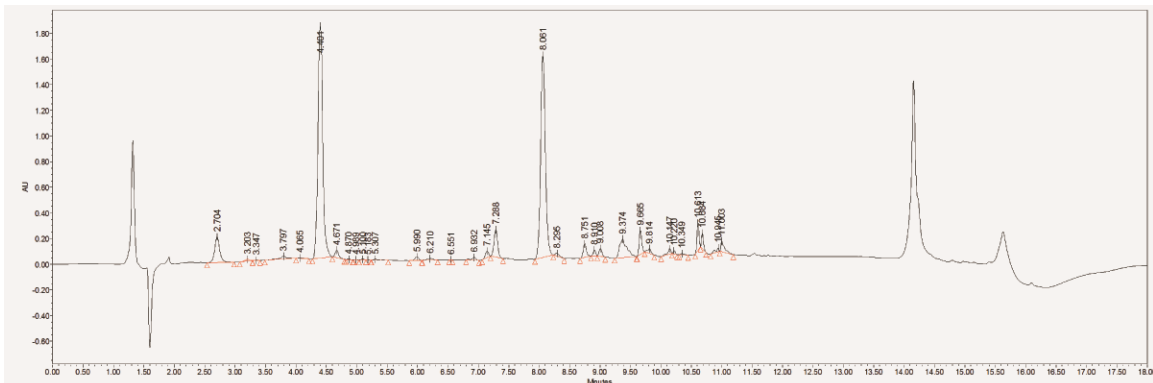
	Retention	Area	% Area		Retention	Area	% Area		Retention	Area	% Area
M3	2.70	1159329	0.044996	M3	2.71	1633076	0.054403	M3	2.73	2065377	0.062355
2	3.20	69799	0.002709	2	3.23	101652	0.003386	2	3.26	131593	0.003973
3	3.35	8050	0.000312	3	3.37	6851	0.000228	3	3.39	7825	0.000236
4	3.80	155806	0.006047	4	3.50	6919	0.00023	4	3.52	5710	0.000172
5	4.07	20732	0.000805	5	3.82	332974	0.011092	5	3.83	384055	0.011595
M4	4.40	9960792	0.3866	6	4.07	17833	0.000594	6	4.08	20129	0.000608
M2	4.67	231527	0.008986	M4	4.41	12047282	0.401335	M4	4.42	13265993	0.400508
8	4.87	10921	0.000424	M2	4.68	312498	0.01041	M2	4.69	358117	0.010812
9	4.99	3619	0.00014	9	4.86	12404	0.000413	9	4.88	15812	0.000477
10	5.10	14604	0.000567	10	4.96	6986	0.000233	10	5.00	7252	0.000219
11	5.18	4175	0.000162	11	5.07	26919	0.000897	11	5.11	34684	0.001047
12	5.31	31565	0.001225	12	5.26	43628	0.001453	12	5.31	47277	0.001427
M3L	5.99	119390	0.004634	13	5.51	8671	0.000289	13	5.47	3133	9.46E-05
14	6.21	72178	0.002801	14	5.79	41741	0.001391	14	5.56	12924	0.00039
15	6.55	1281	4.97E-05	M3L	5.98	226924	0.00756	M3L	6.01	344349	0.010396
16	6.93	92823	0.003603	16	6.19	14855	0.000495	16	6.56	34236	0.001034
17	7.15	178237	0.006918	17	6.91	139368	0.004643	17	6.96	183845	0.00555
D43	7.29	887218	0.034435	18	7.14	315498	0.01051	18	7.17	430150	0.012986
D44	8.06	8565125	0.332431	19	7.29	294629	0.009815	19	7.30	53900	0.001627
20	8.30	102143	0.003964	D43	7.55	332282	0.011069	D43	7.55	410009	0.012378
21	8.75	383014	0.014866	D44	8.05	10683246	0.355894	D44	8.04	11802935	0.356338
22	8.91	129215	0.005015	22	8.29	90019	0.002999	22	8.28	109404	0.003303
23	9.01	199353	0.007737	23	8.51	27751	0.000924	23	8.49	40993	0.001238
	9.37	1189826	0.04618	24	8.91	219912	0.007326	24	8.90	224160	0.006768
T444	9.67	561899	0.021809	25	9.02	339494	0.01131	25	9.00	396185	0.011961
26	9.81	146985	0.005705	26	9.16	34157	0.001138	26	9.49	10049	0.000303
27	10.15	151150	0.005866	27	9.39	233147	0.007767	T444	9.68	1247471	0.037662
28	10.22	55677	0.002161	28	9.57	24229	0.000807	28	10.08	71714	0.002165
29	10.35	46051	0.001787	T444	9.68	1009754	0.033638	D44N	10.63	794094	0.023974
D44N	10.61	490125	0.019023	30	10.09	53615	0.001786	D44N2	10.70	444680	0.013425
D44N2	10.68	272714	0.010585	31	10.17	43972	0.001465	31	11.01	145082	0.00438
32	10.95	118458	0.004598	D44N	10.63	669093	0.02229	T444N	11.39	19766	0.000597
T444N	11.00	331337	0.01286	D44N2	10.70	379754	0.012651				
				34	10.96	74393	0.002478				
				35	11.01	212125	0.007067				
				T444N	11.35	392	1.31E-05				

2. WT + Tn7 MreB
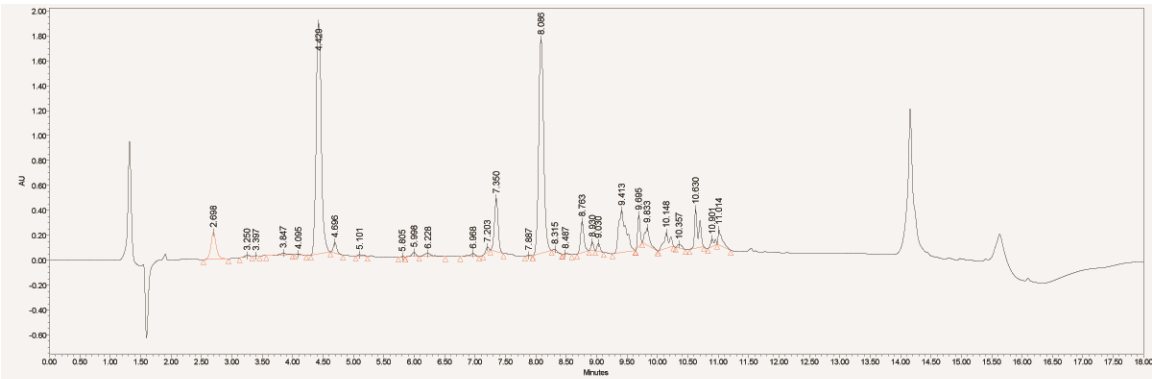
	Retention	Area	% Area
M3	2.69	1028481	0.029173
	3.23	58838	0.001669
	3.37	9116	0.000259
	3.81	236271	0.006702
	4.05	26102	0.00074
M4	4.38	11610666	0.329334
M2	4.66	366595	0.010398
	4.96	3014	8.55E-05
	5.08	53168	0.001508
	5.28	31847	0.000903
	5.54	3902	0.000111
	5.80	14883	0.000422
M3L	5.99	138107	0.003917
	6.20	123925	0.003515
	6.53	4202	0.000119
	6.83	16670	0.000473
	6.94	68371	0.001939
	7.17	143009	0.004056
D43	7.32	1805763	0.05122
	7.57	142355	0.004038
	7.86	21617	0.000613
D44	8.06	10542612	0.299039
	8.46	36980	0.001049
	8.75	831453	0.023584
	8.91	241563	0.006852
	9.02	238679	0.00677
	9.39	2737090	0.077637
T444	9.68	765564	0.021715
	9.83	645274	0.018303
	10.16	812741	0.023053
	10.36	131087	0.003718
D44N	10.63	1519782	0.043108
	10.90	260284	0.007383
T444N	11.02	584952	0.016592

	Retention	Area	% Area
M3	2.69	2070497	0.050011
2	3.23	95214	0.0023
3	3.37	12189	0.000294
4	3.83	313701	0.007577
5	4.08	33092	0.000799
M4	4.40	14330579	0.346145
M2	4.68	527937	0.012752
8	4.99	4579	0.000111
9	5.09	83039	0.002006
10	5.29	49579	0.001198
11	5.45	5934	0.000143
12	5.55	10766	0.00026
13	5.81	188238	0.004547
M3L	5.99	246984	0.005966
15	6.21	92922	0.002244
16	6.55	6670	0.000161
17	6.64	4693	0.000113
18	6.84	23254	0.000562
19	6.95	112285	0.002712
20	7.18	298574	0.007212
D43	7.32	1348824	0.03258
22	7.57	278511	0.006727
23	7.87	32949	0.000796
D44	8.06	13522258	0.326621
25	8.47	65855	0.001591
26	8.76	35817	0.000865
27	8.92	372407	0.008995
28	9.02	394375	0.009526
29	9.16	91889	0.00222
30	9.40	1289480	0.031146
T444	9.68	1684072	0.040678
32	10.09	55206	0.001333
33	10.17	212811	0.00514
D44N	10.63	2460312	0.059427
35	10.89	64113	0.001549
36	11.02	953982	0.023043
T444N	11.36	26921	0.00065

	Retention	Area	% Area
M3	2.70	1293681	0.037917
	3.25	61573	0.001805
	3.40	7563	0.000222
	3.85	103335	0.003029
	4.10	22543	0.000661
M4	4.43	11051053	0.323903
M2	4.70	328802	0.009637
	5.10	76148	0.002232
	5.81	10131	0.000297
M3L	6.00	146680	0.004299
	6.23	200427	0.005874
	6.97	138802	0.004068
	7.20	133738	0.00392
D43	7.35	1797323	0.052679
	7.89	18356	0.000538
D44	8.09	9781534	0.286694
	8.32	76879	0.002253
	8.49	37643	0.001103
	8.76	956451	0.028033
	8.93	199581	0.00585
	9.03	217335	0.00637
	9.41	2851542	0.083578
T444	9.70	691957	0.020281
	9.83	714629	0.020946
	10.15	794893	0.023298
	10.36	147094	0.004311
D44N	10.63	1433799	0.042024
	10.90	271432	0.007956
T444N	11.01	553433	0.016221

3. WT Reconstruction – Line 1 Mutation
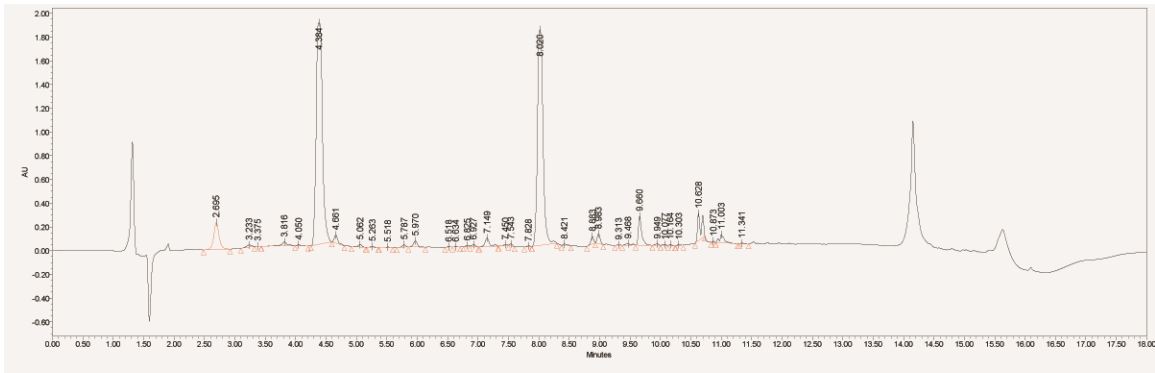
	Retention	Area	% Area
M3	2.69	1518988	0.044621
2	3.23	102255	0.003004
3	3.38	6087	0.000179
4	3.51	6637	0.000195
5	3.82	260967	0.007666
6	4.05	43502	0.001278
M4	4.38	14061927	0.41308
M2	4.66	327351	0.009616
9	5.07	107787	0.003166
10	5.27	40131	0.001179
11	5.53	7877	0.000231
M3L	5.98	232893	0.006841
13	6.20	46303	0.00136
14	6.53	19582	0.000575
15	6.82	29212	0.000858
16	6.93	64765	0.001903
17	7.15	284771	0.008365
D43	7.30	403696	0.011859
19	7.45	16743	0.000492
20	7.55	139813	0.004107
21	7.84	23807	0.000699
D44	8.04	12327007	0.362116
23	8.45	65611	0.001927
24	8.61	22832	0.000671
25	8.74	92884	0.002729
26	8.90	220964	0.006491
27	9.00	280276	0.008233
28	9.38	511827	0.015035
T444	9.66	1130864	0.03322
30	10.08	27846	0.000818
31	10.15	53272	0.001565
32	10.30	21172	0.000622
D44N	10.62	1095611	0.032184
34	10.89	34842	0.001024
35	11.01	386811	0.011363
T444N	11.35	24706	0.000726

	Retention	Area	% Area
M3	2.68	1818166	0.049318
2	3.23	168606	0.004573
3	3.51	3630	9.85E-05
4	3.82	284219	0.007709
5	4.06	45643	0.001238
M4	4.39	14457721	0.392165
M2	4.66	350762	0.009514
8	5.07	107688	0.002921
9	5.28	50069	0.001358
M3L	5.98	280658	0.007613
11	6.19	73581	0.001996
12	6.53	6965	0.000189
13	6.64	5478	0.000149
14	6.83	29082	0.000789
15	6.94	78148	0.00212
16	7.17	301561	0.00818
D43	7.32	723616	0.019628
18	7.48	17552	0.000476
19	7.57	135407	0.003673
20	7.85	26963	0.000731
D44	8.04	12671777	0.343722
22	8.43	66092	0.001793
23	8.60	21792	0.000591
24	8.71	184770	0.005012
25	8.89	229143	0.006215
26	8.99	322746	0.008754
27	9.38	847160	0.022979
T444	9.66	1349904	0.036616
29	10.14	187176	0.005077
30	10.27	34979	0.000949
D44N	10.60	1487618	0.040352
32	10.88	47183	0.00128
33	11.01	423463	0.011486
T444N	11.35	27071	0.000734

	Retention	Area	% Area
M3	2.70	1366206	0.044252
2	3.23	99356	0.003218
3	3.38	6243	0.000202
4	3.82	210205	0.006809
5	4.05	30923	0.001002
M4	4.38	13368778	0.433016
M2	4.66	271941	0.008808
8	5.06	91257	0.002956
9	5.26	34568	0.00112
10	5.52	19454	0.00063
11	5.79	73767	0.002389
M3L	5.97	225067	0.00729
13	6.52	8167	0.000265
14	6.63	2843	9.21E-05
15	6.83	24242	0.000785
16	6.93	55192	0.001788
D43	7.15	366088	0.011858
18	7.45	27439	0.000889
19	7.54	48416	0.001568
20	7.83	23162	0.00075
D44	8.02	11479036	0.371807
22	8.42	61477	0.001991
23	8.88	188779	0.006115
24	8.98	274122	0.008879
25	9.31	12376	0.000401
26	9.47	81455	0.002638
T444	9.66	900757	0.029176
28	9.95	54469	0.001764
29	10.08	33235	0.001076
30	10.16	27016	0.000875
31	10.30	23959	0.000776
D44N	10.63	984045	0.031873
33	10.87	23639	0.000766
34	11.00	355365	0.01151
T444N	11.34	20588	0.000667

4. WT Reconstruction - Line 4 Mutation
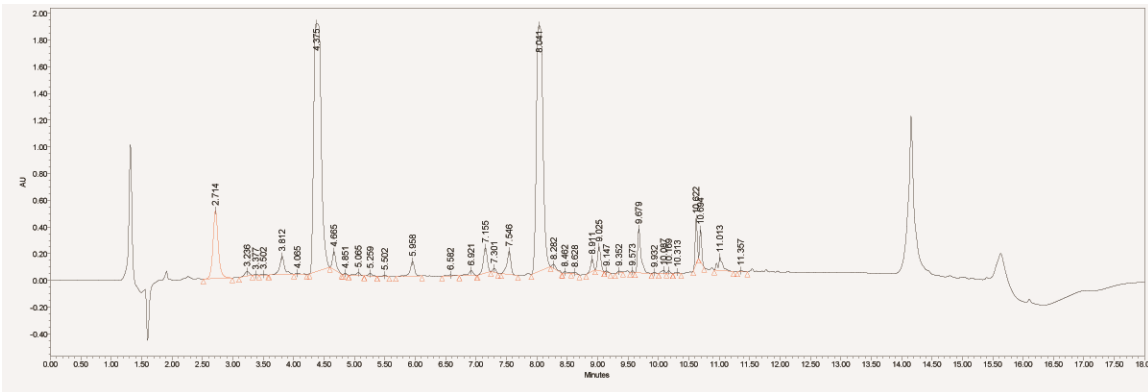
Label		Retention	Area	% Area
M3		2.71	3048615	0.073395
	2	3.24	178595	0.0043
	3	3.38	12422	0.000299
	4	3.50	21808	0.000525
	5	3.81	737059	0.017745
	6	4.07	30261	0.000729
M4		4.38	15832897	0.381175
M2		4.67	538038	0.012953
	9	4.85	29006	0.000698
	10	5.07	111006	0.002672
	11	5.26	80004	0.001926
	12	5.50	40750	0.000981
M3L		5.96	534253	0.012862
	14	6.58	65321	0.001573
	15	6.92	198160	0.004771
	16	7.16	840370	0.020232
	17	7.30	101897	0.002453
D43		7.55	786937	0.018945
D44		8.04	13731337	0.33058
	20	8.28	140998	0.003395
	21	8.46	49400	0.001189
	22	8.63	50541	0.001217
	23	8.91	294897	0.0071
	24	9.03	634928	0.015286
	25	9.15	27337	0.000658
	26	9.35	48015	0.001156
	27	9.57	33536	0.000807
T444		9.68	1255774	0.030233
	29	9.93	25432	0.000612
	30	10.09	87239	0.0021
	31	10.17	49533	0.001193
	32	10.31	44535	0.001072
D44N		10.62	786852	0.018943
D44N2		10.69	545655	0.013137
	35	11.01	507773	0.012225
T444N		11.36	35880	0.000864

Label		Retention	Area	% Area
M3		2.63	718248	0.03757
	2	3.13	49289	0.002578
	3	3.76	118906	0.00622
M4		4.31	8000663	0.418493
M2		4.58	323718	0.016933
	6	4.96	30017	0.00157
	7	5.18	21142	0.001106
	8	5.78	256902	0.013438
M3L		6.05	129226	0.006759
	10	6.33	48347	0.002529
	11	7.21	63207	0.003306
	12	7.60	98483	0.005151
D43		7.76	660316	0.034539
D44		8.52	6006161	0.314166
	15	8.72	123302	0.00645
	16	8.89	73731	0.003857
	17	9.14	204606	0.010702
	18	9.26	107251	0.00561
	19	9.36	170927	0.008941
	20	9.62	663974	0.034731
T444		9.87	332860	0.017411
	22	9.99	80794	0.004226
	23	10.16	104900	0.005487
	24	10.34	70059	0.003665
D44N		10.82	246087	0.012872
D44N2		10.89	211154	0.011045
	27	11.08	37178	0.001945
	28	11.13	16119	0.000843
	29	11.19	106507	0.005571
	30	11.62	524	2.74E-05
T444N		11.72	32974	0.001725
	32	11.90	949	4.96E-05
	33	11.96	9291	0.000486

Label		Retention	Area	% Area
M3		2.66	807441	0.045823
	2	3.16	55159	0.00313
	3	3.78	139817	0.007935
M4		4.33	8012300	0.454701
M2		4.61	266635	0.015132
	6	4.98	26911	0.001527
	7	5.81	57183	0.003245
M3L		6.07	159398	0.009046
	9	7.23	50593	0.002871
	10	7.63	162397	0.009216
D43		7.79	104269	0.005917
D44		8.53	6127614	0.347745
	13	8.72	111348	0.006319
	14	8.89	67540	0.003833
	15	9.27	134713	0.007645
	16	9.37	194472	0.011036
T444		9.89	422912	0.024
	18	10.17	55845	0.003169
D44N		10.82	257307	0.014602
D44N2		10.90	231473	0.013136
	21	11.07	13861	0.000787
	22	11.14	23154	0.001314
	23	11.19	95716	0.005432
T444N		11.72	33457	0.001899
	25	11.96	9507	0.00054

5. WT Reconstruction – Line 7
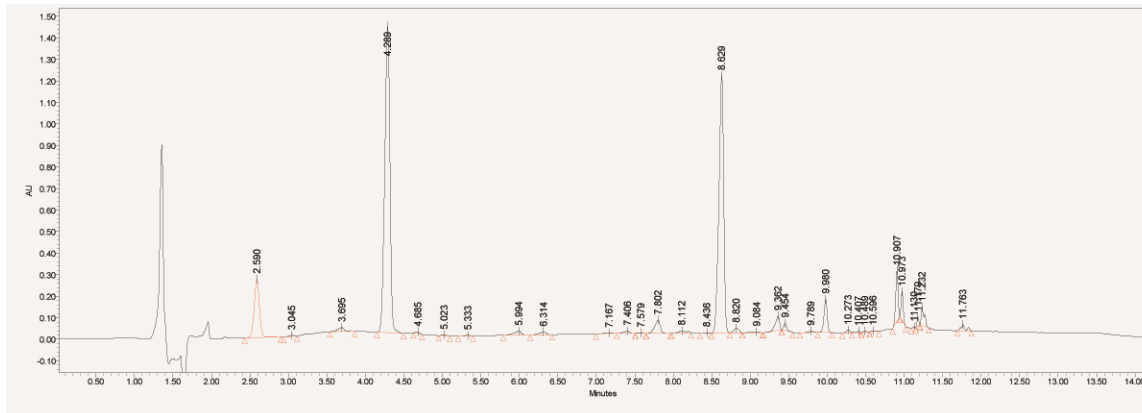
7A	Retention	44202124 Area	% Area
M3	2.76	3291445	0.074464
2	3.31	197790	0.004475
3	3.89	143015	0.003235
4	4.10	426579	0.009651
M4	4.43	14605777	0.330432
M2	4.90	18842	0.000426
7	5.10	34925	0.00079
8	5.20	8749	0.000198
9	5.31	5539	0.000125
10	5.44	34552	0.000782
11	5.84	42257	0.000956
M3L	6.00	281705	0.006373
13	6.25	134948	0.003053
14	6.42	15033	0.00034
15	6.99	74856	0.001693
16	7.14	1011891	0.022892
D43	7.39	1275756	0.028862
18	7.81	621593	0.014063
D44	8.04	11674918	0.264126
20	8.29	113991	0.002579
21	8.55	144760	0.003275
22	8.83	392538	0.008881
23	9.00	1358363	0.030731
24	9.41	858910	0.019431
T444	9.64	1500877	0.033955
26	9.86	122725	0.002776
27	10.15	124724	0.002822
28	10.23	53802	0.001217
D44N	10.62	1757304	0.039756
D44N2	10.69	599064	0.013553
31	10.99	2579945	0.058367
32	11.35	26219	0.000593
T444N	11.50	668732	0.015129

7B	Retention	16150582 Area	% Area
M3	2.59	1264254	0.078279
2	3.05	22781	0.001411
3	3.70	110114	0.006818
M4	4.29	6685321	0.413937
M2	4.69	28299	0.001752
6	5.02	15458	0.000957
7	5.33	15011	0.000929
M3L	5.99	109703	0.006793
9	6.31	82293	0.005095
10	7.17	16831	0.001042
11	7.41	50973	0.003156
12	7.58	10056	0.000623
D43	7.80	303092	0.018767
14	8.11	74076	0.004587
15	8.44	12950	0.000802
D44	8.63	5160203	0.319506
17	8.82	94188	0.005832
18	9.08	35301	0.002186
19	9.36	246170	0.015242
20	9.45	94109	0.005827
21	9.79	26707	0.001654
T444	9.98	440242	0.027259
23	10.27	37001	0.002291
24	10.41	19937	0.001234
25	10.49	13894	0.00086
26	10.60	14186	0.000878
D44N	10.91	495057	0.030653
D44N2	10.97	257598	0.01595
29	11.13	6023	0.000373
30	11.18	64198	0.003975
31	11.23	236516	0.014644
T444N	11.76	108040	0.00669

6. ΔmreB (ancestral)

	Retention	Area	% Area		Retention	Area	% Area
M3	2.70	334360	0.02764	M3	2.69	491668	0.031226
2	3.83	31783	0.002627	2	3.22	21688	0.001377
3	4.06	100088	0.008274	3	3.81	108358	0.006882
M4	4.41	3204745	0.264917	4	4.04	145487	0.00924
M2	4.66	115631	0.009559	M4	4.40	4304564	0.273384
6	5.06	163084	0.013481	M2	4.65	155219	0.009858
7	5.27	15349	0.001269	7	5.05	264949	0.016827
8	5.45	9604	0.000794	8	5.27	19725	0.001253
9	5.80	7763	0.000642	9	5.44	44672	0.002837
M3L	5.98	51448	0.004253	M3L	5.98	71299	0.004528
11	6.18	20865	0.001725	11	6.19	23392	0.001486
12	6.62	6095	0.000504	12	6.63	28407	0.001804
13	6.94	67854	0.005609	13	6.84	8527	0.000542
14	7.19	89073	0.007363	14	6.94	36118	0.002294
D43	7.34	335727	0.027753	15	7.18	124889	0.007932
	7.50	173955	0.01438	D43	7.33	269851	0.017138
17	7.88	16669	0.001378		7.48	347785	0.022088
D44	8.08	4138946	0.342141	18	7.87	18398	0.001168
19	8.45	161308	0.013334	D44	8.08	5434448	0.345143
20	8.74	62228	0.005144	20	8.45	319732	0.020306
21	8.91	134949	0.011155	21	8.75	35848	0.002277
22	9.01	96706	0.007994	22	8.91	175768	0.011163
	9.39	290732	0.024033	23	9.02	126240	0.008018
T444	9.68	626053	0.051752	24	9.39	208860	0.013265
25	9.95	7171	0.000593	T444	9.67	750685	0.047676
26	10.09	29648	0.002451	26	10.08	46110	0.002928
27	10.17	17696	0.001463	27	10.21	21638	0.001374
28	10.30	41608	0.003439	28	10.29	66893	0.004248
D44N	10.64	840249	0.069458	D44N	10.62	993924	0.063124
30	11.02	717218	0.059288	30	10.89	66896	0.004249
31	11.36	19576	0.001618	31	11.01	748571	0.047542
T444N	11.55	168997	0.01397	32	11.35	25681	0.001631
				T444N	11.54	239222	0.015193

7. ΔmreB + Tn7 MreB
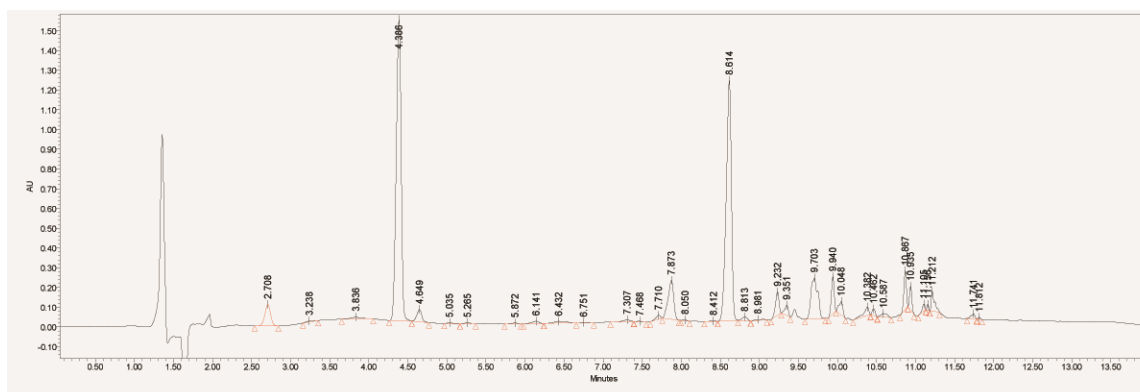
	Retention	Area	% Area
M3	2.78	1479106	0.028755
2	3.33	183494	0.003567
3	3.88	167765	0.003261
4	4.10	23069	0.000448
M4	4.42	11550761	0.224557
M2	4.69	524995	0.010206
7	5.17	114223	0.002221
8	5.31	33057	0.000643
9	5.58	7988	0.000155
10	5.83	196842	0.003827
M3L	6.01	142626	0.002773
12	6.20	581884	0.011312
13	6.55	6685	0.00013
14	6.81	26171	0.000509
15	6.94	121378	0.00236
D43	7.30	6115625	0.118893
17	7.86	50421	0.00098
D44	8.06	7954337	0.154639
19	8.29	185960	0.003615
20	8.46	21315	0.000414
21	8.74	3077397	0.059827
22	8.91	405116	0.007876
23	9.01	221285	0.004302
24	9.39	5911030	0.114915
25	9.59	12907	0.000251
T444	9.67	306152	0.005952
27	9.82	4189728	0.081452
28	10.14	2642327	0.051369
29	10.34	1011049	0.019656
D44N	10.62	1647761	0.032034
31	10.90	488676	0.0095
T444N	11.09	2036956	0.0396

	Retention	Area	% Area
M3	2.70	614119	0.034329
2	3.23	35368	0.001977
3	3.81	82238	0.004597
4	4.03	16952	0.000948
M4	4.36	7459251	0.416974
M2	4.61	267333	0.014944
7	4.99	28514	0.001594
8	5.21	23968	0.00134
M3L	6.09	100624	0.005625
10	7.26	64727	0.003618
11	7.44	12168	0.00068
D43	7.69	182692	0.010213
13	7.88	88651	0.004956
14	8.02	23053	0.001289
15	8.39	10595	0.000592
D44	8.60	6589262	0.368341
17	8.79	89393	0.004997
18	8.97	83581	0.004672
19	9.33	229329	0.01282
20	9.44	163360	0.009132
21	9.66	10901	0.000609
T444	9.93	576134	0.032206
23	10.23	46931	0.002623
24	10.42	14511	0.000811
25	10.51	23454	0.001311
D44N	10.85	412946	0.023084
D44N2	10.92	270802	0.015138
28	11.16	60743	0.003396
29	11.21	218968	0.01224
T444N	11.73	88444	0.004944

M3	2.71	550650	0.029367
2	3.24	28533	0.001522
3	3.84	64333	0.003431
M4	4.39	6674653	0.355965
M2	4.65	271705	0.01449
6	5.04	25072	0.001337
7	5.27	22610	0.001206
8	5.87	21756	0.00116
M3L	6.14	72055	0.003843
10	6.43	96251	0.005133
11	6.75	11390	0.000607
12	7.31	55190	0.002943
13	7.47	10706	0.000571
14	7.71	78203	0.004171
D43	7.87	968972	0.051676
16	8.05	13090	0.000698
17	8.41	10408	0.000555
D44	8.61	5606969	0.299025
19	8.81	83176	0.004436
20	8.98	38475	0.002052
21	9.23	365418	0.019488
22	9.35	160885	0.00858
T444	9.70	1248261	0.066571
24	9.94	465741	0.024838
25	10.05	244707	0.01305
26	10.38	191122	0.010193
27	10.46	86916	0.004635
28	10.59	108668	0.005795
D44N	10.87	428566	0.022856
D44N2	10.94	241707	0.01289
31	11.11	78620	0.004193
32	11.16	43021	0.002294
T444N	11.21	288607	0.015392
34	11.74	78440	0.004183
35	11.81	15968	0.000852

8. ΔmreB Reconstruction – Line 1
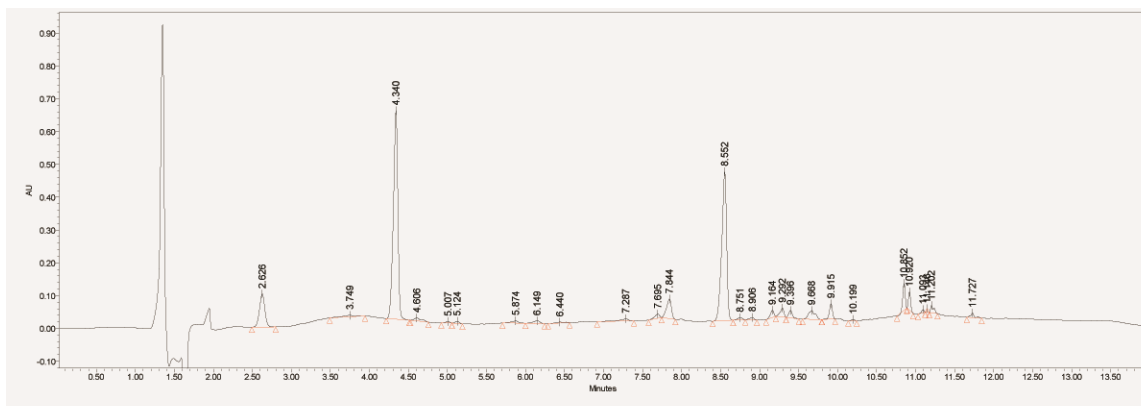
	Retention	Area	% Area
M3	2.728	791357	0.041855
2	3.857	15126	0.0008
3	4.058	106969	0.005658
M4	4.436	5461825	0.288879
M2	4.645	40503	0.002142
6	4.791	83605	0.004422
7	5.08	37044	0.001959
8	5.172	62528	0.003307
9	5.824	274563	0.014522
10	5.992	88943	0.004704
M3L	6.24	235410	0.012451
12	6.965	84447	0.004466
D43	7.35	1501669	0.079424
D44	8.056	3254928	0.172155
15	8.327	2666	0.000141
16	8.788	823655	0.043564
17	8.96	418529	0.022136
18	9.395	1310152	0.069295
19	9.648	213373	0.011285
20	9.843	367562	0.019441
21	9.922	156424	0.008273
T444	10.144	631926	0.033423
23	10.218	130617	0.006908
24	10.335	415865	0.021995
25	10.528	96094	0.005082
D44N	10.615	458884	0.024271
D44N2	10.685	231930	0.012267
28	10.902	393970	0.020837
29	11.029	987151	0.052211
T444N	11.54	229232	0.012124

	Retention	Area	% Area
M3	2.723	450769	0.083681
2	3.836	83356	0.015474
M4	4.383	2276529	0.422617
M2	4.644	57367	0.01065
5	5.016	18525	0.003439
M3L	6.126	56424	0.010475
7	7.294	85482	0.015869
8	7.702	68822	0.012776
D43	8.014	29533	0.005483
D44	8.588	1596068	0.296296
11	8.783	17478	0.003245
12	8.957	40836	0.007581
13	9.332	86107	0.015985
14	9.432	55066	0.010223
T444	9.935	108306	0.020106
16	10.216	8774	0.001629
17	10.342	4064	0.000754
D44N	10.849	149006	0.027662
D44N2	10.919	90033	0.016714
20	11.093	4737	0.000879
21	11.152	17326	0.003216
22	11.209	46013	0.008542
T444N	11.741	36121	0.006706

	Retention	Area	% Area
M3	2.626	478731	0.071949
2	3.749	49590	0.007453
M4	4.34	2551949	0.383535
M2	4.606	56073	0.008427
5	5.007	14493	0.002178
6	5.124	23584	0.003544
7	5.874	40437	0.006077
M3L	6.149	46236	0.006949
9	6.44	23189	0.003485
10	7.287	52001	0.007815
11	7.695	54621	0.008209
D43	7.844	257435	0.03869
D44	8.552	1983876	0.298159
14	8.751	30078	0.00452
15	8.906	31005	0.00466
16	9.164	68267	0.01026
17	9.292	90440	0.013592
18	9.396	70698	0.010625
19	9.668	158768	0.023861
T444	9.915	126644	0.019033
21	10.199	12470	0.001874
D44N	10.852	182617	0.027446
D44N2	10.92	108029	0.016236
24	11.093	19862	0.002985
25	11.146	16708	0.002511
26	11.202	62282	0.00936
T444N	11.727	43668	0.006563

9. *ΔmreB Reconstruction – Line 4*
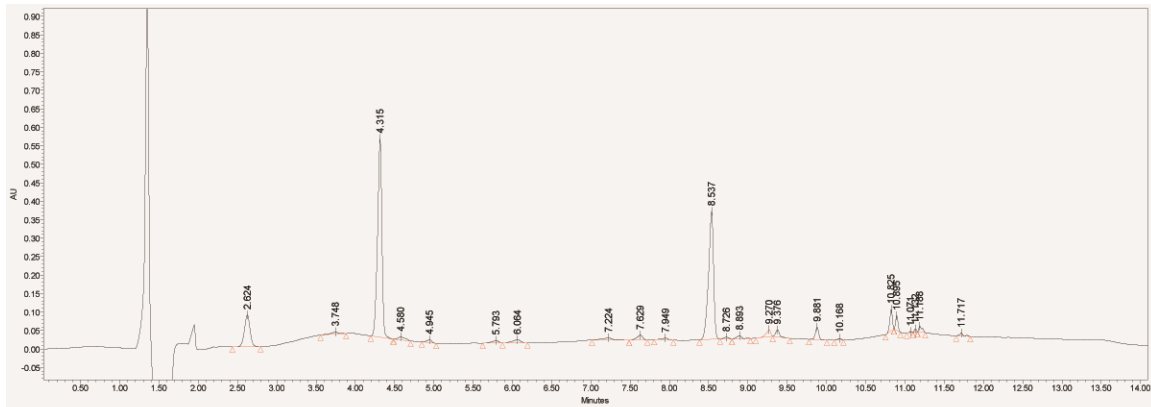
	Retention	Area	% Area
M3	2.70	438958	0.031328
2	3.89	108364	0.007734
3	4.06	13378	0.000955
M4	4.41	4655223	0.332242
M2	4.65	64362	0.004593
6	5.05	61741	0.004406
7	5.28	9967	0.000711
8	5.54	5755	0.000411
9	5.77	44338	0.003164
M3L	5.95	73577	0.005251
11	6.16	88001	0.006281
12	6.61	2938	0.00021
13	6.80	12571	0.000897
14	6.90	25691	0.001834
15	7.12	71904	0.005132
D43	7.28	775076	0.055317
17	7.58	122497	0.008743
18	7.83	10166	0.000726
D44	8.03	3569970	0.254788
20	8.26	46576	0.003324
21	8.41	56334	0.004021
22	8.58	4964	0.000354
23	8.74	390610	0.027878
24	8.90	260525	0.018594
25	9.37	1013161	0.072309
T444	9.64	205043	0.014634
27	9.80	307972	0.02198
28	10.12	204503	0.014595
29	10.34	44857	0.003201
D44N	10.59	770660	0.055002
31	10.88	219074	0.015635
32	10.99	233719	0.01668
T444N	11.53	99075	0.007071

	Retention	Area	% Area
M3	2.69	606364	0.03833
2	3.83	177195	0.011201
3	4.05	12226	0.000773
M4	4.39	5537013	0.350014
M2	4.65	102769	0.006496
6	5.03	73165	0.004625
7	5.25	13072	0.000826
8	5.76	54067	0.003418
9	5.94	103390	0.006536
M3L	6.15	97420	0.006158
11	6.58	2460	0.000156
12	6.76	19113	0.001208
13	6.89	38129	0.00241
14	7.12	83135	0.005255
15	7.27	821027	0.0519
D43	7.55	150187	0.009494
17	7.82	8846	0.000559
D44	8.03	3916538	0.247578
19	8.25	46757	0.002956
20	8.42	30610	0.001935
21	8.72	336070	0.021244
22	8.88	319522	0.020198
23	9.36	1061369	0.067093
T444	9.64	215879	0.013646
25	9.80	225744	0.01427
26	10.13	230495	0.01457
27	10.26	1266	8E-05
28	10.32	32724	0.002069
D44N	10.60	888430	0.056161
30	10.88	227705	0.014394
31	11.00	242486	0.015328
32	11.34	6196	0.000392
T444N	11.53	138022	0.008725

	Retention	Area	% Area
M3	2.62	419959	0.084179
2	3.75	41097	0.008238
M4	4.32	2068323	0.414587
M2	4.58	53080	0.01064
5	4.95	32136	0.006442
6	5.79	33285	0.006672
M3L	6.06	50385	0.010099
8	7.22	56598	0.011345
9	7.63	66836	0.013397
D43	7.95	20847	0.004179
D44	8.54	1537308	0.308147
12	8.73	21679	0.004345
13	8.89	38401	0.007697
14	9.27	73286	0.01469
15	9.38	62169	0.012462
T444	9.88	98886	0.019821
17	10.17	13959	0.002798
D44N	10.83	131181	0.026295
D44N2	10.90	80545	0.016145
20	11.07	5327	0.001068
21	11.13	13004	0.002607
22	11.19	44586	0.008937
T444N	11.72	25999	0.005211
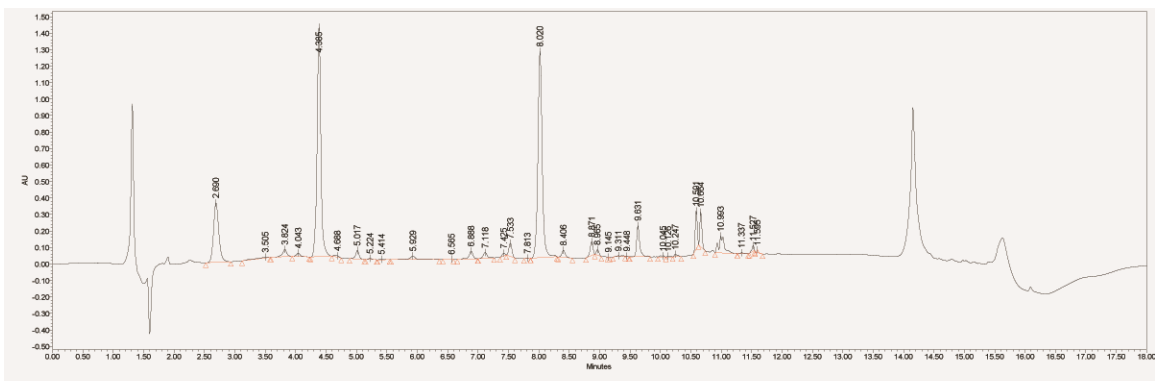
Label	Retention	Area	% Area
M3	2.69	2159223	0.113518
2	3.51	77036	0.00405
3	3.82	211662	0.011128
4	4.04	88401	0.004648
M4	4.39	6078537	0.319571
M2	4.69	46043	0.002421
7	5.02	200320	0.010532
8	5.22	24791	0.001303
9	5.41	17044	0.000896
M3L	5.93	141363	0.007432
11	6.57	2548	0.000134
12	6.89	210769	0.011081
13	7.12	163317	0.008586
14	7.43	52619	0.002766
D43	7.53	275432	0.01448
16	7.81	6017	0.000316
D44	8.02	6133224	0.322446
18	8.41	165702	0.008712
19	8.87	267379	0.014057
20	8.97	98168	0.005161
21	9.15	106	5.57E-06
22	9.31	29828	0.001568
23	9.45	4236	0.000223
T444	9.63	667959	0.035117
25	10.05	34067	0.001791
26	10.13	19408	0.00102
27	10.25	59808	0.003144
D44N	10.59	531943	0.027966
D44N2	10.66	481644	0.025322
30	10.99	645558	0.033939
31	11.34	17001	0.000894
T444N	11.53	77047	0.004051
33	11.60	32724	0.00172

Label	Retention	Area	% Area
M3	2.70	1108204	0.054821
2	3.23	75705	0.003745
3	3.83	174019	0.008608
4	4.05	54775	0.00271
M4	4.39	5855719	0.289671
M2	4.64	62493	0.003091
7	5.10	199711	0.009879
8	5.23	16776	0.00083
9	5.75	37693	0.001865
M3L	5.93	74237	0.003672
11	6.14	70617	0.003493
12	6.88	103004	0.005095
13	7.11	96567	0.004777
D43	7.26	794378	0.039296
15	7.53	248987	0.012317
D44	8.02	5297980	0.262081
17	8.24	44547	0.002204
18	8.72	411955	0.020379
19	8.88	280077	0.013855
20	8.98	136053	0.00673
21	9.36	1403402	0.069424
T444	9.64	570752	0.028234
23	9.80	345617	0.017097
24	10.12	305779	0.015126
25	10.20	106673	0.005277
26	10.36	77670	0.003842
D44N	10.59	592716	0.02932
D44N2	10.67	413831	0.020471
29	10.88	348848	0.017257
30	11.03	715401	0.035389
31	11.34	9123	0.000451
T444N	11.53	151731	0.007506
33	11.60	30039	0.001486

Label	Retention	Area	% Area
M3	2.71	879645	0.072317
2	3.26	68435	0.005626
3	3.83	130029	0.01069
4	4.05	89166	0.007331
M4	4.40	4072507	0.334808
M2	4.65	32491	0.002671
7	5.03	163318	0.013427
8	5.24	17001	0.001398
9	5.43	12670	0.001042
M3L	5.93	59662	0.004905
11	6.78	7112	0.000585
12	6.90	63570	0.005226
13	7.13	73863	0.006072
14	7.29	18693	0.001537
15	7.44	66612	0.005476
D43	7.55	135729	0.011159
17	7.83	4489	0.000369
D44	8.04	3868779	0.31806
19	8.42	175120	0.014397
20	8.89	291165	0.023937
21	9.32	54440	0.004476
T444	9.64	431396	0.035466
23	9.91	1672	0.000137
24	10.06	18946	0.001558
25	10.18	12424	0.001021
26	10.25	39363	0.003236
D44N	10.60	798127	0.065616
28	10.86	30288	0.00249
29	10.99	430416	0.035385
30	11.33	11760	0.000967
T444N	11.53	79885	0.006567
32	11.60	24918	0.002049

UPLC Summary of Results

WT	T1	T2	T3	ave	SD		T1	T2	T3	Average	SD
M3	4.50%	5.44%	6.24%	5.39%	0.87%	Glycan Length					
M4	38.66%	40.13%	40.05%	39.61%	0.83%		23.55	28.61	26.32	26.16	2.53
M2	0.90%	1.04%	1.08%	1.01%	0.10%	D44/M4					
M3L	0.46%	0.76%	1.04%	0.75%	0.29%		0.86	0.89	0.89	0.88	0.02
D44	33.24%	35.59%	35.63%	34.82%	1.37%	Cross-linking					
T444	1.49%	0.09%	0.33%	0.64%	0.75%		38.40%	39.14%	40.06%	39.20%	0.01
D43L	2.18%	3.36%	3.77%	3.10%	0.82%						
D44N	2.96%	3.49%	3.74%	3.40%	0.40%						
T444N	1.29%	0.00%	0.06%	0.45%	0.73%						

WT+mreb	T1	T2	T3	ave	SD		T1	T2	T3	Average	SD
M3	2.92%	5.00%	3.79%	3.90%	1.05%	Glycan Length					
M4	32.93%	34.61%	32.39%	33.31%	1.16%		16.75	16.65	17.17	16.85	0.28
M2	1.04%	1.28%	0.96%	1.09%	0.16%	D44/M4					
M3L	0.39%	0.60%	0.43%	0.47%	0.11%		0.91	0.94	0.89	0.91	0.03
D44	29.90%	32.66%	28.67%	30.41%	2.04%	Cross-linking					
T444	0.10%	0.16%	0.11%	0.12%	0.03%		32.29%	37.05%	30.92%	33.42%	0.03
D43L	2.17%	4.07%	2.03%	2.76%	1.14%						
D44N	4.31%	5.94%	4.20%	4.82%	0.97%						
T444N	1.66%	0.07%	1.62%	1.12%	0.91%						

5 - WT R.L1	T1	T2	T3	ave	SD		T1	T2	T3	Average	SD
M3	4.46%	4.93%	4.43%	4.61%	0.28%	Glycan Length					
M4	41.31%	39.22%	43.30%	41.28%	2.04%		30.39	24.34	30.73	28.49	3.59
M2	0.96%	0.95%	0.88%	0.93%	0.04%	D44/M4					
M3L	0.68%	0.76%	0.73%	0.72%	0.04%		0.88	0.88	0.86	0.87	0.01
D44	36.21%	34.37%	37.18%	35.92%	1.43%	Cross-linking					
T444	0.19%	0.18%	0.20%	0.19%	0.01%		39.92%	38.39%	40.50%	39.60%	0.01
D43L	3.32%	3.66%	2.92%	3.30%	0.37%						
D44N	3.22%	4.04%	3.19%	3.48%	0.48%						
T444N	0.07%	0.07%	0.07%	0.07%	0.00%						

6 - WT R.L4	T1	T2	T3	ave	SD		T1	T2	T3	Average	SD
M3	7.34%	3.76%	4.58%	5.23%	1.88%	Glycan Length					
M4	38.12%	41.85%	45.47%	41.81%	3.68%		30.35	40.98	35.36	35.57	5.31
M2	1.30%	1.69%	1.51%	1.50%	0.20%	D44/M4					
M3L	1.29%	1.34%	0.32%	0.98%	0.57%		0.87	0.75	0.76	0.79	0.06
D44	33.06%	31.42%	34.77%	33.08%	1.68%	Cross-linking					
T444	0.12%	0.64%	0.38%	0.38%	0.26%		36.32%	34.45%	37.94%	36.24%	0.02
D43L	3.02%	1.74%	2.40%	2.39%	0.64%						
D44N	3.21%	2.39%	2.77%	2.79%	0.41%						
T444N	0.09%	0.05%	0.05%	0.06%	0.02%						

7 - WT R.L7	T1	T2	T3	ave	SD		T1	T2	T3	Average	SD
M3	7.45%	7.83%		7.64%	0.27%	Glycan Length					
M4	33.04%	41.39%		37.22%	5.90%		14.61	16.33		15.47	1.21
M2	0.04%	0.18%		0.11%	0.09%	D44/M4					
M3L	0.64%	0.51%		0.57%	0.09%		0.80	0.77		0.79	0.02
D44	26.41%	31.95%		29.18%	3.92%	Cross-linking					
T444	0.26%	0.58%		0.42%	0.23%		30.32%	33.28%		31.80%	0.02
D43L	3.40%	0.17%		1.78%	2.28%						
D44N	5.33%	4.66%		5.00%	0.47%						
T444N	1.51%	1.46%		1.49%	0.03%						

Δmreb

Δmreb	T1	T2	T3	ave	SD		T1	T2	T3	Average	SD
M3	2.76%	3.12%		2.94%	0.25%	Glycan Length					
M4	26.49%	27.34%		26.92%	0.60%		11.99	12.77		12.38	0.55
M2	0.96%	0.99%		0.97%	0.02%	D44/M4					
M3L	0.43%	0.45%		0.44%	0.02%		1.29	1.26		1.28	0.02
D44	34.21%	34.51%		34.36%	0.21%	Cross-linking					
T444	1.33%	2.03%		1.68%	0.49%		42.06%	43.34%		42.70%	0.01
D43L	5.18%	4.77%		4.97%	0.29%						
D44N	6.95%	6.31%		6.63%	0.45%						
T444N	1.40%	1.52%		1.46%	0.09%						

Δmreb+mreb

Δmreb+mreb	T1	T2	T3	ave	SD		T1	T2	T3	Average	SD
M3	2.88%	3.43%	2.94%	3.08%	0.31%	Glycan Length					
M4	22.46%	41.70%	35.60%	33.25%	9.83%		24.08	23.17	25.04	24.10	0.94
M2	1.02%	1.49%	1.45%	1.32%	0.26%	D44/M4					
M3L	0.28%	0.56%	0.12%	0.32%	0.23%		0.69	0.88	0.84	0.80	0.10
D44	15.46%	36.83%	29.90%	27.40%	10.90%	Cross-linking					
T444	0.36%	0.50%	0.44%	0.43%	0.07%		16.78%	41.05%	33.27%	30.37%	0.12
D43L	0.60%	3.22%	2.48%	2.10%	1.35%						
D44N	3.20%	3.82%	3.57%	3.53%	0.31%						
T444N	0.95%	0.49%	0.42%	0.62%	0.29%						

8 - Δmreb R.L1

8 - Δmreb R.L1	T1	T2	T3	ave	SD		T1	T2	T3	Average	SD
M3	4.19%	8.37%	7.19%	6.58%	2.16%	Glycan Length					
M4	28.89%	42.26%	38.35%	36.50%	6.88%		20.55	19.58	19.90	20.01	0.50
M2	0.21%	1.06%	0.84%	0.71%	0.44%	D44/M4					
M3L	0.47%	1.05%	0.61%	0.71%	0.30%		0.60	0.70	0.78	0.69	0.09
D44	17.22%	29.63%	29.82%	25.55%	7.22%	Cross-linking					
T444	4.36%	0.32%	0.45%	1.71%	2.29%		27.06%	32.29%	33.11%	30.82%	0.03
D43L	1.13%	2.01%	2.39%	1.84%	0.65%						
D44N	3.65%	4.44%	4.37%	4.15%	0.43%						
T444N	1.21%	0.67%	0.66%	0.85%	0.32%						

9 - Δmreb R.L4

9 - Δmreb R.L4	T1	T2	T3	ave	SD		T1	T2	T3	Average	SD
M3	3.13%	3.83%	8.42%	5.13%	2.87%	Glycan Length					
M4	33.22%	35.00%	41.46%	36.56%	4.33%		16.11	15.41	20.99	17.50	3.04
M2	0.46%	0.65%	1.06%	0.72%	0.31%	D44/M4					
M3L	0.53%	0.65%	1.01%	0.73%	0.25%		0.77	0.71	0.74	0.74	0.03
D44	25.48%	24.76%	30.81%	27.02%	3.31%	Cross-linking					
T444	0.40%	0.19%	0.43%	0.34%	0.13%		27.75%	26.51%	33.67%	29.31%	0.04
D43L	1.46%	1.36%	1.98%	1.60%	0.33%						
D44N	5.50%	5.62%	4.24%	5.12%	0.76%						
T444N	0.71%	0.87%	0.52%	0.70%	0.18%						

10 - Δmreb R.L7

10 - Δmreb R.L7	T1	T2	T3	ave	SD		T1	T2	T3	Average	SD
M3	11.35%	5.48%	7.23%	8.02%	3.01%	Glycan Length					
M4	31.96%	28.97%	33.48%	31.47%	2.30%		17.44	17.45	13.85	16.25	2.07
M2	0.24%	0.31%	0.27%	0.27%	0.03%	D44/M4					
M3L	0.74%	0.37%	0.49%	0.53%	0.19%		1.01	0.90	0.95	0.95	0.05
D44	32.24%	26.21%	31.81%	30.09%	3.37%	Cross-linking					
T444	0.87%	0.22%	1.44%	0.84%	0.61%		37.50%	29.47%	38.23%	35.07%	0.05
D43L	3.51%	2.82%	3.55%	3.29%	0.41%						
D44N	5.33%	4.98%	6.56%	5.62%	0.83%						
T444N	0.41%	0.75%	0.66%	0.60%	0.18%						

UPLC statistical analyses

M4
WT and WT+MreB
t-Test: Two-Sample Assuming Unequal Variances

	Variable 1	Variable 2
Mean	0.396148	0.333128
Variance	6.85E-05	0.000134
Observations	3	3
Hypothesized Mean Difference	0	
df	4	
t Stat	7.661038	
P(T<=t) one-tail	0.00078	
t Critical one-tail	2.131847	
P(T<=t) two-tail	0.00156	
t Critical two-tail	2.776445	

D44
WT and WT+MreB
t-Test: Two-Sample Assuming Unequal Variances

	Variable 1	Variable 2
Mean	0.348221	0.304118
Variance	0.000187	0.000418
Observations	3	3
Hypothesized Mean Difference	0	
df	3	
t Stat	3.105856	
P(T<=t) one-tail	0.026526	
t Critical one-tail	2.353363	
P(T<=t) two-tail	0.053053	
t Critical two-tail	3.182446	

D44/M4
WT and WT+MreB
t-Test: Two-Sample Assuming Unequal Variances

	Variable 1	Variable 2
Mean	0.878791	0.912243
Variance	0.00027	0.000868
Observations	3	3
Hypothesized Mean Difference	0	
df	3	
t Stat	-1.71718	
P(T<=t) one-tail	0.092223	
t Critical one-tail	2.353363	
P(T<=t) two-tail	0.184447	
t Critical two-tail	3.182446	

Cross-linking
WT and WT+MreB
t-Test: Two-Sample Assuming Unequal Variances

	Variable 1	Variable 2
Mean	0.391986	0.334171
Variance	6.95E-05	0.001035
Observations	3	3
Hypothesized Mean Difference	0	
df	2	
t Stat	3.01258	
P(T<=t) one-tail	0.04739	
t Critical one-tail	2.919986	
P(T<=t) two-tail	0.09478	
t Critical two-tail	4.302653	

Glycan length
WT and WT+MreB
t-Test: Two-Sample Assuming Unequal Variances

	Variable 1	Variable 2
Mean	26.15846	16.85477
Variance	6.424769	0.076716
Observations	3	3
Hypothesized Mean Difference	0	
df	2	
t Stat	6.319889	
P(T<=t) one-tail	0.012067	
t Critical one-tail	2.919986	
P(T<=t) two-tail	0.024134	
t Critical two-tail	4.302653	

M4
WT vs WTRL1
t-Test: Two-Sample Assuming Unequal Variances

	Variable 1	Variable 2
Mean	0.396148	0.412754
Variance	6.85E-05	0.000417
Observations	3	3
Hypothesized Mean Difference	0	
df	3	
t Stat	-1.30497	
P(T<=t) one-tail	0.141488	
t Critical one-tail	2.353363	
P(T<=t) two-tail	0.282977	
t Critical two-tail	3.182446	

D44
WT vs WTRL1
t-Test: Two-Sample Assuming Unequal Variances

	Variable 1	Variable 2
Mean	0.348221	0.359215
Variance	0.000187	0.000204
Observations	3	3
Hypothesized Mean Difference	0	
df	4	
t Stat	-0.96355	
P(T<=t) one-tail	0.194917	
t Critical one-tail	2.131847	
P(T<=t) two-tail	0.389835	
t Critical two-tail	2.776445	

D44/M4
WT vs WTRL1
t-Test: Two-Sample Assuming Unequal Variances

	Variable 1	Variable 2
Mean	0.878791	0.87058
Variance	0.00027	0.000107
Observations	3	3
Hypothesized Mean Difference	0	
df	3	
t Stat	0.732412	
P(T<=t) one-tail	0.258475	
t Critical one-tail	2.353363	
P(T<=t) two-tail	0.516951	
t Critical two-tail	3.182446	

Cross-linking
WT vs WTRL1
t-Test: Two-Sample Assuming Unequal Variances

	Variable 1	Variable 2
Mean	0.391986	0.396026
Variance	6.95E-05	0.000118
Observations	3	3
Hypothesized Mean Difference	0	
df	4	
t Stat	-0.51088	
P(T<=t) one-tail	0.318169	
t Critical one-tail	2.131847	
P(T<=t) two-tail	0.636339	
t Critical two-tail	2.776445	

Glycan Length
WT vs WTRL1
t-Test: Two-Sample Assuming Unequal Variances

	Variable 1	Variable 2
Mean	26.15846	28.4854
Variance	6.424769	12.9228
Observations	3	3
Hypothesized Mean Difference	0	
df	4	
t Stat	-0.91629	
P(T<=t) one-tail	0.205679	
t Critical one-tail	2.131847	
P(T<=t) two-tail	0.411359	
t Critical two-tail	2.776445	

M4
WT vs WTRL4
t-Test: Two-Sample Assuming Unequal Variances

	Variable 1	Variable 2
Mean	0.396148	0.418123
Variance	6.85E-05	0.001352
Observations	3	3
Hypothesized Mean Difference	0	
df	2	
t Stat	-1.01002	
P(T<=t) one-tail	0.209407	
t Critical one-tail	2.919986	
P(T<=t) two-tail	0.418813	
t Critical two-tail	4.302653	

D44
WT vs WTRL4
t-Test: Two-Sample Assuming Unequal Variances

	Variable 1	Variable 2
Mean	0.348221	0.33083
Variance	0.000187	0.000282
Observations	3	3
Hypothesized Mean Difference	0	
df	4	
t Stat	1.39093	
P(T<=t) one-tail	0.118312	
t Critical one-tail	2.131847	
P(T<=t) two-tail	0.236624	
t Critical two-tail	2.776445	

D44/M4
WT vs WTRL4
t-Test: Two-Sample Assuming Unequal Variances

	Variable 1	Variable 2
Mean	0.878791	0.79425
Variance	0.00027	0.004048
Observations	3	3
Hypothesized Mean Difference	0	
df	2	
t Stat	2.228304	
P(T<=t) one-tail	0.077844	
t Critical one-tail	2.919986	
P(T<=t) two-tail	0.155687	
t Critical two-tail	4.302653	

Cross-linking
WT vs WTRL4
t-Test: Two-Sample Assuming Unequal Variances

	Variable 1	Variable 2
Mean	0.391986	0.362359
Variance	6.95E-05	0.000306
Observations	3	3
Hypothesized Mean Difference	0	
df	3	
t Stat	2.649573	
P(T<=t) one-tail	0.038511	
t Critical one-tail	2.353363	
P(T<=t) two-tail	0.077022	
t Critical two-tail	3.182446	

Glycan length
WT vs WTRL4
t-Test: Two-Sample Assuming Unequal Variances

	Variable 1	Variable 2
Mean	26.15846	35.56551
Variance	6.424769	28.247
Observations	3	3
Hypothesized Mean Difference	0	
df	3	
t Stat	-2.76711	
P(T<=t) one-tail	0.034868	
t Critical one-tail	2.353363	
P(T<=t) two-tail	0.069737	
t Critical two-tail	3.182446	

M4
WT vs WTRL7
t-Test: Two-Sample Assuming Unequal Variances

	Variable 1	Variable 2
Mean	0.396148	0.372184
Variance	6.85E-05	0.003487
Observations	3	2
Hypothesized Mean Difference	0	
df	1	
t Stat	0.570213	
P(T<=t) one-tail	0.335043	
t Critical one-tail	6.313752	
P(T<=t) two-tail	0.670085	
t Critical two-tail	12.7062	

D44
WT vs WTRL7
t-Test: Two-Sample Assuming Unequal Variances

	Variable 1	Variable 2
Mean	0.348221	0.291816
Variance	0.000187	0.001533
Observations	3	2
Hypothesized Mean Difference	0	
df	1	
t Stat	1.958937	
P(T<=t) one-tail	0.150241	
t Critical one-tail	6.313752	
P(T<=t) two-tail	0.300483	
t Critical two-tail	12.7062	

D44/M4
WT vs WTRL7
t-Test: Two-Sample Assuming Unequal Variances

	Variable 1	Variable 2
Mean	0.878791	0.785603
Variance	0.00027	0.000377
Observations	3	2
Hypothesized Mean Difference	0	
df	2	
t Stat	5.582305	
P(T<=t) one-tail	0.015312	
t Critical one-tail	2.919986	
P(T<=t) two-tail	0.030624	
t Critical two-tail	4.302653	

Cross-linking
WT vs WTRL7
t-Test: Two-Sample Assuming Unequal Variances

	Variable 1	Variable 2
Mean	0.391986	0.318031
Variance	6.95E-05	0.000438
Observations	3	2
Hypothesized Mean Difference	0	
df	1	
t Stat	4.754362	
P(T<=t) one-tail	0.065989	
t Critical one-tail	6.313752	
P(T<=t) two-tail	0.131978	
t Critical two-tail	12.7062	

Glycan Length
WT vs WTRL7
t-Test: Two-Sample Assuming Unequal Variances

	Variable 1	Variable 2
Mean	26.15846	15.46959
Variance	6.424769	1.471645
Observations	3	2
Hypothesized Mean Difference	0	
df	3	
t Stat	6.301307	
P(T<=t) one-tail	0.004037	
t Critical one-tail	2.353363	
P(T<=t) two-tail	0.008075	
t Critical two-tail	3.182446	

M4
WT and Δmreb
t-Test: Two-Sample Assuming Unequal Variances

	Variable 1	Variable 2
Mean	0.396148	0.26915
Variance	6.85E-05	3.58E-05
Observations	3	2
Hypothesized Mean Difference	0	
df	3	
t Stat	19.88997	
P(T<=t) one-tail	0.000139	
t Critical one-tail	2.353363	
P(T<=t) two-tail	0.000278	
t Critical two-tail	3.182446	

D44
WT and Δmreb
t-Test: Two-Sample Assuming Unequal Variances

	Variable 1	Variable 2
Mean	0.348221	0.343642
Variance	0.000187	4.5E-06
Observations	3	2
Hypothesized Mean Difference	0	
df	2	
t Stat	0.569702	
P(T<=t) one-tail	0.31317	
t Critical one-tail	2.919986	
P(T<=t) two-tail	0.62634	
t Critical two-tail	4.302653	

D44/M4
WT and Δmreb
t-Test: Two-Sample Assuming Unequal Variances

	Variable 1	Variable 2
Mean	0.878791	1.276995
Variance	0.00027	0.000421
Observations	3	2
Hypothesized Mean Difference	0	
df	2	
t Stat	-22.9659	
P(T<=t) one-tail	0.000945	
t Critical one-tail	2.919986	
P(T<=t) two-tail	0.001891	
t Critical two-tail	4.302653	

Cross-linking
WT and Δmreb
t-Test: Two-Sample Assuming Unequal Variances

	Variable 1	Variable 2
Mean	0.391986	0.426997
Variance	6.95E-05	8.28E-05
Observations	3	2
Hypothesized Mean Difference	0	
df	2	
t Stat	-4.35753	
P(T<=t) one-tail	0.024419	
t Critical one-tail	2.919986	
P(T<=t) two-tail	0.048839	
t Critical two-tail	4.302653	

Glycan length
WT and Δmreb
t-Test: Two-Sample Assuming Unequal Variances

	Variable 1	Variable 2
Mean	26.15846	12.37746
Variance	6.424769	0.305933
Observations	3	2
Hypothesized Mean Difference	0	
df	2	
t Stat	9.097692	
P(T<=t) one-tail	0.005934	
t Critical one-tail	2.919986	
P(T<=t) two-tail	0.011867	
t Critical two-tail	4.302653	

M4
WT vs ΔmreB+mreB
t-Test: Two-Sample Assuming Unequal Variances

	Variable 1	Variable 2
Mean	0.396148	0.332499
Variance	6.85E-05	0.009669
Observations	3	3
Hypothesized Mean Difference	0	
df	2	
t Stat	1.117183	
P(T<=t) one-tail	0.190058	
t Critical one-tail	2.919986	
P(T<=t) two-tail	0.380117	
t Critical two-tail	4.302653	

D44
WT vs ΔmreB+mreB
t-Test: Two-Sample Assuming Unequal Variances

	Variable 1	Variable 2
Mean	0.348221	0.274002
Variance	0.000187	0.011887
Observations	3	3
Hypothesized Mean Difference	0	
df	2	
t Stat	1.169915	
P(T<=t) one-tail	0.181292	
t Critical one-tail	2.919986	
P(T<=t) two-tail	0.362584	
t Critical two-tail	4.302653	

D44/M4
WT vs ΔmreB+mreB
t-Test: Two-Sample Assuming Unequal Variances

	Variable 1	Variable 2
Mean	0.878791	0.804016
Variance	0.00027	0.010453
Observations	3	3
Hypothesized Mean Difference	0	
df	2	
t Stat	1.250715	
P(T<=t) one-tail	0.168761	
t Critical one-tail	2.919986	
P(T<=t) two-tail	0.337521	
t Critical two-tail	4.302653	

Cross-linking
WT vs ΔmreB+mreB
t-Test: Two-Sample Assuming Unequal Variances

	Variable 1	Variable 2
Mean	0.391986	0.303699
Variance	6.95E-05	0.015361
Observations	3	3
Hypothesized Mean Difference	0	
df	2	
t Stat	1.231039	
P(T<=t) one-tail	0.171715	
t Critical one-tail	2.919986	
P(T<=t) two-tail	0.34343	
t Critical two-tail	4.302653	

Glycan Length
WT vs ΔmreB+mreB
t-Test: Two-Sample Assuming Unequal Variances

	Variable 1	Variable 2
Mean	26.15846	24.09574
Variance	6.424769	0.88159
Observations	3	3
Hypothesized Mean Difference	0	
df	3	
t Stat	1.321753	
P(T<=t) one-tail	0.139001	
t Critical one-tail	2.353363	
P(T<=t) two-tail	0.278003	
t Critical two-tail	3.182446	

M4 — WT vs MREBRL1
t-Test: Two-Sample Assuming Unequal Variances

	Variable 1	Variable 2
Mean	0.396148	0.365011
Variance	6.85E-05	0.004729
Observations	3	3
Hypothesized Mean Difference	0	
df	2	
t Stat	0.778639	
P(T<=t) one-tail	0.258845	
t Critical one-tail	2.919986	
P(T<=t) two-tail	0.517691	
t Critical two-tail	4.302653	

D44 — WT vs MREBRL1
t-Test: Two-Sample Assuming Unequal Variances

	Variable 1	Variable 2
Mean	0.348221	0.255537
Variance	0.000187	0.005215
Observations	3	3
Hypothesized Mean Difference	0	
df	2	
t Stat	2.184134	
P(T<=t) one-tail	0.080298	
t Critical one-tail	2.919986	
P(T<=t) two-tail	0.160596	
t Critical two-tail	4.302653	

D44/M4 — WT vs MREBRL1
t-Test: Two-Sample Assuming Unequal Variances

	Variable 1	Variable 2
Mean	0.878791	0.691478
Variance	0.00027	0.008301
Observations	3	3
Hypothesized Mean Difference	0	
df	2	
t Stat	3.504364	
P(T<=t) one-tail	0.036333	
t Critical one-tail	2.919986	
P(T<=t) two-tail	0.072665	
t Critical two-tail	4.302653	

Cross-linking — WT vs MREBRL1
t-Test: Two-Sample Assuming Unequal Variances

	Variable 1	Variable 2
Mean	0.391986	0.308173
Variance	6.95E-05	0.001077
Observations	3	3
Hypothesized Mean Difference	0	
df	2	
t Stat	4.28677	
P(T<=t) one-tail	0.025172	
t Critical one-tail	2.919986	
P(T<=t) two-tail	0.050344	
t Critical two-tail	4.302653	

Glycan Length — WT vs MREBRL1
t-Test: Two-Sample Assuming Unequal Variances

	Variable 1	Variable 2
Mean	26.15846	20.00982
Variance	6.424769	0.245405
Observations	3	3
Hypothesized Mean Difference	0	
df	2	
t Stat	4.123546	
P(T<=t) one-tail	0.027042	
t Critical one-tail	2.919986	
P(T<=t) two-tail	0.054084	
t Critical two-tail	4.302653	

M4 — WT vs MREBRL4
t-Test: Two-Sample Assuming Unequal Variances

	Variable 1	Variable 2
Mean	0.396148	0.365614
Variance	6.85E-05	0.001878
Observations	3	3
Hypothesized Mean Difference	0	
df	2	
t Stat	1.198767	
P(T<=t) one-tail	0.176695	
t Critical one-tail	2.919986	
P(T<=t) two-tail	0.35339	
t Critical two-tail	4.302653	

D44 — WT vs MREBRL4
t-Test: Two-Sample Assuming Unequal Variances

	Variable 1	Variable 2
Mean	0.348221	0.270171
Variance	0.000187	0.001095
Observations	3	3
Hypothesized Mean Difference	0	
df	3	
t Stat	3.776107	
P(T<=t) one-tail	0.016265	
t Critical one-tail	2.353363	
P(T<=t) two-tail	0.03253	
t Critical two-tail	3.182446	

D44/M4 — WT vs MREBRL4
t-Test: Two-Sample Assuming Unequal Variances

	Variable 1	Variable 2
Mean	0.878791	0.739158
Variance	0.00027	0.000899
Observations	3	3
Hypothesized Mean Difference	0	
df	3	
t Stat	7.073445	
P(T<=t) one-tail	0.002905	
t Critical one-tail	2.353363	
P(T<=t) two-tail	0.00581	
t Critical two-tail	3.182446	

Cross-linking — WT vs MREBRL4
t-Test: Two-Sample Assuming Unequal Variances

	Variable 1	Variable 2
Mean	0.391986	0.293072
Variance	6.95E-05	0.001463
Observations	3	3
Hypothesized Mean Difference	0	
df	2	
t Stat	4.376289	
P(T<=t) one-tail	0.024225	
t Critical one-tail	2.919986	
P(T<=t) two-tail	0.048451	
t Critical two-tail	4.302653	

Glycan Length — WT vs MREBRL4
t-Test: Two-Sample Assuming Unequal Variances

	Variable 1	Variable 2
Mean	26.15846	17.50259
Variance	6.424769	9.222098
Observations	3	3
Hypothesized Mean Difference	0	
df	4	
t Stat	3.79016	
P(T<=t) one-tail	0.009633	
t Critical one-tail	2.131847	
P(T<=t) two-tail	0.019266	
t Critical two-tail	2.776445	

M4 — WT vs MREBRL7
t-Test: Two-Sample Assuming Unequal Variances

	Variable 1	Variable 2
Mean	0.396148	0.372184
Variance	6.85E-05	0.003487
Observations	3	2
Hypothesized Mean Difference	0	
df	1	
t Stat	0.570213	
P(T<=t) one-tail	0.335043	
t Critical one-tail	6.313752	
P(T<=t) two-tail	0.670085	
t Critical two-tail	12.7062	

D44 — WT vs MREBRL7
t-Test: Two-Sample Assuming Unequal Variances

	Variable 1	Variable 2
Mean	0.348221	0.291816
Variance	0.000187	0.001533
Observations	3	2
Hypothesized Mean Difference	0	
df	1	
t Stat	1.958937	
P(T<=t) one-tail	0.150241	
t Critical one-tail	6.313752	
P(T<=t) two-tail	0.300483	
t Critical two-tail	12.7062	

D44/M4 — WT vs MREBRL7
t-Test: Two-Sample Assuming Unequal Variances

	Variable 1	Variable 2
Mean	0.878791	0.954575
Variance	0.00027	0.002733
Observations	3	3
Hypothesized Mean Difference	0	
df	2	
t Stat	-2.39536	
P(T<=t) one-tail	0.06944	
t Critical one-tail	2.919986	
P(T<=t) two-tail	0.138881	
t Critical two-tail	4.302653	

Cross-linking — WT vs MREBRL7
t-Test: Two-Sample Assuming Unequal Variances

	Variable 1	Variable 2
Mean	0.391986	0.350676
Variance	6.95E-05	0.002362
Observations	3	3
Hypothesized Mean Difference	0	
df	2	
t Stat	1.451176	
P(T<=t) one-tail	0.141916	
t Critical one-tail	2.919986	
P(T<=t) two-tail	0.283831	
t Critical two-tail	4.302653	

Glycan Length — WT vs MREBRL7
t-Test: Two-Sample Assuming Unequal Variances

	Variable 1	Variable 2
Mean	26.15846	16.24887
Variance	6.424769	4.302776
Observations	3	3
Hypothesized Mean Difference	0	
df	4	
t Stat	5.240417	
P(T<=t) one-tail	0.003169	
t Critical one-tail	2.131847	
P(T<=t) two-tail	0.006338	
t Critical two-tail	2.776445	

M4 — Δmreb and Δmreb+mreb
t-Test: Two-Sample Assuming Unequal Variances

	Variable 1	Variable 2
Mean	0.26915	0.332499
Variance	3.58E-05	0.009669
Observations	2	3
Hypothesized Mean Difference	0	
df	2	
t Stat	-1.11275	
P(T<=t) one-tail	0.190817	
t Critical one-tail	2.919986	
P(T<=t) two-tail	0.381633	
t Critical two-tail	4.302653	

D44 — Δmreb and Δmreb+mreb
t-Test: Two-Sample Assuming Unequal Variances

	Variable 1	Variable 2
Mean	0.343642	0.274002
Variance	4.5E-06	0.011887
Observations	2	3
Hypothesized Mean Difference	0	
df	2	
t Stat	1.106027	
P(T<=t) one-tail	0.191975	
t Critical one-tail	2.919986	
P(T<=t) two-tail	0.38395	
t Critical two-tail	4.302653	

D44/M4 — Δmreb and Δmreb+mreb
t-Test: Two-Sample Assuming Unequal Variances

	Variable 1	Variable 2
Mean	1.276995	0.804016
Variance	0.000421	0.010453
Observations	2	3
Hypothesized Mean Difference	0	
df	2	
t Stat	7.781191	
P(T<=t) one-tail	0.008059	
t Critical one-tail	2.919986	
P(T<=t) two-tail	0.016118	
t Critical two-tail	4.302653	

Cross-linking — Δmreb and Δmreb+mreb
t-Test: Two-Sample Assuming Unequal Variances

	Variable 1	Variable 2
Mean	0.426997	0.303699
Variance	8.28E-05	0.015361
Observations	2	3
Hypothesized Mean Difference	0	
df	2	
t Stat	1.716177	
P(T<=t) one-tail	0.114133	
t Critical one-tail	2.919986	
P(T<=t) two-tail	0.228267	
t Critical two-tail	4.302653	

Glycan length — Δmreb and Δmreb+mreb
t-Test: Two-Sample Assuming Unequal Variances

	Variable 1	Variable 2
Mean	12.37746	24.09574
Variance	0.305933	0.88159
Observations	2	3
Hypothesized Mean Difference	0	
df	3	
t Stat	-17.5304	
P(T<=t) one-tail	0.000202	
t Critical one-tail	2.353363	
P(T<=t) two-tail	0.000405	
t Critical two-tail	3.182446	

M4 — ΔmreB vs MREBRL1
t-Test: Two-Sample Assuming Unequal Variances

	Variable 1	Variable 2
Mean	0.26915	0.365011
Variance	3.58E-05	0.004729
Observations	2	3
Hypothesized Mean Difference	0	
df	2	
t Stat	-2.40087	
P(T<=t) one-tail	0.069185	
t Critical one-tail	2.919986	
P(T<=t) two-tail	0.13837	
t Critical two-tail	4.302653	

D44 vs MREBRL1
t-Test: Two-Sample Assuming Unequal Variances

	Variable 1	Variable 2
Mean	0.343642	0.270171
Variance	4.5E-06	0.001095
Observations	2	3
Hypothesized Mean Difference	0	
df	2	
t Stat	3.834479	
P(T<=t) one-tail	0.030888	
t Critical one-tail	2.919986	
P(T<=t) two-tail	0.061777	
t Critical two-tail	4.302653	

D44/M4 vs MREBRL1
t-Test: Two-Sample Assuming Unequal Variances

	Variable 1	Variable 2
Mean	1.276995	20.00982
Variance	0.000421	0.245405
Observations	2	3
Hypothesized Mean Difference	0	
df	2	
t Stat	-65.413	
P(T<=t) one-tail	0.000117	
t Critical one-tail	2.919986	
P(T<=t) two-tail	0.000234	
t Critical two-tail	4.302653	

Cross-linking — ΔmreB vs MREBRL1
t-Test: Two-Sample Assuming Unequal Variances

	Variable 1	Variable 2
Mean	0.426997	0.308173
Variance	8.28E-05	0.001077
Observations	2	3
Hypothesized Mean Difference	0	
df	2	
t Stat	5.937374	
P(T<=t) one-tail	0.013607	
t Critical one-tail	2.919986	
P(T<=t) two-tail	0.027214	
t Critical two-tail	4.302653	

Glycan Length — ΔmreB vs MREBRL1
t-Test: Two-Sample Assuming Unequal Variances

	Variable 1	Variable 2
Mean	12.37746	20.00982
Variance	0.305933	0.245405
Observations	2	3
Hypothesized Mean Difference	0	
df	2	
t Stat	-15.7521	
P(T<=t) one-tail	0.002003	
t Critical one-tail	2.919986	
P(T<=t) two-tail	0.004006	
t Critical two-tail	4.302653	

M4 — ΔmreB vs MREBRL4
t-Test: Two-Sample Assuming Unequal Variances

	Variable 1	Variable 2
Mean	0.26915	0.365614
Variance	3.58E-05	0.001878
Observations	2	3
Hypothesized Mean Difference	0	
df	2	
t Stat	-3.80175	
P(T<=t) one-tail	0.031373	
t Critical one-tail	2.919986	
P(T<=t) two-tail	0.062747	
t Critical two-tail	4.302653	

D44 — ΔmreB vs MREBRL4
t-Test: Two-Sample Assuming Unequal Variances

	Variable 1	Variable 2
Mean	0.343642	0.300862
Variance	4.5E-06	0.001133
Observations	2	3
Hypothesized Mean Difference	0	
df	2	
t Stat	2.194977	
P(T<=t) one-tail	0.079686	
t Critical one-tail	2.919986	
P(T<=t) two-tail	0.159372	
t Critical two-tail	4.302653	

D44/M4 — ΔmreB vs MREBRL4
t-Test: Two-Sample Assuming Unequal Variances

	Variable 1	Variable 2
Mean	1.276995	0.739158
Variance	0.000421	0.000899
Observations	2	3
Hypothesized Mean Difference	0	
df	3	
t Stat	23.81254	
P(T<=t) one-tail	8.11E-05	
t Critical one-tail	2.353363	
P(T<=t) two-tail	0.000162	
t Critical two-tail	3.182446	

Cross-linking — ΔmreB vs MREBRL4
t-Test: Two-Sample Assuming Unequal Variances

	Variable 1	Variable 2
Mean	0.426997	0.293072
Variance	8.28E-05	0.001463
Observations	2	3
Hypothesized Mean Difference	0	
df	2	
t Stat	5.822193	
P(T<=t) one-tail	0.014128	
t Critical one-tail	2.919986	
P(T<=t) two-tail	0.028256	
t Critical two-tail	4.302653	

Glycan Length — ΔmreB vs MREBRL4
t-Test: Two-Sample Assuming Unequal Variances

	Variable 1	Variable 2
Mean	12.37746	17.50259
Variance	0.305933	9.222098
Observations	2	3
Hypothesized Mean Difference	0	
df	3	
t Stat	-2.85302	
P(T<=t) one-tail	0.052017	
t Critical one-tail	2.919986	
P(T<=t) two-tail	0.104033	
t Critical two-tail	4.302653	

M4 — ΔmreB vs MREBRL7
t-Test: Two-Sample Assuming Unequal Variances

	Variable 1	Variable 2
Mean	0.26915	0.314683
Variance	3.58E-05	0.000527
Observations	2	3
Hypothesized Mean Difference	0	
df	2	
t Stat	-3.27182	
P(T<=t) one-tail	0.041039	
t Critical one-tail	2.919986	
P(T<=t) two-tail	0.082079	
t Critical two-tail	4.302653	

D44 — ΔmreB vs MREBRL7
t-Test: Two-Sample Assuming Unequal Variances

	Variable 1	Variable 2
Mean	0.343642	0.300862
Variance	4.5E-06	0.001133
Observations	2	3
Hypothesized Mean Difference	0	
df	2	
t Stat	2.194977	
P(T<=t) one-tail	0.079686	
t Critical one-tail	2.919986	
P(T<=t) two-tail	0.159372	
t Critical two-tail	4.302653	

D44/M4 — ΔmreB vs MREBRL7
t-Test: Two-Sample Assuming Unequal Variances

	Variable 1	Variable 2
Mean	1.276995	0.954575
Variance	0.000421	0.002733
Observations	2	3
Hypothesized Mean Difference	0	
df	3	
t Stat	9.628148	
P(T<=t) one-tail	0.001189	
t Critical one-tail	2.353363	
P(T<=t) two-tail	0.002378	
t Critical two-tail	3.182446	

Cross-linking — ΔmreB vs MREBRL7
t-Test: Two-Sample Assuming Unequal Variances

	Variable 1	Variable 2
Mean	0.426997	0.350676
Variance	8.28E-05	0.002362
Observations	2	3
Hypothesized Mean Difference	0	
df	2	
t Stat	2.651376	
P(T<=t) one-tail	0.058834	
t Critical one-tail	2.919986	
P(T<=t) two-tail	0.117667	
t Critical two-tail	4.302653	

Glycan Length — ΔmreB vs MREBRL7
t-Test: Two-Sample Assuming Unequal Variances

	Variable 1	Variable 2
Mean	12.37746	16.24887
Variance	0.305933	4.302776
Observations	2	3
Hypothesized Mean Difference	0	
df	2	
t Stat	-3.07291	
P(T<=t) one-tail	0.045793	
t Critical one-tail	2.919986	
P(T<=t) two-tail	0.091585	
t Critical two-tail	4.302653	